Materials Science

Photoelectron Spectroscopy of Intercalation Phases: Na and Li in V_2O_5 Thin Films and $LiMn_2O_4$

Qi-Hui Wu

Ph.D. Dissertation

Accepted by Surface Science Institute, Department of Materials Science, Darmstadt University of Technology

Date of delivery: 2003-04-29

Date of oral examination: 2003-07-01

Photoelectron Spectroscopy of Intercalation Phases: Na and Li in V_2O_5 Thin Films and $LiMn_2O_4$

Ph.D. Dissertation

Surface Science Institute, Department of Materials Science,
Darmstadt University of Technology, Darmstadt, Germany

By Qi-Hui Wu

born in Fujian, China

April 2003

The work presented here has been conducted between Sept. 2000 and February 2003 at Darmstadt University of Technology, under the supervision of Prof. Dr. W. Jaegermann and Dr. A. Thißen

1st referee: Prof. Dr. W. Jaegermann
2nd referee: Prof. Dr. H. von Seggern

Oral examination: June, 2003

Zusammenfassung

Aufgrund ihrer hohen Kapazität und Batteriespannung dienen Vanadiumpentaoxid (V_2O_5) und Lithiumpermanganat ($LiMn_2O_4$) als vielversprechende Kathodenmaterialien für Lithium-Ionen-Batterien. Die Forschungsarbeiten wurden bisher schwerpunktmäßig auf die elektrochemischen und strukturellen Eigenschaften während der Lithium-Interkalation fokussiert. Nähere Kenntnisse zu Änderungen der elektronischen Struktur und dem Interkalationsmechanismus liegen jedoch noch nicht vor. Insbesondere fehlt eine allgemein akzeptierte Theorie zur Natur und dem Ausmaß der Wechselwirkung der Alkali-Ionen mit ihrem Wirtsgitter.

Die vorliegende Dissertation befasst sich mit der elektronischen Struktur der Übergangsmetalloxide und deren Umwandlung während des Interkalationsprozesses der Alkalimetalle. Die Interkalation von Natrium und Lithium in dünne Schichten von V_2O_5 und von pulverartigen Proben von $LiMnO_4$ wurde hauptsächlich mittels Röntgen-Photoelektronen-Spektroskopie (XPS), Ultraviolett-Photoelektronen-Spektroskopie (UPS) und Resonant-Photoemissions-Spektroskopie (RPES) untersucht.

Die durch PVD hergestellten dünnen V_2O_5-Filme, waren nahezu stöchiometrisch aufgebaut mit nur ca. 4% Sauerstoff-Defekten. Nach der Abscheidung auf ein HOPG-Substrat erhielt man eine glatte und polykristalline Oxide-Oberfläche. Das Valenzband von V_2O_5 wird durch Hybridisierung der O2p und V3d Zustände gebildet. Im RPES-Spetrum ist ersichtlich, dass die V3d Zustände mit einem Anteil von ungefähr 20% an dem Valenzband beteiligt sind. Daher beträgt die wirkliche Elektronenbesetzung der 3d Valenzzustände des Vanadiumions in Vanadiumpentaoxid V_2O_5 ungefähr 2 (statt 0), und das einfache ionische Modell ist zur Beschreibung der Bindungsverhältnisse ungeeignet. Der Einfluss von Temperaturbehandlungen auf die V_2O_5–Schichten wurde ebenfalls untersucht. Temperung der Schichten führt zur Bildung von unterstöchiometrischem V_2O_{5-x}, was durch die chemisch verschobenen Komponenten in der Emissionslinie des $V2p_{3/2}$ und durch das reduzierte O1s/V2p Intensitätsverhältnis bewiesen werden kann. Während der Behandlung der unterstöchiometrischem Filme bei 400°C in einer Sauerstoff-Atmosphäre werden die Vanadium-Ionen wieder in höhere Oxidationsstufe aufoxidiert.

Alkalimetalle werden augenblicklich in V_2O_5 interkaliert, sobald sie bei Raumtemperatur auf die Oberfläche abgeschieden werden. Aufgrund der Beschränkung der Interkalationskinetik bleibt ein kleiner Anteil der Alkalimetallatome (ca. 10 %) auf der Oberfläche adsorbiert. Die Ergebnisse dieser Arbeit zeigen, dass die Elektronen der s-Orbitale der eingelagerten Alkalimetalle größtenteils in die 3d-Orbitale des Übergangsmetalls

übertragen werden und die Reduktion der Übergangsmetallionen verursachen. Wie aus den XPS und UPS Daten folgt liegt der Wert des effektive Ladungstransfers für Na3s und Li2s jeweils bei ca. 0,42 bzw. 0,55 Elektronen pro Alkaliatom. Bei niedrigem Gehalt der eingelagerten Alkalimetalle ändert sich die elektronische und kristalline Struktur des Wirtsgitters nicht stark. Bei Natrium können die mit Alkalimetall gesättigten V_2O_5-Filme ohne Zersetzung eine Stöchiometrie von $Na_{1.4}V_2O_5$ erreichen, und bei Lithium liegt dieser Sättigungswert ungefähr bei $Li_{2.5}V_2O_5$. Beim Erreichen des Grenzwertes für die Alkali-Interkalation werden die weiter abgeschiedenen Alkaliatome nicht mehr ins Wirtsgitter interkaliert; stattdessen werden Oxide, Peroxide und sogar metallisches Alkali auf der Oberfläche gebildet. Die Bildung der Oxid-Oberflächenschichten auf den Elektroden hat wichtige Auswirkungen auf die Batterie-Performance. Ein besseres Verständnis dieser Schichten und deren Bildung kann von großer Bedeutung sein, das Stabilitätsproblem der Lithium-Ionen-Batterien, wie z.B. Kapazitätsverlust, Leistungsverlust, schlechte Zyklierbarkeit und Selbstentladung zu lösen. Nachdem die Proben mit interkaliertem Alkalimetall einige Tage in einer ultra-hoch Vakuum Kammer gelagert wurden, reagieren die Alkaliionen weiter mit dem Vanadiumoxid und bilden dabei Alkali-oxide und –peroxide auf der Oberfläche. Die Bildung der Alkalioxide und –peroxide stellt vermutlich einen Teil der sogenannten „Solid-Elektrode-Interface (SEI)“ - Schichten dar.

Abschließend wurde die elektronische Struktur und die Oberflächezusammensetzung der $LiMn_2O_4$-Pulver untersucht. Das Ergebnis zeigt, dass sich die Manganionen in zwei Oxidationsstufen befinden: sowohl im trivalenten Zustand (Mn^{3+}) als auch im tetravalenten Zustand (Mn^{4+}). Das Verhältnis der Photoemissionsintensität von Mn^{3+} zu der von Mn^{4+} beträgt ca. 0,9, so dass die durchschnittliche formale Oxidationsstufe 3,55 ist. Dieser Wert liegt wegen eines kleinen Anteils gebildeter Lithiumoxide auf der Oberfläche ein bisschen höher als der theoretisch erwartete Wert von +3,5. UPS und RPES belegen, dass sich die Manganionen in der high-spin Konfiguration befinden und die O2p- und Mn3d-Orbitale stark miteinander hybridisiert sind.

Abstract

V_2O_5 and $LiMn_2O_4$ are promising cathode materials for lithium-ion batteries due to their high capacities and battery voltages. The several work was mainly focused on the study of electrochemical and structural properties during lithium intercalation. But there is no detailed knowledge of the changes in electronic structure and the intercalation mechanism itself. Especially no general agreement has been reached on the nature and the extent of the interactions between host material and alkali guest atoms.

This thesis addresses the electronic stucture of transition-metal oxides and its changes during the intercalation of alkali metals. The intercalation of Na and Li into V_2O_5 thin films and $LiMn_2O_4$ powder samples have been studied mainly using X-ray photoelectron spectroscopy (XPS), ultraviolet photoelectron spectroscopy (UPS) and resonant photoemission spectroscopy (RPES).

The PVD prepared V_2O_5 thin films are nearly stoichiometric with only about 4% oxygen deficiency. After deposition onto the HOPG substrate, the oxide surface is smooth and polycrystalline. The valence band of V_2O_5 is formed by the hybridisation of the O2p and V3d electron states. It has been shown by RPES that the V3d admixture to the valence band is about 20%. Therefore, the real electron occupation number of the 3d electron state of the V ions in V_2O_5 is about 2 instead of 0, and the simple ionic model is not valid. The influence of heating on the V_2O_5 films has also been studied. Elevated temperatures lead to sub-stoichiometric V_2O_{5-x} that can be probed by chemically shifted components in the $V2p_{3/2}$ emission line, and a decrease of O1s/V2p intensity ratios. Annealing of the sub-stoichiometric films at 400°C in an oxygen atmosphere lead to the reoxidation of vanadium to its higher oxidation state.

The alkali metals are instantaneously intercalated into V_2O_5 when they are deposited onto the surface at room temperature. Only a small amount (about 10%) of the alkali metal atoms remain adsorbed on the surface due to the intercalation kinetics. The results obtained in this work demonstrate that the electrons of intercalated alkali metals s orbitals are mostly transferred to the transition-metal 3d orbitals and cause the reduction of the transition-metal ions as proven by the XPS and UPS data. The values of effective electron transfer for Na3s and Li2s are about 0.42 and 0.55 electrons per alkali atom, respectively. With low content of intercalated alkali metals, the electronic and crystalline structure of the host do not change considerately. For Na, an alkali saturation concentration of V_2O_5 films can be reached as $Na_{1.4}V_2O_5$ without decomposition of the host, for Li, this saturation value is about $Li_{2.5}V_2O_5$. When this limit for alkali intercalation is reached, further deposition of alkali atoms will not

intercalate into the host but form oxides, peroxides and even metallic alkali on the surface. The formation of surface oxide films on the electrodes would have a severe impact on battery performance. A better understanding of such films can be essential to solve the stability problem of lithium-ion batteries, such as capacity loss, power-fade, poor cyclability, and self-discharge. After the over-intercalated samples have been kept in the ultra-high vacuum chamber for few days, the alkali metal will react further with vanadium oxides and form alkali oxides and peroxides on the surface. In this work, we have clearly demonstrated the formation of alkali oxides and peroxides species, which are probably part of the so-called solid electrode interface (SEI) layers.

Finally, the electronic structure and surface composition of $LiMn_2O_4$ powder has been studied. The results show that manganese ions exist in two oxidation states: a trivalent state (Mn^{3+}) as well as a tetravalent state (Mn^{4+}). The photoemission intensity ration of Mn^{3+} to Mn^{4+} is about 0.9, so that the average oxidation state is 3.55 which is a little higher than the expected value of +3.5 which is probably due to small amounts of lithium oxides formed on the surface. UPS and RPES indicate that the Mn ions are in a high spin configuration, and O2p and Mn3d orbitals are strongly hybridised.

Table of contents

1 Introduction.....1

2 Fundamentals.....4

2.1 Rechargeable intercalation batteries.....4

2.1.1 Theoretical aspects.....4

2.1.2 Technological aspects.....8

2.2 Transition metal oxides.....10

2.2.1 Crystal structure of layered $LiMO_2$ solids.....10

2.2.2 Crystal structure of $LiMn_2O_4$.....11

2.2.3 Crystal structure of V_2O_5, LiV_2O_5 and NaV_2O_5.....13

2.2.4 Jahn-Teller distortion.....15

2.3 Electronic structure of transition metal oxides.....16

2.4 The intercalation reaction.....21

2.4.1 Structure effect.....22

2.4.2 Electronic effects.....22

2.4.3 Intercalation in UHV.....24

3 Experimental.....26

3.1 Characterization techniques.....26

3.1.1 Photoelectron spectroscopy.....26

3.1.1.1 Basics.....26

3.1.1.2 The photon sources.....29

3.1.1.3 The electron analyzer.....30

3.1.1.4 Spectra and interpretation.....31

3.1.1.5 Resonant PES.....39

3.1.2 AFM.....41

3.2 UHV equipment and spectrometer systems.....42

3.2.1 DAISY-MAT system.....42

3.2.2 BESSY II TGM7 (SoLiAS) system.....43

3.3 Preparation aspects.....45

3.3.1 Samples.....45

3.3.2 Sources.....45

4 Thin film synthesis and electronic structure of V_2O_5.....47

4.1 Physical vapour deposition (PVD).....47

4.2 V_2O_5 thin films.....49

4.2.1 Sources.....49

4.2.2 Substrate.....49

4.2.3 V_2O_5 thin films.....50

4.2.4 Thermal decomposition of thin film V_2O_5.....57

5 Intercalation reaction…….. 65
5.1 Sodium intercalation reaction…… 65
5.1.1 XPS and UPS data……66
5.1.1.1 XPS data for short Na deposition time……..67
5.1.1.2 XPS data for long Na deposition time……...70
5.1.1.3 Charge transfer during intercalation……..73
5.1.1.4 UPS data and electronic structure…… 74
5.1.2 XPS and UPS data for the samples after 4 days in UHV…….78
5.1.3 RPES data……80
5.2 Li intercalation reaction…….. 83
5.2.1 XPS and UPS data……83
5.2.2 Electrochemical intercalation……96
5.2.3 RPES data……99

6 Discussion……..…...102
6.1 The process of alkali intercalation……102
6.2 Structural and electronic effects……103
6.3 Charge transfer…….. 104
6.4 Fermi level shift and work function change……..105
6.5 Battery voltage deduced from the XPS and UPS data…….. 106
6.6 Comparison between Li and Na intercalation……109

7 Electronic structure of $LiMn_2O_4$……110
7.1 XPS data……111
7.2 UPS data……114
7.3 RPES data…… 116

8 Summary and suggestions……. 118
8.1 Summary of this work……118
8.2 Suggestion for future work……120

References…….. 121

List of abbreviations……..137

1 Introduction

A battery is a device that converts the energy released in a chemical reaction directly into electrical energy via electrochemical reactions. In the early 1970's it was discovered that intercalation compounds could be used as electrodes in secondary rechargeable intercalation batteries [1, 2]. An intercalation "host" is a solid which can reversibly incorporate "guest" atoms or molecules within its crystal lattice with only small structural changes. With the widespread use of portable electronic devices lithium-ion batteries, which were first demonstrated in the laboratory by Murphy et al. [3], and then by Scrosati et al. [4], have received a strong interest in scientific and technological research [5-8], due to their numerous advantages: high gravimetric and volumetric energy density, high single-cell voltage, no memory effect, good thermal stability, small self discharge, resistance to shocks and vibrations, and absence of possible pollution due to liquid electrolytes. The technology is based on the use of suitable lithium intercalation compounds for the electrodes. In the same period, numerous inorganic compounds have been shown to react with alkali metals in a reversible way. In a lithium-ion battery Li^+ ions are shuttled back and forth between an anode, where Li reside at a high chemical potential, and a cathode, where the Li chemical potential is low. The capacity of the battery depends directly on the amount of Li that can be inserted and removed reversibly into and from the lithium battery electrodes [9, 10].

Lithium transition-metal oxides Li-M-O (M = Mn, Ni, Co, V), which deliver higher voltage than disulfides owing to the more pronounced ionic character of the 'M-O' bonds compared with 'M-S' bonds [11], are commonly used as cathode materials [12-15], due to their advantageous properties: a high free energy of formation (giving a high energy density), a wide range of stoichiometry (giving a high capacity), high diffusivity of Li-ions in the structure, and only small irreversible structural change etc. These compounds can in general be viewed as "ordered rocksalt structures" in which alternative layers of Li^+ and M^{n+} ions occupy octahedral sites within the cubic close-packed oxygen array. The sites in the lithium plane form a triangular network. Different lithium planes are separated by the transition-metal layers. Many transition metal ions, especially in tetravalent and trivalent states, show ionic radii between 0.5 and 0.8Å. Therefore the tetravalent metal ions can accept electrons forming the trivalent ions at octahedral sites with only small distortion of their coordination, which is a necessary condition for a solid-state redox reaction. The spinel $LiMn_2O_4$, although possessing ≈ 10% less capacity than $LiCoO_2$, has an advantage in terms of cost (it is an abundant material in nature) and is perceived as being a 'green' source of energy (that is, non-toxic). Compared with CoO_2 and NiO_2 the layered compound V_2O_5 has a much higher electrochemical capacity.

Because of its easy preparation as pellets and as thin films [16], V_2O_5 has received strong scientific and technological interest [17-19].

Due to the growing tendency in the microelectronic industry towards complete integration of all functional devices onto a single chip secondary rechargeable solid state batteries of small dimensions are discussed to be a suitable energy sources [20, 21]. The use of thin film technology may offer many advantages: 1) it is well adapted for possible device designs, 2) the absence of the electrolyte-electrode interface may avoid problems e.g. high interface resistances, 3) it is easy to charge the battery by alkali deposition. Therefore, thin films reveal higher current densities and cell efficiencies than bulk materials because of the higher ionic conductivity of thin films. Modern technology has rapidly increased the capability of electronic devices while the size of the devices is still decreasing. There are many devices which require a power supply of low power output in the fields of communication technology and medical applications, such as their applications include implantable medical devices, CMOS-based integrated circuits, anti-theft protection, gas sensors, microcoulometers, and many more [22, 23].

The lithium battery has already been developed more than 30 years. Many regular meetings and symposia (such as the international meeting on Li batteries held in the framework of the electrochemical society meetings, the international power source symposia (New Jersey) and the international seminars on Battery Technology and Application (Florida) have been organized by Scientists. Many books [24-26] have already been published. But obviously most of the people concentrate on the electrochemical properties and crystalline structure of electrode materials and their relationship. Recently, some new concepts have been put forward (see detail in ref. 11, 27). For a decent understanding of the mechanisms and processes related to the intercalation reaction of alkali metal atoms into transition-metal oxides, the in-situ investigation of the intercalation reaction is necessary. In this Ph.D. thesis, the process of alkali intercalation into V_2O_5 thin films and the basic study of the electronic structure of cathode materials and their relationship with the electrochemical properties are discussed using to the various surface science techniques and the thin film preparation methods,. A better understanding of the alkali intercalation process is very important for the working mechanism of solid state batteries. The different oxidation states of a transition metal element do often lead to the formation of different crystal structures and alternative electronic properties. Therefore, the determination of the transition metal oxidation states and the change of the valence band structure of the cathode materials is essential.

This thesis is organized as follows: Chap.2 gives the theoretical background of this work; Chap.3 is devoted to the experimental details; Chap.4 introduces the electronic structure and the thermal properties of V_2O_5 thin films; Chap.5 contains the experimental results of Li and Na intercalation; in Chap.6 the results obtained about intercalation reactions are discussed in detail; Chap.7 outlines the results concerning the electronic structure and surface composition of the commercial $LiMn_2O_4$ material; Chap.8 is the summary of this work and suggestion for future work.

2 Fundamentals

In this chapter the theoretical background of this work will be introduced. In the first part, the fundamentals and technology of lithium battery will be outlined. In the second part, the crystal and electronic structure and some important properties of the transition metal oxides will be described. In the third part, the intercalation reaction will be introduced.

2.1 Rechargeable intercalation batteries

A battery is a device that converts the energy released in a chemical reaction directly into electrical energy via electrochemical reactions at electrodes. Compared with other forms of energy, the electrical energy is easiest to transport, store and convert. Recently the use of batteries as the high energy density power source for portables can be found in all facets of modern life with the fast development and spread of cordless communication tools. So the battery technology plays a critical role in our general living.

2.1.1 Theoretical aspects

A solid state lithium-ion battery consists of three basic parts: two electrodes (a cathode and anode) separated by a solid electrolyte containing mobile lithium ions (shown in Fig. 2.1) [28, 29]. The materials which are used for the electrodes have host structures that can be

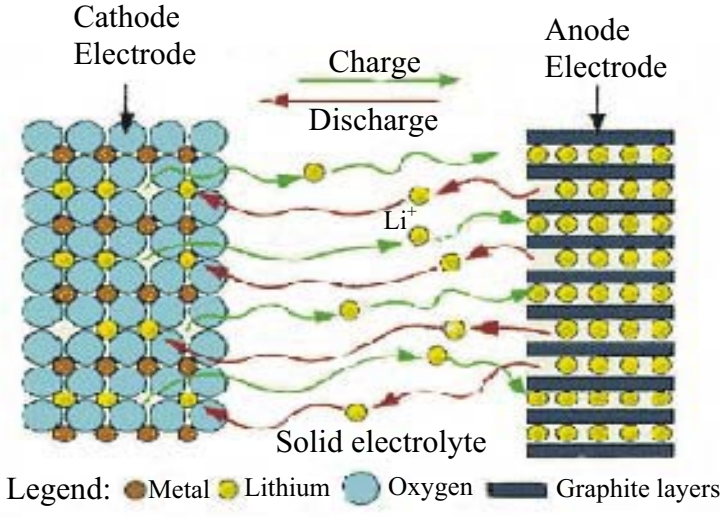

Fig. 2.1 Schematic represen-tation of rechargeable Li-ion solid state battery

intercalated and deintercalated by lithium ions over a wide compositional range. Carbon and intermetallic compounds intercalated with lithium have widely been used as negative electrodes and transition metal oxides as positive electrodes in a battery. Under open circuit

the electromotive force (EMF) can be measured, which arises from the difference of the Fermi levels in the two electrodes. If the electrodes are connected through an external circuit by electronic conductors, electrons will flow from the negative electrode to the positive one. At the same time lithium-ions will move through the electrolyte and intercalate into the positive electrode. This means that during the discharge process, an oxidation reaction occurs at the negative electrode and a reduction at the positive electrode. Hence the first is called the anode and the latter is the cathode. The whole intercalation reaction can be written as,

$$LiC_6 + MO_2 \rightarrow Li_{1-x}C_6 + Li_xMO_2 \qquad (0 \leq x \leq 1) \qquad \text{(Eq. 2.1)}$$

Origin of the cell voltage

The cell potential E can be calculated as the change of the Gibbs energy between products and reactants divided by the Faraday constant F. The Gibbs energy (ΔG) can formally be divided into an electronic part and an ionic part energy, which account for the energy gain of electron transfer and ion incorporation during intercalation. n accounts for the number of charges exchanged in the reaction,

$$E = \Delta G / F \cdot n \qquad \text{(Eq. 2.2)}$$

$$\Delta G = \Delta G_{ionic} + \Delta G_{electronic} \qquad \text{(Eq. 2.3)}$$

The distinction between the ionic and the electronic contribution to the driving force of intercalation can be made by principle considerations. While the ionic contribution is difficult to predict, the electronic contribution is closely correlated to the electronic band structure of the host materials [30]. The electrochemical cell described in Fig. 2.1 can be seen as a system composed of three phases (Anode: A, Electrolyte: E, Cathode: C). The lithium ions can be exchanged at the interfaces and their electrochemical potential η_{Li^+} is the same in the three phases. The cell voltage corresponds to the difference of the Fermi levels (E_F) between cathode and anode. E_F is typically used in solid state physics and corresponds to the electrochemical potential of the electrons in electrochemistry. The electrochemical potential η_i of a species with a charge ze_o contains two components,

$$\eta_i = \mu_i + z_i e_0 \phi \qquad \text{(Eq. 2.4)}$$

Where z_i is the valence of the species, e_o the elementary electric charge, ϕ the electrostatic potential, and μ_i the chemical potential. The electronic energy difference is given by the difference of the electrochemical potential,

$$e_0 \Delta V = {}_C\eta_{e^-} - {}_A\eta_{e^-} = {}_C\mu_{e^-} - {}_A\mu_{e^-} - e_0(\phi_C - \phi_A) \qquad \text{(Eq. 2.5)}$$

This relationship shows that ΔV has two components, one from the difference of chemical potential of the electrons between the C and A phases, the other from the Galvanic potential difference.

In the case the interfaces between phase C and E and equally between E and A can only be passed by the lithium ions, their free energies must be equal in all three phases,

$${}_A\eta_{Li^+} = {}_E\eta_{Li^+} = {}_C\eta_{Li^+} \qquad \text{(Eq. 2.6)}$$

Or more explicitly

$${}_A\mu_{Li^+} + e_0\phi_A = {}_E\mu_{Li^+} + kT\ln\frac{{}_E\alpha_{Li^+}}{{}_E\alpha^0_{Li^+}} + e_0\phi_E = {}_C\mu^0_{Li^+} + kT\ln\frac{{}_C\alpha_{Li^+}}{{}_C\alpha^0_{Li^+}} + e_0\phi_C \qquad \text{(Eq. 2.7)}$$

Where $\mu^0_{Li^+}$ is the chemical potential for the standard state with the activity of the ions being $\alpha^0_{Li^+}$. The chemical potential of the ions in the electrolyte is constant when the salt concentration is not changed. Therefore a relation of the Galvanic potential difference between phase C and A depending on the activity of the intercalated ions can be obtained

$$-e_0(\phi_C - \phi_A) = {}_C\mu^0_{Li^+} - {}_A\mu^0_{Li^+} + kT\ln\frac{{}_C\alpha_{Li^+}}{{}_C\alpha^0_{Li^+}} \qquad \text{(Eq. 2.8)}$$

and represents the ionic contribution to the cell voltage. Therefore an evaluation of the ionic contribution requires the knowledge of the lithium activity coefficient in the host. This must be taken into account for the interactions among intercalated ions themselves and the host. Some theoretical evaluations of the chemical potential of the intercalation, which took the chemical potential of the ions into account, have been attempted [31-35]. They are generally

based on lattice-gas models which consider interactions between intercalated species. An experimental approach for the chemical potential of the electrons in alkali zeolites has been reported by Devautour et al. [36, 37] using thermally stimulated depolarization current spectroscopy. But this technique can only be applied in electronic insulating materials. In the course of intercalation changes of the local environment of the ions may be thought to be quite smooth. The chemical potential of the ion can then be considered to be nearly constant compared to the chemical potential of the electrons, if at a particular guest concentration the density of state (DOS) above the Fermi level is small. Based on this assumption, several authors could successfully explain the voltage-composition curves of intercalation cells in the frame of the rigid band model by considering the electronic valence structure of the host [38-41]. On the other hand, in presence of energetically inequivalent intercalation sites steps may appear in the discharge curves which can be associated to the variations of the chemical potential of the ions, when the more favorable site is no more available. In the case of hosts presenting a mix of different sites and of different electron acceptor levels it has been possible to distinguish steps corresponding to a transition of chemical potential either of the ions or the electrons [41, 42].

In principle, the chemical potential of the electrons can be measured by the difference of the free energy of electrons between phase C and A. However, it varies with the concentration of the intercalated metal because the number of electrons in the respective energy bands increase with x. This corresponds to an upward shift of the Fermi energy,

$$\mu_{e^-} = \mu^0_{e^-} + \Delta E_F(x) \qquad \text{(Eq. 2.9)}$$

Where $\Delta E_F(x)$ is the lithium concentration-dependent shift of the Fermi level with respect to the level of the Galvanic potential. Then the electron component of the cell voltage is given by,

$$\Delta G_{electronic} = {}_C\mu_{e^-} - {}_A\mu_{e^-} = {}_C\mu^0_{e^-} - {}_A\mu^0_{e^-} + \Delta E_F(x) \qquad \text{(Eq. 2.10)}$$

The combination of Eq.2.5, 2.6, and 2.10 shows

$$\Delta G_T = \Delta G_{ionic} + \Delta G_{electronic} = -e_0 \Delta V \qquad \text{(Eq. 2.11)}$$

If the surface potential can be considered constant, the variation of the work function (Φ) is equivalent to $\Delta E_F(x)$, if the battery voltage is also know, the ionic contribution could be extrapolated as,

$$\Delta G_{ionic} = -e_0 \Delta V - \Delta\Phi(x) \qquad \text{(Eq. 2.12)}$$

Unfortunately it is experimentally difficult to avoid a variations in the surface dipoles leading to a strong additional change in the work function.

Since ionic and electronic chemical potentials in the cathode are expected to increase, the voltage will decrease with intercalation. But the average voltage can theoretically be predicted with a precision of 10-20% [43, 44] according to

$$\overline{V} = \int_0^1 V(x)\,dx = -\frac{\Delta G_{int}}{e} \qquad \text{(Eq. 2.13)}$$

giving

$$\Delta G_{int} = \Delta E_{int} + P\Delta V_{int} - T\Delta S_{int} \approx \Delta E_{int} \qquad \text{(Eq. 2.14)}$$

Therefore the Gibbs free energy can be approximated by the internal energy ΔE_{int} at 0K, which is of the order of 1-4 eV/molecule, because the term $P\Delta V_{int}$ is of order 10^{-5}eV/molecule [44], and the term $T\Delta S_{int}$ is in the range of the thermal energy, that is about 1% of the internal energy at room temperature [43]. From total energy calculations of the three phases e.g. $LiMO_2$, MO_2 and Li it is then possible to deduce the average discharge potential of the cell.

2.1.2 Technological aspects

In 1990, the first commercially available lithium-ion rechargeable batteries have been put on the market with its remarkably improved volumetric/gravimetric energy densities compared to other battery devices. The market demand for small rechargeable batteries in the field of telecommunication and personal computers was dramatically increased afterwards [45-47]. As a practical device a battery has to meet several design and material criteria. The compositional range, over which the alkali metal can reversibly be intercalated, determines the battery capacity. High alkali diffusivity is important to satisfy the current-density requirements. In the last few years, $LiNiO_2$, $LiCoO_2$, $LiMn_2O_4$ as well as LiV_2O_5 have been

considered as the promising positive electrode materials, carbon and intermetallic compounds as negative electrode materials. The potential range of these compounds versus lithium is shown in Fig.2.2.

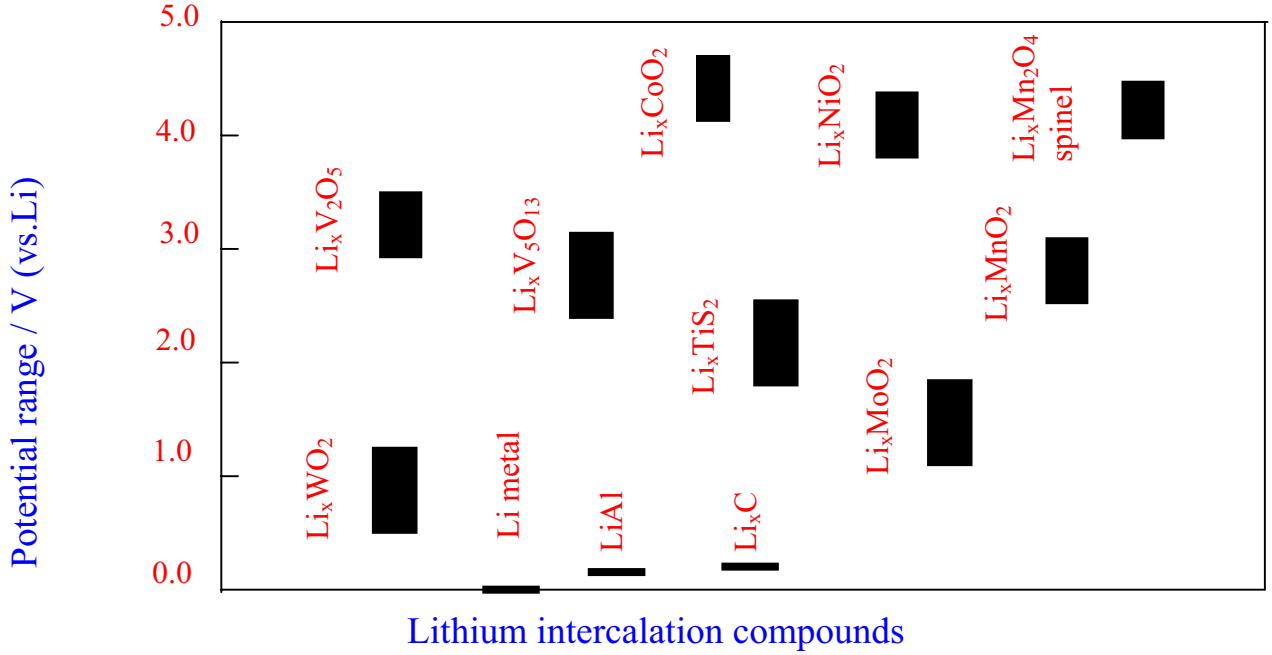

Fig.2.2 The potential range of different electrode materials versus Li

In order for an alkali-ion battery to perform adequately, it is essential that the structural integrity of the electrodes should be maintained throughout the discharge and charge processes for many hundreds of cycles. But recent results [48] discovered that after many charge/discharge cycles, the structural integrity of these materials is lost. It was tried to find more stable cathode materials by partly substituting M with other elements [49, 50]. Also some groups used nano-sized materials as electrodes materials with the aim to reach faster Li exchange [27]. But the problem has not completely been solved, yet. Carbon electrodes have been the anode material for many years. But there seems to exist a theoretical limit for the capacity, if one remains within the simple graphite system allowing for the formation of the lithiated compound LiC_6 (372 mA/g). Also the formation of the so-called solid electrolyte interface (SEI) layer is a problem for carbon electrodes. Today's research on negative electrodes is mainly split between 1) enhancing the electrochemical properties of the carbonaceous negative electrode by chemical or physical means, and 2) finding alternative materials to substitute for the presently used carbonaceous negative electrodes. The second approach has sequentially led to the study of new oxide and alloy based electrodes with large electrochemical capacities using Li counter electrode at low voltages. Currently, further improvements in energy density and the cycle life of the cell themselves are being pursued.

For this purpose, the materials for cathodes and anodes, the shapes or structures of batteries, and the methods for cell connection are being reinvestigated. This should lead to the improvement of the performance of battery modules. If the right combination of materials can be found, lithium-ion rechargeable batteries may become economical competitive and provide a long enough running time which is important for the application in electric cars and implantable medical devices as well.

Based on many possibilities offered by solid state chemistry important improvements can be expected on both performance and fields of application. Thin film deposition technology allows the miniaturization of batteries [51, 52]. The realization of integrated devices, such as non-volatile random access memory or the combination of battery and solar cell will be possible.

2.2 Transition metal oxides

As shown in Fig.2.2 several kinds of materials can be used as cathode electrodes for the rechargeable lithium battery such as transition metal dichalcogenides. But transition metal oxides are the most promising cathode materials for secondary lithium batteries, because they provide higher battery voltages. They are predominantly ‘ionic’ in their bonding character. The closest interatomic distances are formed between metal and oxygen atoms and it is the metal-oxygen bonding that provides stability to the structure. The most significant geometrical factor is the way, in which the metal atom is surrounded by oxygen. Different aspects of this are the bond lengths, bond angles and the coordination number.

Due to their wide range of electronic properties transition metal oxides have many unique applications, such as ‘high-temperature’ superconductors, semiconductors, electrochromic displays, as well as intercalation battery electrodes. Some books about transition metal oxides have been published by Cox and Henrich [53, 54] giving a survey of the various properties of these oxides. In this section, we just want to describe the crystal and electronic structure of transition metal oxides in their relation to solid state rechargeable batteries.

2.2.1 Crystal structure of layered $LiMO_2$ solids

A large number of ternary transition metal oxides as general formula AMO_2 (where A is an alkali and M a first-row transition metal) adopt the structure illustrated in Fig. 2.3 with alternating layers of A and M residing in the octahedral sites between close-packed layers of oxygen of variable stacking order [55]. As far as the transition metal M is concerned, the

structure contains layers of trigonally packed M with a large interlayer spacing compared to the M-M distance within the lattices. We may therefore expect the metal 3d electrons forming the valence band structure in these materials to behave in a manner appropriately described by two dimensional, rather than three.

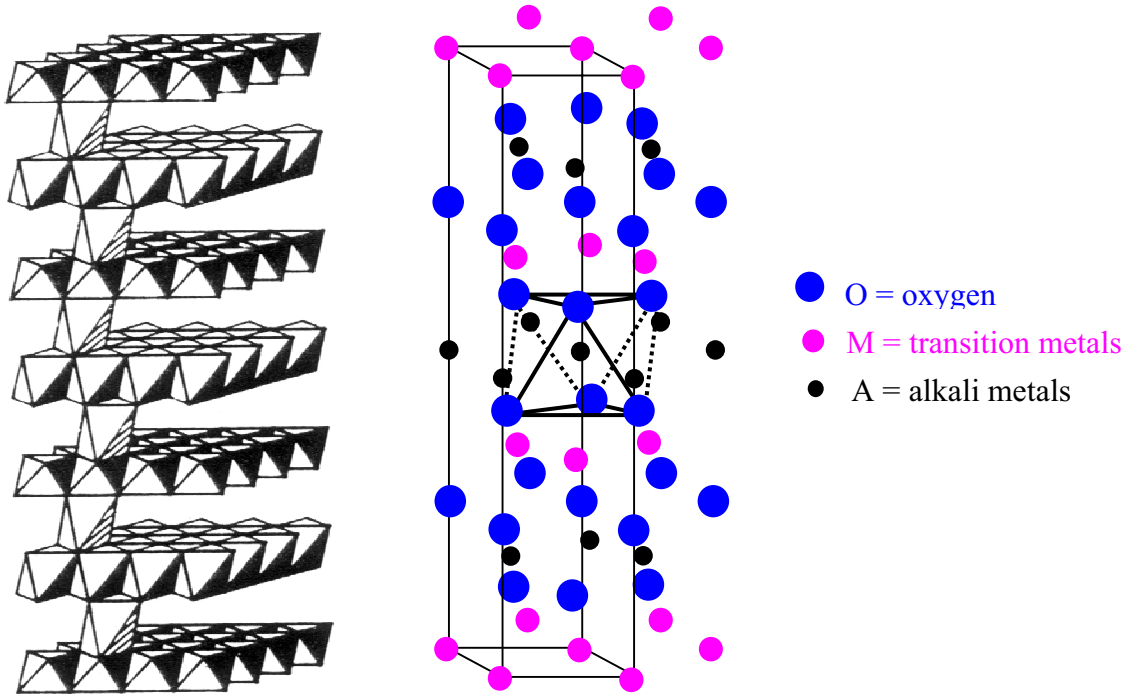

Fig. 2.3 The crystal structure of AMO_2

2.2.2 Crystal structure of $LiMn_2O_4$

Manganese oxide exists in many structural modifications [56], such as α-MnO_2, β-MnO_2, γ-MnO_2, Ramsdellite-MnO_2, layered-MnO_2, or orthorhombic-$LiMnO_2$. The structure and intercalation chemistry of manganese oxide have been reviewed by Thackeray [57]. In this section mainly the spinel $LiMn_2O_4$ is discussed because its structure and electrochemical properties provide much more information about its behavior as a cathode in secondary lithium-ion batteries than other lithiated manganese oxides electrodes.

$Li[Mn_2]O_4$ is a cubic spinel with space group symmetry Fd3m. It can be prepared by a simple solid state reaction of intimately mixed lithium and manganese oxide compounds, such as Li_2CO_3 and $MnCO_3$, in air at elevated temperatures, typically 750°C [29]. The Li ions are located on the 8a tetrahedral sites of the structure, the Mn ions are positioned on the 16d octahedral sites. The oxygen ions, which are cubic-close-packed (CCP), occupy the 32e

positions. The structure of $Li[Mn_2]O_4$, showing the relative positions of Li, Mn and O is illustrated in Fig.2.4 [58]. The $[Mn_2]O_4$ spinel framework with the octahedral coordination of the manganese ions and the three-dimensional interstitial pathways for lithium-ion diffusion is illustrated in Fig.2.5. It is important to note that in the spinel structure the MnO_6 octahedra are edge-shared and form a continuous three-dimensional cubic array (the manganese ions being distributed between alternate oxygen layers of the CCP array in a 3:1 ratio). This leads to a large robustness and stability of the $[Mn_2]O_4$ spinel framework. Furthermore, of all the interstitial tetrahedra (8a, 8b, and 48f) and octahedra (16c), the 8a tetrahedra are situated farthest from the 16d octahedra occupied by manganese atoms, they share each of their four faces with adjacent vacant 16c octahedra.

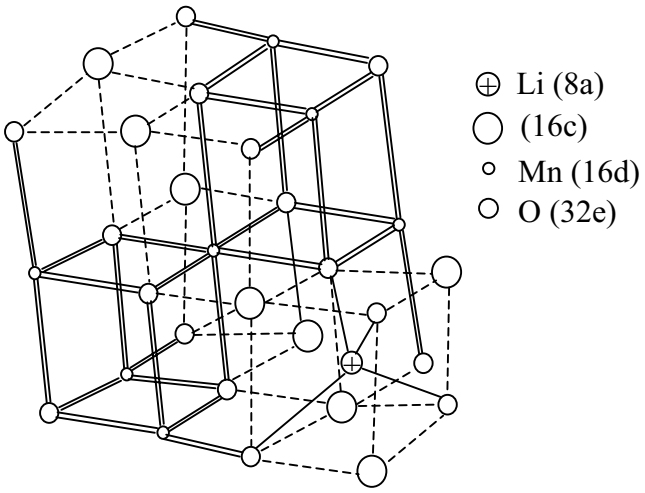

Fig. 2.4 The structure of the $Li[Mn_2]O_4$ spinel framework

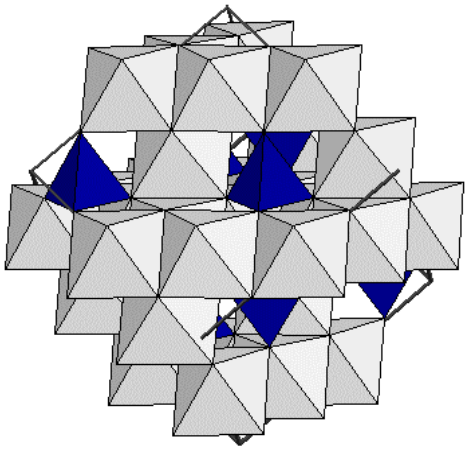

Fig. 2.5 Representation of the $[Mn_2]O_4$ spinel framework

The electrochemical data demonstrate that the lithium ion is extracted from the tetrahedral sites of the spinel structure at approximately 4V in a two-stage process, separated only by 150 mV [59] at a composition of $Li_{0.5}[Mn_2]O_4$. The two-step process is due to a structural ordering of the lithium ions on one-half of the tetrahedral 8a sites [60]. The high voltage associated with these reactions has been attributed to the deep energy well in which the tetrahedral lithium ions reside, and the high activation energy, ΔE, that is required for the lithium ions to move from one 8a tetrahedral into another 8a site via an energetically unfavorable neighboring 16c octahedron. Lithium insertion into $Li[Mn_2]O_4$ occurs at approximately 3V. During this process, lithium ions are inserted into octahedral 16c sites of the spinel structure. Because the 16c octahedra share faces with the 8a tetrahedra, electrostatic interactions between the lithium ions on these two set of sites cause an immediate displacement of the tetrahedral-site lithium ions into neighboring vacant 16c octahedra. These

intercalation process induces a Jahn-Teller distortion due to the predominance of d^4 Mn^{3+} ions, reducing the $Li[Mn_2]O_4$ crystal symmetry from a cubic to a tetragonal rock salt structure.

2.2.3 Crystal structure of V_2O_5, LiV_2O_5 and NaV_2O_5

V_2O_5 has been widely studied by scientists and engineers, in view of its interest as electrochromic materials [16], thermal sensors, transparent conductors [61-63] and cathode for batteries [64, 65].

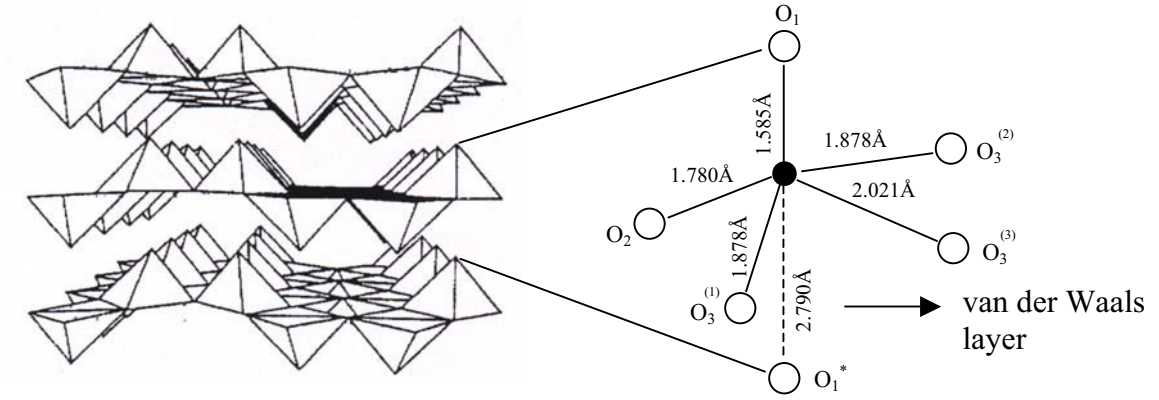

Fig. 2.6 (a) The perspective representation of the V_2O_5 lamellar structure; (b) the five-fold co-ordination of vanadium by oxygen in V_2O_5 with the V-O bond lengths

V_2O_5 exhibits an orthorhombic layered structure [66] with either 2-D layer or 3-D cavities that allow the intercalation of small metal cations, such as Na, Mg and Li [67-69]. It can be thought of as built from corner-sharing and edge-sharing VO_6 octahedra. V_2O_5 crystallizes in the orthorhombic unit cell, it belongs to the P_{mnm} space group and has lattice parameters **a** = 11.510Å, **b** = 3.563Å, and **c** = 4.369Å, where the **b** and **c** axes are often interchanged. The structure of V_2O_5 is given in Fig.2.6. The vanadium atoms form five bonds with oxygen (V-O bond lengths vary from 1.585Å to 2.027Å): one with the O_1 atoms, one with the O_2 atoms and three with the O_3 atoms. The electrostatic repulsion between neighboring vanadium atoms leads to a displacement of the vanadium atoms from the base of each pyramid in the direction of the apical oxygen. From the structure of V_2O_5, it is evident that the V-O_3 bonds form puckered chains in the **b**-direction, which are linked to each other in the **a**-direction by the bridging oxygen O_2. The layers formed are held together by week V-O_1^* bonds. The shortest V-O bond length corresponds to a double vanadyl bond (V=O_1).

V_2O_5 was first suggested as a cathode material in the 1970s [70]. $Li_xV_2O_5$ can adopt many phases depending on temperature and lithium concentration x, the phase diagram is

shown in Fig.2.7. Some phases, such as α-$Li_xV_2O_5$ and ε- $Li_xV_2O_5$ involve very little structural distortion of the bulk oxide, while others, such as β- $Li_xV_2O_5$ have a square-based pyramidal arrangement and form tunnels within the lattice [71] which is significantly different from that of V_2O_5 [72].

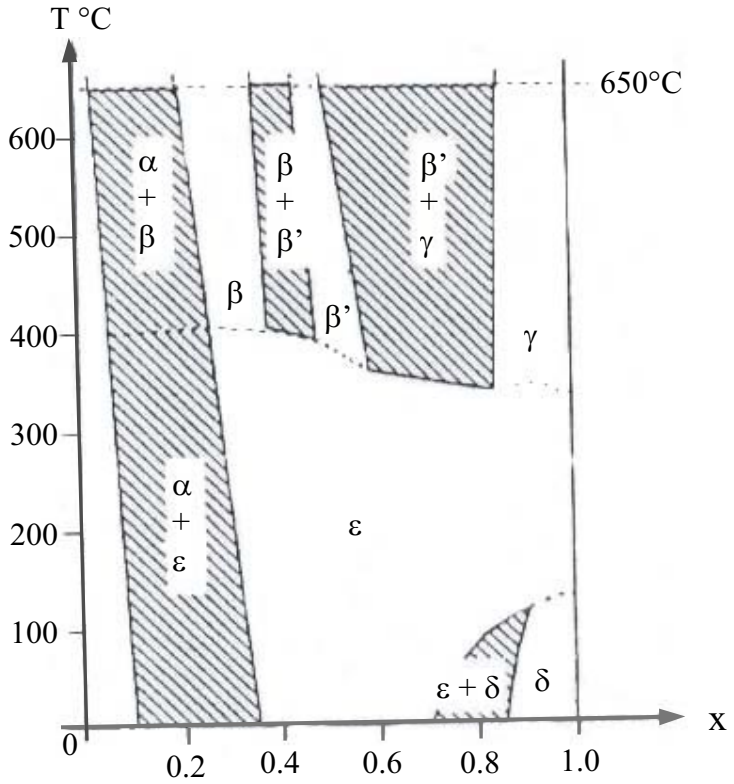

Fig. 2.7 Phase diagram for $Li_xV_2O_5$

The sodium vanadate (α'-NaV_2O_5) has an orthorhombic unit cell [73] and belongs to the centrosymmetric space group Pmmn (**a** = 11.3, **b** = 3.61, **c** = 4.80Å [74]). Such a crystalline structure assumes only one crystallgraphic position for the vanadium atoms in the mixed-valence state (formal oxidation state is +4.5). Each vanadium atom is surrounded by five oxygen atoms, forming VO_5 pyramids. These pyramids are connected via common edges to form layers in the (**ab**) plane. The Na atoms are situated between these layers as intercalants. A schematic representation of two layers of the NaV_2O_5 crystal structure is given in Fig.2.8. Double chains of edge-sharing distorted VO_5 square pyramids are running along the **b** direction. The main structural distinction between NaV_2O_5 and V_2O_5 is a larger layer spacing of NaV_2O_5 ($\Delta c / \overline{c} \approx 9\%$) and related differences of oxygen z-positions. The average V-O distance as a function of the coordination and oxidation number suggests that the V^{4+} and V^{5+} ions are segregated within the square pyramids and tetrahedra, respectively [75]. At high pressure, the layered structure of α'-NaV_2O_5 and the pyramidal oxygen coordination of V

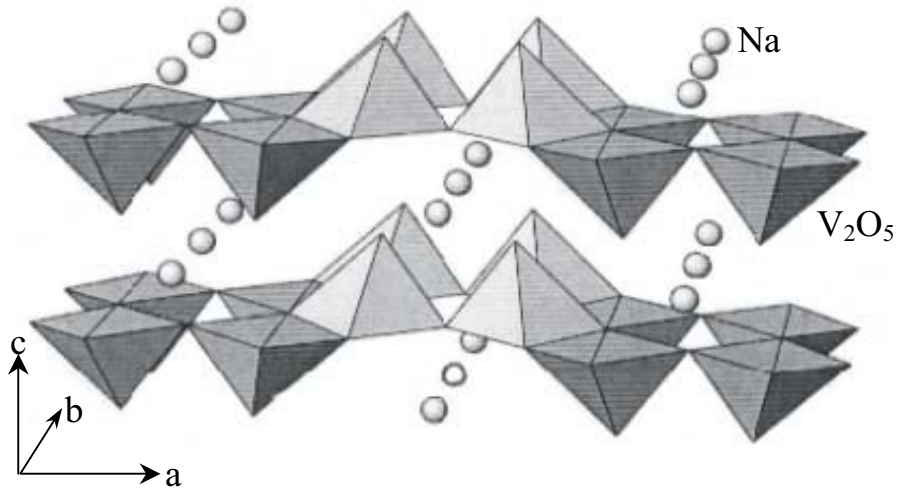

Fig. 2.8 Crystal structure of NaV_2O_5 at the (001) plane, sheets of distorted VO_5 square pyramids are stacked along the c direction with the intercalated Na

atoms are not stable any more. The coordination of the V atoms changes from square pyramidal towards a distorted octahedral one, and the structure of the high-pressure phase is proposed to be a distorted monoclinic variant of the "idealized" V_2O_5 structure with parameters **a** = 11.29, **b** = 3.47, and **c** = 3.46Å [76].

2.2.4 Jahn-Teller distortion

The cooperative Jahn-Teller distortion is an energetic instability of the crystal structure with respect to certain vibrational modes of distortion due to electronic degeneracy. In 1937, U. Jahn and E. Teller demonstrated that degenerated electronic states in a molecule will always be unstable with respect to some distortion, with the exception of the linear molecule [77]. The vibration of an octahedron can be described exactly by 21 effective modes [78]. Fig.2.9 shows some selected symmetrized modes. van Vleck used perturbation theory to explicitly solve the E×e Jahn-Teller problem demonstrating that the degenerate e_g states in an octahedral complex will be split by the Q_2 and Q_3 modes [79]. In a solid with octahedrally coordinated transition metal ions a set of bonding (e_g) and antibonding (e_g^*) states will be formed, with the antibonding states consisting primarily of metal d orbitals and bonding states of oxygen p orbitals. The cooperative distortion of all the octahedra in the Q_2 or Q_3 mode will result in the energy splitting of the e_g^* bands. In the simplest mode the Hamiltonian for an isolated octahedron or a Jahn-Teller defect in an otherwise perfect crystal can be written as a sum of the elastic and electronic energy [80]. However, there are several important differences in the solids. For the solids, the Jahn-Teller-active octahedra share edges and thus

they are not distorted independently. Whether the octahedra share edges or not, a given octahedron will be strained due to the distortion of the neighboring octahedra. So far the structural distortion has been considered for an isolated octahedron. The Jahn-Teller effect in a crystal is much more complicated as the e_g electrons form energy bands and are not localized energy levels. A better description for the Jahn-Teller effect in a solid is an array of local Jahn-Teller centers having several different types of interactions: magnetic, quadruple, and electronic-vibration interaction [81]. The problem of the Jahn-Teller effect for electronic states in a crystal lattice may thus be addressed in the same way as Jahn and Teller did for molecules.

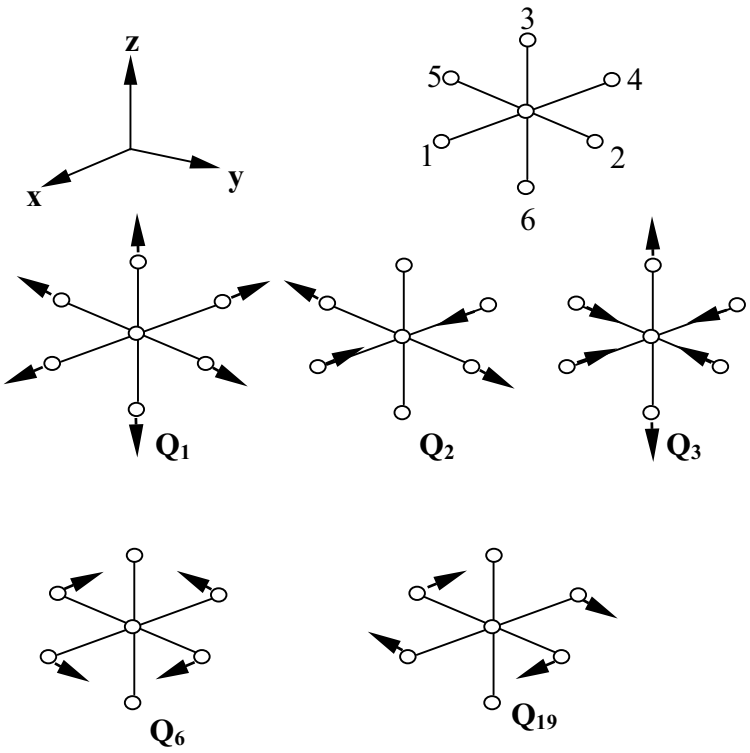

$$Q_1 = (x_1 - x_4 + y_2 - y_5 + z_3 - z_6) / \sqrt{6}$$

$$Q_2 = (x_1 - x_4 - y_2 + y_5) / 2$$

$$Q_3 = (2 \cdot z_3 - 2 \cdot z_6 - x_1 + x_4 - y_2 + y_5) / \sqrt{12}$$

$$Q_6 = (y_1 - y_4 + x_2 - x_5) / 2$$

$$Q_{19} = (x_2 - x_5 - y_1 + y_4) / 2$$

Fig. 2.9 Selected symmetrized octahedral modes. Only the Q_2 and Q_3 modes are Jahn-Teller active

2.3 Electronic structure of transition metal oxides

Different oxidation states of an elements do often give rise to different structural and electronic properties. Even if the concept has occasional limitations, it is surprisingly powerful in interpreting the electronic structure of the transition metal oxides. Therefor a better understanding of their electronic structure is necessary to clarify the electrochemical properties and changes in crystal structure of transition metal oxides during alkali metals intercalation.

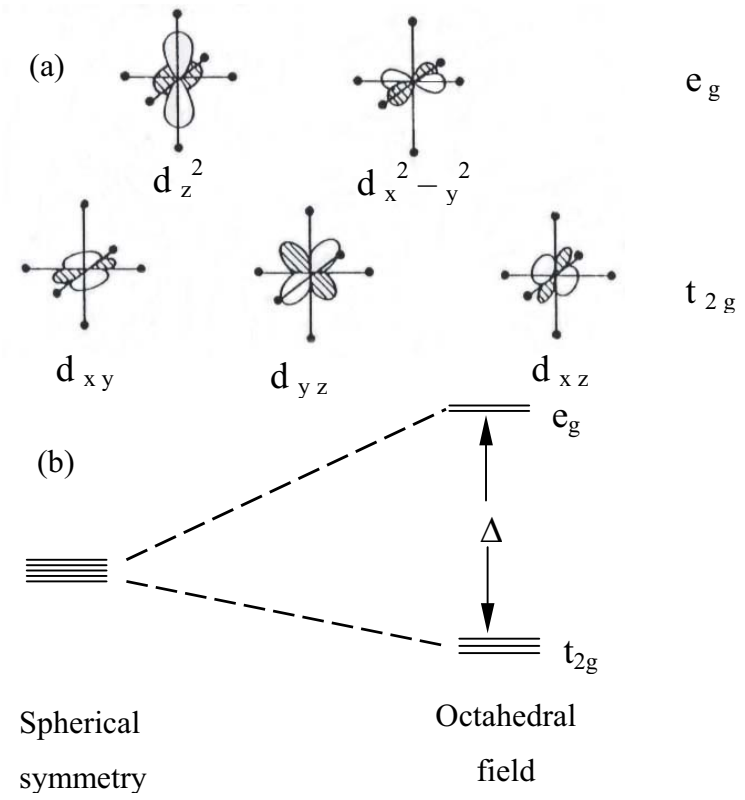

Fig. 2.10 The d orbitals of a transition metal ion in an octahedral site, showing (a) the different orientations of the e_g and t_{2g} sets, and (b) the resulting orbital energies with the crystal field splitting

For a transition metal ion with octahedral coordination, the five d orbitals can be divided into two sets: two orbitals have lobes of maximum probability pointing directly to the nearest-neighbor oxygen, whereas the other three have nodal planes in these three directions (see Fig.2.10(a)). These sets of orbitals are conventionally denoted as the e_g and the t_{2g} representations of symmetry point group O_h of an ideal octahedron [82]. Δ is the related crystal-field splitting, which is larger in higher oxidation states, leading to energy changes of $-2/5\Delta$ for the t_{2g} and $+3/5\Delta$ for the e_g orbitals [83] (see Fig.2.10(b)). The electron configurations, spectroscopic term symbols, and crystal field stabilization energies are given for n = 1 to 9 (n is the number of electrons in the metal 3d orbital) in table 2.1 for low and high spin states. All the group states show orbital degeneracy except those with the term symbol A, which arise when both t_{2g} and e_{2g} sub shells are either emptily, half or completely filled. The occupation of e_g having a higher energy and strong antiboding character (discussed below) leads to a stretching of the M-O bond. d^4 (high-spin) and d^9 ions in non-metallic solids induce a tetragonal distortion of an otherwise octahedral site, with two stretched M-O bonds, or occasionally a square planar coordination [84], due to Jahn-Teller distortion (as has been mentioned in the last section). Fig.2.11 shows a qualitative MO energy scheme for a transition

metal atom (3d series) octahedrally surrounded by six oxygen atoms. On the left- and right-hand sides, respectively, the atomic orbital energies of the metal and oxygen atoms are

Table 2.1 High- and low-spin states for d^n ions in octahedral sites [53]

	High spin			Low spin		
n	Configuration	State	CFSE/Δ	Configuration	State	CFSE/Δ
1	t_{2g}^1	$^2T_{2g}$	2/5	—	—	—
2	t_{2g}^2	$^2T_{2g}$	4/5	—	—	—
3	t_{2g}^3	$^4A_{2g}$	6/5	—	—	—
4	$t_{2g}^3 e_g^1$	^5E_g	3/5	t_{2g}^4	$^3T_{1g}$	8/5
5	$t_{2g}^3 e_g^2$	$^6A_{1g}$	0	t_{2g}^5	$^2T_{2g}$	2
6	$t_{2g}^4 e_g^2$	$^5T_{2g}$	2/5	t_{2g}^6	$^1A_{1g}$	12/5
7	$t_{2g}^5 e_g^2$	$^4T_{1g}$	4/5	$t_{2g}^6 e_g^1$	^2E_g	9/5
8	$t_{2g}^6 e_g^2$	$^3A_{2g}$	6/5	—	—	—
9	$t_{2g}^6 e_g^3$	^2E_g	3/5	—	—	—
10	$t_{2g}^6 e_g^4$	$^1A_{1g}$	0	—	—	—

Electron configurations, spectroscopic term symbols, and crystal field stabilization energies are given for n = 1 to 9. Low-spin states are specified only when they are different from high-spin.

presented. In the middle the resulting MO energies are shown [82, 85, 86]. The e_g and t_{2g} combinations with oxygen 2p are illustrated in Fig.2.12. The e_g set is composed of σ type orbitals with lobes pointing along the metal-oxygen bond direction, whereas the t_{2g} set is π type, pointing to a perpendicular direction. Mixing between these oxygen 2p and the metal 3d orbitals predominately produces bonding MOs with oxygen, and antibonding MOs with metal character. For example,

$$\varphi_{bonding} = \alpha\phi(M3d{:}e_g) + \beta\phi(O2p{:}e_g) \quad \text{(Eq. 2.15)}$$

and

$$\varphi_{antibonding} = \gamma\phi(M3d{:}e_g) - \delta\phi(O2p{:}e_g) \quad \text{(Eq. 2.16)}$$

Where the ϕs are the appropriate symmetry adapted atomic orbitals, and α, β, γ, δ are positive coefficients. The ‘oxygen 2p’ orbitals form mostly the bonding, and the ‘metal d’ electrons mostly the antibonding states. The degree of mixing between the MOs depends inversely on the amount of overlap. As shown in Fig.2.10, the perturbation resulting from orbital mixing is

larger for the e_g orbitals than for t_{2g}. This is because the overlap of σ type is larger than those of π type [86, 87] of the 'metal d' orbitals. Therefore, the e_g states show a stronger antibonding character than the t_{2g} states. The larger overlap interaction of the e_g orbitals gives rise to the octahedral crystal field splitting Δ, and also means that electrons in these orbitals have more influence on the metal-oxygen bonding.

Interaction between metal 3d orbitals and the 2p orbitals of surrounding oxygen can then be included by mixing in different configuration, for example Ni^{2+}, $\varphi(d^9\underline{L})$ and $\varphi(d^{10}\underline{L}^2)$ where $\underline{L}$ is used to represented a hole in the ligand (oxygen) orbitals. Thus overlap interactions between metal and oxygen are included by making linear combinations of these different many-electron states. The wave function of the ground state can be written as:

$$\varphi_G = A\,(d^8 + \alpha d^9\underline{L} + \beta d^{10}\underline{L}^2) \qquad \text{with } A^2 = (1 + \alpha^2 + \beta^2)^{-1} \qquad \text{(Eq. 2.17)}$$

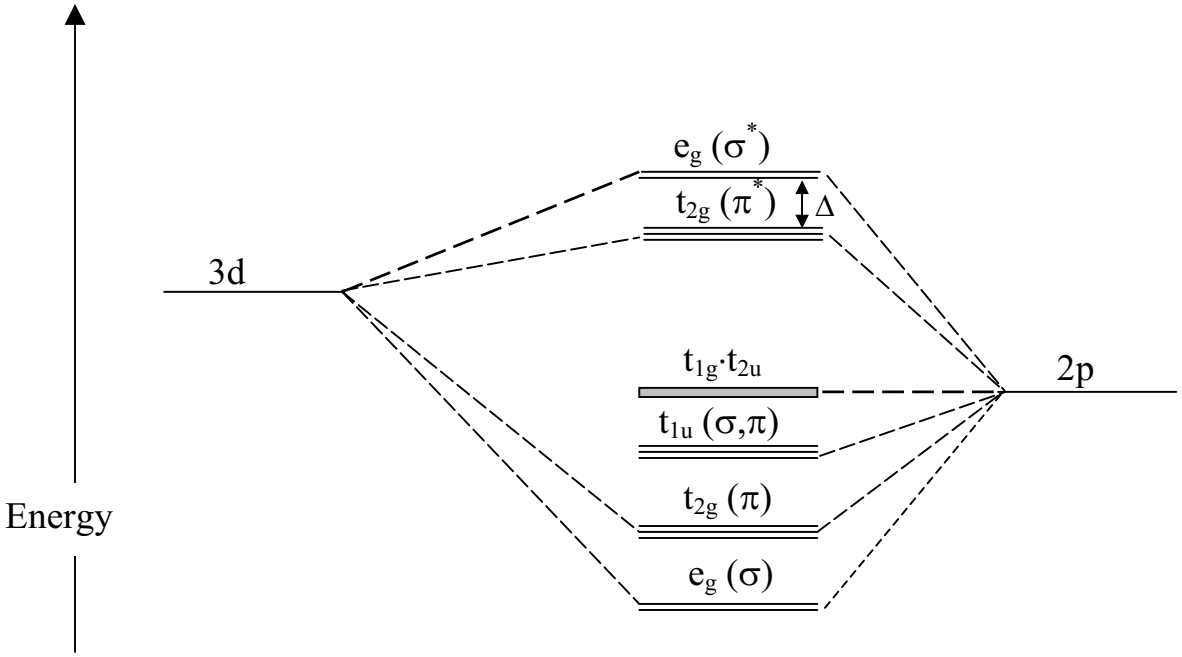

Fig. 2.11 Qualitative molecular orbital diagram of a transition metal in an octahedral coordination surrounded by six oxygen atoms. The atomic orbital energies of the metal and the oxygen is shown on the left and right, respectively; in the middle the energies of the molecular orbitals are shown. Symmetry labels corresponding to the irreducible representations of the O_h point group are used [88]

For the fully lithiated compound $LiCoO_2$, the electronic structure of the Co ions in $LiCoO_2$ is relatively well understood, it is agreed on that the Co ions are in a trivalent low-spin state with $(t_{2g})^6$ configuration [89, 90]. $LiCoO_2$ has a very short Co-O interatomic

distance, resulting in a ligand field strong enough to stabilize a Co^{3+} low-spin ground state. $LiCoO_2$ is usually regarded as a semiconductor with a gap of 2.7 eV [91].

In contrast, the electronic structure of $LiNiO_2$ is still controversially discussed. It is usually assumed that Ni ions are in a trivalent state [89] although sometimes from the spectroscopic data a divalent state is assumed [92, 93]. Non-stoichiometric $Li_{1-x}Ni_{1+x}O_2$ ($0<x<0.4$) is usually obtained due to the difficult oxidation of Ni^{2+} to Ni^{3+}. The impurity Ni^{2+} ions disturb further the long-range order of the Li and Ni ions, which, in turn, deteriorate the electrochemical properties of $Li_{1-x}Ni_{1+x}O_2$. Small additives of Co to $LiNiO_2$ improve the reactivity and may stabilize both the Ni^{3+} ions and the layered crystal structure [94].

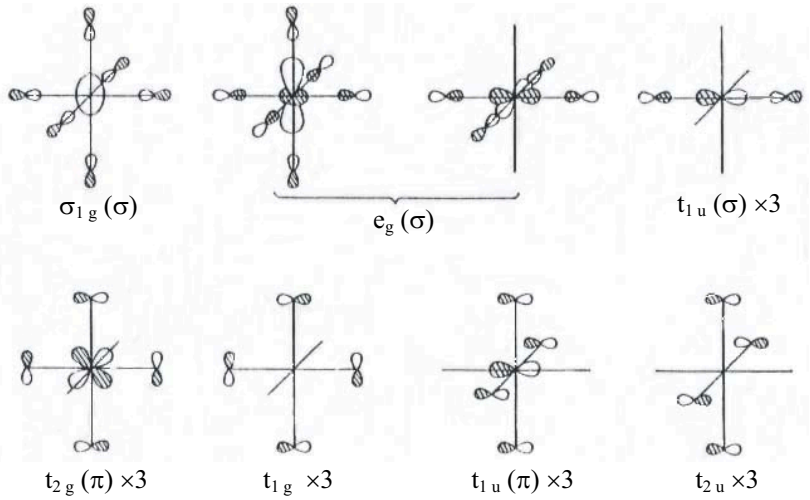

Fig. 2.12 Symmetry-adapted linear combinations of oxygen 2p orbitals arising in an octahedron, shown with a bonding combination of an appropriate metal orbital. The type of bonding (σ or π) is indicated. In the case of the triply degenerate t orbitals only one of each is drawn

$LiMn_2O_4$ has an average oxidation state close to +3.5 for Mn, i.e. 50% of the Mn ions are in a trivalent and 50% in a tetravalent oxidation state. Mn ions in $LiMn_2O_4$ are in a high spin state [95]. d^4 (high spin) Mn^{3+} ions reduce the $LiMn_2O_4$ crystal symmetry from a cubic to a tetragonal rock salt structure [59, 96]. The high oxidation state of maganese can suppress or delay the Jahn-Teller distortion, on the other hand, the increase in oxidation state of Mn leads to a decrease in capacity. The electronic and electrochemical properties of the $LiMn_2O_4$ spinel in relation to its electronic structure is still not finally understood [97].

The characteristic chemistry of vanadium based systems results from a number of different interrelated electronic and structural facts. Interatomic bonding in V_2O_5 has both ionic and reasonable covalent contributions. The negative charging of oxygen increases with the coordination number leading to the smallest charge for terminal O_1 and the largest for

triply coordinated bridging oxygen O_3. This indicates for the V_2O_5 surface that the bridging oxygen sites are more nucleophilic than terminal vanadyl sites which becomes important in view of the reactivity of the different sites with respect to surface chemical reactions [98].

2.4 The intercalation reaction

In this section the concept of intercalation will be introduced. Especially, the intercalation of lithium ions into transition metal oxides is discussed here.

The intercalation reaction, generally reversible, involves the introduction of a guest species into a host structure without major structural modifications of the host. Some crystal structures contain spaces free of any atom or charge density. Depending on the dimensionality of these regions the resulting lattice can contain cavities, tunnels, planes, or a three-dimensional network that partially or totally may be occupied by guest species. The related insertion phases are called intercalated compounds. Depending on the nature and amount of guest species the intercalated compounds may strongly differ in their chemical and physical properties from the host compounds.

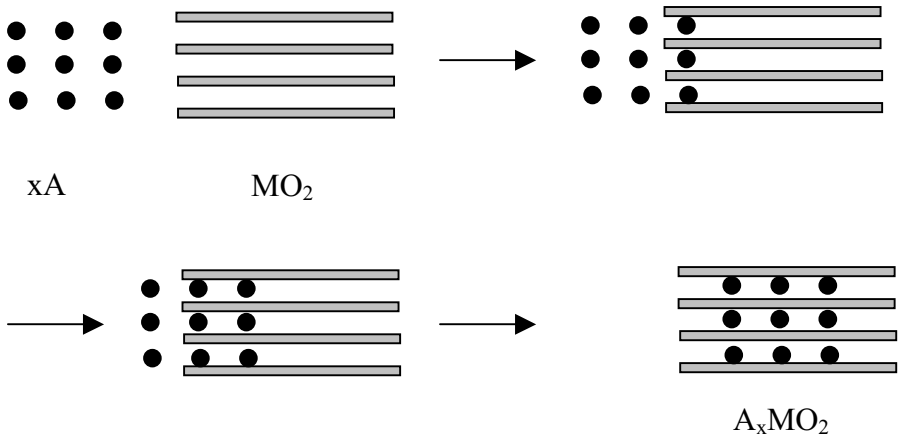

Fig. 2.13 The process of the intercalation reaction

Intercalation compounds can be prepared by direct synthesis [99]. However, if access pathways to the intercalating sites are available, they can also be obtained from the host and guest compound by an intercalation reaction. For example, if x mol A are intercalated into 1 mol MO_2, the reaction should be written as:

$$xA + MO_2 \rightarrow A_xMO_2 \qquad \text{(Eq. 2.18)}$$

The process of ideal intercalation reaction is shown in Fig. 2.13

2.4.1 Structural effects

In the ideal case the intercalation reaction is considered to be topotatic, which means that the host structure undergoes no distortion. Layered materials are close to the ideal situation because, due to the weak inter-layer interactions, the main effect to the structure is the expansion along the **c** axis with nearly no change within the slab structure. Many transition metal ions especially in tetravalent and trivalent states show ionic radii between 0.5 and 0.8Å, suggesting that the tetravalent metal ions can accept electrons forming trivalent ions at octahedral sites without the destruction of octahedral coordination, which is a necessary condition for a topotactic solid-state redox reaction. The ionic radii of lithium ions are 0.90Å (CN = 6) and 0.73Å (CN = 4) that are larger than those of trivalent and tetravalent transition metal ions. One needs quite opposite requirements for cations in a solid matrix, that is, the smaller transition metal ions at octahedral sites have to be immobile and larger lithium ions also at octahedral sites have to be mobile. The transition metal ions may be immobile, when the covalence between the transition metal and the oxygen ions to form $MO_6^{8-/9-}$ is strong enough to fix the transition metal ions at octahedral sites. Lithium species surrounded by six or four oxygen ions are believed to be more ionic. Although the ionic radius of a lithium ion is too large to move freely in a solid matrix, lithium ions at octahedral sites may move from one site to the other with the aid of lattice vibrations and fluctuations of oxygen ion positions mainly due to the electrons accepted by neighboring transition metal ions. When an upper limit amount of intercalated lithium ion is overpassed, the host is no longer stable and an irreversible structure modification occurs. This behavior, generally found for all intercalation compounds, is particularly critical for oxides.

2.4.2 Electronic effects

The lithium intercalation consists of a lithium ion insertion into vacancies of the host phase occurring simultaneously with the reduction of the host filling an empty conduction band state. If these occupied states can be described as bands or localized states depend on the nature of the host. In this case the intercalation reaction can be written as:

$$xA + MO_2 \rightarrow A_x^{+}MO_2^{x-} \qquad \text{(Eq. 2.19)}$$

The intercalation compounds stability depends dramatically whether the acceptor level is bonding, antibonding or non-bonding. Each oxygen at the vertex of an octahedron is

connected through $2p_x$, $2p_y$, and $2p_z$ orbitals to the 2s orbital of a lithium ion. Hence, if the Li site is occupied, the lithium ion shares an O-2p orbital with M. This multiple bonding model of M(3d)-O(2p)-Li(2s) is represented in Fig.2.14. Li(2s), O(2p), and metal d_{x2-y2}, d_{z2} orbitals have the proper symmetry to hybridize with each other. Dompablo et al. argued that these orbitals in Li_xNiO_2 generate attractive interactions between Li ions in 180° Li_A-O-M-O-Li_B moieties, and suggested that the presence of Li at the extension of a M-O bond lowers the energy of that e_g^* orbital. The Jahn-Teller distortion leads to charge localization in filled and unfilled orbitals [100]. In any case, intercalation implies changes in bond angles and distance, which are reflected in the electronic structure. But also stabilization of injected electrons can be a consequence of structural distortions like Jahn-Teller effects. In the ideal case such changes can be neglected [101, 102], which leads to the often applied rigid band model of intercalation. It was actually found that the alkali valence electron is transferred to the lowest unoccupied transition metal 3d states, without drastic changes of the density of states. However, in general this rigid band model is not valid, because the band dispersion and their relative position can be significantly changed [103] and must be investigated in detail.

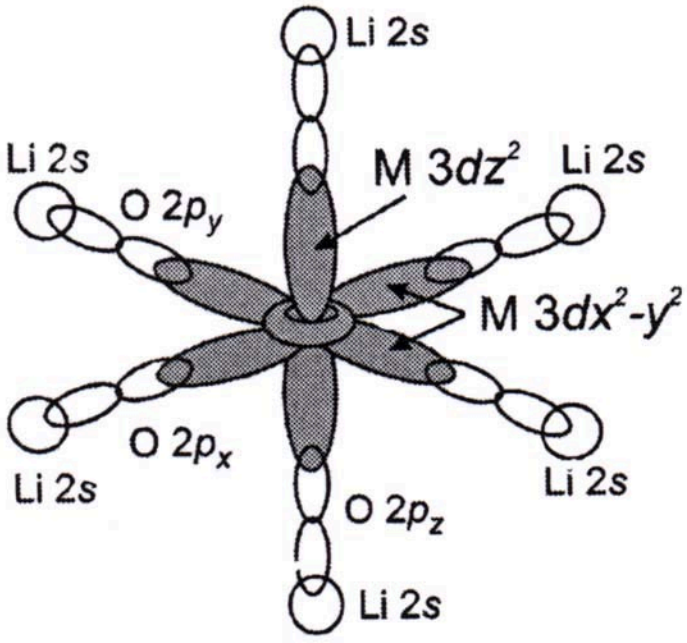

Fig. 2.14 Overlapping of atomic orbitals involved in the Li(2s)-O(2p)-M(3d) interactions

In addition to the gain in electronic energy, an ionic term favors the intercalation process, which is due to the electrostatic interaction between the cationic guest and the anionic host lattice. Both electronic and ionic energy gains related to the charge transfer contribute to the redox reaction – the driving force for intercalation. This approach of evaluating the reaction energy by considering the two distinct electronic and ionic contributions is based on the rigid band model [104, 105]. But it was criticized by some

authors considering the strong ion-host interaction in the intercalation compound: the filling of the empty states would be compensated by lowering the band energy due to the potential generated by the positive ion [106, 107]. Calculation of the total energies of intercalated and deintercalated compound with pseudopotential methods may clarify the question [108].

The extents of charge transfer from intercalated alkali into the host has been a matter of debate for a long time, and still no complete agreement has been reached. Experimental data and calculations based on Mulliken population numbers indicate a wide range of fractional values [109]. NMR investigations indicated that the negative charge on the oxygen around Li would increase with its concentration [110]. Carewska examined both ^{6}Li and ^{7}Li NMR spectra, the results showed that only a small fraction of the excess lithium enter interstitial sites of the structure in close proximity to paramagnetic Co^{2+} ions [111]. Gummow et al. found that small amounts of excess Li intercalating into $LiMn_2O_4$ will improve its cyclic capacity [112] and Li^+ is preferably inserted into the interstitial 16c sites [113]. Excess Li intercalation is effective in changing the transition metal valence state and crystal structure. The charge distribution is continuously modified as the positive charge of the transition metal element decreases while positive charge (Li^+) appears in the vacancies of the pristine material. As a result the intercalated phase becomes gradually metastable with increasing amount of intercalation. When an upper limit is overpassed, the host material is no longer stable and irreversible structure modifications occur.

2.4.3 Intercalation in UHV

Alkali metal adsorption onto a metallic surface has been well investigated [114, 115]. The low ionization potential of alkali metals induces a charge transfer when adsorbed on a surface with larger electronegativity. The creation of a strong surface dipole significantly reduces the work function of the substrate. This treatment has important applications in catalysis and electronics. With the same technique alkali metals have been evaporated onto the surface of host materials, and the appreciated intercalation reaction has been demonstrated [86, 87]. This method is particularly simple and useful, if applied in UHV environment. The host materials can be intercalated by a progressively larger alkali amount and subsequently analyzed at each step by a number of surface science techniques [116-118] without any contamination due to contact to the air; for this reason this preparation method has been called “in situ”. The deposition rate can be easily controlled, but for alkali metals an absolute calibration, such as with a quartz microbalance, is usually difficult, because of their complicated adsorption process. Only estimations related to surface coverage on non-

intercalating substrates can be attempted. For this reason the deposition rate is typically kept constant and the amount is controlled by the deposition time. Generally the experimentally observed intercalated amount of guest species is found to increase rapidly with deposition time in the first stage and then settle at a limiting value dependent on the metal and the crystal substrate despite further repeated evaporation [119, 120]. This suggests that a metastable state forms, in which the guest, at least initially, accumulates in the topmost layers due to a kinetic barriers of diffusion into the non-intercalated phase. When the chemical potential of alkali increases, the activation barriers becomes smaller and diffusion is eventually obtained [89]. The alkali concentration in the topmost layers is thus limited and fully intercalated phases have not been reported in literature with this method, yet.

Some important differences are found between intercalating and non-intercalating surfaces. On the latter, the work function decreases rapidly. A change of 1 eV can be induced by a coverage θ of 1%, but higher coverages produce a depolarization of the adsorbent, and a work function minimum can be observed. At higher coverages the valence electron may not be completely donated, and the formation of a metallic phase occurs at low substrate temperatures. On intercalating substrates the work function has a smoother decrease and minima are not observed [121]. The electrostatic repulsion prevents a direct interaction among ions, which remain homogeneously distributed on the surface.

3 Experimental

The number of studies of solid surfaces and the number of techniques available for these studies have increased enormously since the early 1960s. In this work, the surface structure, the chemical composition and the electronic structure of V_2O_5, V_2O_{5-x}, $Na_xV_2O_5$, $Na_xV_2O_{5-x}$, $Li_xV_2O_5$ and $LiMn_2O_4$ have been studied by photoelectron spectroscopy (XPS, UPS, and resonant PES), low energy electron diffraction (LEED), Atomic Force Microscopy (AFM), as well. In the first part of this chapter, a short introduction to some of these techniques will be given, as far as it concerns this study. In the second part, the UHV systems used in this work will be introduced. In the third part, the sample preparation is summarized.

3.1 Characterization techniques

3.1.1 Photoelectron Spectroscopy

Photoelectron spectroscopy is a common method to investigate the occupied electronic (core-and valence-) states in a solid [122]. Literature on photoelectron spectroscopy is abundant [123-126]. X-ray Photoelectron Spectroscopy (XPS) has been widely used to determine the oxidation state of elements and surface chemical composition of compounds [127]. Ultraviolet Photoelectron Spectroscopy (UPS) has been used to study the valence band structure of compounds, which is directly related to the electronic states occupied by the valence electrons and which reveals the interactions between the atoms in chemical compounds.

3.1.1.1 Basics

The phenomenon of photoemission was observed by Hertz in 1887 [128], and then, in 1905, Einstein explained the principle of photoemission by invoking the quantum nature of light [129].

$$E_{kin} = h\nu - W \qquad \text{(Eq. 3.1)}$$

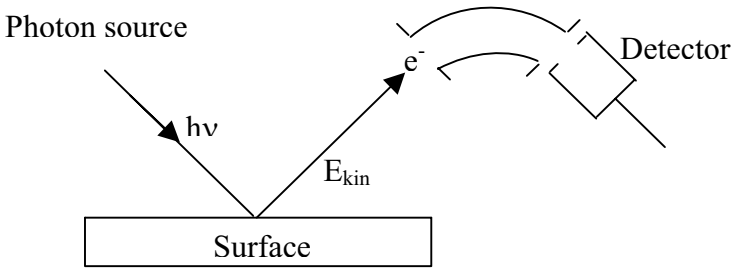

Fig. 3.1 Sketch of a modern PES experiment

A photon with an energy hν penetrates the surface, and is absorbed by an electron with a binding energy W below the vacuum level. If the excitation energy hν is larger than the binding energy W of the electron, the electron will be emitted from the solid with a kinetic energy (E_{kin}). The process is shown in Fig.3.1

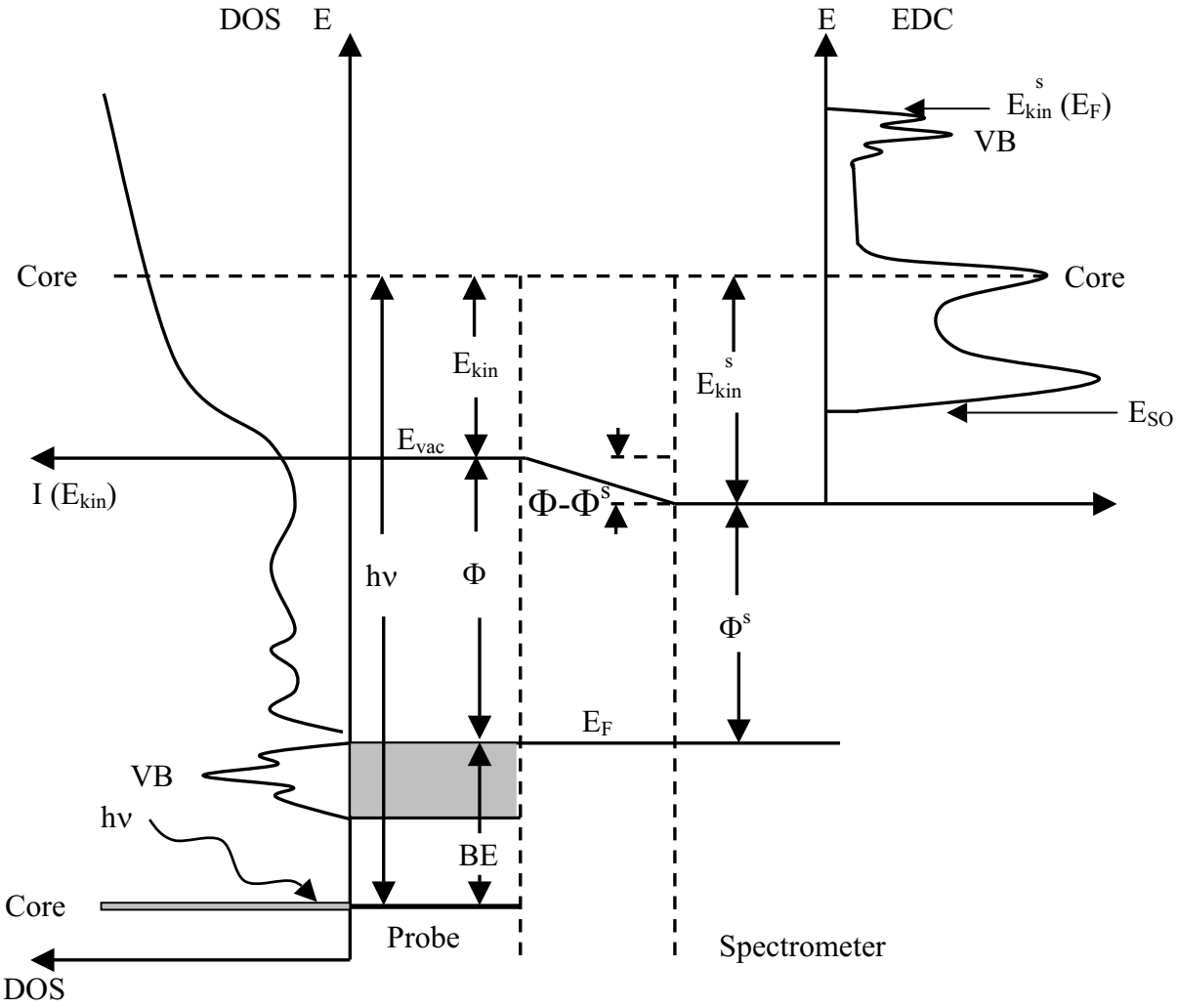

Fig. 3.2 Scheme of the photoemission process as measured by an electron spectrometer

The emitted electrons are detected (in most cases) by an electrostatic analyzer, where they are counted in a selected energy range. It is then possible to obtain the energy distribution curve (EDC), a plot of the number of electrons collected as a function of their kinetic energy. The number of collected electrons corresponds, in a first approximation, to the density of (occupied) electronic states (DOS). For convention W is divided into two terms, the binding energy BE which is below the Fermi level of the sample and the work function Φ, so that Eq. 3.1 can then be written as,

$$E^{s}_{kin} = h\nu - (BE + \Phi) \qquad \text{(Eq. 3.2)}$$

Sample and spectrometer are kept in electric contact, as a consequence a common Fermi level is established, but the analyzer work function Φ^s is in general different from that of the sample. The kinetic energy $E_{kin}{}^s$ measured by the analyzer differs from E_{kin} because of the acceleration (or retardation) of electrons due to the electrical field between sample and analyzer (see Fig.3.2). The measured kinetic energy is then,

$$E^{s}_{kin} = h\nu - BE - \Phi^s \qquad \text{(Eq. 3.3)}$$

If a metallic sample is used, $E_{kin}{}^s$ measured for the Fermi edge (BE = 0) can readily be identified at the largest kinetic energy where emission intensity is detected. Given the photon energy Φ^s is obtain and then also the BE scale,

$$E^{s}_{kin}\ (E_F) - E^{s}_{kin} = BE \qquad \text{(Eq. 3.4)}$$

Between about 10 and 2000 eV, the escape depth of the photoelectrons is only of the order of a few Å. This means that any spectroscopy of a solid surface involving electrons probes only from a very thin surface layer of the solid. The mean free path λ of electrons in a solid depends on their kinetic energy and is nearly independent of the material. A “universal” electron mean free path as a function of the electron kinetic energy is reported in Fig.3.3. A minimum is found at E_{kin} = 50-70 eV with a depth of about 5Å, corresponding to about 2 atomic monolayer. For larger energies λ increases proportionally to $E_{kin}{}^{1/2}$ and reaches a value of 25Å, or about 10 monolayers, for 2000 eV.

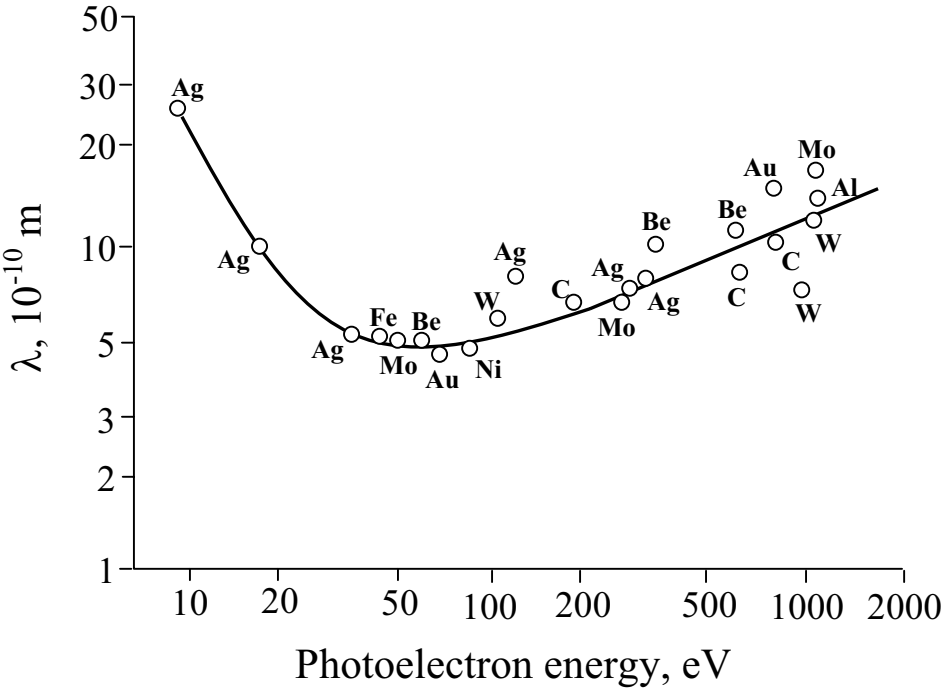

Fig. 3.3 Mean free path of photoelectrons emitted from different elements and lines as functions of their kinetic energy

3.1.1.2 The photon sources

Photoelectron spectroscopy is mostly performed in two fundamental energy ranges defined by convenient laboratory sources. The first range is provided by light from gas discharge sources using the intense emission lines from He and other inert gases. For He, the two main lines HeI and HeII have energies of 21.22 and 40.82 eV, respectively. For the other inert gases the main emission lines have lower energies. Therefore, discharge sources are not capable to access the core levels. For this reason, UPS can only be used to study valence levels.

The second photon energy range is defined by the use of X-ray tubes. Mainly two characteristic emission lines, the Al and Mg Kα X-ray emissions at 1486.6 and 1253.6 eV, are used. These radiation energies are sufficient to excite electrons from characteristic core energy levels. With a monochromator it is possible to improve the width and the signals to noise ration leading to higher energy resolutions (see Table 3.1).

In a synchrotron electron packets run along a circular ring, and because of their centripetal acceleration they emit electromagnetic radiation tangential to their orbit. The light has a broad spectral distribution, and the energy can range from far-infrared to high energetic X-rays. In the orbit plane the light is linearly polarized. The experiments of this work have been carried out at the beam line TGM 7 located at the Synchrotron radiation facility (BESSY II) in Berlin. The light beam has an area of less than 1 mm^2 and with a monochromator the

required light can be selected in a range from 20-120 eV. The line width is typically much smaller than with XPS depending on the monochromator specifications. With such soft X-ray PS (SXPS) experiments, it is possible to investigate states at variable excitation energy and/or constant kinetic energy. The technique is particularly important, because of the ability to adjust the information depth and the photoionitation cross section. Core level lines like Li1s with weak XPS intensities may easily be measured with appropriate signal intensities, as for example at hν = 80 eV.

The following table lists the photon light sources used in this work.

Emission	Photon energy (eV)	Line width (meV)
Mg Kα	1253.6	700
Al Kα	1486.6	750
Mono-Al Kα	1486.6	300
He I	21.22	3
He II	40.81	17
BESSY II (TGM7)	20-120	100

Tab.3.1 Photon energy and line widths of the excitation radiations used in this work

3.1.1.3 The electron analyzer

The basic purpose of any electron spectrometer is to separate electrons of a certain kinetic energy and emission direction from all electrons entering the spectrometer in a wide range of energies and angles. This can be achieved by passing through a dispersing field in which the deflection is a function of the electron energy. Such an instrument can be based on either electrostatic or magnetic fields. Magnetic analyzers are normally used only for a very high energies where the strong magnetic field outside the analyzer is not a problem. Here only the hemispherical electrostatic deflection analyzers will be discussed.

The concentric hemispherical analyzer (HSA) is nowadays probably the most widely used in commercial electron spectrometers. It consists of two metallic hemispheres with a radius difference $\Delta R = R_1 - R_0$ with R_0 and R_1 are the radii of the inner and outer spheres, respectively (see Fig.3.4). The two hemispheres are set to different potentials (ΔV) with the outer sphere at a more negative potential compared to the inner one. The electrons which enter the analyzer passing an entrance slit are transmitted and leave the analyzer passing an exit slit into a channeltron or a multichannel electron detector. Only the electrons with kinetic energies equal to the pass energy E_0 which is a function of ΔV can pass through the analyzer and reach the detector. The sample is general grounded, and in the so called constant analyzer energy (CAE) mode, the spectrometer potentials is swept so that electrons of all energies could be retarded to the constant pass energy value at the entrance slit.

The energy resolution is defined as ΔE/E, which gives for a HSA as S/R, where R is the radius of the central path through the analyzer and S is the size of the entrance (out) slit. The ideal condition for electron transmission is,

$$E_0 = \frac{1}{R_1 / R_0 - R_0 / R_1} \cdot e \cdot \Delta V \qquad \text{(Eq. 3.5)}$$

Where E_0 is the kinetic energy of the transmitted electrons (= pass energy), and e is the electron charge.

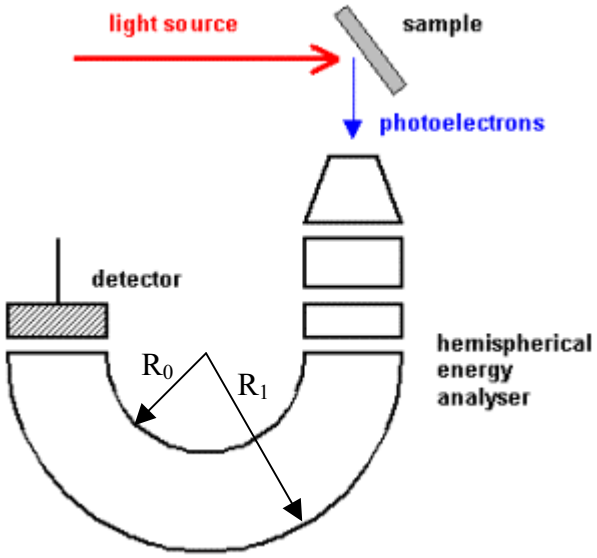

Fig. 3.4 A concentric spherical deflection analyzer

3.1.1.4 Spectra and interpretation

In this work the electron binding energy (BE) is given with respect to the Fermi energy (E_F = 0). Lower kinetic energies generally correspond to higher BE. The emission lines corresponding to the core levels are denoted with the main quantum number and the orbital angular momentum (s, p, d, f) of the hole left in the final state (see Fig.3.5).

For each element the core level lines have characteristic BE, only H and He can not be detected. These core level lines indicate the presence and the amount of a specific element in the sample under study. A closer inspection of the spectrum (see Fig.3.6) shows that the emissions from the p, d and f levels are not single photoemission lines, but doublet lines due to the hole spin-orbit coupling effect in the final state. The spilt into two components corresponds to the two possible total angular momenta j, which are therefore indicated as l-1/2 and l+1/2; their intensities are proportional to the degeneracy of these state (2j+1). For p lines,

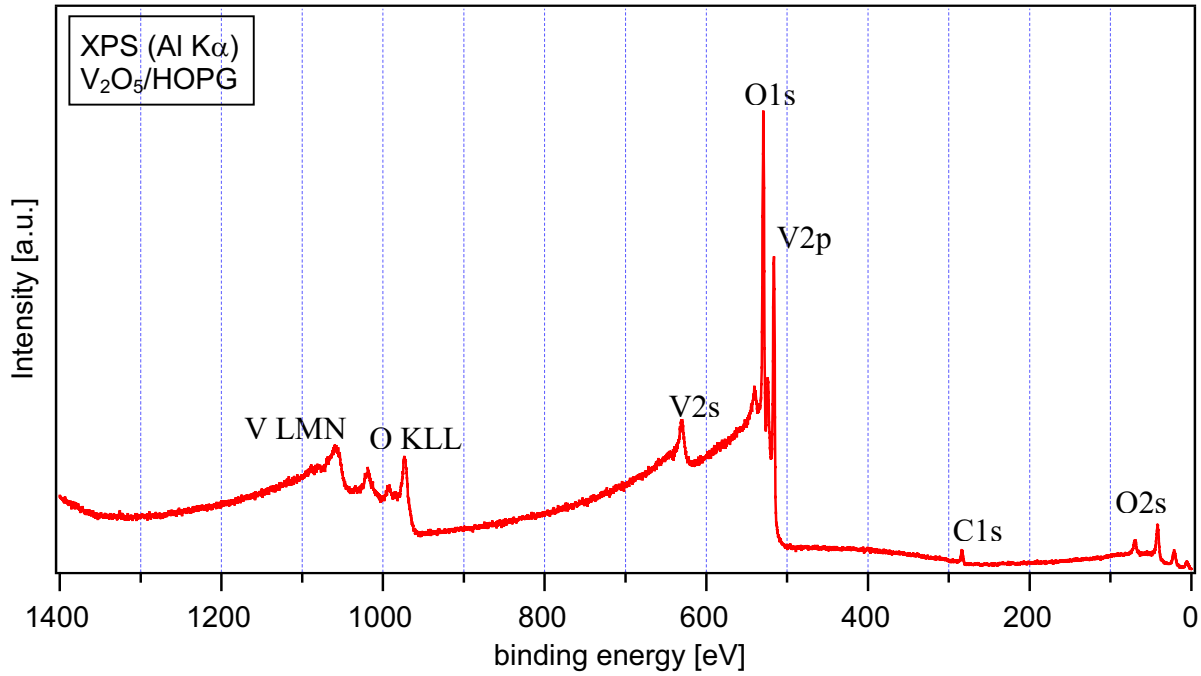

Fig. 3.5 Survey XP spectra of V_2O_5 deposited on a HOPG substrate

for example, the intensity ratio is 2:1. In general, when the BE for a doublet is given, it identifies the position of the (l+1/2) component. Some additional satellite peaks, mostly found on the high BE side of a main photoemission line, are frequently observed in photoelectron spectra. They are called shake-up satellites, if an excitation into a bound state, and shake-off satellites, if the excitation into the continuum appears. All these satellites are final state effects in contrast to chemical shifts which results from initial state effects. The peak position can

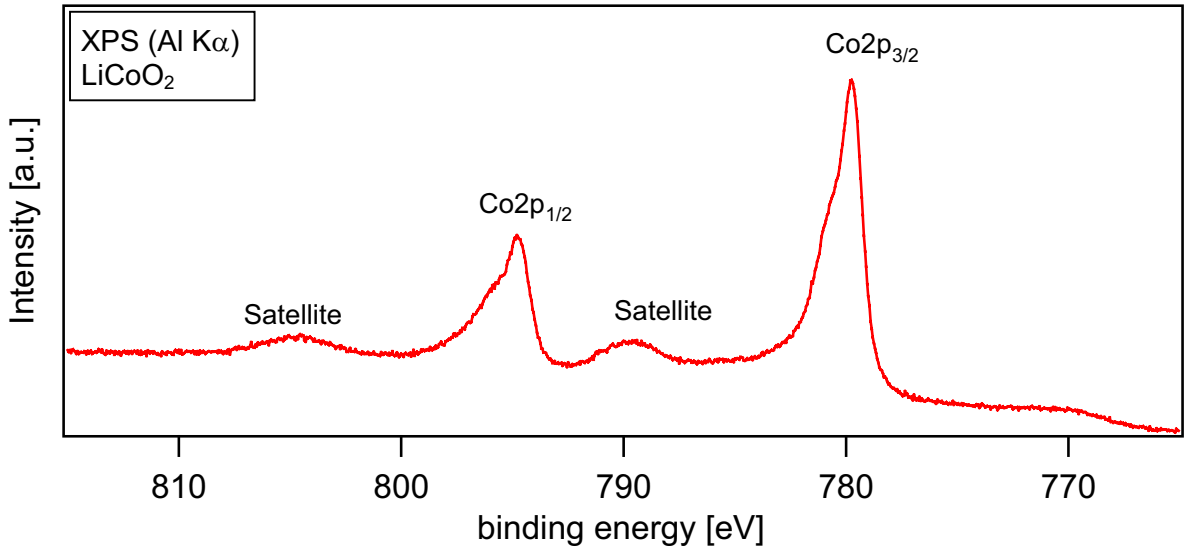

Fig. 3.6 Core level XP spectra of Co2p in $LiCoO_2$

vary within several eV in dependence of the element's chemical environment, which can be used for chemical identification. In general it can be stated, if the electron density at one atom is larger, the BE of the corresponding core level is lower. As a consequence the largest influence on this chemical shift is the oxidation state: electrons from a more reduced (oxidized) atom have a lower (higher) BE [130]. The peak position may also change due to sample charging after the ionizing process. For conducting specimens this can be avoided, because emitted electrons are replaced with an electron from the spectrometer in electric contact with the sample. For insulators, which have much lower conductivity, a static positive charge will be accumulated, which will increase the observed BEs by up to several eV. It will then be necessary to refer BE values to the position of an element of known BE.

The secondary emission background

The electrons leaving the sample without further interactions after their excitations are called primary electrons. Their energy distribution is generally a lifetime-broadened Lorentzian, modified by the immediate reponse of the conduction-electron system to the positive photohole. But during the escape process the photon electrons lose part of their energy due to inelastic scattering in the sample, accompanied by the formation of secondary electrons. Being a random process the inelastic and secondary emissions shows no specific energy level. The Energy Distribution Curve (EDC) results from the overlapping of both primary and secondary emission. For statistic reasons the intensity of the secondary emission for a given energy is roughly proportional to the total emission at high kinetic energy. Starting from the Fermi level towards lower kinetic energies the EDC is typically increased in intensity due to the secondary emission background. At the point corresponding to the zero (sample) E_{kin} the EDC drops suddenly, since electrons with lower energy can no longer be emitted (see Fig.3.7). This point is called secondary emission onset, and from its binding energy BE^{so}, given the spectral excitation energy based on Eq. 3.2, the samples work function Φ can be calculated as,

$$\Phi = h\nu - BE^{so} \qquad \text{(Eq. 3.6)}$$

The overall shape of secondary emission can give information on the sample morphology. In XPS a flat secondary emission is generally considered as a sign of sample homogeneity. Usually quantitative information is obtained from the primary emission. In order to recover the "primary spectrum" this secondary electron background has to be

removed by suitable procedures. This can be done by subtracting a function fitted to the peak tails. The choice of the background function influence both the peak shape and intensity and is not straightforward for many compounds. For example, metals are affected by shake-up process involving the conduction electrons. When conduction electrons are excited simultaneously with the photoelectron, the emission appears at lower kinetic energy. This causes a so-called intrinsic background affecting the peak symmetry and may extend for hundreds eV. For practical purposes, simplified functions for background correction are used. In XP spectra the Shirley method was used, assuming background emission originated only from inelastic scattering of electrons having higher kinetic energy. The integrated EDC [131, 132] is a step-like function. For SXP spectra instead a 2nd or 3rd grade polynomial is more appropriate. The intensity and the shape of the background-removed peaks can then be evaluated. All mathematical treatments of PES data for quantitative analysis were executed with procedures written for the Wavemetrics IGOR application [133].

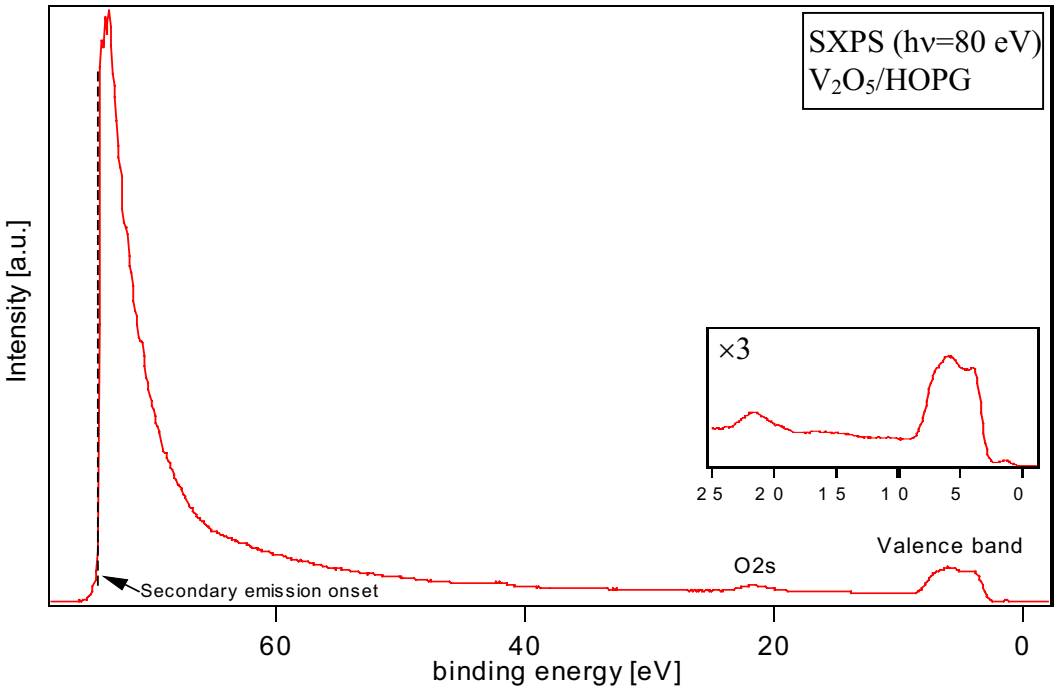

Fig. 3.7 Overview SXP spectrum taken at BESSYII/TGM7 of V_2O_5 deposited onto HOPG surface with an excitation energy hν = 80 eV. Insert: amplified valence band region

Quantitative information in XPS

In 1974, Fadley et al. [134] published an extensive theoretical background for quantitative analysis in XPS. With minor modifications, the procedure proposed by these

authors is commonly used until present time. The formalism is based on many assumptions: (i) elastic scattering of photoelectrons is neglected, (ii) the solid surface should be ideally flat, (iii) the analyzed sample should be amorphous or polycrystalline, (iv) in-depth composition within an analyzed volume should be uniform, (v) the x-ray refraction and reflection are neglected, (vi) the x-ray attenuation within the analyzed volume is negligible. Under the above assumptions, the photoelectron current dI, emitted from the layer with a thickness dz at a depth z, is expressed by,

$$dI = CI_0 AMx \frac{d\sigma}{d\Omega} \exp[-\frac{z}{\lambda_i \cos\alpha}] \cdot dz \qquad \text{(Eq. 3.7)}$$

Where the constant *C* gives the instrumental factor, I_0 is the flux of x-rays, *A* is the analyzed area, M is the total atomic density, *x* is the atom fraction of a given element, λ_I is the elements mean free path depending on the material (matrix), α is the angle between the surface normal and the direction of analysis (emission angle) and $d\sigma/d\Omega$ is the differential photoelectric cross-section [135].

$$\frac{d\sigma}{d\Omega} = \frac{\sigma_t}{4\pi}\{1 - \frac{\beta}{4}(3\cos^2\theta - 1\} \qquad \text{(Eq. 3.8)}$$

Where σ_t is the total photoelectric cross-section, β is the asymmetry parameter and θ is the angle between X-ray propagation direction and direction of the outgoing photoelectron.

In the typical experimental configuration of XPS, a large area specimen is exposed to a broad beam of X-ray irradiating a much larger area than the area being analyzed. Hence, we assume the analyzed area depends on the detection angle according to

$$A = \frac{A_0}{\cos\alpha} \qquad \text{(Eq. 3.9)}$$

Where A_0 is the area seen by the analyzer at the normal direction of analysis. Integrating Eq.3.7 over all depths with account of Eqs.3.8) and 3.9, we obtain

$$I = CI_0 A_0 Mx \frac{d\sigma}{d\Omega} \lambda_i \qquad \text{(Eq. 3.10)}$$

which is valid for homogeneous semi-infinite solids. Therefore a base for calculations of the surface composition is formed.

There are two different experimental procedures used for the quantitative analysis: analysis using standard materials and the so-called relative sensitivity factor approach.

Standard materials approach

This approach is now the most reliable in quantitative applications. The standards and samples are measured using the same experimental geometry with the same parameter used for all recorded spectra. An obvious selection for a standard is the clean surface of the element present in the studied sample. In the simplest experimental procedure of quantitative analysis a given peak intensity is measured for a sample and for the standard. The Eq.3.10 can be modified as follows,

$$\frac{I}{I^{s}} = \frac{M\ \lambda_{i}}{M^{s}\lambda_{i}^{s}} x \qquad \text{(Eq. 3.11)}$$

To obtain the total composition, we should use several standards corresponding to all elements present in the analyzed volume of the sample. Eq.3.11 for the j-th element can be written,

$$x_{j} = \frac{I_{j} M_{j}^{s} \lambda_{j}^{s}}{I_{j}^{s} M_{j} \lambda_{j}} \qquad \text{(Eq. 3.12)}$$

and the sum of x_j should be normalized to 1. Resulting experimental uncertainty in determination of concentrations by this method can be as low as 5%.

Relative sensitivity factor approach

Current industrial samples are frequently far from ideal ones. They have usually rough and contaminated surface or can also be in the form of a powder. In such a case it is difficult to find proper standards. The only method of quantitative analysis, which can be used in practice, is the relative sensitivity factor approach. The signal intensity I_i due to any elemental constituent of the sample is proportional to its concentration

$$I_{i} = S_{i} x_{i} \qquad \text{(Eq. 3.13)}$$

Where S_i is the sensitivity factor, the concentration of the i-th element is calculated from

$$x_i = \frac{I_i / S_i}{\sum_k I_k / S_k} \qquad \text{(Eq. 3.14)}$$

There are tabulation of the sensitivity factors available in the literature [136]. However, the relative sensitivity factor approach is generally less precise than the method described above for the standard sample.

An alternative way may be a modification of the approach to perform the analysis of complex materials with a good accuracy. These modification consist in different methods of introducing corrections accounting for the characteristics of the instrument [137], properties of the sample and the experimental geometry used [138, 139], and elastic scattering effects [140].

The peak shape

The measured spectra deviate from the ideal lines because of a broadening caused by the hole-state life time and the instrumental energy resolution. The two effects on the signal shape are represented by a Lorenzian and a Gaussian function, respectively, which are convoluted in a Voigt profile. For practical purposes, at least square fit of experimental data with the convoluted function is too much time demanding, and the approximation below is preferred [141]

$$I(E) = I_0 / \{(1 + \frac{4\Delta^2 M}{\Gamma^2}) \exp \frac{4 \cdot \Delta^2 (1 - M) \ln 2}{\Gamma^2}\} \qquad \text{(Eq. 3.15)}$$

$$\text{where } \Delta = \frac{E - E_0}{1 - \alpha \frac{(E - E_0)}{\Gamma}} \qquad \text{(Eq. 3.16)}$$

The parameters for fitting a single peak are: I_0 intensity, E_0 binding energy, Γ the peak full width at half maximum (FWHM), α asymmetry factor (which can account for effects like inelastic electron-phonon scattering as typical in metals), M the Gauss-Lorenz fraction (M = 0 pure Gauss, M = 1 pure Lorenz). To reduce the degree of freedom during parameter fitting and obtain acceptable values constrains are applied, or theoretical or known (from literature or

reference measurements) values are taken. For a doublet, the same Γ, α and M are taken, while the intensity ratio must be a value close to the theoretical [2(l-s)+1]/[2(l+s)+1] = l/(l+1).

Auger emission

When an atom is ionized by the production of a core hole, the hole can be filled by an electron transfers from a energetically higher core level. The energy of electron may either be transferred to a photon (X-ray fluorescence) or to an emitted electron of a certain kinetic energy (Auger electron). These competing processes are dominated by the photon emission only when the initial core hole has BE values exceeding about 10 keV. The emission of an electron (see Fig. 3.8) is known as the Auger effect, after its first observer, Pierre Auger.

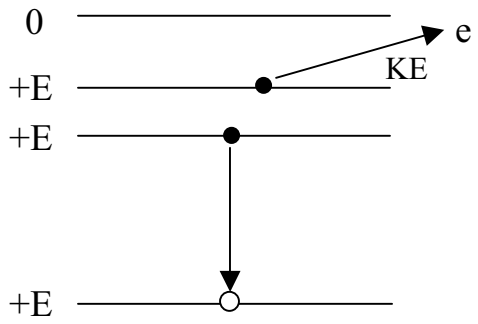

Fig. 3.8 Energy level diagram showing the Auger process

In this case, the kinetic energy (KE) of the Auger electron can be defined as

$$KE = E_A - E_B - E_C \qquad \text{(Eq. 3.17)}$$

Auger signals can also be detected in XPS. They can easily be recognized by changing the excitation source, because their kinetic energy is constant, the BE of Auger emission lines should change their positions. It is usual to label the Auger transition using the X-ray level notation. For example (see Fig.3.8) an Auger transition involving the 1s level as A and 2p levels as both B and C would be labeled as KLL according to the spectroscopic K, L, M, N, ……V nomenclature.

3.1.1.5 Resonant PES

Resonant photoelectron spectroscopy (RPES), first observed by Guillot et al. [142] in Ni metal, has proven to be an efficient tool to study the electronic structure of solid state materials [143, 144]. Detailed reviews are given in references [144-146], therefore only a brief summary of the main concepts will be given.

RPES is based on the quantum-mechanical interference between two excitation processes that transform a certain initial state to the same final state via two different pathways. The direct photoemission process produces electrons with the kinetic energy E:

$$3p^6 3d^n + h\nu \Rightarrow 3d^6 3d^{n-1} + e^-(E) \qquad \text{(Eq. 3.18)}$$

Concurrent to Eq.3.18, optical adsorption may lead to excitation of the 3p to 3d level:

$$3p^6 3d^n + h\nu \Rightarrow [3d^5 3d^{n+1}]^* \qquad \text{(Eq. 3.19)}$$

The excited state decays and an electron is emitted with the same kinetic energy as in the direct process:

$$[3d^5 3d^{n+1}]^* \Rightarrow 3d^6 3d^{n-1} + e^-(E) \qquad \text{(Eq. 3.20)}$$

The scheme of the so called autoionization process involving 3p and 3d orbitals is shown in Fig.3.9,

For a photon energy hν near the threshold at which the 3p core levels are excited, it was found that the 3d photoionization cross section is enhanced [142]. Usually, the resonance is shifted to higher photo energies than expected from the separation of the contributing energy levels (such as E(3d) – E(3p)) due to the phase shift of direct photoemission and autoionization. The photoionization cross section (σ) as a function of photon energy (ε) can be discribed by a Fano profile as given in Fig.3.10.

$$\sigma \propto \frac{(q + \varepsilon)^2}{1 + \varepsilon^2} \qquad \text{(Eq. 3.21)}$$

and

$$\varepsilon = \frac{E - E_0}{\Gamma} \qquad \text{(Eq. 3.22)}$$

Where q is the asymmetry parameter, ε the relative energy, and Γ the FWHM of resonance,

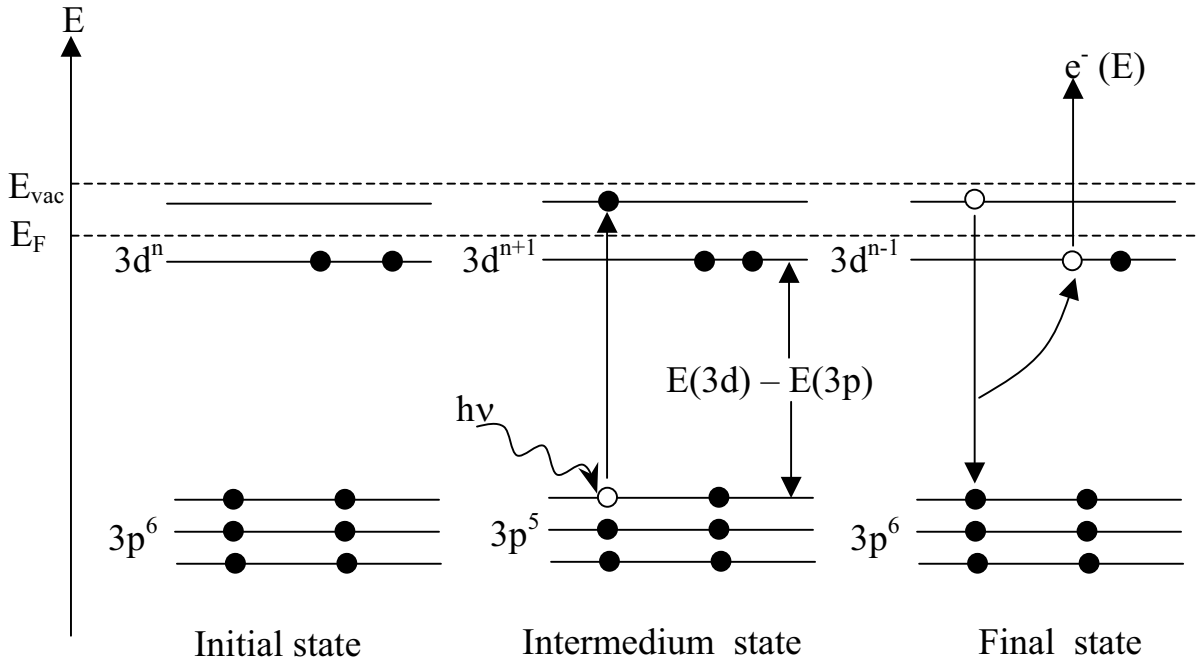

Fig. 3.9 The process of autoionization

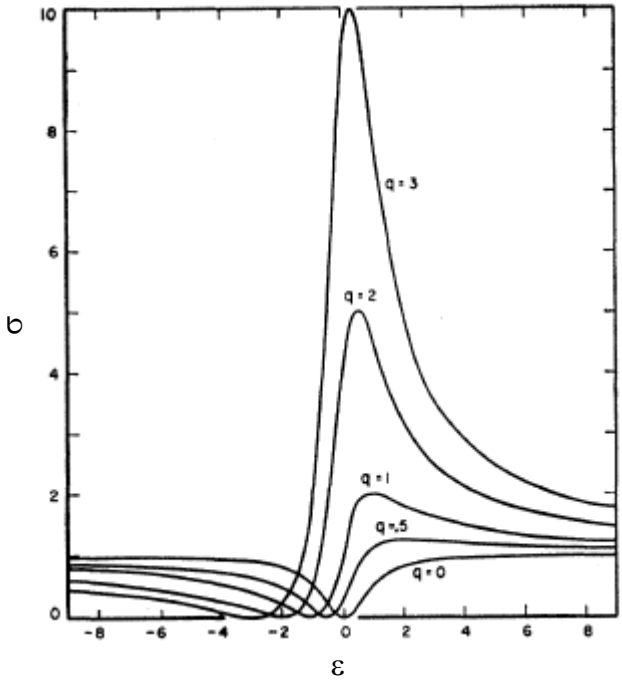

Fig.3.10 The Fano profile for different values of q as a function of relative

3.1.2 AFM

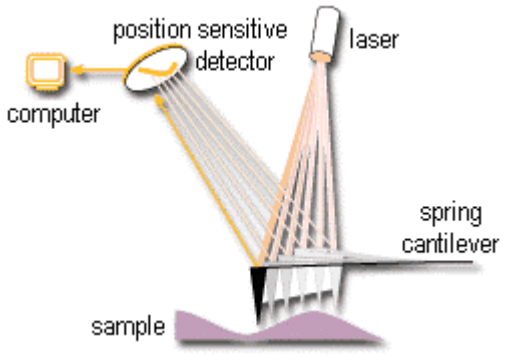

Fig. 3.11 The working mechanism of AFM

The atomic force microscope (AFM), invented in 1986 by Binnig, Quate and Gerber [148], provides topographic pictures of surfaces with in the best case, atomic resolution. The AFM works by scanning a fine tip over a surface similar to a phonograph needle scanning a record. The tip is positioned at the end of a cantilever which bends in response to the force between the tip and the sample. The light from a laser is reflected by the cantilever onto a position-sensitive detector (see Fig.3.11). As the tip is repelled by or attracted to the surface, the cantilever beam deflects. The magnitude of the deflection is captured by a laser that reflects at an oblique angle from the very end of the cantilever. A plot of the laser deflection versus tip position on the sample surface provides the resolution of the hills and valleys that constitute the topography of the surface. The AFM can work with the tip touching the sample (contact mode), or the tip can vibrate above the surface (non-contact mode). In the non-contact mode (of distances greater than 10Å between the tip and the sample surface), van der Waals, electrostatic, magnetic or capillary forces produce images, whereas in the contact mode, electronic repulsion forces take the leading role. Because its operation does not require a current between the sample surface and the tip, the AFM can move into potential regions inaccessible to the Scanning Tunneling Microscope (STM) or image fragile samples, which would be damaged irreparably by the STM tunneling current. Insulators, organic materials, biological macromolecules, polymers, ceramics, and glasses are some of the many materials, which can be imaged in different environments, such as liquids, vacuum, and low temperatures.

3.2 UHV equipment and spectrometer systems

Ultra high vacuum (UHV) is required for most surface science experiments for two reasons: 1) to enable atomically clean surface can be prepared for the study; 2) to permit the use of low energy electron and ion-based experimental techniques without interference from gas phase scattering. Generally, a vacuum of at least 10^{-6} mbar is required for the electrons travelling from the sample to the analyzer. But due to the technique's surface sensitivity any kind of absorbates chemically or physically interacting with the sample alter the spectra significantly. With a partial pressure of 10^{-10} mbar one monolayer of a species with a sticking probability would be deposited in 3 hours. In practical cases a total pressure of 10^{-10} mbar generally prevents from contamination within a time much longer than that required for measurement, as the sticking coefficient will be low. These vacuum levels can be achieved with standard UHV equipment based on turbo molecular pumps connected to rotary vane or membrane roughing pumps. In absence of leaks, a pressure in the order of 10^{-10} mbar can be reached by pumping and backing the system for at least 8h at about 150°C. This process speeds up the desorption of atmospheric adsorbates from the chamber walls. Rest gas molecules can also temporarily be captured by cooling traps or permanently by titanium sublimation pumps.

During this work two spectrometer systems have been used for photoemission measurements: one is located at the Surface Science Division of the TU-Darmstadt, while the other is permanently located at the BESSY II TGM7 beamline.

The system used at TU-Darmstadt is the so called integrated system DAISY-MAT equipped with an UHV surface science analysis system and several UHV preparation chambers. The pass energies used in our study are reported in table 3.2.

Photon source	XPS (overview)	XPS (Core level, Auger, Valence band)	UPS (HeI and HeII)
Pass energies (eV)	187.85	5.85	2.95

Tab. 3.2 Typical pass energies values (in eV) used in this work

3.2.1 The DAISY-MAT system

The XPS and UPS experiments have been carried out at room temperature in the integrated system combining different in-situ preparation techniques connected to a transfer chamber with the surface analysis system (Phi 5600) (see Fig.3.12). The base pressure during the measurements has been better than 10^{-9} mbar. Al K_α radiation ($h\nu$=1486.6eV) from a

monochromatized X-ray source has been used for XPS, and UV light ($h\nu_1$=21.22 eV (HeI) and $h\nu_2$=40.81 eV (HeII)) from a discharge lamp for UPS measurements.

The spectra are given in binding energy scale (BE) referred to the Fermi level of a Ag reference sample. Sample stoichiometry ratios $S_{i,j}$ have been calculated from the XP spectra using the following formula (see also in Ch.3.1.1.4):

$$S_{i,j} = \frac{C_i}{C_j} = \frac{I_i / ASF_i}{I_j / ASF_j} \quad . \qquad \text{(Eq. 3.23)}$$

Where C_i and C_j are the concentrations of the ith and jth element, I_i and I_j the background corrected intensities of the photoelectron emission lines for element i and j, and ASF_i and ASF_j the atomic sensitivity factors of the emission lines (1.275 for V2p$_{3/2}$, 0.711 for O1s, and 1.685 for Na 1s, respectively) as given for the Phi 400. For stoichiometric V_2O_5 the result should of course be $S_{i,j}$=2.5. The above formula is only valid for homogenous element distributions in the sample.

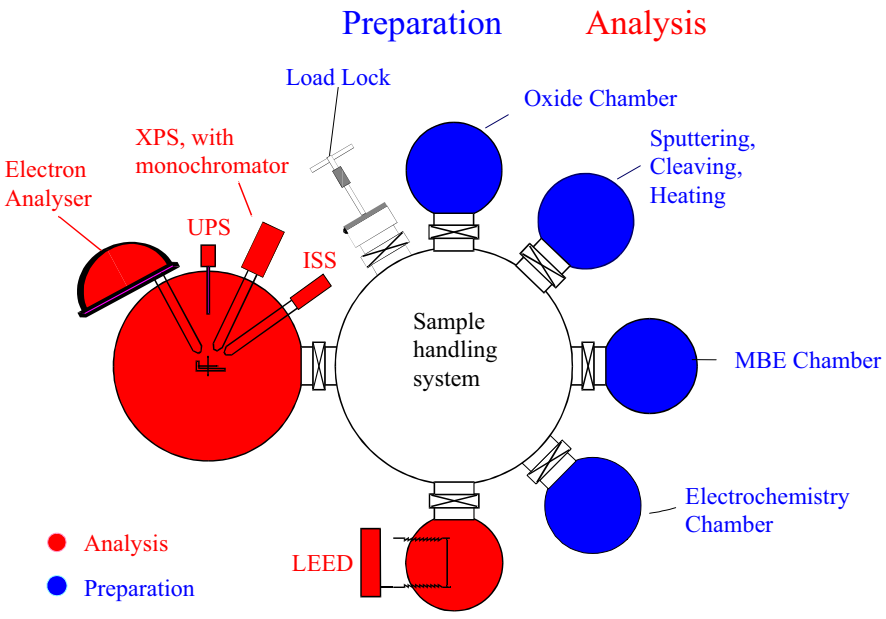

Fig. 3.12 Schematic view of the Darmstadt integrated preparation and analysis DAISY-MAT system

3.2.2 BESSY II TGM7 system (SoLiAS)

An angle resolving VG ADES 400 spectrometer with an acceptance angle of 2° and a pass energy of 2 eV was used at the BESSY II TGM7 beam line. Due to collisions of the ring

electrons with residual gas molecules (pressure inside the ring is about 10^{-9} mbar) the photon intensity is decreasing exponentially with time ($t_{1/2}$ = 4h), in the mean time the emission intensity also decreases proportionally. To compare different lines and their intensity all spectra have to be normalized in respect to the photoemission current measured on the last refocusing mirror. The intensities will be given in arbitrary units proportional to the signal measured at a constant photon flux. The picture of SoliAS and scheme of the TGM 7 beamline set up is shown is Fig.3.13 and 3.14.

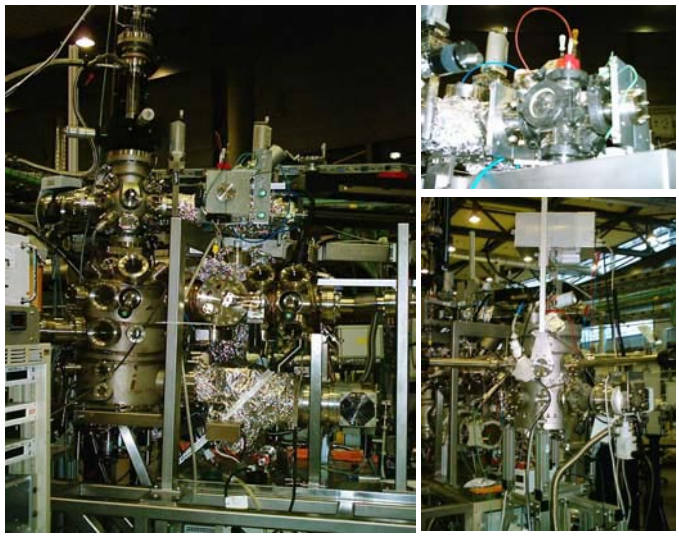

Fig.3.13 The picture of SoLiAS

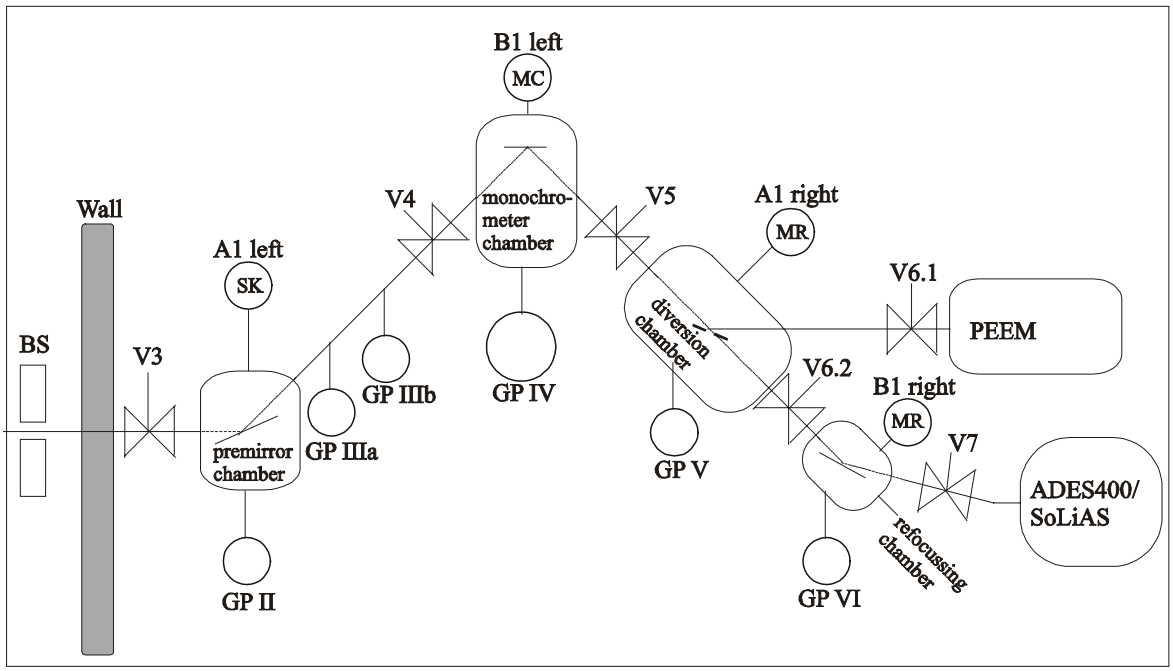

Fig. 3.14 The scheme of the experimental set-up at the BESSY II TGM 7 beam line

3.3 Preparative aspects

3.3.1 Samples

HOPG substrate

Highly Ordered Pyrolytic Graphite (HOPG) delivered from Agar Scientific Limited, England have been used as substrates for thin films preparation. It is high purity carbon providing renewable and smooth surfaces. The samples were freshly cleaved by riving off the top surface layers before inserting them into the UHV chamber.

3.3.2 Sources

Alkali metals

Alkali metals were evaporated from commercial dispensers produced by SAES Getters SpA. The dispensers are made of a mixture of the respective alkali chromate (A_2CrO_4) and an Al alloy (ST101:16% Al/84% Zr) enclosed in a nickel boat. By resistive heating at currents larger than 4.5 A (temperatures > 500°C) the alkali is reduced by the alloy. Due to its special shape the boat opens and the alkali is emitted through a narrow slit. For Li and Na, currents of 6.5 A has been used, corresponding to temperatures of about 700°C. The evaluation of the evaporation rate is particularly difficult and depends on the operation time of the source. A measure of the deposition rate with a quartz microbalance is impossible, as at room temperature alkali metals are known to stick only up to about one monolayer coverage on different substrates. Practically the amounts of alkali on the samples are always evaluated from their XPS signal relative to the substrate.

V_2O_5

V_2O_5 has been delivered as powder from Heraeus, Germany, with a purity of 99.99%. V_2O_5 thin films were deposited onto freshly cleaned HOPG substrates at room temperature from a homemade PVD effusion cell using a BN_2 crucible containing V_2O_5 powder with a NiCr/Ni thermocouple attached (see Fig.3.15). During deposition the source temperature was approximately 670°C at a pressure of about 1.2×10^{-6} mbar indicating the partial reduction of V_2O_5 in the crucible. At these conditions the deposition rate has been determined to be 0.23Å per minute by a quartz microbalance (QMB).

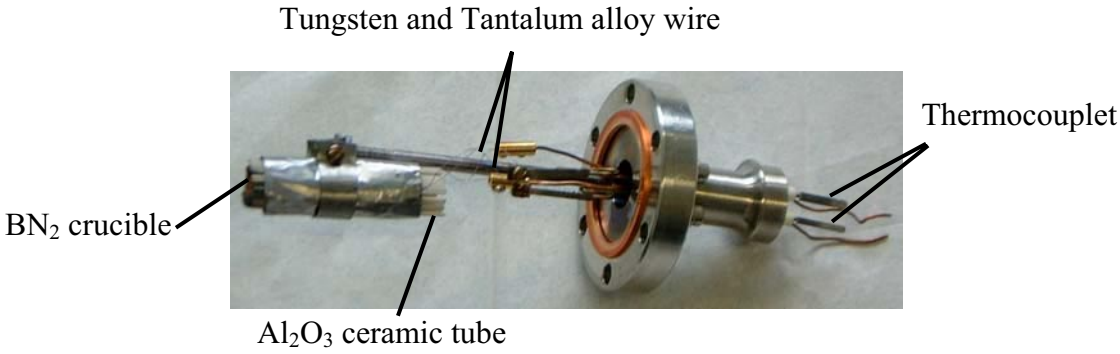

Fig.3.15 The picture of the V_2O_5 source

4 Thin film synthesis and electronic structure of V_2O_5

In this chapter the synthesis and the thermal properties of vanadium pentoxide (V_2O_5) thin films will be introduced. The purpose of this chapter is to investigate the electronic structure of V_2O_5 by means of XPS, UPS and resonant photoemission spectroscopy (RPES). XPS is used to determine the composition of the V_2O_5 surfaces and the oxidation states of the elements. UPS is an ideal surface analysis technique to provide the information about the electronic structure of the valence band region. V_2O_5 is a transition metal oxide with interesting potential for technological applications [149, 150]. It has been studied intensively by theoretical calculation and experimental techniques [151-154]. It is a n-type semiconductor with low electron mobility [155]. The band gap is about 2.35 eV [156, 157]. V_2O_5 exhibits an orthorhombic layered structure [66] (see Fig.2.6) with very weak metal-metal interactions. Thin film V_2O_5 can be prepared by a variety of deposition techniques [158-164]. Polycrystalline films exhibit multicoloured electrochromism allowing the use in electrochromic displays, colour filters, and other optical devices [165, 166]. In addition, bulk and thin films of V_2O_5 have been used as an oxidation catalyst [167]. As a functional inorganic material V_2O_5 can be used in gas sensors [168]. All these interesting properties are strongly related to oxygen vacancies leading to changes in the electronic structure and to crystal relations which will be discussed later on. In particular, V_2O_5 films are promising candidates for active cathode materials for thin film lithium microbatteries, because of their layered structure, high energy density, and capacity [169-174]. The performance of the active layer is strongly dependent on the synthesis procedure [16]. Different techniques, such as sol-gel process [175], dc and rf magnetron sputtering [176-178], pulsed laser deposition [156, 179], and plasma enhanced MOCVD [180] have been applied to prepare V_2O_5 thin films. In this work the V_2O_5 thin film have been prepared by physical vapour deposition with the aim to study the intercalation processes in V_2O_5 cathodes of alkali-ion batteries.

4.1 Physical vapour deposition (PVD)

The deposition of thin films at high- or ultra-high-vacuum conditions has emerged in the last two decades. In general, there are two categories of vapour deposition processes: physical vapor deposition (PVD) and chemical vapour deposition (CVD). CVD is based on chemical reactions transforming gaseous molecules, usually called precursors, into solid thin films or powders on the surface of a substrate. This technique will not be discussed in detail in this work.

The basic idea behind PVD is the physical change of state of the material that is being deposited (target material). All deposition processes including PVD processes can be classified in terms of the following three steps during the deposition [181]: 1). Creation of a vapour phase, for instance by thermal evaporation, arc evaporation, or sputtering in the source. The technique of thermal evaporation is used in our experiments, because V_2O_5 vapour can be evaporated out of the source at relatively low temperatures of about 600°C. 2). Transport of

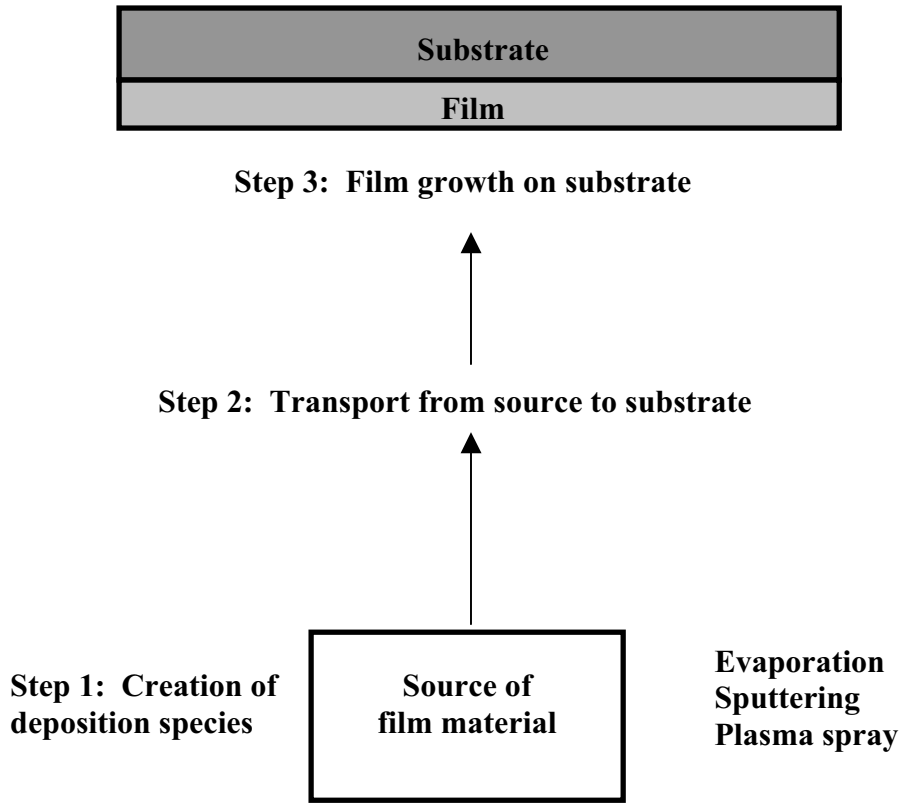

Fig. 4.1 Schematic of three steps in PVD process

the vapour from the source to substrate (line-of-sight, molecular flow, and vapour ionization by creating a plasma). 3). Film growth on the substrate. The model is illustrated in Fig.4.1. These steps can be independent or superimposed on each other depending on the desired thin film characteristics. The deposition of PVD can be reactive or non-reactive. In the case of reactive deposition, the deposited material reacts with a gaseous environment of co-deposited material to form a film of a compound material, such as nitrides, oxides, carbides or carbonitrides. The non-reactive deposition is an atom-by-atom transfer of material from the solid phase to the vapour phase and back to the solid phase.

The selection criteria to determine the best method of PVD is dependent on several factors, such as, material to be deposited, rate of deposition, adhesion of the adsorbate on the

substrate, purity of initial materials, cost, equipment requirements, and their availability, as well.

4.2 V_2O_5 thin films

4.2.1 Sources

As base material, commercial high purity V_2O_5 (99.99%, Heracus, Germany) powder has been used in our study. The V_2O_5 thin films were deposited onto a freshly cleaved HOPG substrate at room temperature (RT). During deposition, the temperature of the source (see Fig.3.15) was approximately 670°C. The pressure of about 1.2×10^{-6} mbar compared to a base pressure of 10^{-10} mbar indicates the partial reduction of V_2O_5 in the source to V_2O_{5-x}. After several hours of deposition metallic V remains in the crucible. The deposition rate in our experiments was about 0.23 Å per minute, which was determined by a quartz microbalance (QMB), resulting in an about 35 Å think V_2O_5 film after a deposition time of 2.5 hours.

4.2.2 Substrate

The HOPG (highly oriented pyrolytic graphite) crystals have been provided by Agar Scientific Limited, Germany. The planes are highly oriented to each other, while in the planes, there is a statistical orientation of single crystalline regions. This crystal structure allows a simple air cleavage using adhesive tape leading to a clean renewable and smooth surface.

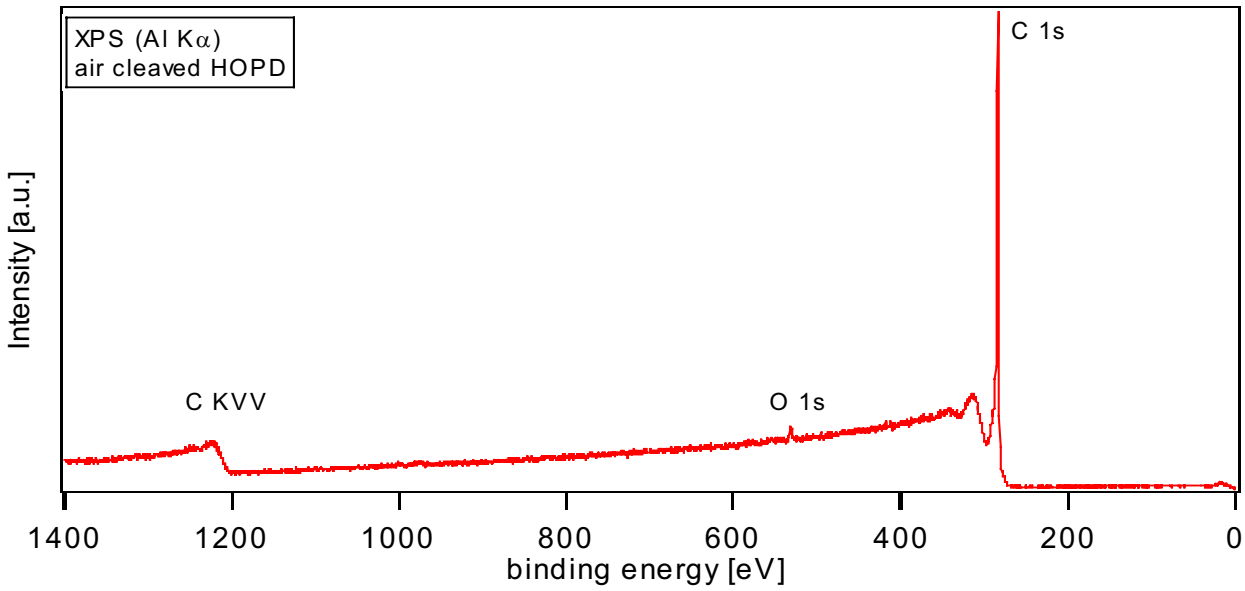

Fig. 4.2 Survey XP spectrum of the HOPG substrate

Unlike mica, HOPG is completely non-polar and, for samples where elemental analysis will also be done, it provides a single elements with only two emission lines (C1s and C KLL).

The overview XP spectrum of HOPG is shown in Fig.4.2. Except a very weak oxygen contamination (O1s line) only pure carbon is found on the surface.

4.2.3 V_2O_5 thin films

The survey XP spectra of stepwise deposited V_2O_5 films on HOPG are shown in Fig.4.3.

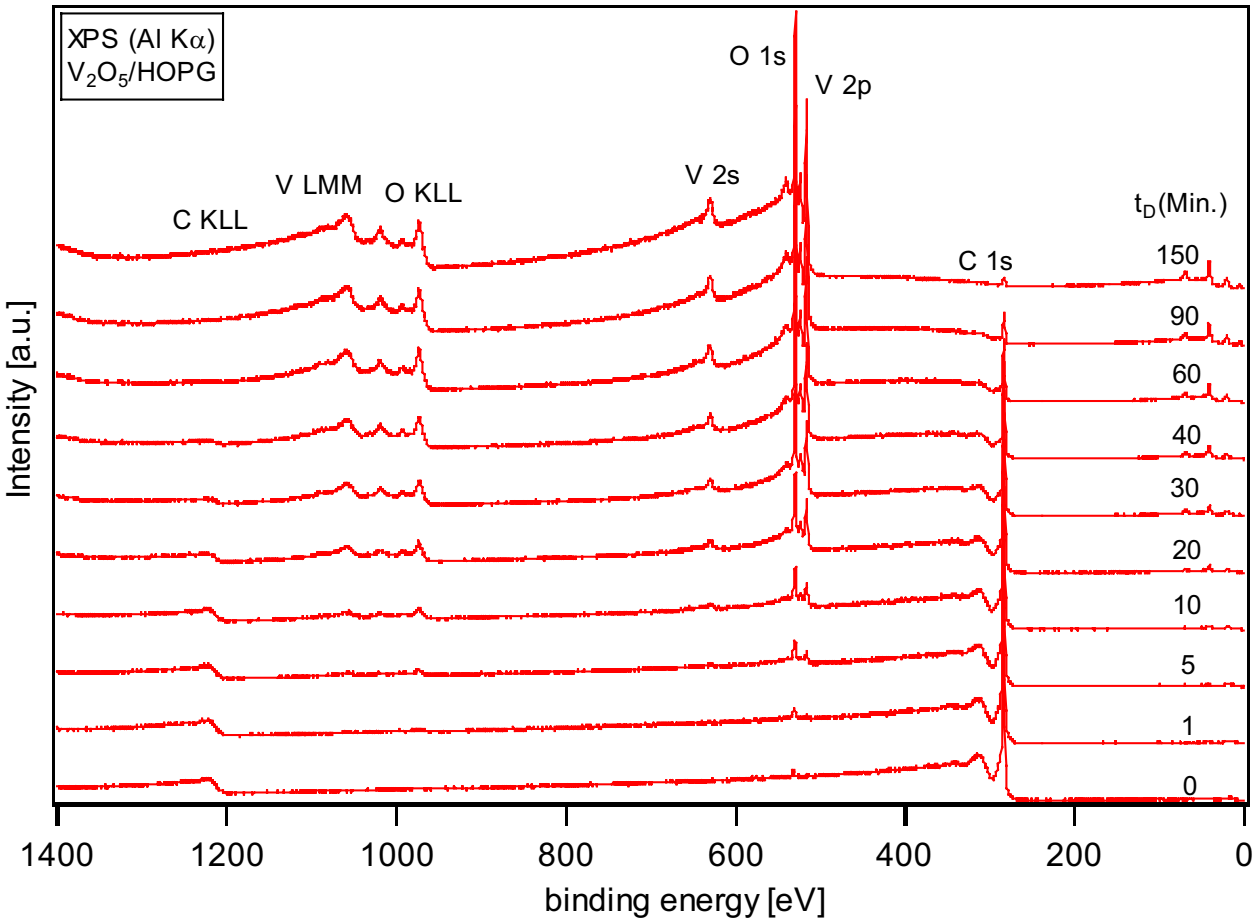

Fig. 4.3 XPS overview spectra for the step by step deposition of V_2O_5 on HOPG

The intensity of the C1s core line and the C KLL Auger line decrease while the intensities of the adsorbate emission line (O1s and V2p) increase gradually with increasing deposition time (t_D). After 150 minutes deposition the C1s signal is almost completely damped by the V_2O_5 film and only V and O can be found on the surface by XPS. The O1s and V2p core level XP spectra are shown in more detail in Fig.4.4. The $V2p_{3/2}$ peak shows up well-shaped even for lowest coverages with a very weak shoulder line on the low binding energy side due to a small amount of V^{4+} species. The intensity ratio of $O1s/V2p_{3/2}$ is nearly constant as a function of deposition time (see Fig. 4.5). The binding energies of the $V2p_{3/2}$ and O1s core levels do also not change appreciably with increasing V_2O_5 coverage (see Fig.4.4). Thus the spectra

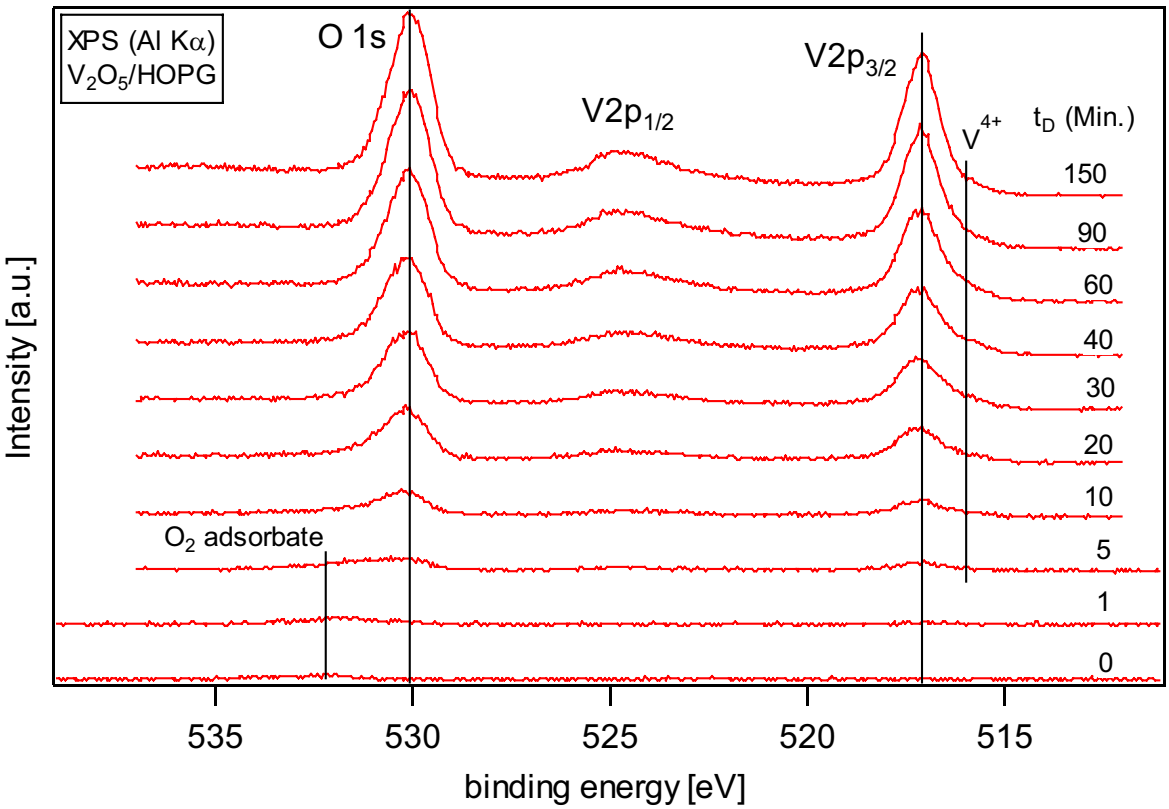

Fig.4.4 O1s and V2p core level XP spectra of successive deposition of V_2O_5

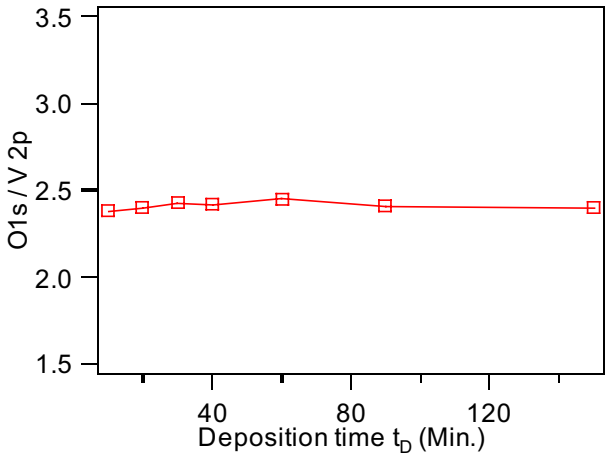

Fig. 4.5 The ratio of O1s / V2p against the deposition time

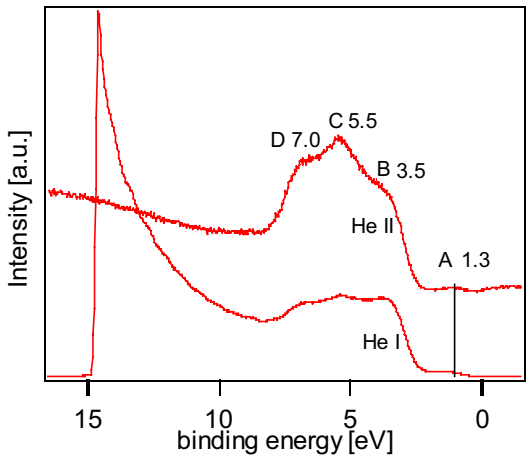

Fig.4.6 UP spectra of V_2O_5 thin film

appear similar for all the investigated coverages, and a growing film of the same oxide composition after each growth step is evident. The binding energies of the V2p levels are 516.8 and 524.5 eV for V $2p_{3/2}$ and V $2p_{1/2}$, respectively, with a splitting of 7.5 eV, whereas that of the O1s level is 529.6 eV. These are very close to the literature values for stoichiometric V_2O_5 at room temperature [182]. The ratio of O1s/V$2p_{3/2}$ is about 2.46, also indicating that the V_2O_5 thin films in this work is nearly stoichiometric. The line width of V$2p_{1/2}$ is much broader than that of V$2p_{3/2}$ due to the Coster-Kronig Auger transitions [183].

The UP spectra (He I and He II) of V_2O_5 thin film are shown in Fig.4.6 containing the valence band region of V_2O_5 between 3 and 9 eV and the emission of a gap state A in the optical gap (BE ≈ 1.3 eV), which will later be assigned to V3d-like states occupied due to oxygen vacancy formation. From the He I spectrum, the work function of thin film V_2O_5 can be determined to be about 6.2 eV.

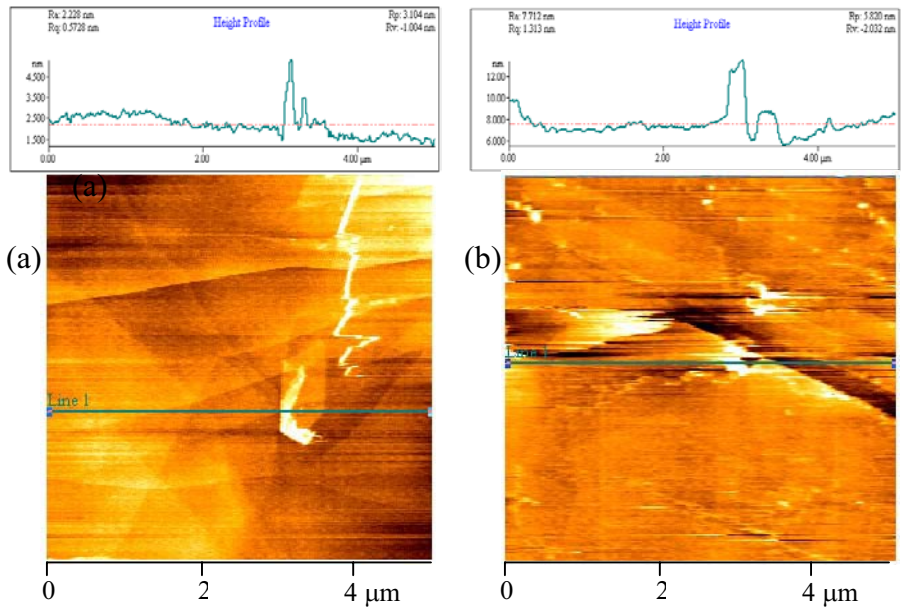

Fig. 4.7 The AFM images and the height profile of HOPG substrate (a) and V_2O_5 thin film (b)

The surface morphology of the V_2O_5 films has been studied by atomic force microscopy (AFM) which is shown in Fig.4.7. The AFM data demonstrate that the PVD grown V_2O_5 thin films are homogeneous and uniform compared to the substrate. The average surface roughness of the V_2O_5 film over the 5×5 µm is found to be about 1 nm, which is slightly larger than that of the HOPG substrate (0.7 nm). It seems that the 2D V_2O_5 film forms a layer-by-layer grown overlayer on the 2D graphite substrate. Within the present study we have not observed any ordered V_2O_5 thin film on the HOPG substrate by low energy electron

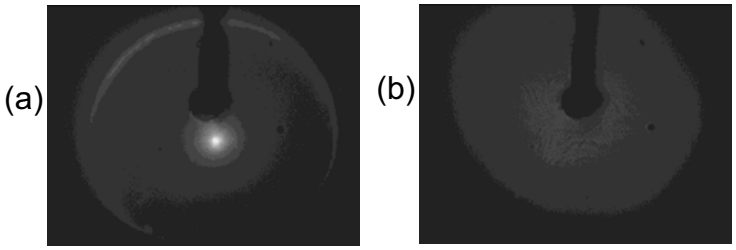

Fig.4.8 LEED patterns of HOPG substrate (a) and V_2O_5 thin film (b), electron energy: 66 eV

diffraction (LEED) (see Fig.4.8), indicating the films to be not single crystalline in a long range order. If it is possible to get crystalline growth at elevated temperatures is of interest but needs more systematic study.

4.2 V_2O_5 thin films

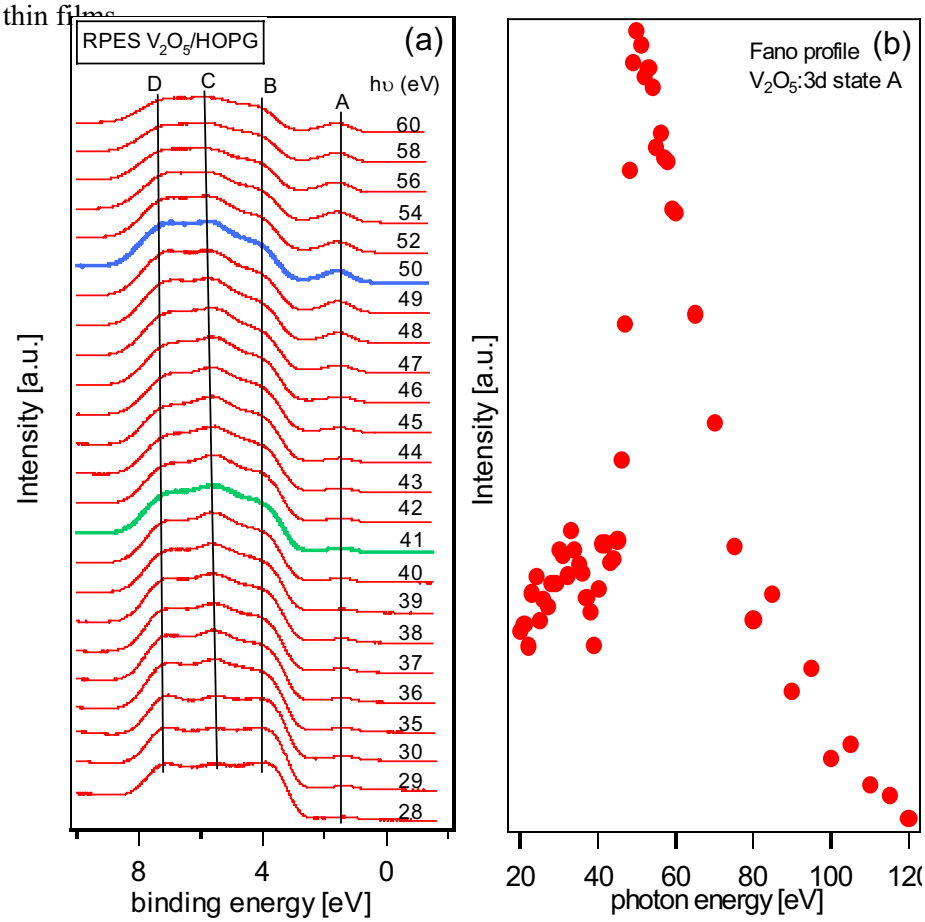

Fig. 4.9 Vanadium 3p resonant photoemission spectra of V_2O_5 in the energy range from 28 to 60 eV (a) and the intensity change of feature A with the photon energy (b)

The mechanism of resonant photoemission in 3d metals and their compounds is well known [184-186]. For transition-metal oxides it is generally believed that the 3p-3d excitation is localised at the metal atom involving only 3d-derived final states. Therefore the different contribution of O2p and M3d states in the valence band of transition-metal oxides can be separated by obtaining spectra just above and below the resonance. The V_2O_5 resonant photoemission spectra are shown in Fig.4.9(a) for photon energies from 28 to 60 eV. The feature A connected with the antibonding O2p-V3d states is mostly of V3d-like character. This is indicated by the strong enhancement of its intensity in the energy range of the V3p-V3d transition which can be fitted by a Fano profile (see Fig.4.9(b)). Features B, C and D form the valence band region of V_2O_5, which is thought to be mainly due to O2p states [187]. From the spectra in Fig.4.9(a), it is obvious that the intensity of feature A at BE=1.3 eV

increases with increase of photon energy starting at 40 eV, and reaches a maximum at about 51 eV, and then decreases again with increasing photon energy (see detail in Fig.4.9(b)). Feature B at 3.6 eV shows only small intensity variations, and features C and D at 5.5 and 7.0

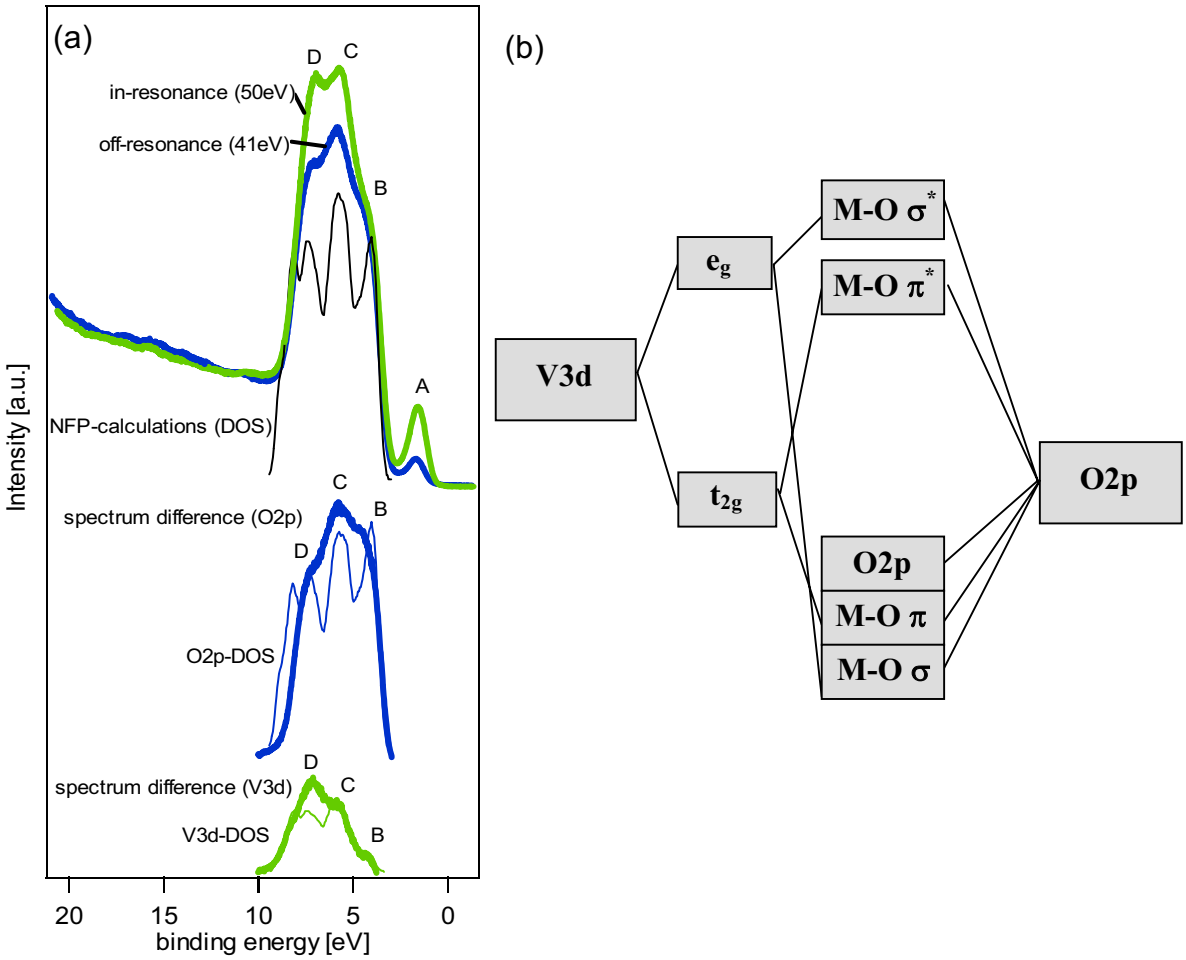

Fig.4.10 The band structure calculation data of O2p and V3d contribution to the V_2O_5 valence band region [189] and comparison with the experimental data (a), and the schematic electronic structure of V_2O_5 for the undistorted octahedral crystal structure.

eV, respectively, show a resonance enhancement in between, when the photon energy increases from 41 to 50 eV. The broadness of the feature A (V3d) has been discussed earlier by Egdell et al. [188] in their PES study by a strong electron-phonon (polaron) interaction, related to the strong polarization of the lattice by the valence electrons. The enhancement of the valence band indicates a large amount of V3d character in this band, i.e. a strong O2p-V3d hybridization. Judged from our RPES data, feature B is assigned to the nonbonding O2p band which mainly consists of O2p components. On the other hand, the features C and D are assigned to the bonding bands hybridised with 3d orbitals which contain an appreciable amount of V3d hybridization. Our experimental results demonstrate that the O2p-V3d bonding states have a higher binding energy than the non-bonding O2p states. Band structure

calculations supports this conclusion that the high binding energy side of the valence band consists of the O2p-V3d bonding states [151, 152]. Fig.4.10(a) shows the band structure calculation data of O2p and V3d contributions to the valence band region and the comparison with the experimental data. The band structure calculations are DFT calculation using full potentials and the GGA approximation [189]. We can see again that the V3d contributions are mostly located on the higher binding energy region of the valence band, and feature B is mostly of pure O2p character. Therefore the electronic structure of V_2O_5 can be roughly summarised as shown in Fig.4.10(b)

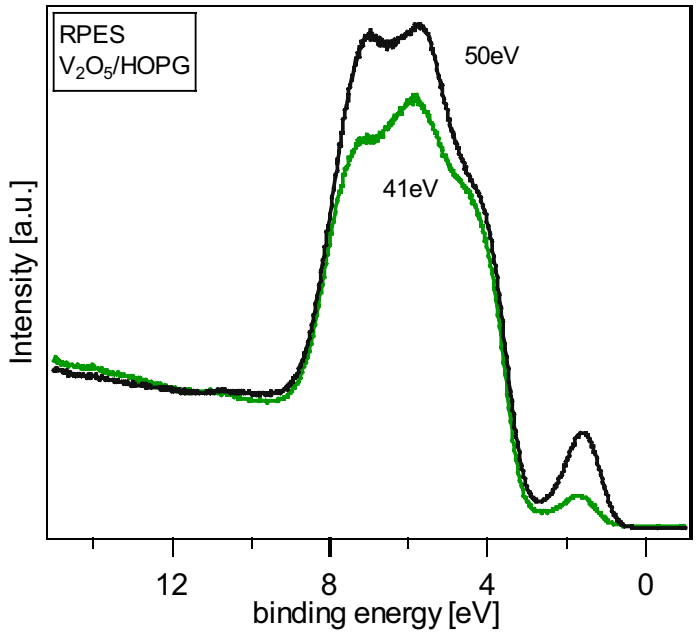

Fig.4.11 Comparison of the normalized spectra with photon energies of 41 and 50 eV, which are before and at the maximum of resonance effect respectively

In order to calculate the number of 3d electrons per V ion in the valence band region of V_2O_5, the spectra with a photon energy of 41 and 50 eV are chosen (see Fig.4.11). The binding energy of V3p in vanadium oxides is about 41 eV [190]. Therefore the energies of 41 and 50 eV are expected to be at the threshold and the maximum of resonance, respectively (see Fig.4.9). According to the following formulas [191, 192]
the VB-occupation numbers can be calculated from the V_2O_5 RPES data:
the electron concentration of V_2O_5 has two contribution, one is from oxygen 2p states and the other is from the vanadium 3d states,

$$\int_{VB} I(E)dE = \int_{VB} \sigma_O \rho_O(E)dE + \int_{VB} \sigma_V \rho_V(E)dE \qquad \text{(Eq.4.1)}$$

ρ is the partial DOS of O2p and V3d states, respectively.

Divided by the photoionization cross section of oxygen (σ_O), we get,

$$\int_{VB}\frac{I(E)}{\sigma_O}dE = \int_{VB}\rho_O(E)dE + \int_{VB}\frac{\sigma_V}{\sigma_O}\rho_V(E)dE \qquad \text{(Eq.4.2)}$$

After Yeh and Lindau [193], for E = 41eV, $\frac{\sigma_V}{\sigma_O} \approx 1$, the Eq.4.2 can be simplified as,

$$\int_{VB}\frac{I(E,41eV)}{\sigma_O}dE = \int_{VB}\rho_O(E)dE + \int_{VB}\rho_V(E)dE \qquad \text{(Eq.4.3)}$$

The valence band electrons for two V_2O_5 unit cell are 2 × (5m + 2n) = 60 where m and n are the occupation numbers of O2p and V3d states, respectively ($m = \int_{VB}\rho_O(E)dE$ and $n = \int_{VB}\rho_V(E)dE$). Therefore, we have 60 = 10m + 4n (Eq.4.4)

For E = 50eV,

$$\int_{VB}\frac{I(E,50eV)}{\sigma_O}dE = \int_{VB}\rho_O(E)dE + \frac{\sigma_V(50eV)}{\sigma_V}\cdot\int_{VB}\frac{\sigma_V}{\sigma_O}\rho_V(E)dE$$

$$\downarrow$$

$$\frac{\sigma_V(50eV)}{\sigma_V(41eV)}\cdot\frac{\sigma_V(41eV)}{\sigma_O}\cdot\int_{VB}\rho_V(E)dE \qquad \text{(Eq.4.5)}$$

$$\downarrow \qquad \downarrow \qquad \downarrow$$

$$f_{VB}\cdot 60 \quad = \quad 10\text{m} \quad + \quad f_V\cdot 4\,\text{n} \qquad \text{(Eq.4.6)}$$

Where *f* is the gain factor due to the resonant effect, $\sigma_{O2p}(50eV) = 5.7$, $\sigma_{O2p}(41eV) = 6.81$. Integration over the areas of valence band and gap regions of the spectra with photon energies of 41 and 50 eV, we get that f_{VB} = 1.4, and f_V = 3.88. According to Eq.4.4 and 4.6, we have,

60 = 10m + 4n

83.6 = 10m + 4 × 3.88n

Thus the values of m and n are calculated to be 5.2 and 2.0, respectively, leading to the oxidation states of oxygen and vanadium of 4 – 5.2 = -1.2 and 5 – 2.0 = 3, respectively. By this means we get that the real "oxidation state" as deduced by the occupation of states by electron of V and O in V_2O_5 to be $V_2^{+3}O_5^{-1.2}$ but not $V_2^{+5}O_5^{-2}$ as can be expected by a purely ionic approximaton.

4.2.4 Thermal decomposition of thin film V_2O_5

The reduction behaviour and phase transitions of vanadium oxides at various temperatures have already been studied [146-201]. The earlier investigations on the bulk reduction of V_2O_5 were concentrated on the V_2O_5-H_2 reactions for the synthesis of vanadium oxides with oxidation states lower than 5+ [201-204]. Other methods for the reduction of vanadium oxides are also reported, such as electron beam-induced reduction [197, 198, 205]. The thermal decomposition of bulk V_2O_5 at a temperature of up to 400°C in vacuum was investigated using TEM by Tilley and Hyde [197]. A number of new phases were reported, two of them being described as ordered super-lattices of anion vacancies in V_2O_5. These authors could not find any evidence for the occurrence of crystallographic shear, which is thought to be necessary for the phase transformation. In the present work the thermal decomposition of a V_2O_5 thin film up to 400°C without and with additional oxygen pressure in the chamber has been investigated with the aim to determine the reduction and re-oxidation

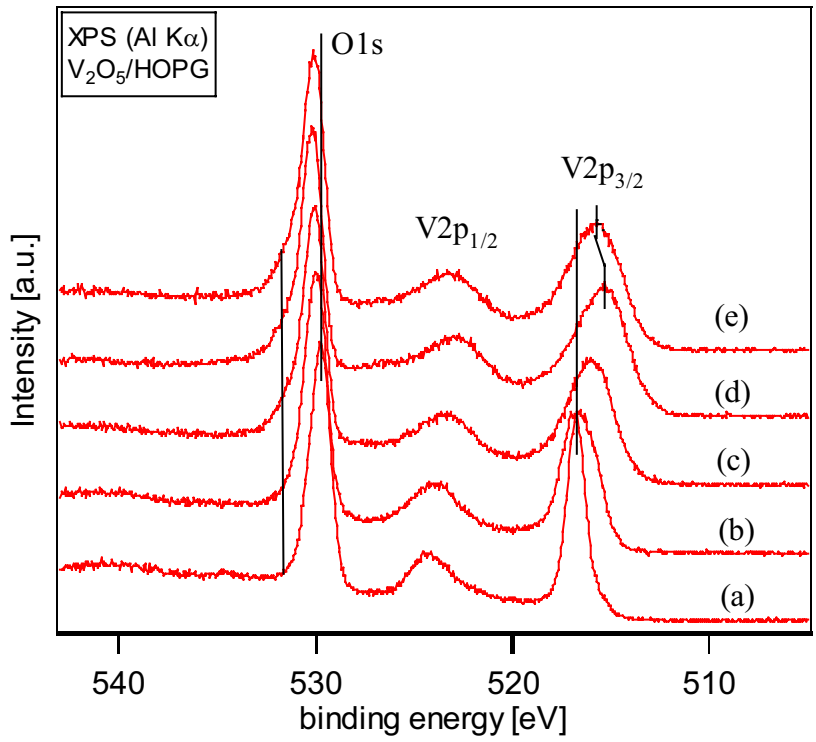

Fig. 4.12 XP spectra of O1s and V2p core level after different preparation, (a) RT, (b) 200°C, (c) 300°C, (d) 400°C, and (e) 400°C with 10^{-5} mbar oxygen

path of V_2O_5 under controlled temperature condition. Fig.4.12 shows the XP spectra of the O1s and V2p core level emission lines before (a) and after (b, c, d, e) reduction by heating in UHV at the specified temperatures. Spectrum e is heated in oxygen with a partial pressure of 10^{-6} mbar. After deposition of V_2O_5 at RT (spectrum a), the binding energies (BEs) of O1s and $V2p_{3/2}$ are 529.6 and 516.8 eV, respectively, which are consistent with literature values for stoichiometric V_2O_5 [206]. But a very small shoulder at the lower BE side is found indicating a small amount of vanadium in the reduced +4 oxidation state. Spectra b-e show

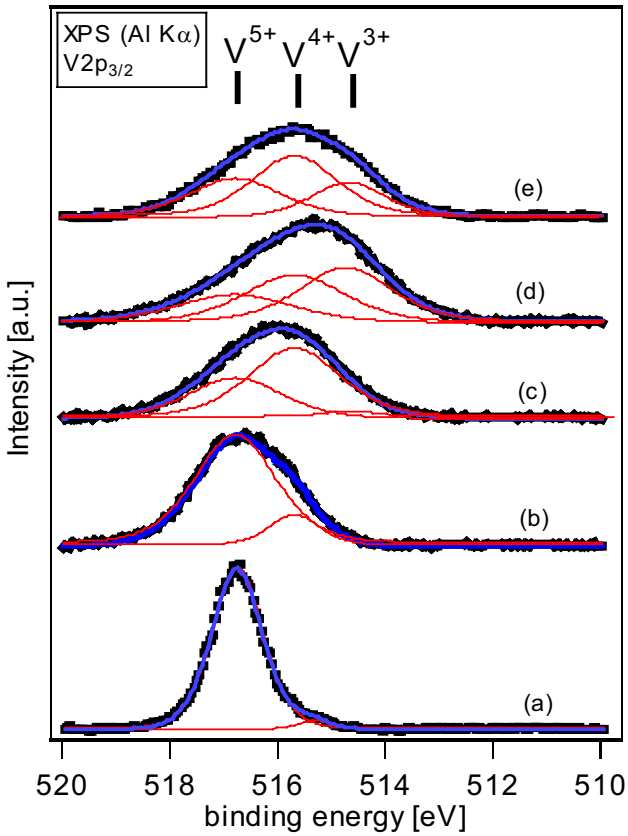

Fig.4.13 Fitted data of $V2p_{3/2}$ lines after removal of background, (a) RT, (b) 200°C, (c) 300°C, (d) 400°C, (e) 400°C in 10^{-5} mbar oxygen

that the $V2p_{3/2}$ and $V2p_{1/2}$ lines become broader and shift to lower binding energies with increasing temperature. The decrease in the binding energy of the core level (chemical shift) usually indicates a decrease in the positive charge of the transition metal atoms. The O1s line is slightly asymmetric, suffers a small shift to higher binding energies (~0.3 eV), and becomes a little broader due to the formation of V_2O_{5-x} species [206] with the FWHM increasing from 1.25 to 1.45 eV. But no significant change in the signal shape can be seen over the whole series. In the spectrum e we note that the V2p emission lines are slightly shifted back to higher binding energy after heating in oxygen atmosphere indicating a slight re-oxidation of

vanadium ions. In order to analyse the reduction process in more detail, the background corrected XP spectra of the $V2p_{3/2}$ lines were fitted by Voigt lines (see Fig.4.13). At 200°C only V^{4+} species are formed. With increasing temperature, V^{3+} species grows up gradually. When heated in oxygen, the V^{3+} species decreases again and the V^{4+} species increases compared with spectrum d, because the V^{3+} oxidation state is re-oxidised to V^{4+} again.

The S_{OV} intensity ratios of $O1s/V2p_{3/2}$ calculated with Eq.3.23, the average oxidation states of vanadium n (calculated from the fitted data as $5\times V^{5+}\% + 4\times V^{4+}\% + 3\times V^{3+}\%$) and the central BEs of the $V2p_{3/2}$ line are presented in Table 4.1. S_{OV} for the as-deposited film is about 2.46, The 4% oxygen vacancy is due to the partial reduction during evaporation from the source. The decrease of the $O1s/V2p_{3/2}$ ratios implies the decomposition of V_2O_5 at higher temperatures. The removal of the originally negatively charged oxygen ion as neutral species leads to the reduction of the nearest-neighbour vanadium.

Temperatures (°C)	S_{OV}	n	BEs
RT	2.46	4.96	516.9
200	2.33	4.75	516.6
300	2.00	4.25	516.1
400	1.75	3.86	515.3
400 in O_2	1.90	4.08	515.7

Table 4.1 S_{OV}, n, and binding energies (BEs) of $V2p_{3/2}$

The defect electrons will become localised at the vanadium as will be discussed based on the UPS data later on. Empty 3d orbitals of vanadium atoms adjacent to a vacancy are able to localise excess electrons. This leads to the formation of V^{4+} and even V^{3+} in the vicinity of the vacancy. The removal of oxygen from the V_2O_5 lattice causes the formation of defects or reduced phases in the resulting film [207]. We note that the $O1s/V2p_{3/2}$ ratio shows a small increase and vanadium becomes slightly oxidised after heating in oxygen as shown in spectrum e. It implies that oxygen atoms can re-enter the crystal lattice of V_2O_5. From Table 4.1, the effective charge transfer per oxygen (ECTO) can be calculated as:

$$ECTO = \frac{n(1) - n(2)}{S_{OV}(1) - S_{OV}(2)} \qquad \text{(Eq. 4.7)}$$

According to the above equation and the data in Tab.4.1, the ECTO were computed and shown in Tab.4.2,

RT – 200°C	200°C – 300°C	300°C – 400°C	400°C – 400°C in O_2
1.4	1.5	1.5	1.5

Table 4.2 The effective charge transfer per oxygen (ECTO) in V_2O_5

Therefore an average of 1.5 ECTO is estimated, which is 0.5 electron higher than Bullett's result [208, 209]. This result implies that with one oxygen leaving from the V_2O_5 crystal only 1.5 extra electrons locate on the vanadium ions but not 2 electron.

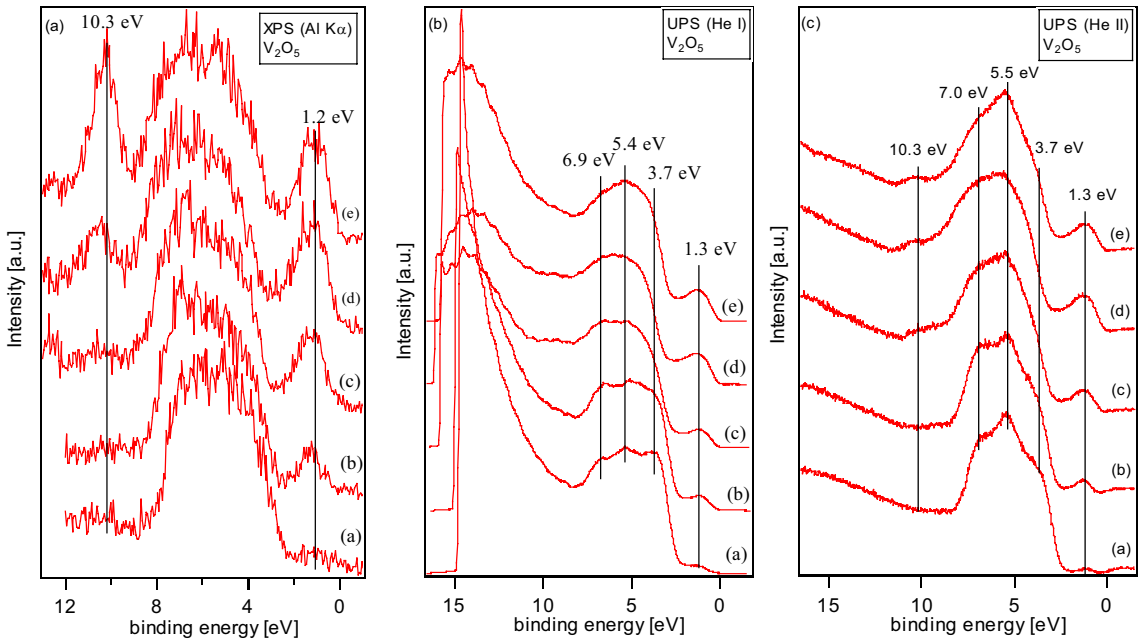

Fig. 4.14. Valence bands of V_2O_5 thin films measured from the same samples as shown in Fig.4.10, (a) XPS, (b) HeI (21.2 eV), and (c) HeII (40.8 eV)

Fig. 4.14 reports the valence bands (XPS and UPS) measured from the same samples as those shown in Fig.4.12. In both XP and UP spectra, it is clear that with increasing temperature, a broad V3d signal appears at ~1.3 eV due to the formation of V^{4+} and V^{3+} species. V_2O_5 is a non-magnetic insulator. The ligand coordination around the V ions in V_2O_5 deviates from the ideal octahedra and direct metal-metal interactions are very weak. The broadening in the spectra is probably given by the variation in boundary distance and geometric bonding of the V sites. At the same time the peak at 10.3 eV exhibits a similar tendency. In the UP spectra there are three distinct lines between 3 and 8 eV, they exhibit a well defined valence band shape with binding energies at about 3.6, 5.5 and 7.0 eV, respectively. When the heating temperature is increased, the intensities of the emissions at 3.6 and 5.5 eV decrease clearly, and only that of 7.0 eV peak is nearly constant. It is interesting to observe that the emission line at 5.5 eV increases evidently when the sample is heated in

oxygen. The shoulder appearing at 10.3 eV due to reduction is located near to the position of OH emissions [210]. However, the feature is already present after thermal evacuation in UHV and is significantly increased with sample temperatures. Moreover, its intensity increases parallel to the V3d peak. Therefore, it is not likely to originate from OH- or H_2O- adsorbates.

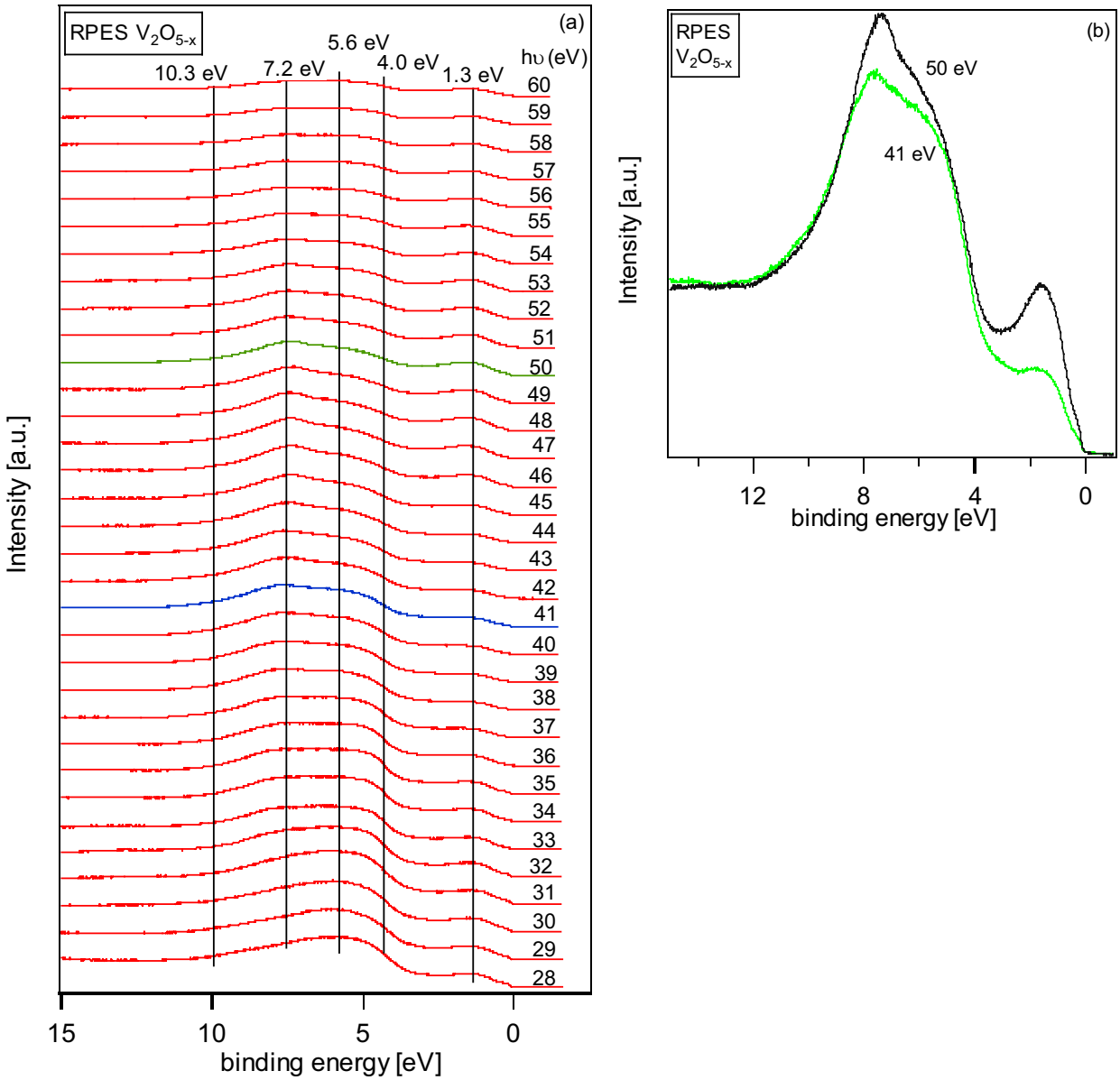

Fig. 4.15 The resonant photoemission spectra of V_2O_{5-x}, (a) photon energy range from 28 to 60 eV, (b) comparison of photon energies with 41 and 50 eV

The signal is possibly due to oxygen defects on the surface, which has been discussed above because its intensity increases with the temperature. In order to clarify the origin of the feature at 10.3 eV, resonant PES measurements have been performed after the sample is heated in UHV chamber at 400°C for 1 hour. The spectra are shown in Fig.4.15(a) for photon energies from 28 to 60 eV. For a better comparison the spectra for 41 and 50 eV photon energies are shown separately in Fig.4.15(b). It can clearly be seen that the intensity of the feature at ~

10.3 eV does not increase with the increase of the V3d feature at ~1.3 eV due to the 3p-3d resonance effect. Due to this result, we can assume that the feature at ~ 10.3 eV is origined from an oxygen based crystal defect. We note that after heating in oxygen at 400°C the intensity of the feature at 10.3 eV in the XP spectrum does not decrease, but increases, which is different from the signal of the He II spectrum. It is possible that due to the higher temperatures the concentration of oxygen defects below the surface is higher than in the topmost surface layer which can be probed by VB-XPS but not by UPS.

From the HeI spectra (see Fig.4.14(b)), the work function change has been determined and is shown in Fig.4.16. It decreases with increasing temperature and increases again when heated in oxygen. This phenomenon is possibly due to the concentration change of reduced V species on the surface. The higher the concentration of V^{4+} and V^{3+} species the more electrons are transferred to the V ions in the surface leading to a decrease in the work function. From Fig.4.16, it is obvious that the work function after heating at 400°C in oxygen is slightly higher than that after heating at 300°C, which means that the concentration of V^{4+} and V^{3+} on the first sample is lower than that on the latter one. The oxidation state of the V ions on the sample surface after heated at 400°C in O_2 should be higher than that after heat treatment at 300°C. But in the XPS data (see Tab.4.1) a lower oxidation state of vanadium ion was found on the first sample. These results are consistent with the comparison of valence band spectra because the escape depth in XPS and UPS is different as we have mentioned before. These results imply that the re-oxidation reaction only occurs in the surface region (10Å) but not in the bulk (30Å). Therefore, the feature at 10.3 eV can be assigned to a crystal defect due to an oxygen vacancy.

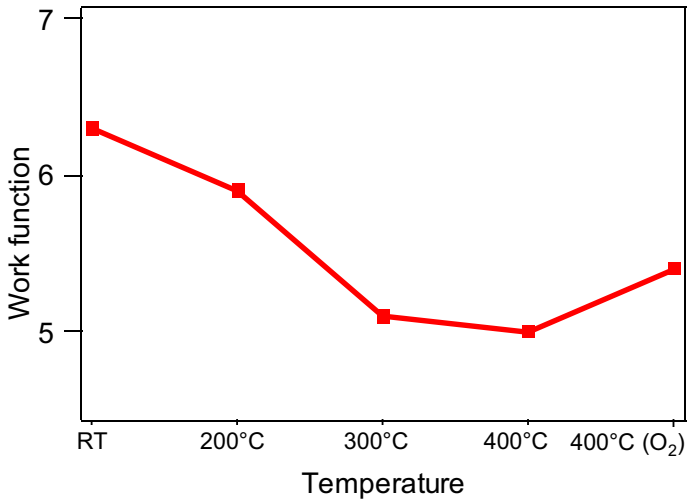

Fig.4.16 The changes of work function of thin V_2O_5 film after different preparation steps as calculated from He I spectra

Hermann et al. [211] offered the chance to differentiate vanadyl oxygen and bridging oxygen by their contribution to the valence-band signal. It may be expected to reveal which type of oxygen is removed during reduction. According to Hermann's theoretical studies [211], the valence-band feature at 5.5 eV is almost exclusively due to vanadyl oxygen, while the feature at 7.0 eV is dominated by contributions of bridging oxygen. The 3.7 eV feature arises from bridging and vanadyl oxygen at a ratio of ~2:1[212, 213]. It is, however, also expected that the valence band contain considerable V3d character because of covalent bonding. Sawatzky [206] obtained that 2.5, 1.6, and 1.1 of 3d electrons per V ion are in the O2p region of the valence band in V_2O_5, VO_2, and V_2O_3, respectively. However, it is important to note that the broad region of the valence band spectra is mainly of O2p character. It is reasonable to distinguish different kinds of oxygen in the valence bands due to the different chemical environments.

It is well known that vanadium forms several different oxides, the most stable is V_2O_5 [214]. Any oxide can be transformed into each other depending on the temperature and oxygen ambient pressure [196-198, 215-217]. The thermal decomposition of bulk V_2O_5 at a temperatures up to 400°C in vacuum was investigated previously by Tilley and Hyde using TEM [197]. A number of new phases were reported, two of them being described as ordered super-lattices of anion vacancies in V_2O_5. But these authors could not find any evidence for the occurrence of crystallographic shear, which is said to be necessary for the phase transformation. But when the temperature went up to 600°C, the co-existence of V_2O_5, V_6O_{13}, VO_2, and V_3O_7 were found by Gillis [198]. However, Su et al. [218] reported the thermal decomposition of V_2O_5 in high vacuum after heating up to 600°C using TEM and EELS. They revealed a sequence of transformation from V_2O_5 via VO_2 to V_2O_3. In the absence of gas-phase reducing gas such as H_2 or CO, the decomposition occurs slowly, allowing the coalescence and the stabilization of the reduced phase. For thin film oxides grown on the foreign substrates the situation may be very different because the chemical interaction across
59
the phase boundary are not similar due to structural and electronic effects [219]. From the valence band spectra no distinct difference was observed except the change of relative intensities of the features. Therefore it is not likely to conclude on any phase transformation during our experiments.

Based on the UPS results it is clear that the intensities of the vanadyl oxygen (at 5.5 eV) and the mixed oxygen (at 3.5 eV) decrease relatively faster and the bridging oxygen (at 7.0 eV) decrease correspondingly slower. After heating in oxygen the vanadyl oxygen increases distinctly in the UP spectra. Interatomic bonding in V_2O_5 is described by both ionic and

significant covalent contributions. The negative charging of the oxygen increases monotonically with the coordination number, which leads to negative charging being smallest for terminal O_1 and largest for triply coordinated bridging oxygen O_3 [211]. This conclusion indicates that there is more covalent bonding in the interatomic action of vanadium and O_1, which is in correspondence to the RPES results. The intensity decrease in the features at 5.5 and 3.7 eV is partly due to the smaller contribution of V3d electrons because of the reduction of vanadium atoms. Both STM [220] and X-ray photoelectron diffraction [221] studies have shown that vanadyl oxygen is easier to be removed upon reduction of V_2O_5 (010) or imperfect cleavage of crystals along this plane. This conclusion is likely supported by our experimental data due to the faster decrease of the feature at 5.5 eV and its increase after heat treatment in oxygen.

5 Intercalation reaction

The principal steps involved in the intercalation reaction have been summarised in Chap.2. In this chapter the results obtained from the intercalation experiments will be summarised. The changes in electronic structure due to Na (part I) and Li (part II) intercalation into V_2O_5 thin films have been studied using XPS, UPS and RPES. For Li intercalated V_2O_5 also electrochemical measurements will be discussed. The main aim of this chapter is to understand the mechanism and process of the intercalation reaction.

The layered transition metal oxides and their intercalation compounds are of significant interest as model systems for studies of reduced dimensionality [222-224]. V_2O_5 was first suggested as a cathode material for intercalation batteries by Day in the 1970s [70] and has since then been a matter of extensive experimental and theoretical studies [65, 68, 225, 226].

The intercalation may be carried out by electrochemical treatments or by exposing the samples at elevated temperatures to metal vapours in closed ampoules. But a powerful approach in detailed studies of intercalation reactions is to combine standard surface science techniques with in-situ intercalation [116, 119, 227-230], i.e. the guest species is deposited under UHV conditions onto the host surface, from where it may intercalate spontaneously into the host material. The particular strength of this approach is the possibility of characterising the sample at every step of the reaction from pure host material to fully intercalated and even to over-intercalated compounds. Intercalation with alkali metals is particularly interesting due to their strong tendency to intercalate spontaneously and to donate their single valence electron. Although V_2O_5 was studied from both the structural and electrochemical point of view [231-234] the mechanism of alkali metal intercalation into V_2O_5 thin films has not been fully characterized to date [235]. Especially a detailed analysis of the changes in electronic structure have not been performed yet [236]. As V_2O_5 as base material is a semiconductor with an optical band gap of E_G = 2.35 - 2.4 eV [156, 237], strong shifts in the Fermi level position due to intercalation are expected.

5.1 Sodium intercalation reaction

The presence of V^{4+}-V^{4+} singlet pairs in the $Na_xV_2O_5$ bronze, which are so-called bipolarons, was suggested as a precondition of superconductivity [238], but superconducting behavior has not been reported for the vanadium bronze until now. $Na_xV_2O_5$ belongs to the fascinating class of highly correlated low-dimensional electronic systems. Recently, its

physical properties have been intensively investigated theoretically as well as experimentally [239-241]. It is believed to be a nearly perfect realization of a quarter-filled low-dimensional system due to a twofold degenerate conduction band with possible charge ordering below the critical temperature [73, 242, 243]. Moreover, $Na_xV_2O_5$ has attracted considerable interest after it was proposed to be an inorganic Peierls spin system [244-246].

In this part, the intercalation mechanism of Na into the V_2O_5 lattice, the charge transfer from intercalated Na to the host material, and the chemical change due to intercalation will be introduced.

5.1.1 XPS and UPS data of Na intercalation reaction

Fig.5.1 shows the XP spectra of the O1s and the V2p core levels and the Na KLL Auger emission lines for different Na deposition times $t_{D,Na}$. For a clean V_2O_5 film deposited onto HOPG ($t_{D,Na}$=0) the binding energies of the V2p and O1s core levels are EB($V2p_{3/2}$)=517.0eV (b_1), EB($V2p_{1/2}$)=524.5eV (b_1') and EB(O1s)=529.9eV (a_1). After Na deposition the initial oxygen (a_1) and vanadium (b_1, b_1') emission lines are attenuated with

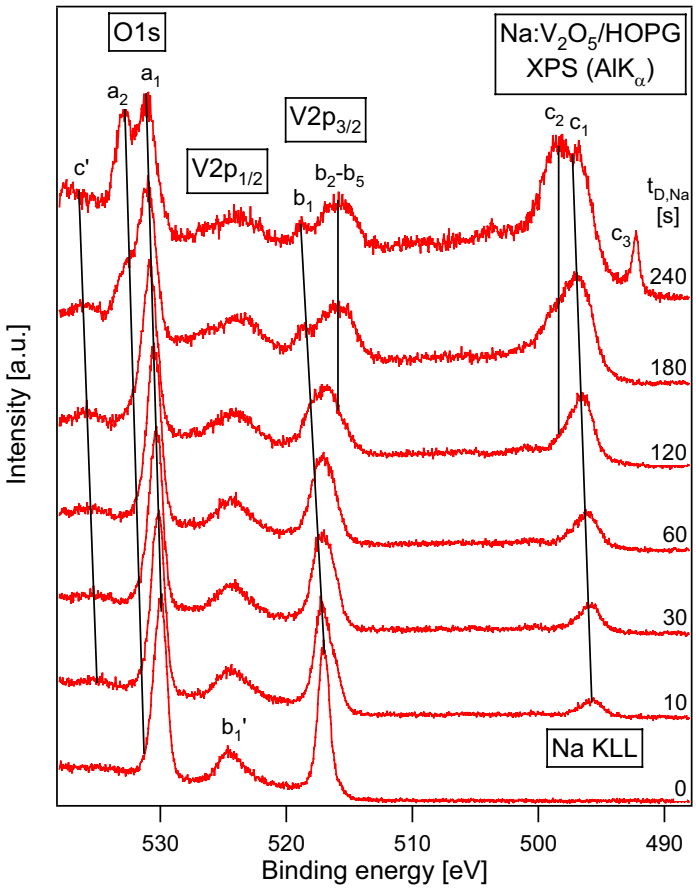

Fig.5.1 XP spectra of O1s and V2p core level and Na KLL Auger emissions for different Na deposition times $t_{d,Na}$

increasing $t_{D,Na}$ and additional components (a_2, b_2-b_5,) appear, which will be discussed in detail later on. Furthermore the Na KLL-Auger emissions (c_1-c_3, c') indicate an increasing amount of Na in the sample. The most intense Na $KL_{23}L_{23}$ Auger line (c_1,c_2) (E_{kin}=982.5eV) appears at $E_{kin,F}$-E_{kin}=495.6eV (the BE scale referred to the Fermi level $E_{kin,F}$ = 0) and the small emission (c') at about $E_{kin,F}$-E_{kin}=533.1eV originates from the Na KL_1L_{23}-transition (E_{kin}=945.0eV). The Na KLL Auger contribution in the energy range 510eV≤$E_{kin,F}$-E_{kin}≤530eV is very weak and does therefore not influence the analysis of the O1s and V2p lines. To distinguish the different chemical components the background corrected O1s (Fig.5.2a), $V2p_{3/2}$ (Fig.5.2b) and Na KLL (Fig.5.2c) lines have been fitted using a linear combination of Lorentzian and Gaussian line shape (pseudo-Voigt-profile) to include the natural broadening, due to finite photohole lifetimes, and the broadening because of finite experimental energy resolution, respectively. From the core level lines in Fig.5.1 and Fig.5.2 it is obvious that strong changes in the PE spectra occur for Na deposition times $t_{D,Na}$≥120s. Therefore the discussion of the XPS data is divided into two parts (5.1.1.1 and 5.1.1.2) in relation to the Na deposition time $t_{D,Na}$, followed by a discussion of the charge transfer during intercalation (5.1.1.3) and the UPS results concerning the electronic structure (5.1.1.4).

5.1.1.1 XPS data for short Na deposition times ($t_{D,Na}$<120s):

For $t_{D,Na}$<120s the O1s emission (Fig.5.2(a)) is slightly asymmetric. It consists of a main emission line (a_1) at BE=530.0eV originating from the V_2O_5 substrate film accompanied by a very weak "satellite" structure (a_2') shifted from the main emission by an increasing binding energy difference of ΔBE=1.1...1.5eV, which already appears for the clean V_2O_5 substrate. In Fig.5.3(a) the normalized O1s intensities are shown. The relative intensity of the main line (a_1) decreases and that of the satellite structure (a_2') increases with increasing $t_{D,Na.}$ The line shape of a_1 remains unchanged, while the line width of a a_2' is increasing significantly indicating a new Na-induced components. Also derived from the fitting data of Fig.5.2(a) the O1s binding energies are shown in Fig.5.3(d). With increasing $t_{D,Na}$ the main O1s emission line a_1 and also a_2' is shifted to higher binding energies by about 0.9 eV, due to a shift of E_F within the bandgap of V_2O_5. The weak satellite structure (a_2') can be explained as a shake-up process (see below) mostly for small Na exposure superposed by a second component originating from Na_2O (a_2). The Na_2O is evident from the O1s binding energy [130] and by the spectral information discussed below. But a_2' is also visible for the clean V_2O_5 film,

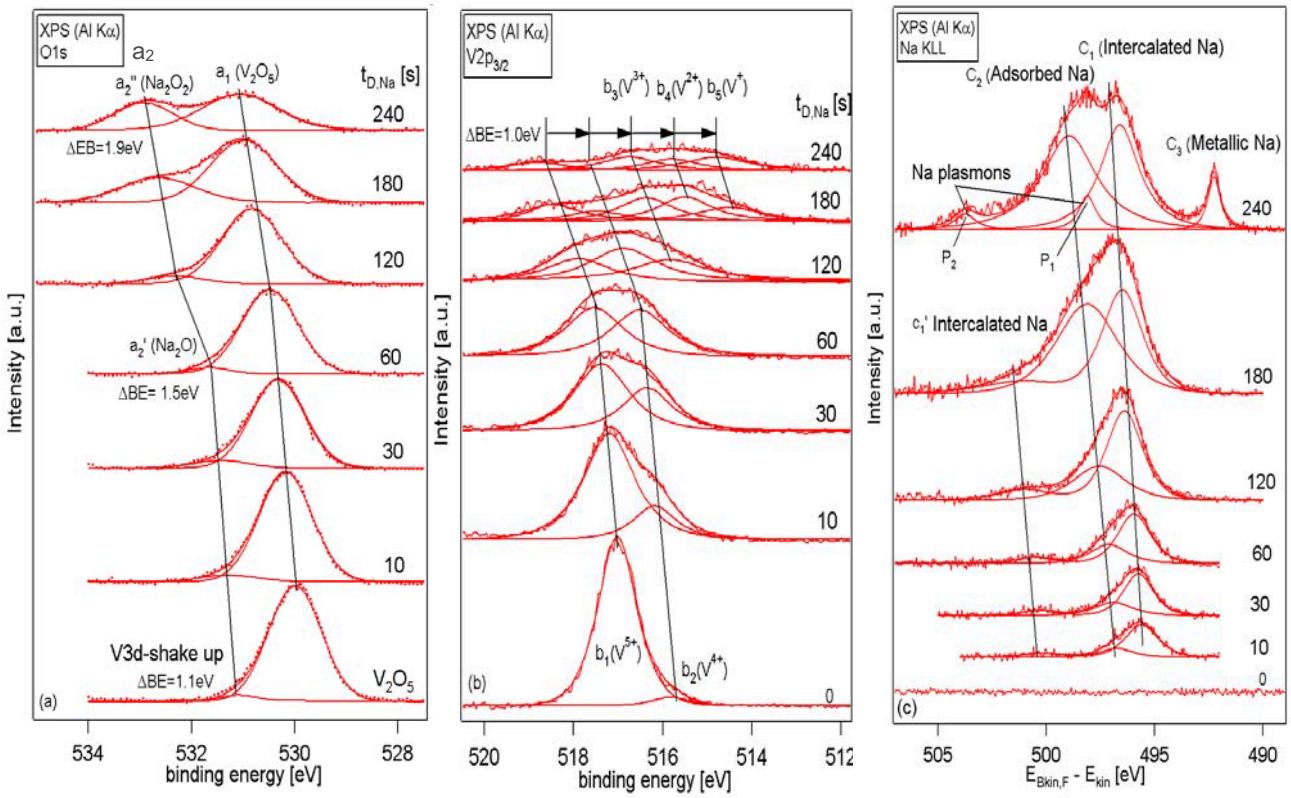

Fig.5.2 Fitting data of the XP O1s (a) and V2p (b) core level spectra and Na KLL Auger emission (c) for different Na deposition times $t_{D,Na}$

where no Na_2O can be present. The shake-up process (a_2') results from a coexcitation of O1s core electrons and electrons from the occupied V3d-like gap state (A) (see Fig.5.8) at BE=1.3 eV, that will be discussed later, into unoccupied V3d-like conduction band states. The gap state can be filled by a charge transfer to the V^{5+}-ions due to reduction either realized by oxygen vacancies and non-stoichiometry [38] or by adsorption or intercalation of electropositive atoms like sodium. The $V^{5+}2p_{3/2}$ line b_1 (Fig.5.2(b)) is shifted to higher binding energies with increasing $t_{D,Na}$ by the same value of about 0.9 eV as the O1s lines (see Fig.5.3(e)) due to the shift of E_F. At the clean V_2O_5 surface a small $V2p_{3/2}$ shoulder peak b_2 at lower BE is found indicating that a small amount of about 4% of the vanadium atoms are already in a "4+"-oxidation state due to the oxygen vacancies without any Na exposure. The fitting data show (see Fig.5.3(b)) that the normalized b_1 intensity decreases, while the b_2 intensity increases with increasing $t_{D,Na}$, indicating a Na-induced charge transfer to vanadium ions (reduction of the vanadium ions). After $t_{D,Na}$=120s the V^{3+} species (b_3) appears, accompanied by a slight intensity decrease of b_1 and b_2. Every formal oxidation state of V is chemically shifted by ΔBE=1.0eV (see Fig. 3(e)) with respect to the "5+" component b_1. The binding energies of all $V2p_{3/2}$ components shift parallel to higher values with increasing deposition time due to the shift in Fermi level position with intercalation. In Fig.5.2(c) the broad

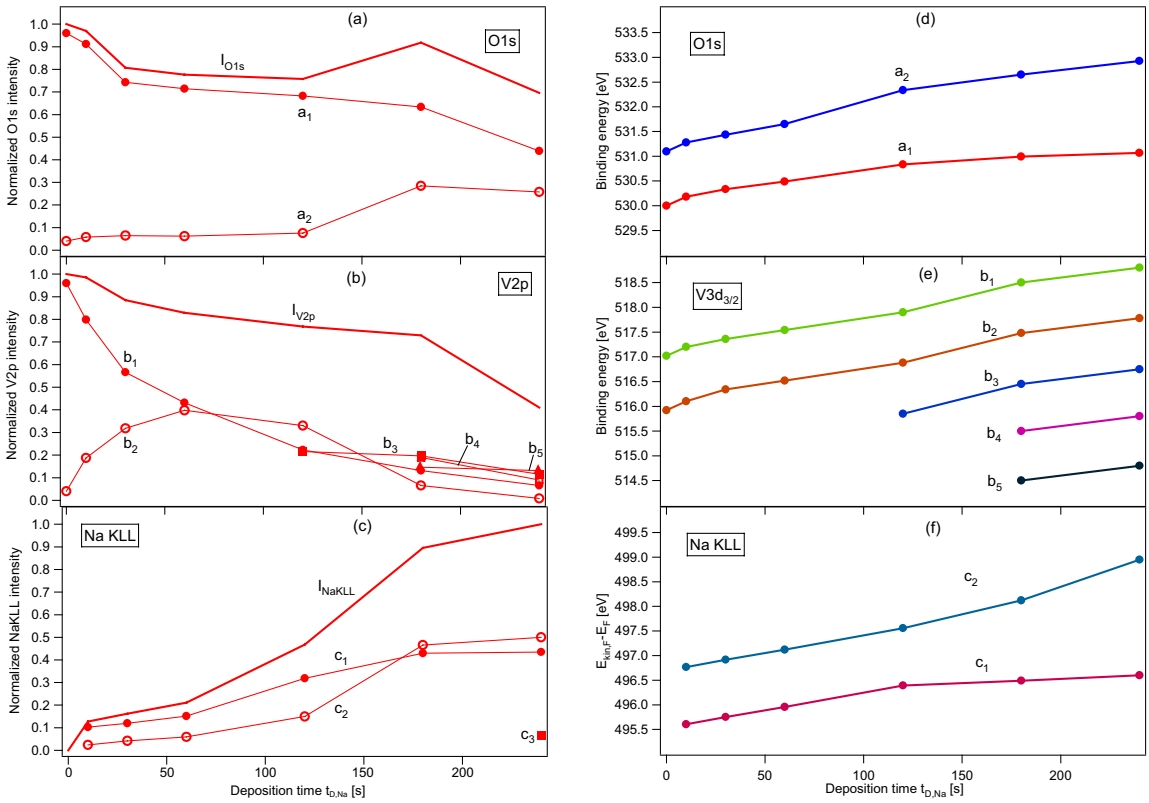

Fig.5.3 O1s, V2p and Na KLL normalized intensities (a,b,c) and binding energies (d,e,f) as a function of deposition time $t_{D,Na}$

Na KLL-Auger emission is shown. Its intensity increases with increase of $t_{D,Na}$ (see Fig.5.3(c)), while it is shifted to higher BE also by about 0.9 eV (see Fig.5.3(f)). The fitting data reveal two different Na species with a splitting of ΔBE=1.1eV. They can be assigned to the intercalated Na atoms (c_1 and c_1') and to the adsorbed Na on the V_2O_5 surface (c_2) [103]. The intensity ratio $I(c_1)/I(c_2)$ as a function of $t_{D,Na}$ is nearly constant (see Fig.5.3(c)), Therefore the same relative fraction of the Na atoms deposited is intercalated and adsorbed, respectively. The stoichiometry of the V_2O_5 film as a function of $t_{D,Na}$ can be calculated using formula Eq.3.23. In Fig.5.4 the oxygen to vanadium surface concentration ratio $S_{O,V}=C_O/C_V$ is shown, as derived from the XPS intensities of the O1s and V2p core level lines and the atomic sensitivity factors [130]. For $t_{D,Na}$ < 30s the ratio is constant showing the small oxygen understoichiometry of about 4% ($S_{O,V}$=2.46), which has already been deduced from the $V2p_{3/2}{}^{4+}/V2p_{3/2}{}^{5+}$ ratio. For 30s < $t_{D,Na}$ < 120s a small surface enrichment with oxygen atoms of about 8% is evident. The intensity of the Na KLL component c_2, which is assigned to the surface adsorbed Na atoms and of the O1s "satellite" a_2', are also increasing in this regime by about the same amount, which evidences the formation of a surface sodium oxide (Na_2O).

5.1.1.2 XPS data for long Na deposition times ($t_{D,Na}$≥120s):

From Fig.5.4 it is obvious, that for $t_{D,Na}$≥120s the oxygen to vanadium stoichiometry increases dramatically. The fitting of the O1s line (Fig.5.2(a)) reveals that the reason for this increase is a dramatic change in intensity and binding energy of the a_2 emission line. Its

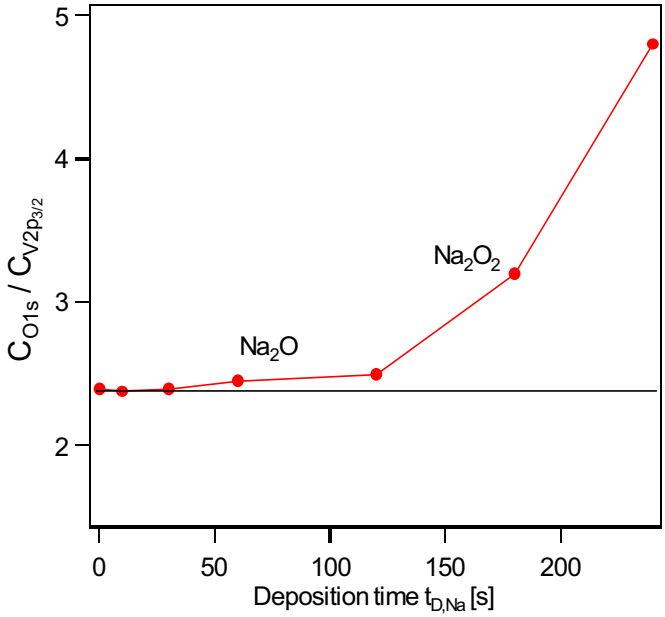

Fig.5.4 I_{O1s}/I_{V2p} intensity ratio as a function of the Na deposition time $t_{D,Na}$

intensity is increased by a factor 3 (Fig.5.3(a)), while the energy shift of a_2" from the main O1s emission a_1 now increases to 1.9eV (Fig.5.3(d)) and the full width at half maximum (FWHM) becomes larger. The binding energy of BE_{a2}=533eV identifies the a_2" emission to correspond to a large amount of sodium peroxide (Na_2O_2) on the surface [247, 248]. Due to the high overlap of O1s for Na_2O_2 and Na_2O species it is difficult to separate clearly the two oxides by simple fitting, especially when their intensities are not high enough. For $t_{D,Na}$>120s the $V2p_{3/2}$ spectra also show the formation of the V^{2+} and V^{+} components (see Fig.5.2(b)) indicating a considerable charge transfer to the V atoms. This strong reduction of vanadium ions can only occur due to the massive formation of oxygen vacancies in the V_2O_5 lattice or by the formation of reduced oxides as VO_2, V_2O_3, as well as VO due to a chemical decomposition reaction between Na and vanadium oxides. This can also be proven by the formation of Na_2O_2 and Na_2O on the surface. In Fig.5.2(b) we notice that the BEs of V^{5+} and V^{4} have BE higher shifts than before, and their intensities decrease very fast. These results imply that the crystal structure of V_2O_5 has been strongly destroyed for large Na exposures which will be discussed also based on UP spectra later on.

In the Na KLL signal (see Fig.5.2(c)) the c_1 component assigned to the intercalated Na atoms does not shows any significant increase in intensity any longer (see Fig.5.3(c)) and also its binding energy is constant (see Fig.5.3(f)). But the number of surface adsorbed Na atoms

increases by a factor of 4, obviously all in a Na_2O_2 bonding state, leading to an increase of the respective binding energy (see Fig.5.3(f)). In addition, in the last spectrum another Na KLL emission line (c_3) appears at a binding energy of 492.2 eV corresponding to the metallic Na, accompanied by two small emissions (P_1 and P_2) at higher binding energies ($E_{B,P1}$=498.0eV and $E_{B,P2}$=503.7eV). P_1 and P_2 are the first and second plasmon losses of metallic Na showing that for very long Na deposition time a metallic Na layer is formed. The plasmon loss energy is 5.75 eV which is in good aggreement to the literature value of 5.76 eV for the Na bulk plasmon [249].

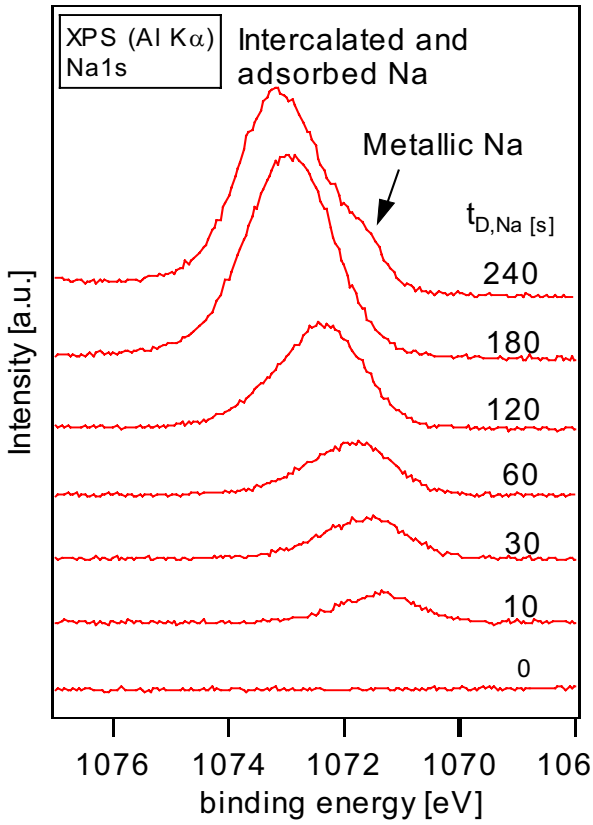

Fig. 5.5 XP spectra of the Na1s core level line for different deposition time $t_{D,Na}$

Fig.5.5 reports the Na 1s core level XP spectrum. It also shifts to higher binding energy with the increase of Na concentration, and its intensity increases quickly with the Na deposition time $t_{D,Na}$. It has a large FWHM and is slightly asymmetric because of the coexistance of intercalated and surface-absorbed Na. But due to the small BE difference for the intercalated and absorbed Na it is hard to distinguish these two species in the Na1s spectrum. The Na1s XP spectrum for $t_{D,Na}$=240s shows a small shoulder peak on the low binding energy side indicating the formation of metallic Na which corresponds to the c_3 line in the Na KLL Auger spectrum. Compared to the Na KLL Auger line the binding energy difference of Na1s for different kinds of Na ions is much smaller showing a low sensitivity of the Na1s emission line for chemical shifts. The larger energy distance between the two

components in the Na KLL Auger signal is due to its higher sensitivity to the chemical changes because of the formation of a two hole final state [130].

Fig.5.6 shows the Intensity ratio of $S_{Na1s/V2p3/2} = C_{Na1s}/C_{V2p3/2}$ against $t_{D,Na}$. When $t_{D,Na}$ = 120s, the chemical composition of the surface is roughly $Na_{2.5}V_2O_5$. If we subtract the surface absorbed Na, which can be calculated from the Na KLL Auger spectrum by the ratio of absorbed Na/total Na, a composition of the intercalated compound of $Na_{1.4}V_2O_5$ is obtained, which is probably the maximum amount of Na that can intercalate into V_2O_5 without changing the crystal structure. The maximum amount of Na is somewhat lower than that of Li which can reach as $Li_{3.3}V_2O_5$ [64]. With further Na deposition ($t_{D,Na}$ > 120s) the ratio of $I_{Na1s}/V_{2p3/2}$ increase very quickly due to the formation of sodium oxides which indicates that further deposited Na will not intercalate into the V_2O_5 lattice but adsorb on the surface and cause the Na induced decomposition of V_2O_5 on the top layers of the surface.

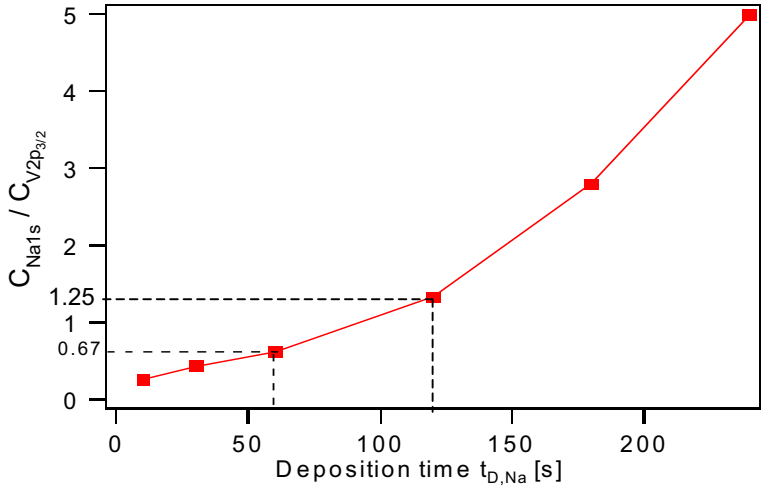

Fig. 5.6 $I_{Na1s}/I_{V2p3/2}$ intensity ratio as a function of the Na deposition time $t_{D,Na}$

From these results, the process of sodium deposition on V_2O_5 layers can be summarised as,

Lower Na concentration:

$$xNa + V_2O_5 \rightarrow Na_{1.4}V_2O_5 + (x\text{-}1.4)Na_{absorbed}\ (0 \le x \le 1.4) \qquad \text{(Eq. 5.1)}$$

Higher Na concentration:

$$yNa + Na_{1.4}V_2O_5 \rightarrow Na_{1.4}V_2O_{5\text{-}c} + aNa_2O + bNa_2O_2 \qquad \text{(Eq. 5.2)}$$

where a + b = y/2, and c = a + 2b.

5.1.1.3 Charge transfer during intercalation:

To calculate the charge transfer from the Na3s orbital to the empty V3d states of the V_2O_5 layers during intercalation stoichiometry calculations involving Na emission lines are necessary. But for Auger lines no atomic sensitivity factors are available. Therefore the Na1s spectra are used. Unfortunately the energy splitting between adsorbed sodium oxide and intercalated sodium is too small to be distinguished in the Na1s emission [130]. But for $t_{D,Na}$<120s the amount of surface adsorbed Na is small (<20%). In this regime an approximate calculation of the charge transfer based on the XPS data seems to be reasonable. Furthermore Na is supposed to intercalate as Na^+ ion, and a similar oxidation state is expected for Na oxide on the surface [103]. Therefore the uncertainty in the calculations are estimated to be smaller than 10%. The reduction of V ions in V_2O_5 is mostly due to the intercalation and by minor amounts to the absorption of Na^+ ions with the formation of Na_2O and oxygen defect formation. The intercalated Na atoms will completely or partly be ionized [232, 233] and the transferred electrons will mostly be located on the V3d states [250-252]. The charge transfer per Na atom can approximately be calculated from the following formula,

$$n_{e,Na\ 3s \rightarrow V\ 3d} = 0.5 \frac{\frac{I_{V^{4+}_{2p_{3/2}}} + 2\, I_{V^{3+}_{2p_{3/2}}}}{ASF_{V\ 2p_{3/2}}}}{\frac{I_{Na\ 1s}}{ASF_{Na\ 1s}}} \qquad \text{(Eq. 5.3)}$$

Where 0.5 is the factor of V 3d electrons in the valence band region which is obtained from our RPES data (see Chap. 4.2.3) and from theoretical calculations [189] indicating that for a reduction of V^{n+} to $V^{(n-1)+}$ 0.5 electrons have to be transferred [206].

The intensities have been taken from the XP spectra (Fig.5.2(b) and 5.6) and the atomic sensitivity factors $ASF_{V2p_{3/2}}$ and ASF_{Na1s} from the literature [130]. The calculated electron numbers for per intercalated Na atom transferred from the 3s states to the V3d states of the V_2O_5 film as a function of $t_{D,Na}$ are shown in Fig.5.7. A mean value of 0.42e^-/Na-atom was obtained, showing that the Na atoms do not get completely ionized during intercalation. Because of the hybrization between O2p and V3d orbitals, and also due to hybridization between alkali metal and the host layer, we should expect these occupied bands to have at least some fraction of alkali-metal s character mixed into them, which would still leave some of the charge on the alkali metal and oxygen ions. The theoretical band structure calculation

shows that the contribution of O2p, V3d and Na3s electron states to the valence band are 71%, 21% and 8%, respectively [189].

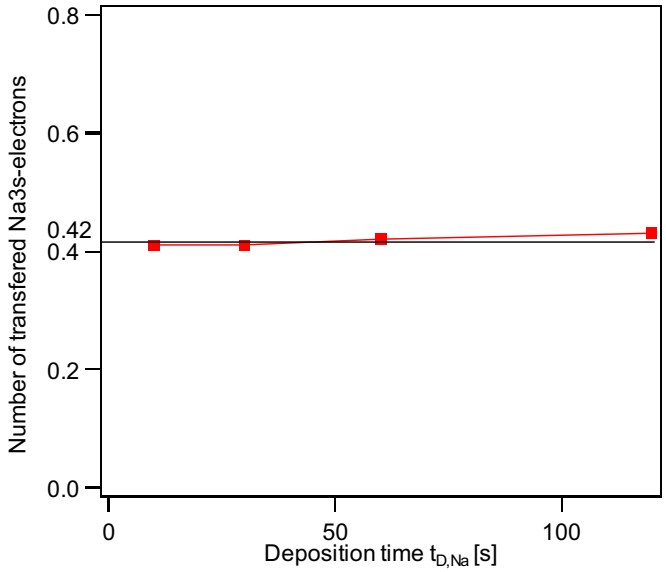

Fig.5.7 Approximate number of electrons per Na atom transferred from Na3s to V3d-like states during intercalation

5.1.1.4 UPS measurements and electronic structure:

In Fig.5.8 the normalised valence band spectra excited by He I (a) and He II (b) radiation are shown. In the binding energy region between 2eV and 8eV the valence band of V_2O_5 does not change much for deposition times $t_{D,Na} < 120$s. There are three distinct emission lines which exhibit a well defined valence band shape with binding energies at about 3.6, 5.5 and 7.0 eV, respectively. According to several theoretical calculations they have mainly been contributed to O2p states with a weak V3d admixture [206, 211]. In Fig.5.8 it is clearly evident that the energy distance between the O2p valence band and the V3d conduction band increases with sodium intercalation. This band gap opening has already been theoretically and experimentally studied for several intercalation compounds [253, 254]. The reason is the decreasing orbital overlap along the **c** axis. In the sodium-vanadium bronze system $Na_xV_2O_5$, there exist several phases denoted by α-, β-, δ-, τ-, α'-, η-, and κ-phases in the ascending order of x [255-257]. The structure parameters for α-, β-, δ- and α'-phases with $0 \leq x \leq 1$ show no significant differences except that the lattice parameter **c** is extended from 4.37 to 10.08 Å [72, 258-260]. Interatomic bonding in V_2O_5 is described by both ionic and covalent contributions [211]. Sawatzky [206] obtained that 2.5, 1.6, and 1.1 of 3d electrons per V ion are hybridised into the O2p region of the valence band in V_2O_5, VO_2, and V_2O_3,

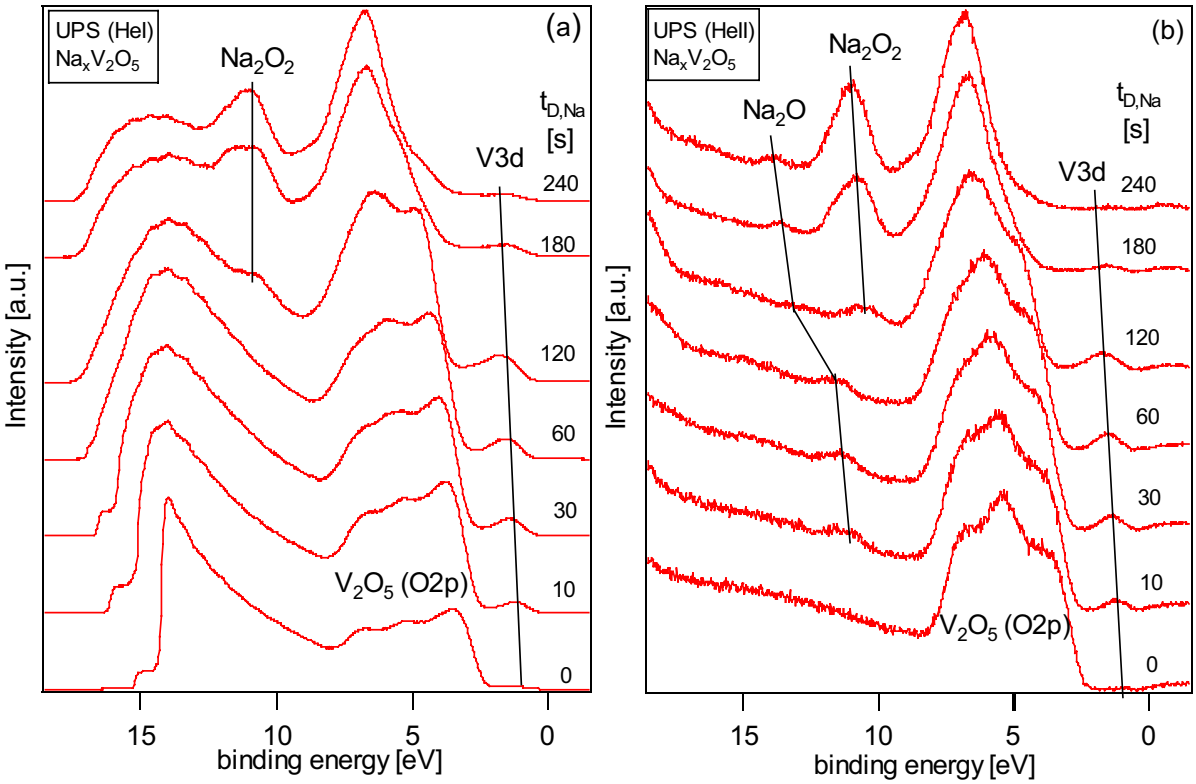

Fig.5.8 UP spectra for HeI excitation (21.22eV) (a) and HeII excitation (40.81eV) (b)

respectively. When V^{5+} ions are reduced to V^{4+} and V^{3+} states, the covalence between oxygen and vanadium is reduced and causes the decrease of orbital overlap along the **c** axis. From the energetic position of the valence band maximum the position of the Fermi level with respect to the original valence band edge can be derived. The values are given in Fig.5.9(a). For a deposition time of $t_{D,Na}$=120s an overall shift of 1.2eV is found compared to the non-intercalated V_2O_5 film. From the XP spectra (see Fig.5.3) a value of 0.9 eV has been obtained. The large deviation between these values of 0.3 eV should be explained by the changes in the electronic structure, therefore the rigid band model is not longer valid leading to a changed DOS. Because of this, also the valence band maximum to core level position are changed. Because its value is proportional to the number of induced electron hole pair and thus to the excitation energy [261] the Fermi level shift derived from XPS must be smaller than from UPS. Therefore 1.2 eV is the lower limit for the Fermi level shift at $t_{D,Na}$=120s. From the secondary electron onset (SEO) in the HeI spectra (see Fig.5.8(a)) the work function Φ can be calculated by subtraction of BE^{SEO} from the excitation energy. These values are given in Fig.5.9(b). A decrease in work function of $\Delta\Phi$=2.1eV for $t_{D,Na}$ =120s is observed. For longer deposition times the work function is nearly constant and finally increases again. The work function changes due to the Na intercalation reaction and the formation of surface dipoles

from the absorbed and oxidized Na atoms on the surface. The influence of the surface dipoles can be estimated using the following formula [261],

$$\Delta\Phi = \Delta\Phi_{\text{surface dipole}} + \Delta E_F \qquad \text{(Eq. 5.4)}$$

For $t_{D,Na}$=120s, the values are ΔE_F =1.2eV and $\Delta\Phi$=2.1eV, thus the work function change due to surface dipoles is $\Delta\Phi_{\text{surface dipole}}$=0.9eV. The increase of Φ for $t_{D,Na}$>120s can be explained by depolarisation effects [261] and the formation of metallic sodium on the surface. In addition to the valence band structures of V_2O_5 additional emission lines can be observed in the UP spectra (see Fig.5.8) at binding energies around 1.3 eV, 0 eV and11.7 eV. The broad structure at about 1.3eV is assigned to a V3d-like gap-state (A). It is already known from literature [188] and appears due to charge transfer from the Na to V^{5+}-ions which leads to an occupation of originally empty V3d states forming the conduction band. This charge transfer can also be due to oxygen vacancies [262] (see the discussion in Chap.4). The width and the

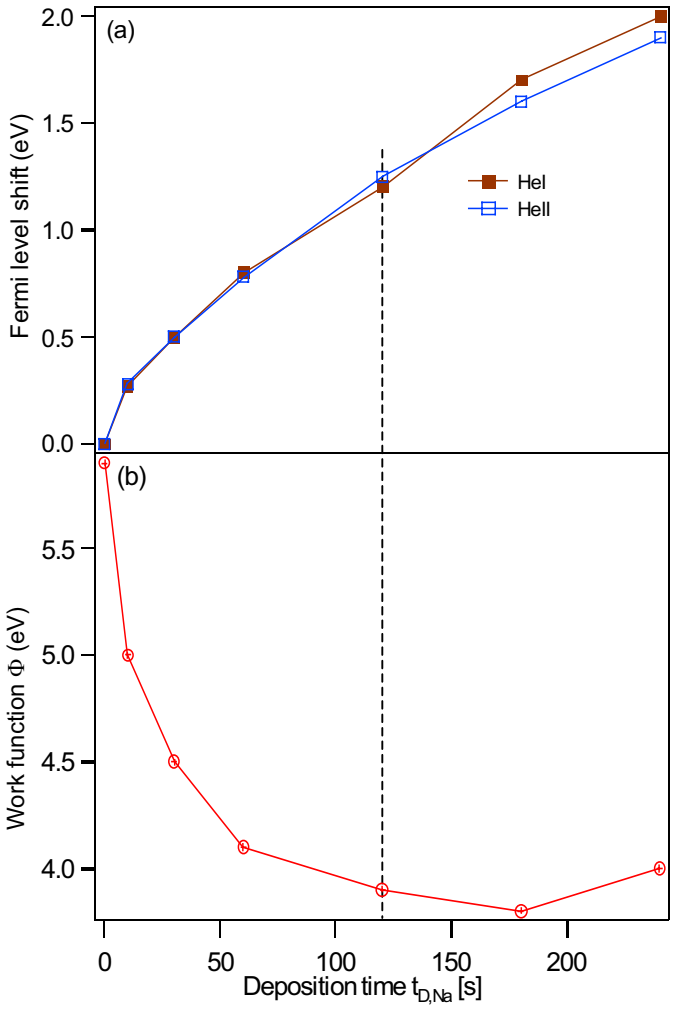

Fig.5.9 Fermi level position (a) and work function (b) as a function of the deposition time $t_{D,Na}$ derived from the UP spectra of Fig.5.7

shift from the Fermi level of the V3d gap state has been discussed earlier by Egdell et al. [188] in a PES study on $La_{1-x}Sr_xVO_3$. They attributed it to strong electron-phonon interactions (polaron formation) related to the strong polarization of the lattice by the valence electrons. The binding energy of A as a function of $t_{D,Na}$ is presented in Fig.5.10(a). After an initial increase from BE=1.1eV for $t_{D,Na}$=0 to BE=1.65eV for $t_{D,Na}$=120s the binding energy decreases again when the decomposition reaction of the host sets in. In Fig.5.10(b) the intensity of the gap-state A normalized to the valence band intensity is shown derived from the HeI spectra. The intensity of A increases for $0<t_{D,Na}<120$s with increase of deposition time. Then it decreases again. Assuming the simplest approach for the electronic structure of V_2O_5 the valence band is thought to be O2p-like and the conduction band V3d-like. The V3d-like gap-

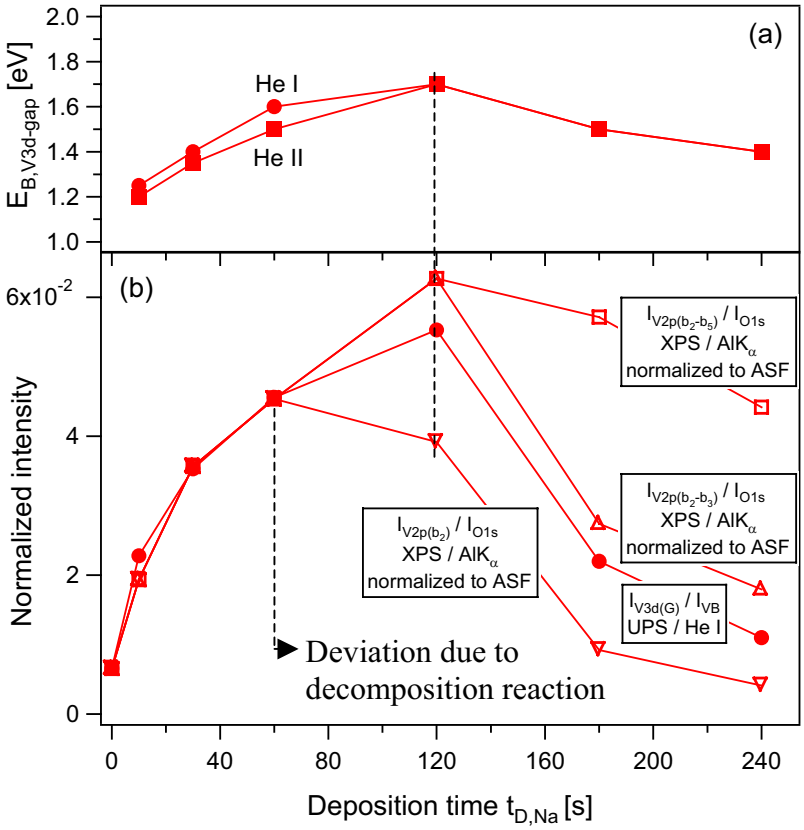

Fig.5.10 Binding Energy (a) and intensity normalized to the VB of the V3d-like gap state in comparison to XPS intensity ratios (b) as a function of deposition time $t_{D,Na}$[s]

state A is only occupied due to charge transfer to the V atoms, also leading to the chemically shifted reduced V2p species $V^{4+}(b_2)$, $V^{3+}(b_3)$, $V^{2+}(b_4)$ and $V^{+}(b_5)$. Therefore the intensity ratios of the reduced V2p species to O1s ($I_{V2p(b2-b5)}$ / I_{O1s}) (XPS ratio) should be equal to the intensity ratio gap-state to valence band ($I_{V3d(G)}$ / I_{VB}) (UPS ratio), when corrected to the different atomic sensitivity factors. But from Fig.5.10(b) it is obvious, that the XPS ratio is higher than the UPS ratio for $t_{D,Na}>120$ s. When only the V^{4+} species is used ($I_{V2p(b2)}$ / I_{O1s}) the

XPS ratio is smaller than the UPS ratio for $t_{D,Na} > 120$ eV. Using also the V^{3+} species ($I_{V2p(b2-b3)} / I_{O1s}$), the best match is reached. These data indicate that for small Na deposition times ($t_{D,Na} < 120$ s), the intercalation follows a modified rigid band model, which means that the structure of the host remains intact and the electrons are transferred to originally unoccupied conduction band states of V3d characters. As a consequence a structural reorganisation is induced (polaron formation) leading to an energetic stabilisation of the occupied electron states. For $t_{D,Na} > 120$ s, a complex decomposition of the host has to be considered leading to the formation of new reduced V-oxides as well as to the formation of the Na_2O and Na_2O_2. In these region the valence band spectra are a superposition of a number of new phases.

A pronounced structure in the valence band around 10 eV appears for $t_{D,Na}>120$eV. By comparing this structure with the XPS data (see Fig.5.3) it can be related to the formation of Na_2O_2. To date there is no good explanation for the weak structure around BE = 12 eV. But from the binding energy shift and the intensity ratio to the valence band it can be assumed by comparison to the XPS data (Fig.5.3) that it originates from the O2p-like states of Na_2O. Further experiments with resonant photoemission at the synchrotron are needed to clarify the orbital characters of these valence band structures.

5.1.2 XPS and UPS data for samples after 4 days in UHV

Fig.5.11 shows the O1s and V2p core level XPS and Na KLL Auger spectra after the sample has been kept 4 days in UHV. It is obvious that after 4 days in UHV, the metallic Na disappears in the Na KLL Auger signal and the compounds of the intercalated Na (Na1) decrease with the increase of adsorbate sodium oxides line (Na2). The same phenomena can be seen from the Na1s line (see Fig.5.12) with the central maximum shifting to lower binding energies by about 0.2 eV after 4 days in UHV. The O1s line related to vanadium oxides (O1) also decrease, while the O2 line corresponding to sodium oxides increases dramatically. All the above results illustrate that the metallic Na surface layers will further react with vanadium oxides and form sodium oxides on the surface. Moreover, the intercalated Na will also be extracted in part to the surface and reacts with the oxygen, which is supported by the decrease of the Na1 and O1 lines and the increase of the Na2 and O2 lines. According to the binding energy of O2, the newly-formed surface oxide is mostly Na_2O_2 [263] which is also proven by the UPS data. The valence band spectra of HeI (a) and HeII (b) are shown in Fig.5.13. The main change after 4 days is the increasing intensity of the line at about 10 eV, which is assigned to the O2p state of Na_2O_2. The line at about 12 eV defined as O2p for Na_2O almost does not change. These UPS results correspond to those obtained from XPS. Metallic Na and

intercalated Na will react with vanadium oxides and form Na_2O_2 on the surface with in a few days. With the full occupation of π and π^* electron states, the peroxideanion $(O_2)^{2-}$ is relatively stable [264, 265].

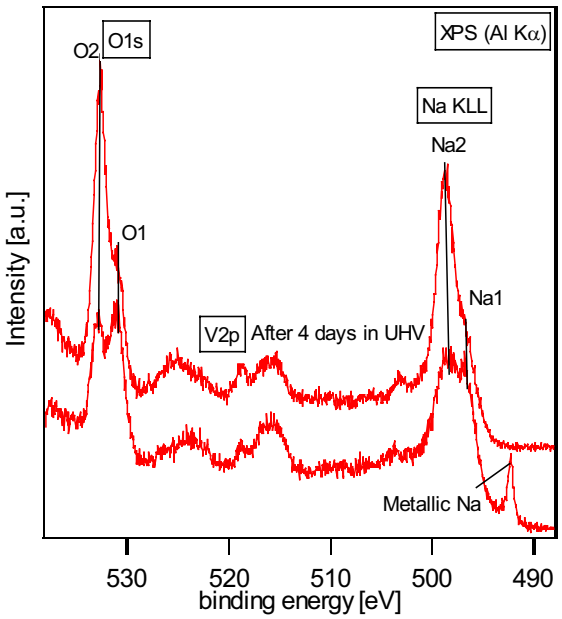

Fig.5.11 Comparison of the O1s and V2p core levels XP spectra and Na KLL Auger line before/after the sample is kept in UHV for 4 days

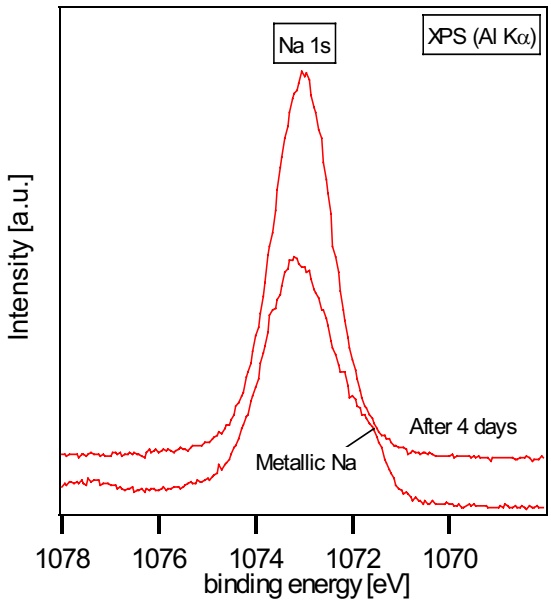

Fig.5.12 Comparison of the XP spectra of the Na1s core level before/after the sample is kept in UHV for 4 days

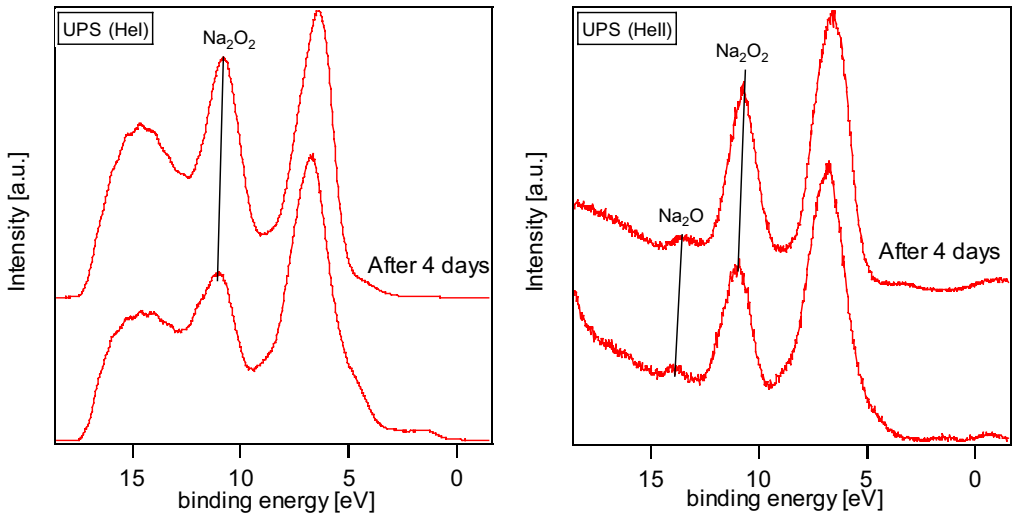

Fig.5.13 The valence band spectra of the same samples as those in Fig.5.11

5.1.3 RPES data

The resonant photoemission spectra of $Na_xV_2O_5$ (x < 1) are shown in Fig.5.14. $Na_xV_2O_5$ is a mixed valence compound with some of the V ions in +4 oxidation state and the rest are in the +5 oxidation state. The basic building block of the crystal structure of $Na_xV_2O_5$ is formed by VO_5 pyramids (see Fig.2.8). Two pyramids are arranged by sharing their edges pointing into different directions and form a quasi one-dimensional backbone of the structure. The bonding within this backbone is formed by the oxygen 2p and V3d states. Our photoelectron spectroscopy data has provided crucial information on the occupied electronic levels (see also

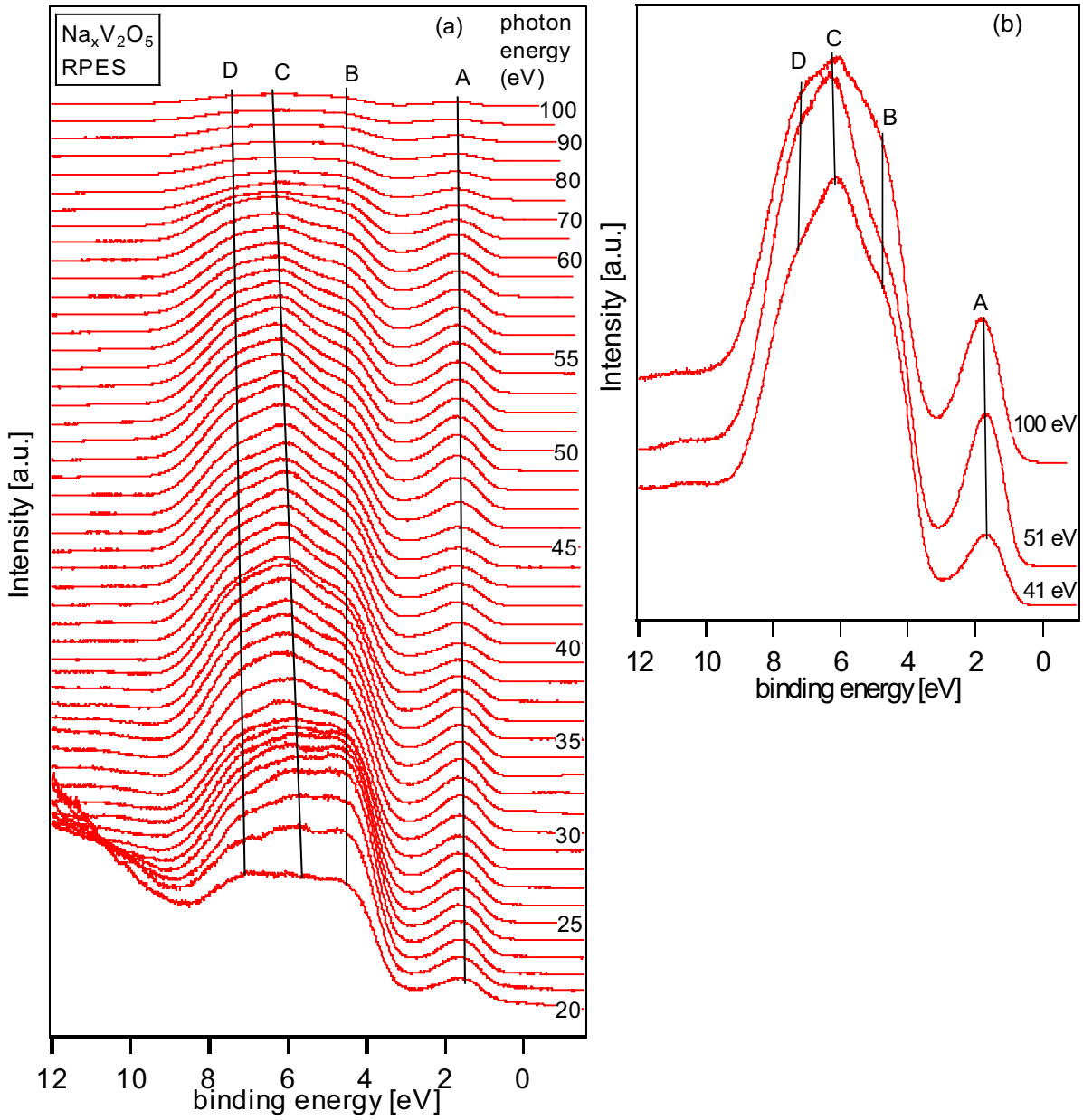

Fig.5.14 Vanadium 3p resonant photo-emission spectra of $Na_xV_2O_5$ (x<1) in the energy range from 20 to 120 eV (a), and the spectra with photo energies of 41, 51, and 100 eV (b)

the reference 248): the oxygen 2p states have the lowest energy (the highest binding energy); the occupied part of the V3d states is located about 3 eV above the top of the oxygen bands. The electron transfer from the intercalated Na into V ions are located on the $V3d_{xz}$ or d_{yz} levels which have weaker contribution to the bonding states [266, 267] which do not interact along the ladder-like structure of $Na_xV_2O_5$. In Fig.5.14, nearly the same results are obtained as compared to Fig.4.8 except that the intensity of feature A is much higher due to the charge transfer from Na into the V 3d orbital [268, 269]. It is well known that the O 2p cross section [193] gradually decreases with photon energies in the given *hv* region (in Fig.5.14), while the V3d cross section resonantly increases at photon energies corresponding to the V 3p core excitation. The feature A at BE = 1.3 eV is assigned to the V 3d state. The feature B at 3.6 eV in the lowest binding energy region of the O2p bands is related to the nonbonding O 2p orbital state of π-character. Its intensity almost does not change with the increasing intensity of the V3d state. On the other hand, the feature C and D are assigned to the bonding O2p states, which contain an appreciable amount of the V3d admixture due to hybridization, as is judged from the strong resonant intensity enhancement around the energy region of the V3p → V3d core excitation as shown in Fig.5.14. The band structure calculation [167, 270] suggests that this strong σ bonding type of interaction between O and V exist in the energy region of this feature C and D and the weakly bonding orbitals from the oxygen "lone pair" exist in the energy region of the feature B. Thus our experimental data are consistent with the band structure calculation.

Fig.5.15 shows the valence band spectra of $Na_xV_2O_5$ ($x > 2$) for various photon energies. Due to the formation of sodium oxide layers on top of the surface the shape of spectra changes significantly. In Fig.5.15(b) we still can find some resonant effect with the intensity increase of feature A from 41 to 51 eV. But no any other features show the same phenomenon. These results reveal that, in this case of reacted surfaces, the features B, C, D, E, and F can not be easily interpreted in their electronic characters due to the superposition of different chemical phases. The intensity decrease of features E and F with the photon energy confirm that these two peaks can be assigned to the O 2p states of Na_2O and Na_2O_2 (due to the photon energy dependent decrease of cross section).

The feature M at photon energy of 33 and 34 eV is the second order radiation of the monochromater exciting the Na2p core level electrons.

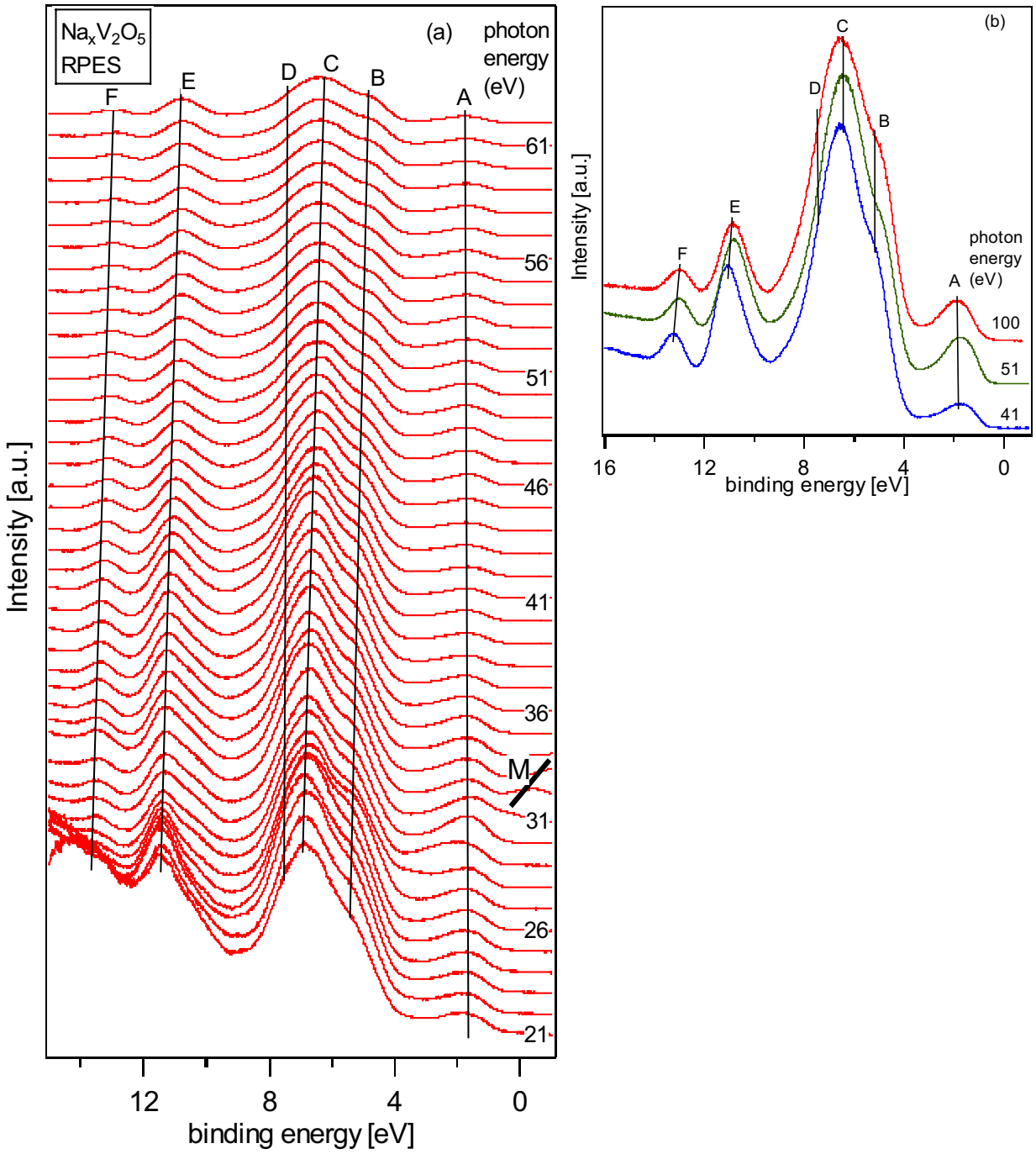

Fig.5.15 Vanadium 3p resonant photo-emission spectra of $Na_xV_2O_5$ (x>2) in the energy range from 21 to 62 eV (a), and the spectra with photo energies of 41, 51, and 100 eV (b)

5.2 Li intercalation reaction

V_2O_5 has been studied as a cathode material for lithium intercalation batteries for decades because of its high specific energy [271] and the nearly negligible expansion or contraction of the crystal structure during the intercalation/deintercalation of Li ions. For these reasons Li-intercalated V_2O_5 has been attracting considerable attention in theory and technology [231, 232, 236, 272-274]. It has been shown that as a cathode in a battery set-up crystalline V_2O_5 can reversibly be intercalated by about $2Li^+$ per crystalline V_2O_5 over many cycles [232, 274]. Insertion of larger amounts of Li results in irreversible degradation of performance. Still, the intercalation mechanism has not been fully characterized, especially regarding the accommodation of electrons donated to the V_2O_5 host during the insertion of lithium [275]. Electrochemical measurement, Raman spectroscopy, electron paramagnetic resonance (EPR), x-ray diffraction (XRD), and nuclear magnetic resonance (NMR) have shown that the crystalline material maintains several structural phases dependent on temperature and lithium content, namely: α, β, ε, γ, δ, and ζ (see Fig. 2.7) [276-278].

For higher Li content, the exact mechanism of Li_2O and Li_2O_2 formation on the surface is not fully understood at the moment, but a direct Li induced decomposition reaction of the V_2O_5 host can be considered [236]. In addition, effects of prolonged cycling or prolonged storage degrade their theoretical and initially found excellent performance [279, 280]. The degradation effects are typically capacity losses, which can be related to surface phenomena occurring at the anode and cathode. The central aims of this work are, 1) to improve the understanding of the electronic changes taking place during intercalation of Li ions into V_2O_5 thin films, and the intercalation mechanism of Li, which is the basis for the material's application as an electrode in a rechargeable battery; 2) to shed light on some of the unwanted surface processes also taking place during the Li intercalation reaction. The formation of surface films on the electrodes of lithium-ion batteries has a vital impact on battery performance. A basic understanding of such films is essential for the development of next-generation power sources. The main techniques used in this study are XPS, UPS and RPES, which are proven to be the best techniques to analyze the chemical composition of surface layers and the oxidation state of the elements present as well as the electronic structure of the solids [201, 207].

5.2.1 XPS and UPS data

Fig.5.16 shows the core level XP spectra of O1s and V2p for various Li deposition time ($t_{D, Li}$) ranging from 0 to 14 minutes. For a clean V_2O_5 film the binding energies of O1s,

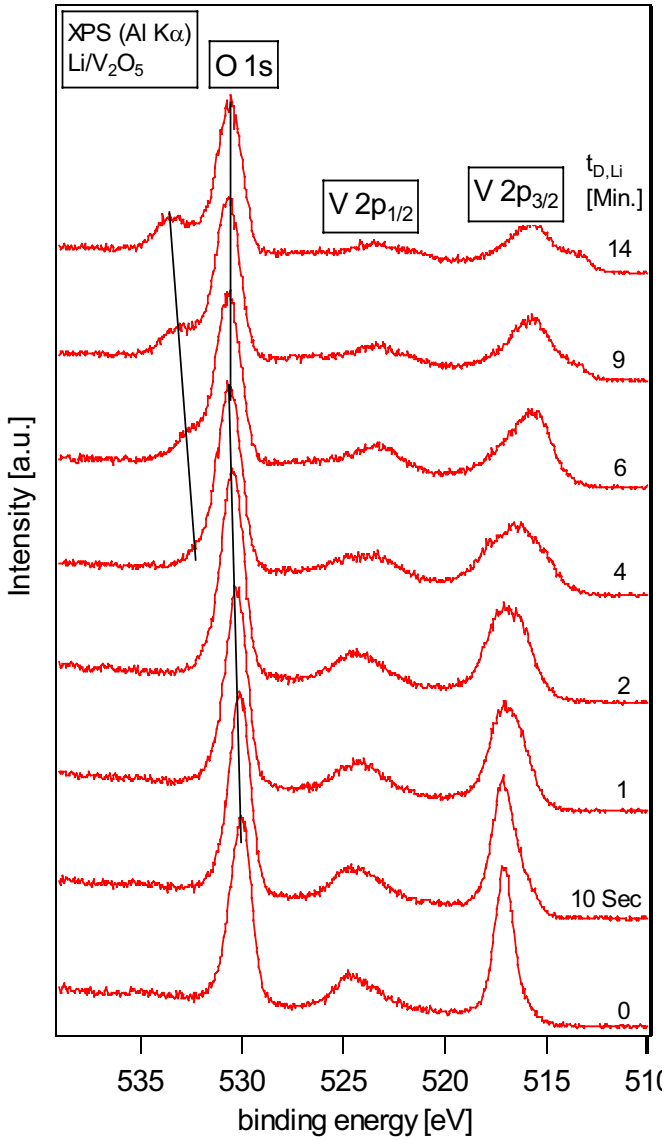

Fig.5.16 Core level XP spectra of O1s and V2p during Li deposition onto a clean V_2O_5 thin film from 0 to 14 minutes

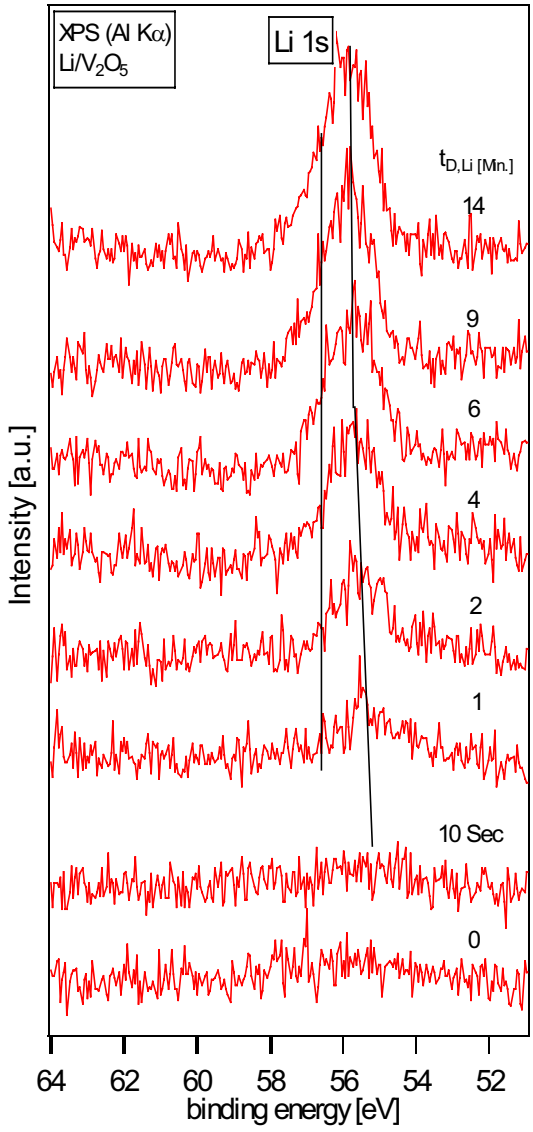

Fig.5.17 Core level Li1s XP spectra at various Li deposition time ranging from from 0 to 14 minutes

$V2p_{3/2}$ and $V2p_{1/2}$ are 529.9, 517.0 and 524.5 eV, respectively. After the deposition of lithium the O1s emission becomes broader, shows a strong asymmetry, and suffers a small shift to higher binding energies (~ 0.6 eV). The full width at half maximum (FWHM) of O1s increases from 1.25 to 1.50 eV for $t_{D,Li} \leq 4$ minutes. Larger deposition time ($t_{D,\,Li} \geq 4$ minutes), leads to additional emissions on the higher binding energy side of the O1s line, which are shifted to even higher binding energies with increasing $t_{D,Li}$. But in the high coverage region the binding energy of the O1s main line is constant. The broadening of the O1s main line can be either related to the different inequivalent crystallographic sites in the

bronzes formed and the random Li distribution, which will both leading to variations in the Madelung potential at the vanadium sites. The asymmetry is probably due to the formation of surface Li species, e.g. it is easy to form Li_2O. The V2p lines ($V2p_{3/2}$, and $V2p_{1/2}$) become broader and shift to lower binding energies with increase of $t_{D,\,Li}$. For high Li content ($t_{D,Li} \geq 9$ minutes), the vanadium lines even split into two lines, with the additional emission on the lower binding energy side. The decrease in the binding energy of the core level usually indicates a decrease in the positive charge of the transition metal ions, which implies that V ions are gradually reduced to lower oxidation state with the intercalation of lithium. Li1s XP spectra for different $t_{D,Li}$ are shown in Fig.5.17. A broad Li1s emission with the maximum at a binding energy of about 55.7 eV is found. The intensity increases rapidly with $t_{D,Li}$ and the shape of the emission also shows a strong asymmetry with larger $t_{D,Li}$. When $t_{D,Li}$ = 10s nearly no lithium signal is found at all. This is due to the high diffusion rate of lithium into the bulk V_2O_5. Furthermore, due to the low atomic sensitivity factor for X-ray the Li1s lines are not very intense, which will impede us to perform a detailed analysis of these lines. But the development of a shoulder peak with a binding energy of about 56.5 eV is evident with increasing $t_{D,Li}$.

For more detailed information the background corrected O1s and $V2p_{3/2}$ spectra are fitted by Voigt profiles (see Fig.5.18(a) and (b)). Three different oxygen compounds are detected in the O1s spectrum assigned as O1, O2 and O3 in Fig.5.18(a). Before the O3 line appears, the O1 and O2 lines suffer the same binding energy shift by about 0.6 eV to higher binding energies. This is evidently due to Fermi level shift resulting from the charge transfer during intercalation of lithium [281]. This effect will be discussed later on in more detail. With the appearance of O3 line originating from the surface oxides, the binding energy and the parameters of the O1 line are constant, which evidences that the Fermi level of the sample does not shift any longer when lithium oxide is formed on the surface. Simultaneously, the intensity of the O2 line decreases. This phenomenon clearly indicates that the properties of the sample's surface have changed when the lithium surface concentration has become too high. The intensity ratio of (O2 + O3)/O1 calculated after Eq.2.23 is shown in Fig.5.19. We can see that the ratio increases slowly with increase of lithium content for low exposure. For $t_{D,Li} \geq 6$ minutes, the value of (O2 + O3)/O1 strongly increases, proving that the O2 and the O3 components correspond to different surface oxides. The O1 component can be assigned to the vanadium oxides (or $Li_xV_2O_5$). Comparing the parameters of O2 and O3 at different $t_{D,Li}$, it is evident that for the O3 line the FWHM is larger and its BE shifts faster to higher binding

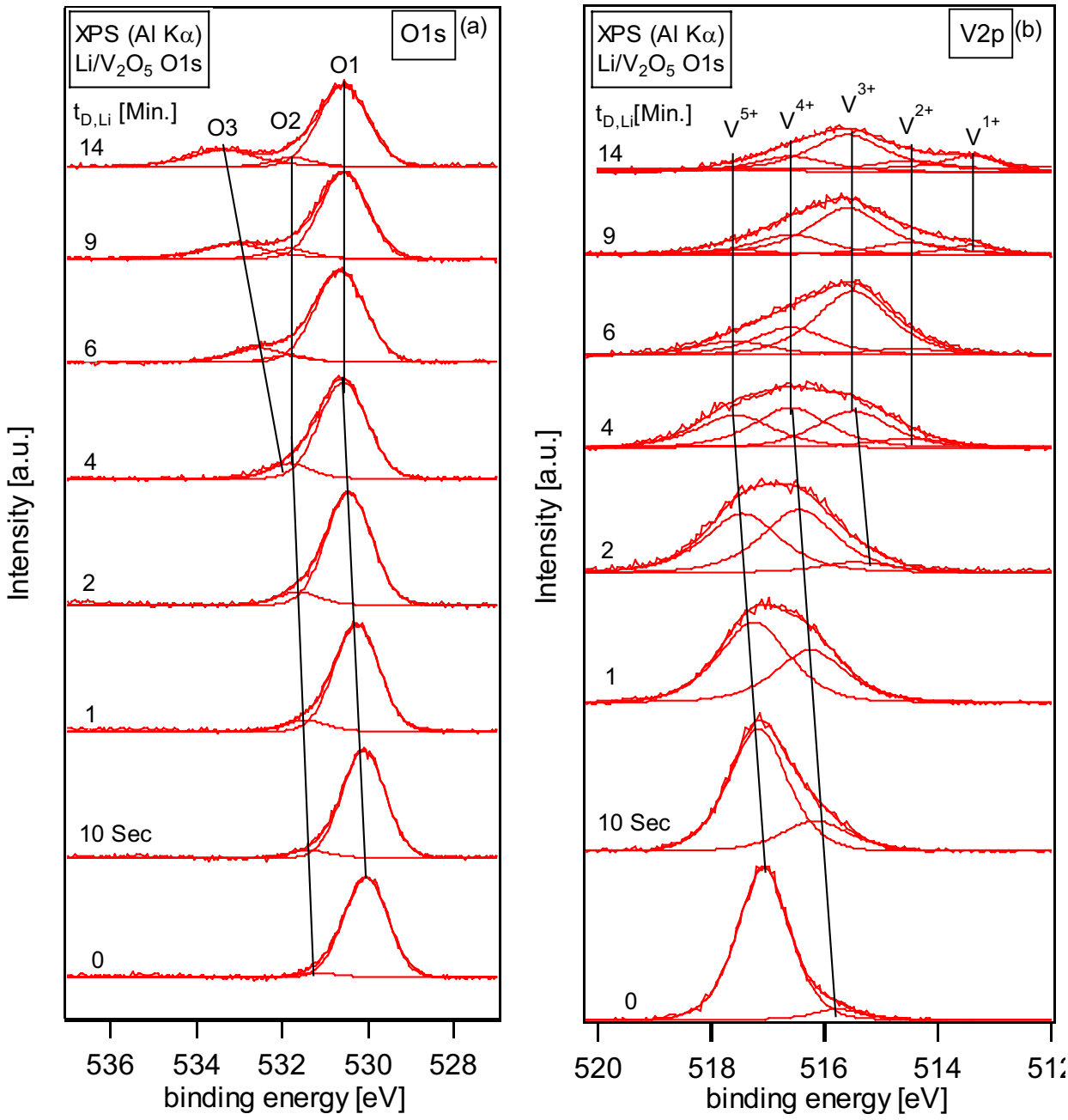

Fig.5.18 The fitted emission lines of O1s (a) and V2$p_{3/2}$ (b) core level spectra for different deposition time after the correction of the background

energy. According to the binding energies O2 is probably originated from Li_2O, whereas the O3 component is associated to Li_2O_2 [282, 283].

In Fig.5.18(b), the V2p XP spectra are shown as a function of $t_{D,Li}$. We can see that with the increase of $t_{D,Li}$ at first a V^{4+} species appears, and then at higher exposures V^{3+}, V^{2+} and even V^{1+} species arise, which indicate a strong reduction of the V ions in relation to the formation of O3 oxide. The binding energy difference between every charge in oxidation states is about 1 eV (in agreement to Ref.153). The V^{5+} and V^{4+} lines show the same binding

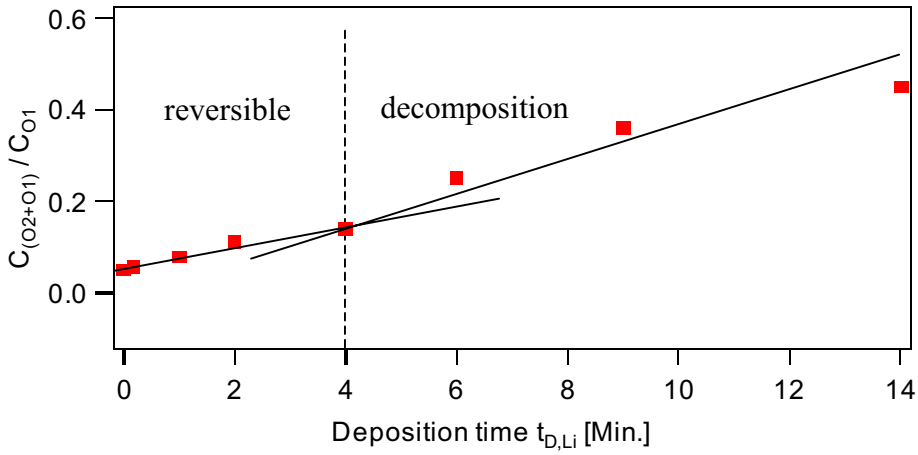

Fig.5.19 The intensity ratio of (O_2 + O3) / O1 against the $t_{D,Li}$

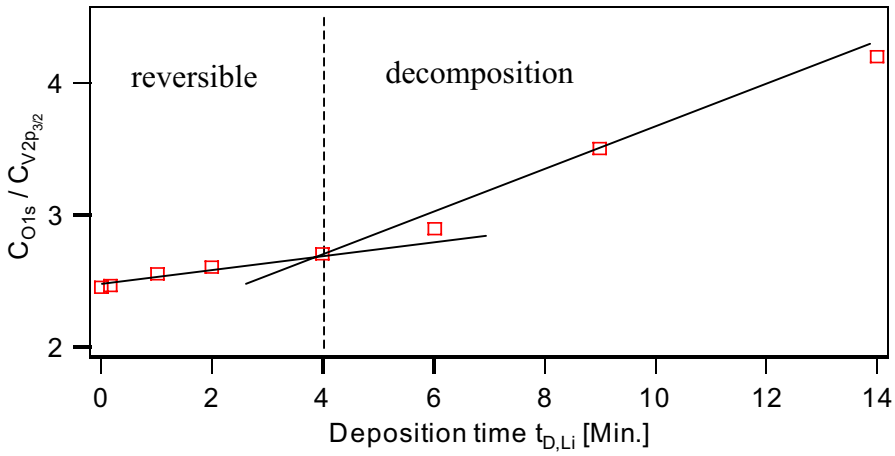

Fig.5.20 The intensity ratio of O1s / $V2p_{3/2}$ at different $t_{D,Li}$

energy shift as the O1 and O2 lines of about 0.6 eV as a function of $t_{D,Li}$ between 0 and 4 minutes. With the appearance of the O3 component, the binding energies of all vanadium and oxygen lines are constant (see Fig.5.18(b)). The V^{3+} line increases very quickly with larger values of $t_{D,Li}$. When a certain Li exposure is reached, even V^{2+} and V^{1+} lines arise, which implies that a decomposition reaction between lithium and $Li_xV_2O_5$ takes place, because such a strong reduction of vanadium ions can not be expected by lithium intercalation. The reduction of the vanadium ions is accompanied by a reduction in the electron density between the metal and the oxygen [65], because the O ions may hybridize less with V^{n+} (n<5) than with V^{5+} ions.

The intensity ratios of O1s / $V2p_{3/2}$ calculated after Eq.2.23 are shown in Fig.5.20. The intensities of O1s, and $V2p_{3/2}$ are derived from the spectra shown in Fig.5.18. It shows the same tendency of change as the ratios of (O2+O3)/O1. For $t_{D,Li}$ < 4 Min., the O1s / $V2p_{3/2}$ ratio is nearly 2.50 and increases very slowly indicating that the reduction of V ions is mostly due to the electron transfer from the 2s orbitals of intercalated Li, but not due to the formation

of oxygen vacancy or any decomposition reaction. A number of ab initio calculation [44, 97, 284, 285] using density functional theory on a range of transition metal oxide cathode materials suggest that the intercalated lithium is fully ionized and that this charge is transferred to the transition metal centers and, to a small degree, to the oxygen atoms. This makes it possible to control the band filling of the host material by varying the Li content. In electrochromic applications band filling is used to adjust the electronic and optical properties [286]. When Li oxides on the surface are formed, however, the ratio of O1s / $V2p_{3/2}$ increase strongly implying that due to a chemical decomposition reaction the oxygen is enriched on the surface in the form of lithium oxides. In Fig.5.19, the (O2 + O3) / O1 intensity ratio indicates the same behavior.

Based on this discussion it is suggested that the saturation value of the intercalated Li into V_2O_5 thin films is reached when $t_{D,Li}$ = 4 minutes. The concentration ratio of Li / V_2O_5 as calculated from the Eq.2.23 is about 2.5. Therefore, the saturation value of Li intercalated into V_2O_5 leads to a stoichiometry of about $Li_{2.5}V_2O_5$. This value is quite similar to the value given by Almeida et al. in their publication [236]. It is somewhat lower than that of V_2O_5 formed in a xerogel which is 3.3 [273]. But it is known that the intercalation into amorphous materials is easier than into crystalline films [287, 288]. Sakurai et al. [289], studying the electrochemical properties of crystalline and amorphous V_2O_5 compounds for lithium secondary batteries, reported that the amorphous cathodes exhibit superior cyclic performance compared to the crystalline ones. Bates et al. [174] demonstrated rechargeable thin-film lithium microbatteries with high energy densities and long cycle life time using amorphous V_2O_5 films.

As we have discussed above the Li oxides on the sample's surface are most probably Li_2O_2 and Li_2O. From the results presented above, the whole process of Li interaction with V_2O_5 following the deposition process can be written as:

Intercalation: $xLi + V_2O_5 = Li_x^+V_2O_5^{x-}$ $(x \leq 2.5)$ (Eq.5.5)

Surface oxidation: $yLi + Li_{2.5}V_2O_5 = Li_{2.5}\,V_2O_{(5-c)} + aLi_2O + bLi_2O_2$ (Eq.5.6)

Where a + b = y/2, and c = a +2b.

In Fig.5.21, the valence band spectra excited by HeI (a) and HeII (b) are shown. For low Li concentration ($t_{D,Li} \leq 4$ minutes), a broad peak at about 1.3 eV assigned to the occupation of originally empty V3d state grow up with Li deposition time and the peak maximum slightly shifts to higher binding energy by about 0.6 eV, which is as the same as that obtained for the O1s and V2p lines. The intensity increase is due to the charge transfer from the intercalated Li

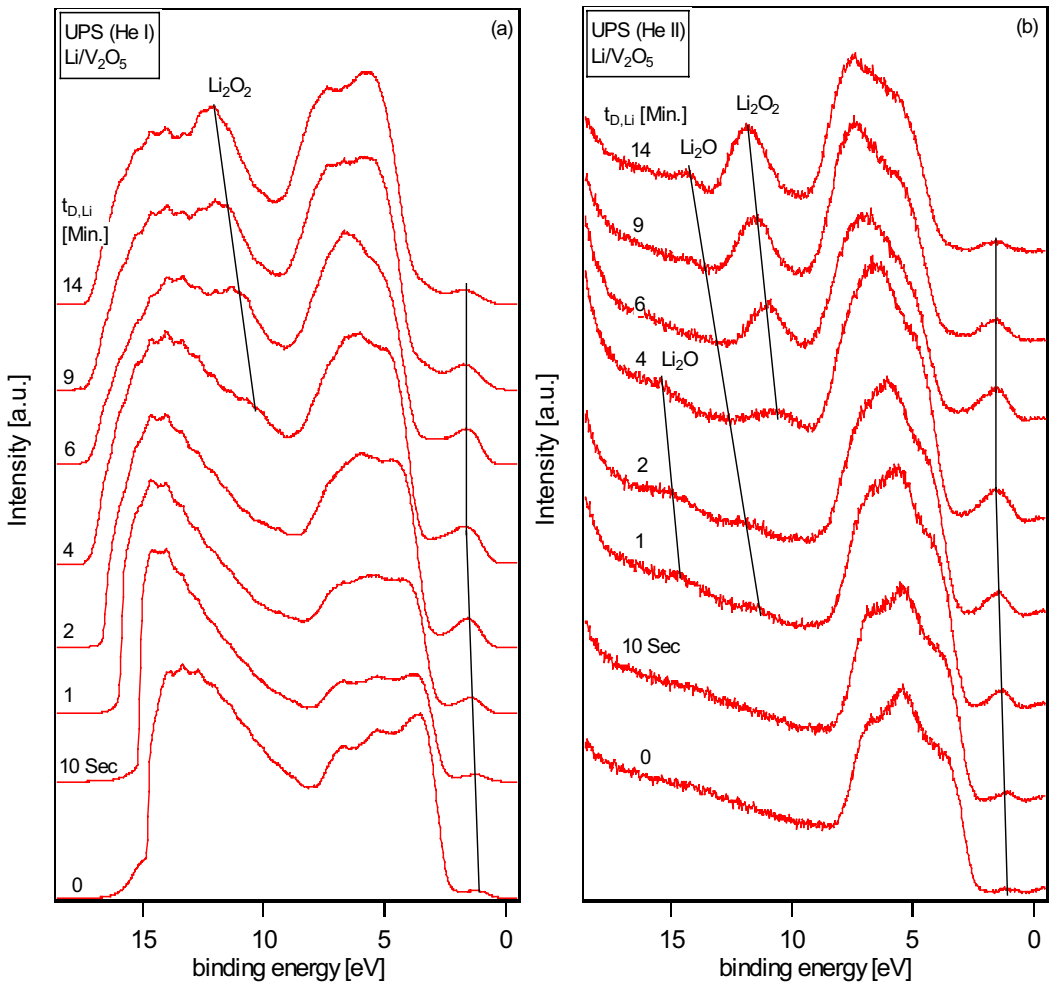

Fig.5.21 The valence band spectra of HeI (a) and He II (b) at various Li deposition time

into the unfilled V3d conduction band states. In order to determine the number of electrons transferred from the 2s orbitals of the intercalated Li into the V3d states, we have investigated this problem by integrating the V3d electron density for different amounts of intercalated lithium. It is possible to calculate the distribution of the electrons due to the intercalation reaction as already presented for Na intercalation (see Chap.5.1.1.3). The ratio of the integrated V3d-band spectral weights (after subtracting a constant background and normalizing to the intensity of the O2p-valence band) between 4 and 2 minutes of lithium deposition time is 1.5. The ratio of the integrated Li1s spectral weights (after removing a constant background and normalizing to the intensity of the O1s core line) between 4 and 2 minutes of lithium deposition is 2.8. Therefore the electron transfer from Li to the V3d orbital is about 0.55 (1.5/2.8) per intercalated atom. We find that the electrons which are transferred from the lithium during the intercalation are almost exclusively localized on the vanadium ions. These results are in quite good agreement with Braithwaite et al's calculation and simulation data [65]. The intensity of the V3d emission decreases again for long deposition

times ($t_{D,Li}$>6 Min.) due to the formation of Li oxides on the surface. The valence band region from 3 ~ 9 eV corresponds to the bands originated mostly from the O2p states. There are three distinct emission lines which form a well defined valence-band spectrum with binding energies at about 3.6, 5.5 and 7.0 eV. According to several theoretical calculations, they have mainly the character of O2p states with a weak V3d admixture [98, 153] (see also Chap.4.2.3). They are not significantly modified by the intercalation with low Li concentration. When the Li concentration is higher ($t_{D,Li} \geq 6$ minutes), pronounced changes are found in the valence band region. The valence band range from 3 to 9 eV has no longer three distinct peaks and the relative intensities are changed. This indicates a severe structural change of the host. Some phases, such as α-$Li_xV_2O_5$ ($x \leq 0.1$) and ε-$Li_xV_2O_5$ ($0.35 \leq x \leq 0.70$), involve very little structural distortion of the bulk oxide, while others, such as β-$Li_xV_2O_5$, have a square-based pyramidal arrangement, which is significantly different from that in V_2O_5 [72]. For α- and ε-$Li_xV_2O_5$ the only distortion of the V_2O_5 structures is a slight puckering of the pyramidal units parallel to the **a** direction, which results in a reduction of the cell parameter in that direction. The formation of Li_2O and Li_2O_2 on the surface also changes the valence band shape due to the superposition of their valence band feature. Two small peaks appear at about 11.5 and 14.8 eV for $t_{D,Li} < 4$ minutes, respectively, resulting from the formation of surface adsorbed oxide (Li_2O). For longer deposition time ($t_{D,Li} \geq 6$ minutes), two additional broad peaks appear at 10.8 and 14.3 eV, respectively, which can be assigned to the O2p states of lithium peroxide and lithium oxide (details will be discussed later on).

Fig.5.22(a) shows the binding energy shifts of O1s and $V2p_{3/2}$. For $t_{D,Li} \leq 4$ Min., the core levels of O1s and $V2p_{3/2}$ shift to higher binding energies by about 0.6 eV. The Li intercalation leads to a filling of the conduction band states of the host material and causes the Fermi level shift [104, 281, 290]. The work function has been determined from the He I spectra. Initially, the work function decreases with increase of $t_{D,Li}$, and then slight increases again (at $t_{D,Li} > 6$ minutes) due to the formation of the surface oxides (see Fig.5.22(b)). The quick decrease of work function with the first deposition step of Li onto the V_2O_5 thin films indicates a dramatic modification of surface potentials with the formation of a surface dipole due to Li adsorption. The ionized Li surface adsorbates can be identified in the Li core level spectra by the higher BE component (see Fig.5.17). The initial formation of a surface dipole is accompanied by the shift of the Fermi level due to the intercalated electrons. The decrease of work function adds up these two contributions, whereas the BE shift only depends on the Fermi level shift. The decrease progresses more smoothly with further deposition, which indicates an in-depth penetration of most deposited Li. At last, the work function increases again due to

depolarization effect and the decomposition of the host with the formation of lithium oxides on the surface. The two contributions in the change of work function ($\Delta\Phi$), one is the surface dipole and the other is Fermi level shift (ΔE_F) lead to:

$$\Delta\Phi = \Delta\Phi_{\text{surface dipole}} + \Delta E_F \qquad \text{(Eq.5.7)}$$

When $t_{D,Li} \leq 4$ minutes, ΔE_F is calculated as 0.6 eV, $\Delta\Phi$ is about 2.2 eV, thus $\Delta\Phi_{\text{surface dipole}}$ is about 1.6 eV. The adsorbed alkali ions on the surface cause a stronger reduction of work function compared to the same amount of alkali as intercalated species [172, 230, 291, 292].

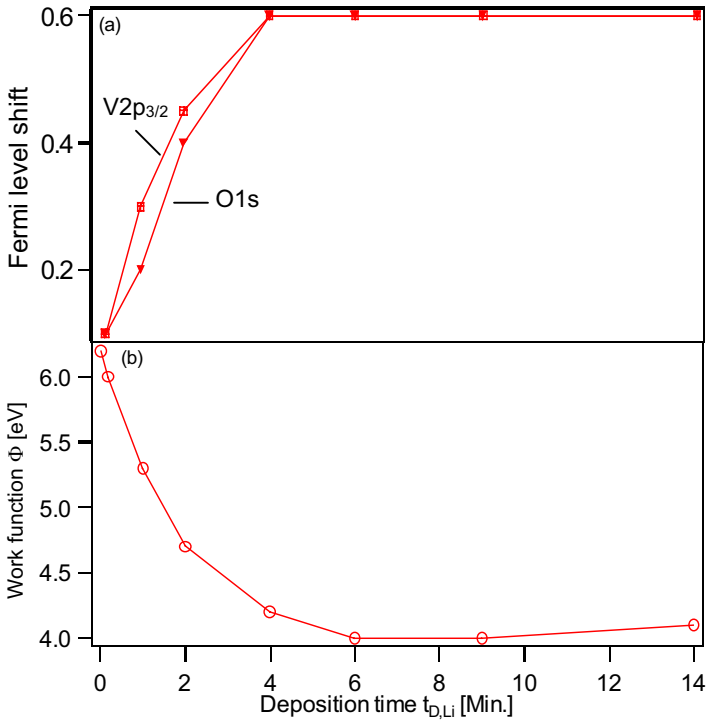

Fig.5.22 The binding energy shift of O1s and V2p$_{3/2}$ core line (a) and change of the work function ($\Delta\Phi$) (b) during the deposition of lithium

Fig.5.23 shows the O1s and V2p (a) and Li1s (b) core level spectra taken after keeping the sample inside the UHV chamber (base pressure is 1×10^{-10} mbar) and air for different days. It has been noticed that in UHV the O2 line increases gradually with time. The O1 line scarcely change in binding energy, but it becomes much narrower in FMHW from 1.6 to 1.1 eV after 9 days in UHV. At the same time the vanadium lines decrease quickly. These results indicate that the O1 line has gradually changed from vanadium oxides into lithium oxide (Li_2O) with time. In Fig.5.23(b), the Li1s spectra are shown. The intensity increases with the storage time corresponding to the O1s line. To explain these observations, the concentration ratios of O1s / Li1s after 0, 2, 5 and 9 days in UHV has been calculated from the spectra in

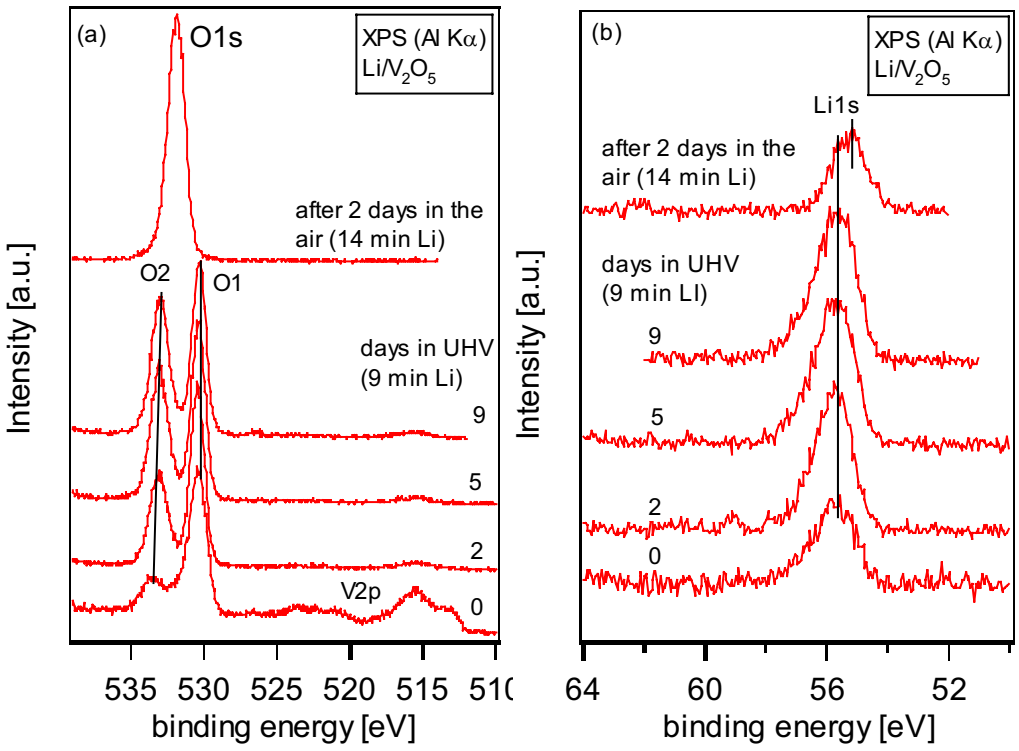

Fig.5.23 The core level spectra of O1s and V2p (a) and Li1s (b) after keeping the Li/V_2O_5 sample in the UHV chamber and the air after different days

Fig.5.23 and the results are presented in Fig.5.24. First, the ratio decreases fast from 0 to 2 days and then it increases very slowly. This tendency indicates that no more oxygen in the chamber reacts with the surface due to the decrease of the O1s/Li1s ratio. For a reference experiment, the sample with 14 minutes Li deposition has been taken out of the UHV chamber into the air for 2 days. The spectra obtained thereafter are quite different from those in UHV: only one O1s emission with a central BE at 531.9 eV is found, and the intensity of

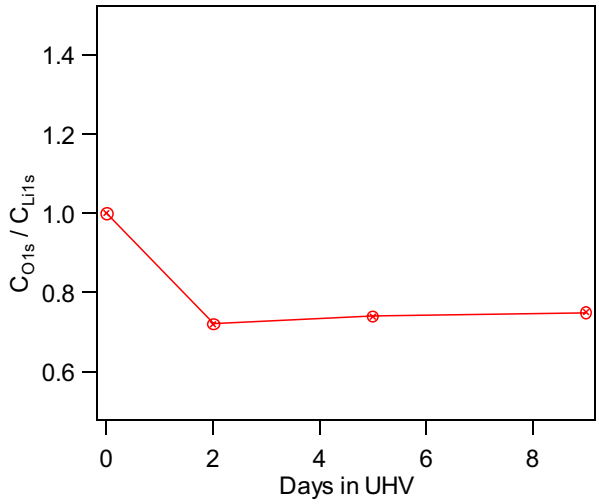

Fig.5.24 The concentration ratios of O1s / Li1s after 0, 2, 5, 9 days in UHV

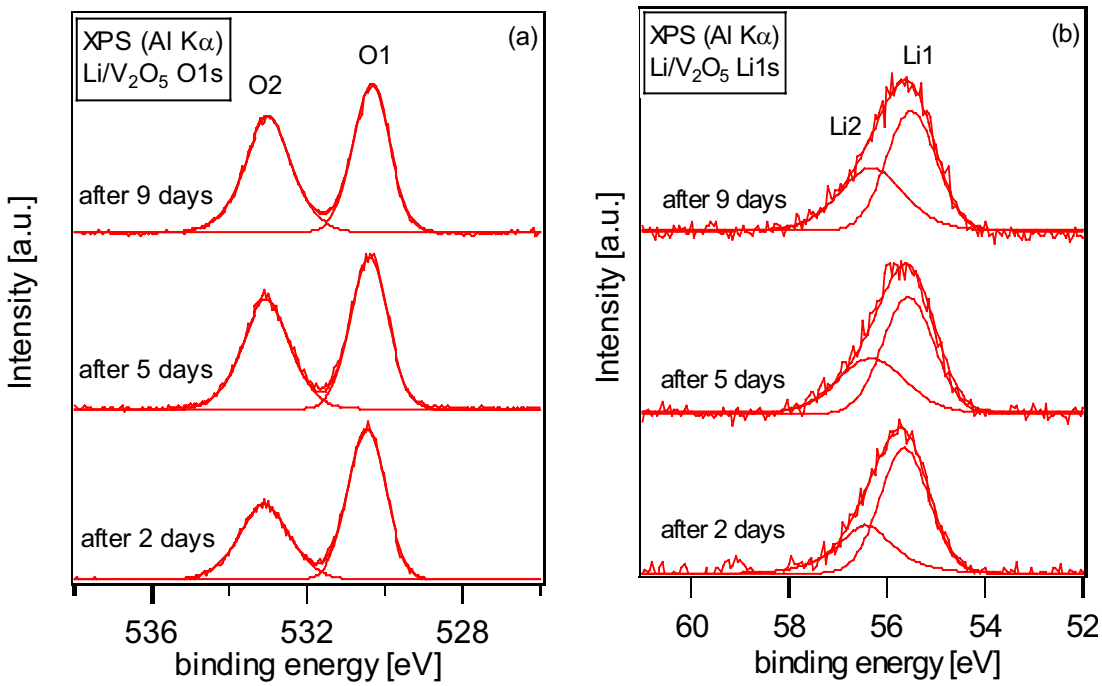

Fig.5.25 The fitted spectra of core level O1s (a) and Li1s (b) of Li/V_2O_5 sample after different days in UHV

the Li1s emission line is lower. The ratio of O1s/Li1s is about 1.5, which is much higher than that in UHV. This experiment indicates that in UHV environment the surface does not react with oxygen and water which is different from what is found after the sample is kept in the air. The above discussion indicates that inside the UHV chamber, for an over deposited sample as $Li_5V_2O_5$, the decomposition reaction still takes place due to the instability of the crystal structure of the host. The decrease of the O1s/Li1s ratio evidences that lithium is first deintercalated from the $Li_xV_2O_5$ lattice. This deintercalated lithium will further react with vanadium oxides to form lithium oxides on the top of the surface as is evidenced by the strong reduction of the vanadium signal. To investigate the compositions of the lithium oxides on the surface, the background removed O1s (a) and Li1s (b) lines (after 2, 5, and 9 days) are fitted in Fig.5.25. The ratios of Li1/O1' and Li2/O2 are calculated, where the intensity of O1' is calculated from O1 – O_V (O_V is the oxygen for vanadium oxides which is calculated from the intensity of the vanadium lines). The results show that the ratio of Li1/O1' is about 2, which means that the first oxide signal is due to Li_2O, and Li2/O2 is about 1, which implies that the second oxide signal is due to Li_2O_2. These results support the assignments already given above. In order to clarify the distribution of the lithium oxide layers, angle dependent XP spectra have been recorded after 5 days in UHV (see Fig.5.26). Variation of the emission angle leads to different ratios between these two oxide compounds. The Li_2O_2 increases with increasing emission angle indicating that Li_2O_2 is on the topmost surface (0° means normal

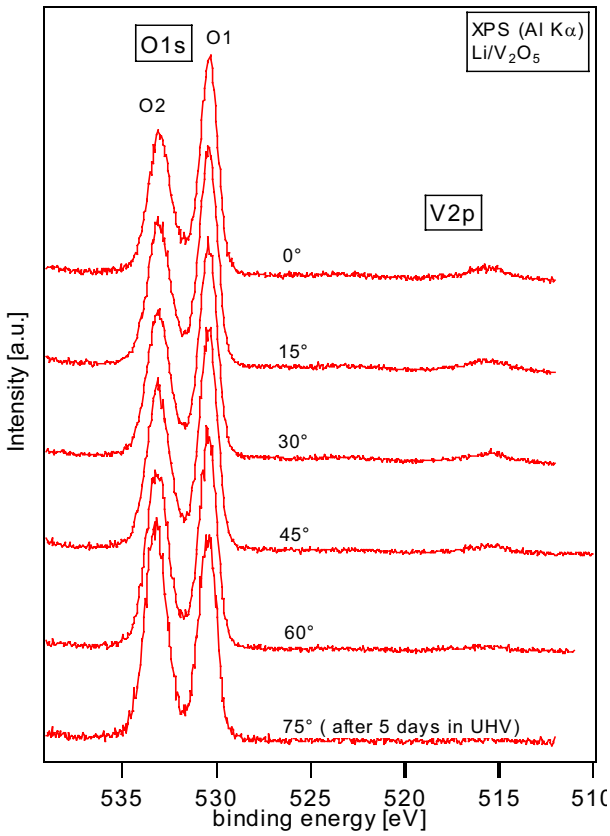

Fig.5.26 Angle resolved XPS measurements after the sample is kept in UHV for 5 days

emission). The lines of Li_2O and V decrease slowly with the increasing emission angle, showing that Li_2O and lithium vanadium oxides are in the second and third layers. The surface layers composition of the sample can roughly be imagined as shown in Fig.5.27.

Fig.5.28 shows the valence band spectra (He I and He II) of the same samples as shown in Fig.5.23. For the sample stored in the UHV chamber, the feature at 10.8 eV increases quickly with the increase of Li_2O_2 intensity, which evidences that this line is due to the O2p state of Li_2O_2. While the feature at 14.3 eV related to the Li_2O decreases with the increase of the Li_2O_2 species. The broad line centered at 5.95 eV is a mixture of O^{2-} and O_2^{2-}. The shoulder line at 3.9 eV corresponds to the O2p level of atomic oxygen bound to Li [293]. The valence band spectra after the sample was exposed to air for 2 days are quite different.

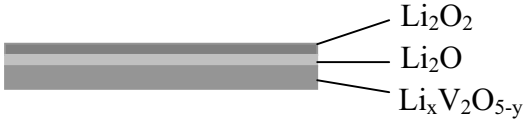

Fig.5.27 A model of the layer composition of thesample after 9 days in UHV

No Li_2O_2 is found on the surface, but OH or H_2O are found with BEs of 9.2 and 11.3 eV, respectively. This results indicates that after the Li/V_2O_5 sample exposure to air LiOH will form on the surface. The ratio of O1s/Li1s is calculated as 1.5, which is higher than the expected value of 1. This is probably due to the presence of additional oxide species absorbed on the surface.

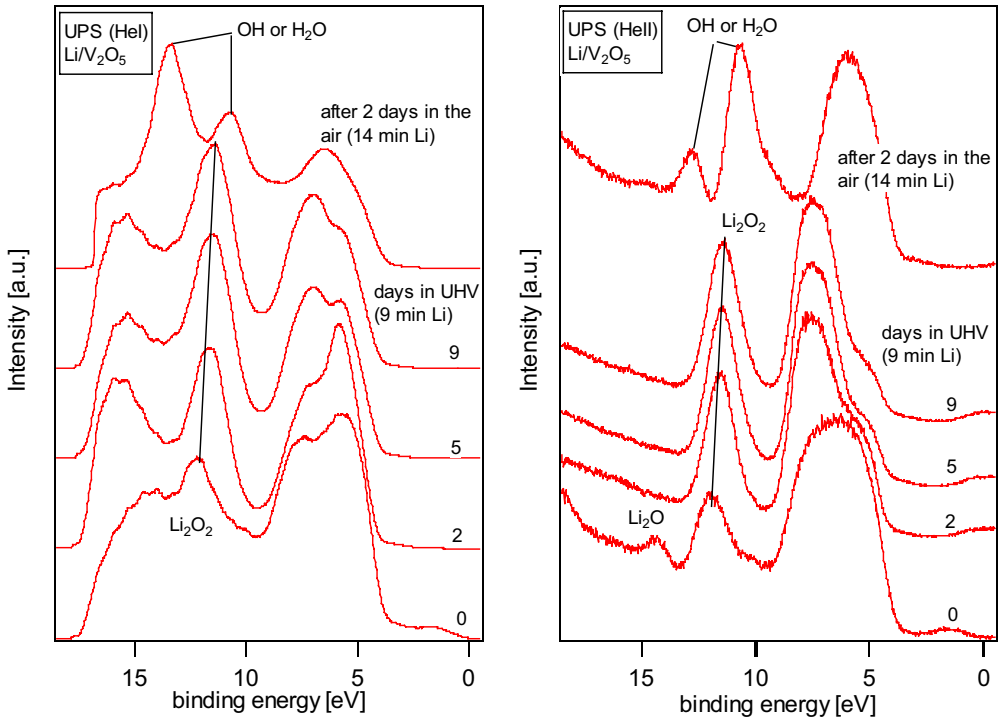

Fig.5.28 Valence band spectra (HeI (a) and HeII (b)) of Li/V_2O_5 samples kept different days in UHV and in air

In order to analyze the depth profile of the sample, after 9 days in UHV the sample is gradually sputtered with Ar^+ ions. The core level spectra of O1s, V2p and Li1s as a function of sputtering time are shown in Fig.5.29 (a) and (b), respectively. The intensity of the O2 line decreases quickly with the sputtering time, and the O1 line become broader and asymmetric again. Simultaneously, the signal of the vanadium 2p line appears gradually. These results show again that Li_2O_2 is on the topmost layer. With increasing sputtering time the intensity of the Li1s line decreases and shifts to lower binding energy due to the removal of lithium oxides from the top surface layers. Fig.5.30 shows the valence bands (HeI (a), HeII (b)) after 15 and 25 minutes sputtering. The feature at 11.3 eV decreases with the decrease of O2, and the feature at 7.5 eV becomes broader and changes the intensity ratio again due to the reappearance of vanadium oxides. The V3d gap state emission in the valence band spectrum increases with the increase of vanadium core level lines resulting from the removal of the lithium oxides surface layers and appearance of the vanadium oxides. The final core and

valence band spectra are again rather similar to the spectra obtained during the deposition process.

5.2.2 Electrochemical intercalation

The electrochemical experiments have been performed in the chemistry department of Xiamen University. All experiment are carried out in an argon-filled glovebox (< 1 ppm O_2 and H_2O) or in a closed cell assembly. Slow scan rates used for the cyclic voltammogram can reveal the electrochemical behavior of Li intercalation/deintercalation into/from V_2O_5 lattices. The working electrodes used were V_2O_5 powder mixed with an electric conductor (acetylene

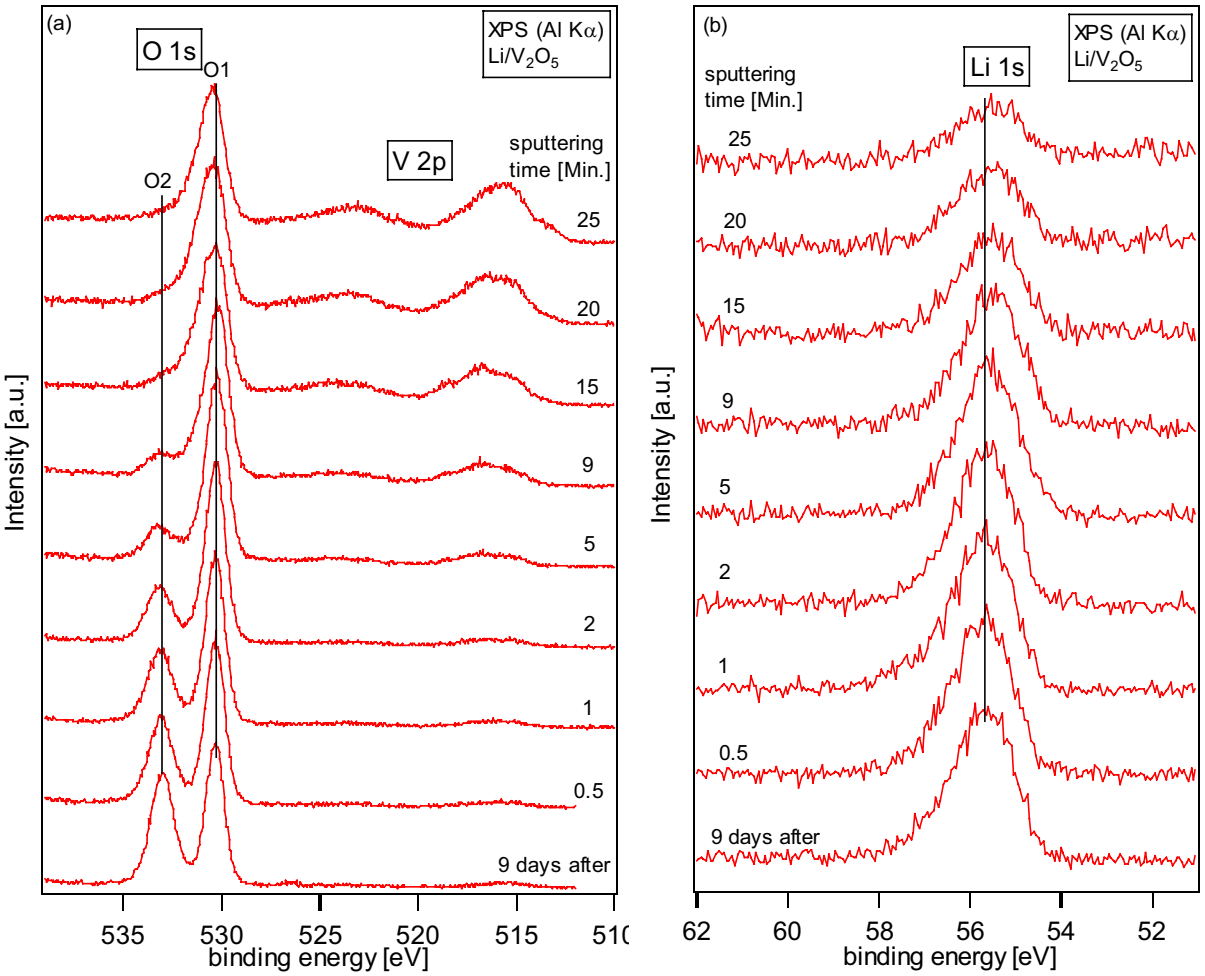

Fig.5.29 XP spectra depth profile of the Li/V_2O_5 sample after 9 days in UHV

black and graphite) and a binder (polytetrafluoroethylene (PTFE) and Poly-vinylidene flouride (PVDF)) by the ratio of 85:10:5 in quantity, respectively. The mixture was pressed onto a rough Cu foil for good electric contact. Before electrochemical measurements the electrodes are dried in an infrared oven for more than 6 hours. The electrolyte used in our

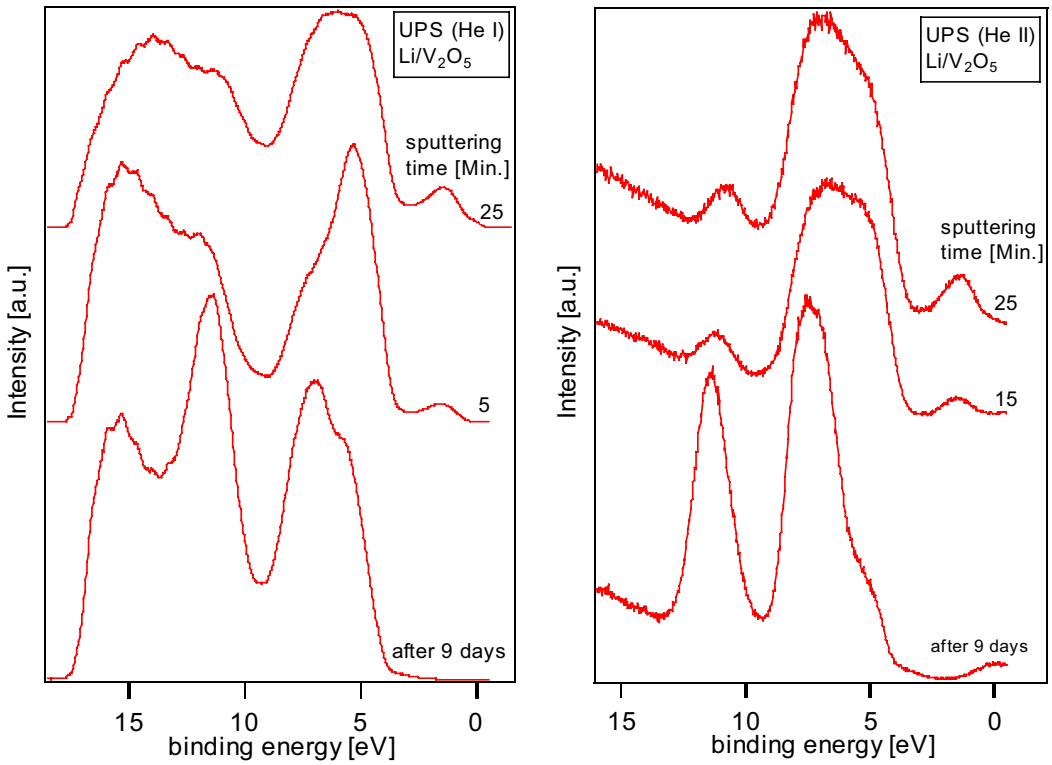

Fig.5.30 Comparison of the valence band spectra of the Li/V_2O_5 sample stored in UHV before and after 15 and 25 minutes sputtering

measurements is LP30 which is produced by Merck KgaA. Its composition is 1mol L^{-1} $LiPF_6$ / (EC + DMC) (50 : 50 wt%). The conductivity is 11.7 $mScm^{-1}$. The reference and the counter electrodes are both Li foils. The cyclic voltammograms are shown in Fig.5.31 with different potential windows: (a) 3.6 ~ 1.7 V, and (b) 3.5 ~ 2.8 V at a sweep rate of 0.1 mV/s. In Fig.5.31(a), five reduction peaks are identified at the first negative potential going sweep (NPGS), which imply that five different $Li_xV_2O_5$ phases form at different content of Li intercalation into V_2O_5. But at the following positive potential going sweep (PPGS), no distinct oxidation peaks can be observed, but only a very broad and low current peak is found. In the second scan, nearly no reduction and oxidation peaks can be found any more in the both NPGS and PPGS. This is due to the high Li content intercalated into V_2O_5 during the first scan. For a higher degree of Li intercalation the V_2O_5 crystal structure will collapse and lead to irreversible changes in the cyclic voltammogram. These results are in good agreement to the data presented above from the XPS and UPS surface science studies on the intercalation process. If the potential window is reduced, it will reduce the concentration of intercalated Li. For a voltage between 3.5 and 2.8 V, only two reduction and oxidation peaks are found, respectively (see Fig.5.31(b)). Li deintercalation reactions are found at 3.40 and 3.25 V, respectively. These values are in good agreement with previous works [394-297]. The voltage range then determines the composition range over which Li can reversibly be intercalated and

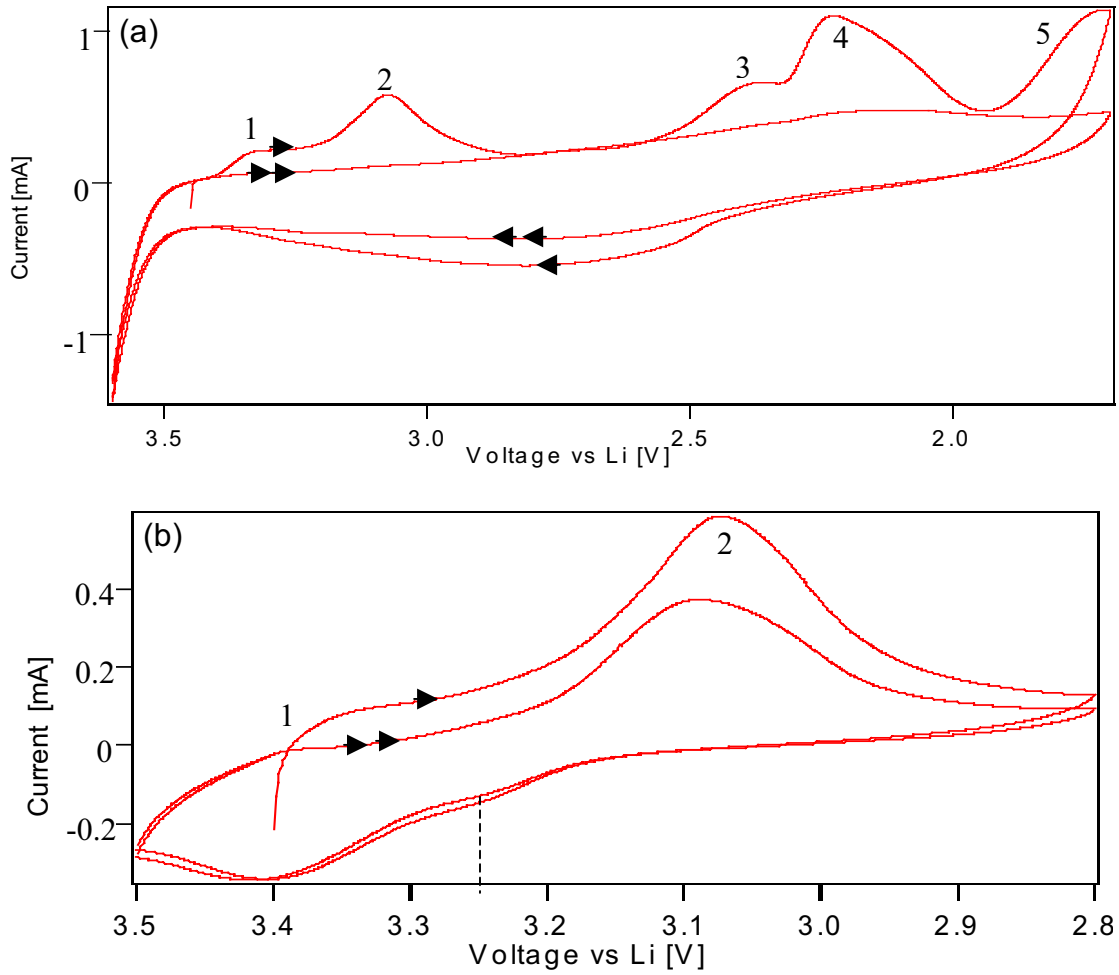

Fig.5.31 Cyclic voltammograms of powder V_2O_5 at different width of the potential window: (a) 3.6 ~1.7 V; (b) 3.5 ~ 2.8 V vs Li (Scan rate: 0.1 mV/s)

deintercalated and determines the battery capacity. Again this first electrochemical reduction/oxidation reaction can be compared to the stable range of intercalation from the surface studies found for low Li depositions. A gradual decay of the current wave is observed upon prolonged scanning with a reversible potential of 2.8 V, but their shape and position are nearly unaltered. This effect is ascribed to a partial loss of active material. For low Li content part of the lithium intercalated V_2O_5 undergoes an irreversible structural change, thereby destroying part of its capacity that can not be used in the next discharge cycle. It is reasonable to assume that the same principle mechanism are operative as at higher intercalation degrees due to an inhomogeneous distribution of alkali during the intercalation process.

5.2.3 RPES data

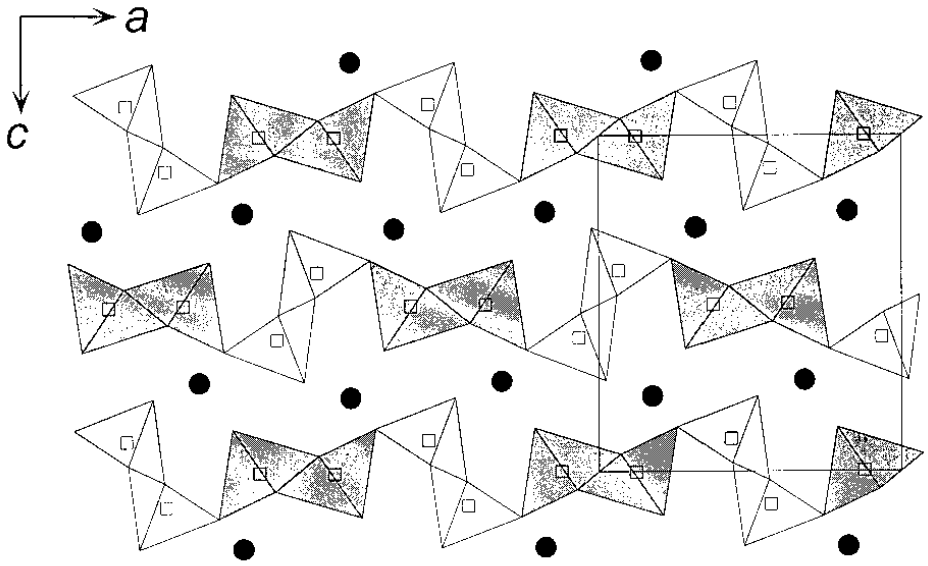

Fig.5.32 Schematic crystal structure of orthorhombic γ-LiV_2O_5. The dark and white VO_5 square pyramids represent $V^{4+}O_5$ and $V^{5+}O_5$ pyramids, respectively

The orthorhombic γ-LiV_2O_5 has a layered structure with lithium ions between the layers (see Fig.5.32). In this structure there are two crystallographic vanadium sites that form two kinds of zigzag chains, the shaded and white chains. The valence states of vanadium ions are inferred from the results of a structural analysis to be V^{4+} for the shaded zigzag chains, and V^{5+} for the white zigzag chains [298]. Within the layers, $V^{4+}O_5$ (shaded) zigzag chains are linked to $V^{5+}O_5$ (white) zigzag chains by sharing corners. In the structure of γ-LiV_2O_5, there are two kinds of $V^{4+}O_5$ pyramids with apex oxygen above and below the sheet. Each kind of $V^{4+}O_5$ pyramid forms an infinite linear chain by sharing a corner with the same kind of pyramid or one kind of pyramid forms an infinite zigzag chain by sharing an edge with the other kind of pyramid. In this case, γ-LiV_2O_5 is expected to be a quasi-1-D-spin system because each double-linear chain is isolated by the $V^{5+}O_5$ double-linear chains. Resonant photoemission spectra of $Li_xV_2O_5$ are shown in Fig.5.33 with various contents of lithium. The shape of the spectra changes and the lowest binding energy state (V3d) increases with increasing lithium deposition time. In all $Li_xV_2O_5$ phases (with changed x) we clearly notice that the 3d states have been shifted considerably from the Fermi level. For the low lithium concentration (Fig.5.33(a)), we can see that the O2p bands do not show a significant change

from that of V_2O_5. They show the same resonant effect as we have found in pure V_2O_5 (see Chap.4.2.3). An additional line (E) arise at around 12 eV which is assigned to the O2p state of Li_2O (see discussion above). It does not show any resonant effect confirming our

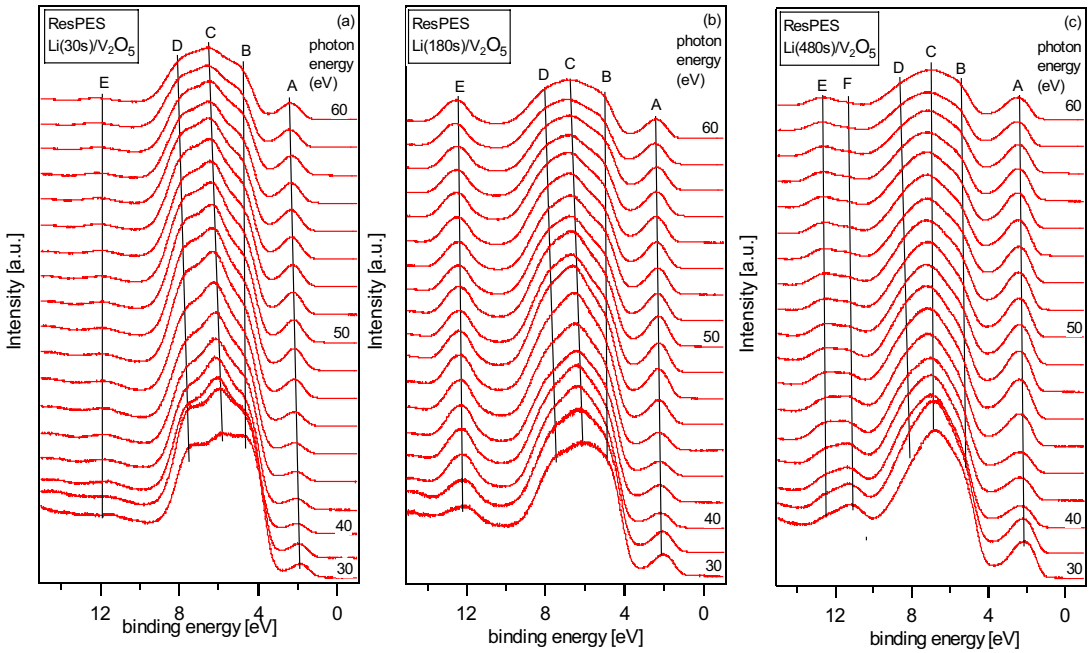

Fig.5.33 The RPES data of $Li_xV_2O_5$ at different lithium deposition time, (a) 30 seconds, (b) 180 seconds, (c) 480 seconds

discussion above, because the O2p orbital of Li_2O should not have any hybridization with V3d electron states. In Fig.5.33(b), the intensity of feature E increases due to more Li_2O species formed on the surface. Because more lithium is intercalated into the V_2O_5 layers, the crystal structure has changed somewhat. The shape of the valence band vary from the distinct 3 lines, but they still show the same resonance effect as those in Fig.5.33(a). In Fig.5.33(c) more lithium oxides (Li_2O and Li_2O_2) have been formed on the surface, as a consequence the shape of the valence band has changed much and the O2p bands do not show any remarkable resonant effect any more. One more line appears at about 11 eV (F) which is assigned to the O2p of Li_2O_2, and the feature E shifts to 12.5 eV. With increasing photon energy the intensity of feature F decreases, while that of feature E increases. The mean free path of electrons in a solid depends on their kinetic energy. The minimum is found at E_{kin} = 50-70 eV with a depth of about 5 Å (see Chap.3.1.1.1). Therefore, the RPES data imply that the Li_2O_2 layer is below the Li_2O layer, because its intensity decreases with the increase of photon energy. When the photon energy increases, the shallower layer of the surface contribute more to the emission signal. This result does not agree with the layers composition we have proposed before. This is maybe due to the different sample treating process, as the samples we have discussed

before were kept 5 or 9 days in UHV which leaves time for the surface to rearrange. In this RPES experiments the samples are measured immediately after Li deposition, and it seems that there is not enough time for the surface rearrangement.

6 Discussion on intercalation reaction

In this chapter the general effects of alkali metal intercalation in the UHV experiments as observed by photoemission spectroscopy will be summarized and discussed in order to understand the involved intercalation mechanisms and their kinetics and implications. The correlation of work function changes and Fermi level shifts with the charge transfer and changes of host crystal structure induced by the intercalation will be outlined. Finally, the contribution of different mechanisms to the battery voltage as deduced from these data and a comparison between Na and Li intercalation will be given.

6.1 The process of alkali intercalation into V_2O_5 layers

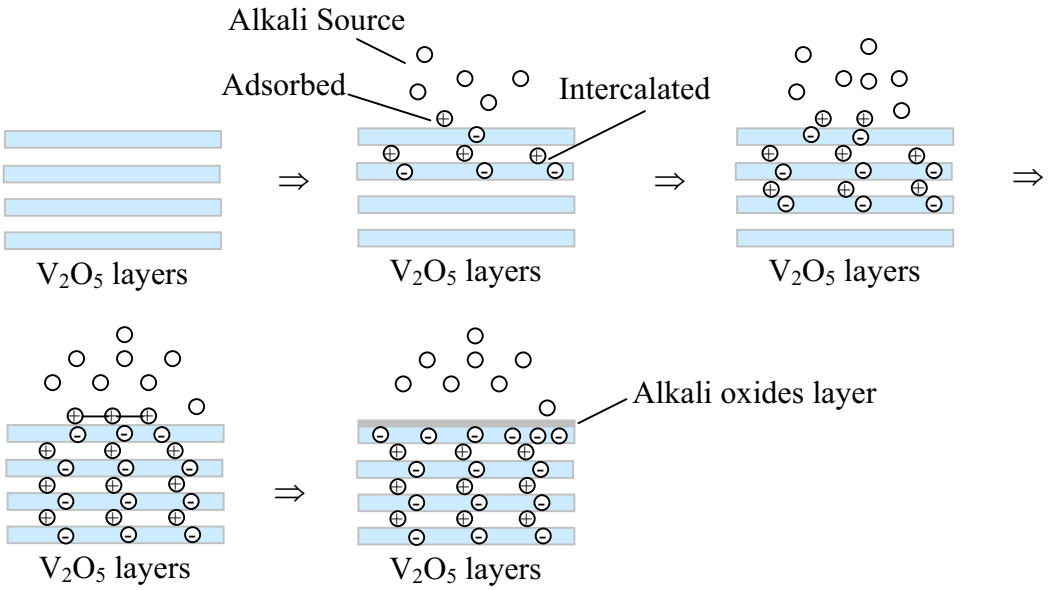

Fig.6.1 The scheme for the formation of intercalated and adsorbed alkali ions, and alkali oxides on the topmost surface using a vacuum deposition process

The XPS core level data show that alkali metals intercalate spontaneously at room temperature when they are deposited onto V_2O_5 thin films. But a small amount remains adsorbed on the surface. The adsorbed and intercalated alkali ions are both considered as fully ionized [299]. But our results have given experimental data for the amount of hybridization and the effective charge transfer from the alkali to transition metal ions which will be discussed in detail later on. When the limitation value of reversibly intercalated alkali into V_2O_5 is reached ($A_xV_2O_5$: x=1.4 for A=Na; x=2.5 for A=Li), alkali oxides or metallic alkali layers will form on the surface layers, which are proved by the XPS data. These decomposition products as the alkali oxides will effect the cycling life and storage volume of

batteries and lead to capacity loss, poor cyclability, and power fade [236]. The process of the intercalation is shown schematically in Fig.6.1. For an explanation of this process we assume a constant alkali metal sticking coefficient and thus a constant deposition rate. The limiting concentration is then determined by kinetic and energetic factors affecting the intercalation reaction. Bronold et al. attributed limitations of the intercalation behavior to the existence of a diffusion barrier for the alkali ions [119]. Alkali ions diffuse into deeper van der Waals gaps only if at a particular composition further increase of x (the amount of alkali metal compared to the host) can be only realized by the occupation of less favorable sites in the host by the guest species. For small values of x the site energy is nearly independent of the guest atoms concentration due to negligible Coulomb interaction among the intercalated ions.

From our XPS and UPS data it is suggested that when the concentration of alkali ions is low, the vanadium ions are partially reduced from V^{5+} to V^{4+}. Also the shape of the UP spectra does not change very much, which indicates no big structural change during the intercalation. In this range the electronic structure of the intercalation phase may be described by a "modified rigid band model", which keeps the overall electronic band structure with some modification in their energetic position of the bands. But when the concentration of alkali is high, the vanadium ions are strongly reduced and the UP spectra change dramatically. In this range the host is decomposed reductively loosing its structural integrity and as a consequence the electronic structure is completely modified.

6.2 Structural and electronic effects

V_2O_5 has a layered structure with O = V ---O bonds between the layers (see Fig.2.6). It has been noticed in experimental studies that alkali migration takes place parallel to the **b** direction along channels formed by vanadyl bonds. The changes to the lattice parameters, as the alkali content is increased for $0 < x < 1$, is mostly an increase in the **c** lattice parameter [65]. As a consequence the band gap is increased with increased alkali metal content. The lattice parameter **a** decreases somewhat and **b** is almost unchanged [66]. Upon intercalation the weak O---V bonds between two layers of V_2O_5 are extended and the sheets buckle as the layers are separated to allow the alkali to be incorporated into the structure (see Fig.6.1). At low lithium contents the intercalation reaction is reversible. During the intercalation of alkali the M-O bond length are increased leading to a smaller σ overlap between the O2p and metal 3d orbitals. As a consequence the bonding bands are pushed upwards and the antibonding bands downwards. The level of the t_{2g} band remains almost unchanged (as this is a nonbonding band), but the width of the band changes somewhat [44]. As A^+ ions are

introduced between the negatively charge oxygen slabs, the repulsive interaction of these slabs is reduced and the electrostatic energy of the system decreases. This causes the upper part of the oxygen p band to drop to lower energy levels [107]. Compared with the literatures the same results have been obtained in this work: 1) The band gap increases with the increase of alkali metal deposition time, due to the increase of parameter **c**; 2) the valence band spectra do not change much when $0 < x < 1$ indicating no strong change in the crystal structure; 3) the O2p band shift to higher binding energy during the intercalation of Na and Li suggesting that the O2p band drops to lower energy level.

Excess Li intercalation is effective in changing the transition metal valence state and crystal structure. The charge distributions is continuously modified as the positive charge of the transition metal element decreases while positive charge (A^+) appears in the vacancies of the pristine materials. As a result the intercalated phase becomes more and more metastable as the amount of intercalation increases. When an upper limit is overpassed ($A_xV_2O_5$: $x>1.4$ for Na; $x>2.5$ for Li), the intercalated material is no longer stable and irreversible structure modification occurs as we have found in the surface science and electrochemical experiments. If the concentration of intercalated alkali is too high, this leads to decomposition reactions of the host and the strong reduction of the transition metal ions, thus intercalation becomes irreversible in this range, which is proven by the electrochemical experiments.

6.3 Charge transfer

The determination of electron transfer is an important step for characterizing the intercalation mechanism. Guo and Liang found a transfer of only 0.45 electron per Li atom to the TiS_2 host using rigid-band model calculation [300]. However, as they argued themselves, this charge transfer is probably significantly underestimated due to the large spherical size used to count the Li charge. Moreau et. al. [301] obtained an even smaller charge transfer for the same compound from a Mulliken population analysis in an extended Hückel model. This result is likely due to the somewhat artificial charge assignment made in the Mulliken population analysis.

It is found that Li 2s is fully ionized in the intercalated compounds with its charge transferred to the anion and to the metal by ab initio study [44]. Up to now, to my knowledge, there are not any experimental data to calculate the charge transfer from alkali metal to the transition metal ions. In this work the charge transfer from intercalated Na into V ions is calculated from photoelectron data. A value of 0.42 is obtained for the charge transfer from the intercalated Na atoms to vanadium ions, which is in good agreement with results in the

above cited literature. A charge transfer number of 0.55 electrons is also calculated from the photoelectron data for per intercalated Li atom to V3d.

6.4 Fermi level shift and work function change

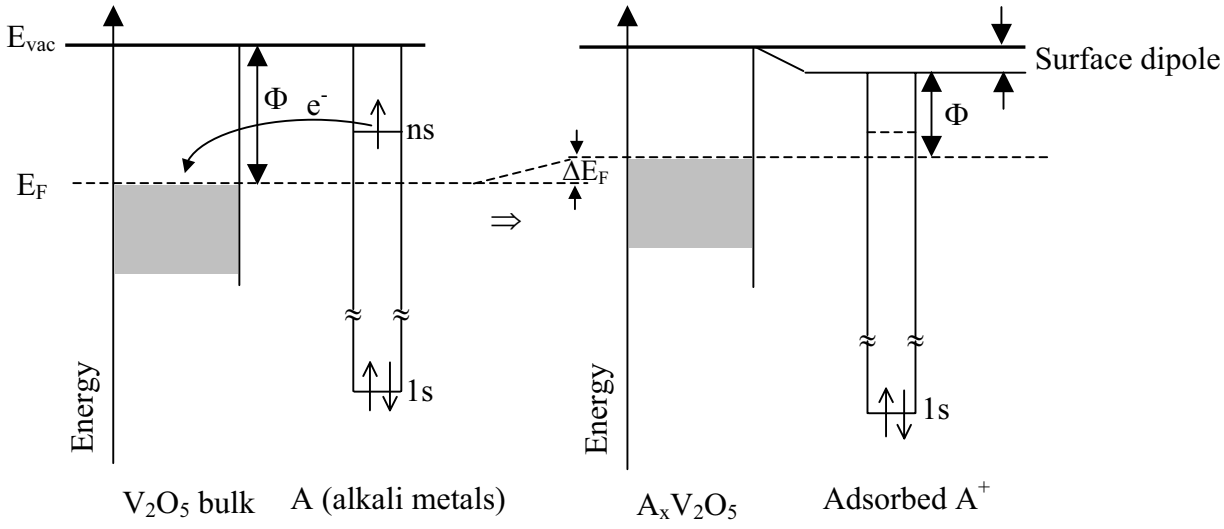

Fig.6.2 The schematic diagram of Fermi level shift and surface dipole formation

The intercalation of alkali metal leads to a Fermi level shift and to the formation (modification) of a surface dipole (see Fig.6.2). The Fermi level of the host shifts towards the vacuum level with of intercalated alkali due to the charge transfer from the alkali s orbital to initial empty states of the host. If alkali ions are also adsorbed on the surface, the work function is decreased due to the formation of surface dipoles. Experimentally, this has been proven by the formation of broader emission peaks shifted to higher binding energy compared to the same intercalated species as measured in the XP spectra (see also ref. 118, 230, 302, 303). Adsorbed atoms on the surface can form an interface dipole due to a big difference in work function leading to an electron transfer (see Fig.6.2). In the low coverage region (below one monolayer) the adsorbed alkali metal atom evidently donates its electron to the substrate. This leads to a dipole layer at the surface directed with its positive end towards vacuum which decreases the work function.

Many theoretical and experimental studies have already shown that the outermost s orbital electrons of the intercalated alkali metal atom will be transferred to the lowest unoccupied band of the host material [44, 65, 101, 304] leading to the shift of Fermi level towards the vacuum level [230].In the case of V_2O_5 the charge transfer changes the host from an insulator (semiconductor) to a metallic conductor [16, 44, 64, 305]. The electron transfer

process is schematically shown in Fig.6.3. The alkali valence band formed from the valence state s orbitals have a much lower binding energy than the unoccupied conduction bands of the host. Our experimental data show that the work function of V_2O_5 is about 6.1 eV, which may be compared to the work function of Na and Li to be 2.5 and 2.9 eV, respectively. Therefore, it is easy for the electrons to be transferred from alkali metal to the unoccupied valence state of the host because the process will reduce the overall electron energy. Our experimental results are in reasonable agreement to this model of intercalation related changes in electronic structure: 1) the intensity of V3d gap state increases with the increase of intercalated alkali; 2) the Fermi level of the host shifts with the intercalation of alkali; 3) the V ions are partially reduced from V^{5+} to V^{4+} during the intercalation of alkali.

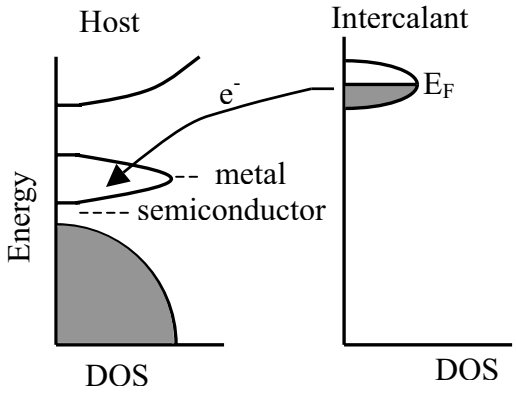

Fig.6.3 The schematic diagram of the electron transfer process from the alkali to the metal 3d band of the host

However a more detail view of the intercalation induced changes also indicates additional effect which must be taken into account. In the UPS data, it is clearly to be seen that the V3d state is separated from the Fermi level position. This phenomenon has not been experimentally observed and discussed before. There may be in princible two contribution to this effect, one is electron-electron interaction, and the other is polaron formation which may be compared to the Jahn-Teller distortion. As for the V_2O_5 system the initial V3d state is empty, therefore electron-electron interaction seems to be impossible, because there will be only one electron in the V3d state neglecting the effect of hybridization. Thus the most probable interpretation is due to the formation of a polaron. For better understanding of this effects, further theoretical calculation seems to be necessary.

6.5 Battery voltage deduced from the XPS and UPS data

As given in previous work by other authors [44, 306], the average cell voltage can be estimated from the well-known relationship:

$$\Delta G = -nFE_{CELL} \quad \text{(Eq.7.1)}$$

Where ΔG is the Gibbs energy, F is the Faraday constant, and E_{CELL} is the cell voltage.
In the following reaction of Li intercalation into V_2O_5:

$$Li_xV_2O_5 + yLi \rightarrow Li_{x+y}V_2O_5 \quad \text{(Eq.7.2)}$$

we approximate the free energy change (ΔG) with the internal energy change per intercalated lithium ion (ΔE); by taking the difference between the total energies of the reaction and the products:

$$\Delta G \approx \Delta E = (E_{PROD} - E_{REACT})/\text{no. of lithium atoms} \quad \text{(Eq.7.3)}$$

This approximation excludes effects of entropy and volume change. However, the contribution of the vibrational and configurational entropy terms to the cell voltage is expected to be small (< 0.1 V) at room temperature, and there is little change in volume during the intercalation. The change in the total energy of the system per intercalated lithium atom can be given by:

$$\Delta E(x') = \{E(x_2) - [E(x_1) + (x_2 - x_1)\, E(Li)]\}/(x_2 - x_1) \quad \text{(Eq.7.4)}$$

Where E(x) = total energy of $Li_xV_2O_5$, $x_2 > x_1$, and $x' = (x_1 + x_2)/2$, E(Li) is the total energy of pure lithium metal. From this equation the battery voltage is expected to change with the amount of intercalated Li (x). When the amount of x increases, the battery voltage will decrease.

In this work the model for calculating the voltage of the Na and Li intercalation batteries is shown in Fig.6.4 based on our PES data. It also shows that the voltage of the batteries will change with the shift of the Fermi level, which is strongly dependent on the intercalated amount of alkali metal. If the contribution of the ions to the voltage is neglected (assuming negligible changes of ion energies in the host compared to the pure alkali metal). The voltage difference of the working electrodes can be writen as:

$$V_{WE} = \Phi_{V2O5}(x) - \Phi_A - \Delta E_F(x) \quad \text{(Eq.7.5)}$$

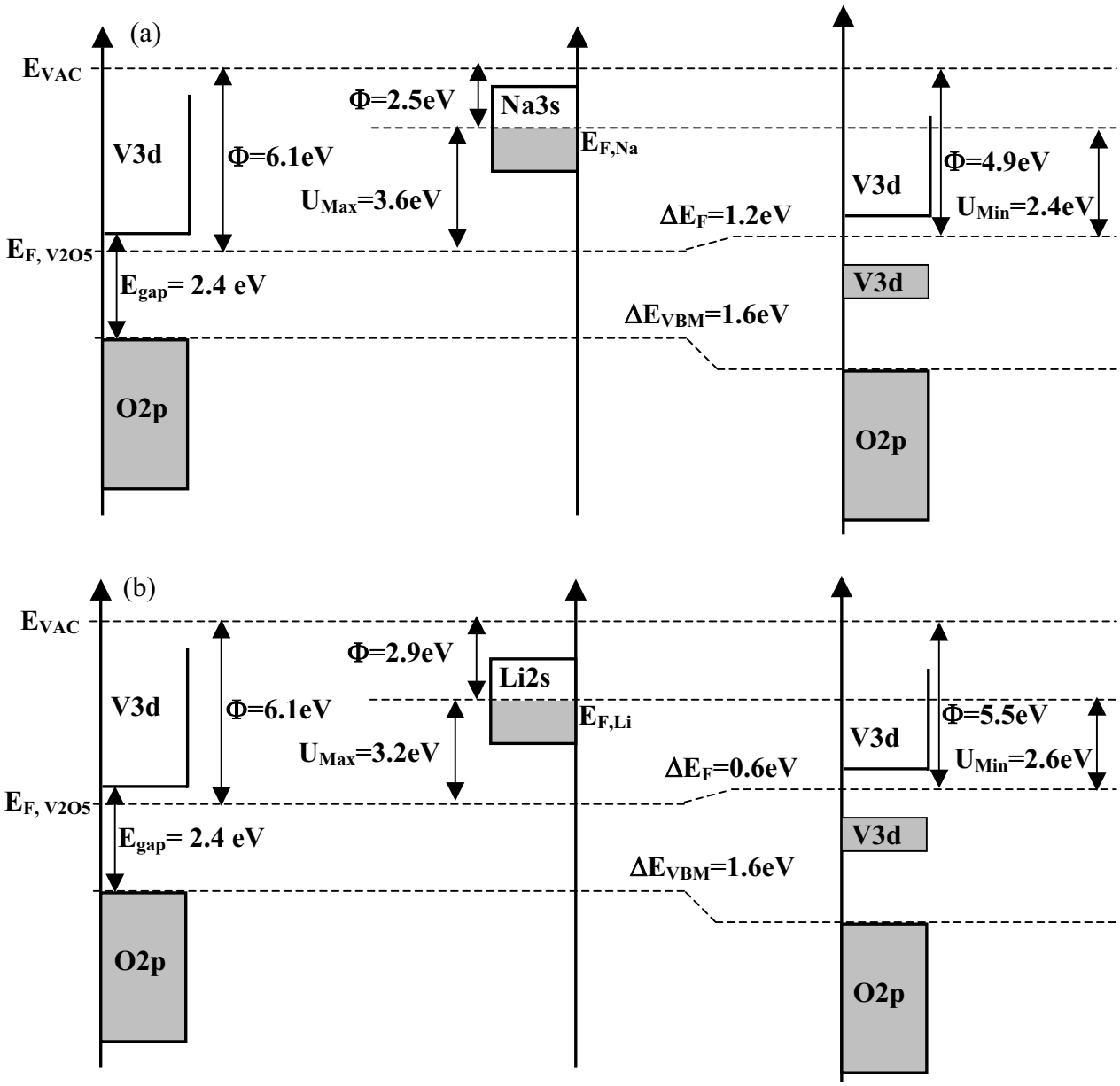

Fig.6.4 The schematic electron energy diagram for calculating the voltage of the Na (a) and Li (b) intercalation batteries

Where $\Delta E_F(x)$ is the shift of Fermi level, which depends on the amount of intercalated alkali (x). For A = Li, when x = 0, the theoretical voltage is 3.2 V, which is about 0.4 V lower than that measured from the electrochemical data [236, 307]. The lose of 0.4 V is probably due to the contribution of the ionic energy during the intercalation of Li ions (see details in Chap.2.1.1). When Li is fully intercalated to x = 2.5, the voltage is reduced to about 2.6 V, which is about 0.6 V higher than the data found in the electrochemical measurements [236, 307]. This deviation is probably due to the ideal condition used in the model calculation. In general, the voltage predicted in this model diagram agrees fairly well with the electrochemical data. For A = Na, due to the lower work function, the initial potential is 3.6 V

which is slightly higher than that of Li, but due to the larger Fermi level shift during intercalation of Na, the theoretical minimum voltage is about 2.4 V which is lower than that of Li.

6.6 Comparison between Li and Na intercalation

It is quite clear from the results that Na and Li behave very differently after deposition onto the V_2O_5 surface despite having similar properties in many other respects. Looking first at the reaction of each alkali metal alone, it appears that V_2O_5 is intercalated much more easily with Li than with Na: the saturation intercalation concentration is much higher for Li ($Li_{2.5}V_2O_5$) than for Na ($Na_{1.4}V_2O_5$); Li intercalation causes a smaller Fermi level shift of the host material due to its higher work function. There are also less adsorbed oxide species on the surface. Comparing the physical and chemical properties of Li and Na: for Li, atomic radius is 2.05 Å, and electronegativity is 0.98; for Na, atomic radius is 2.23 Å, and electronegativity is 0.93. Intercalation with Li could be favored by the smaller size of the Li ions, which requires less deformation of the host layers, and by the higher electronegativity. But the fact that Cs intercalates as easily as Na rules out the idea that the intercalation tendency should be a pure size effect [308, 309]. The lower intercalation rate of Na is possibly due to the fact that the intercalation compound is less stable than for Li. But it may also be due to a greater stability of the Na surface species compared to that of Li. To pursue this question further investigation is necessary.

Chapter 7 Electronic structure of $LiMn_2O_4$

In this chapter, the electronic structure and surface composition of $LiMn_2O_4$ electrode will be studied by photoelectron spectroscopy (XPS, UPS) and resonant photoelectron spectroscopy (RPES).

$Li[Mn_2]O_4$ is a cubic spinel with space group symmetry Fd3m. The structure of $Li[Mn_2]O_4$ is shown and described in detail in Fig.2.4. Most of the earlier works on these oxides are focused on the electrochemical properties and crystalline structure of $LiMn_2O_4$ [9, 59, 60, 310-315], while studies on the fundamental electronic and magnetic properties of $Li_xMn_2O_4$ (where $0 \leq x \leq 2$) have been published recently [316-319]. The characteristic properties of transition metal oxides are mainly determined by the oxidation states of the transition metal. Thackeray et. al. [320] pointed out that due to an increase of the Mn^{3+} ion concentration and the related Jahn-Teller distortion within the spinel framework the symmetry of the structure is reduced from cubic in $LiMn_2O_4$ to tetragonal in $Li_2Mn_2O_4$. Calculations have shown that the bonding interaction in $[Mn^{4+}O_6]$ are of higher covalence than that in $[Mn^{3+}O_6]$ [321]. It is generally assumed from the chemical point of view that the average oxidation state of Mn in $LiMn_2O_4$ is +3.5 [322, 323]. This would mean that the ionic ratio would be $Mn^{+4}/Mn^{+3} = 1$. But there is not any direct proof of this assumption, yet. Recent publications [93, 324] concerning the electronic structure of $LiNiO_2$ have for example shown that the Ni ions are not in trivalent but in divalent state. Therefore, an experimental determination of the oxidation states of the metal ions in Li containing metal oxides as e.g. of Mn ions in $LiMn_2O_4$ by photoemission spectroscopy is interesting.

Sample preparation

The $LiMn_2O_4$ was donated as powder from Merck (Germany). The same materials is commonly used in lithium-ion batteries. The samples were pressed into pellets for easier handling. Before the measurements, the samples were heated in oxygen atmosphere with a partial pressure of about 10^{-6} mbar for about 3 hours to clean the sample's surface. Afterwards the samples have been cooled down in the same oxygen pressure for 1 hour before the measurements. Alternative surface cleaning procedure as Ar^+ ion sputtering has been tried but lead to stronger decomposition of the sample.

7.1 XPS data

The O1s XP spectrum of $LiMn_2O_4$ is shown in Fig.7.1. One main emission line is detected accompanied by a small but broad shoulder. The binding energies are determined as 529.76 and 531.65 eV, respectively. The main line is assigned to O^{2-} ion of the metal oxide [318], while the small shoulder on the higher binding energy side could be attributed to the concomitant formation of a surface lithium oxide species (Li_xO_y) similar to that formed on the surface of $LiNiO_2$ due to heat treatment in oxygen [319]. From the photoemission intensities the relative amount of Li_xO_y to $LiMn_2O_4$ on the surface is about 16%.

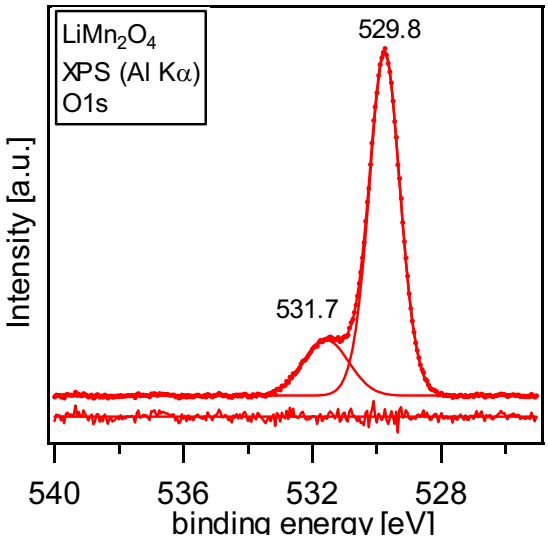

Fig.7.1 XPS core level spectrum of O1s

Fig.7.2 shows the Mn2p XP spectrum of $LiMn_2O_4$. It displays a broad emission line with a maximum near 642.4 eV, and a distinct shoulder near 641.3 eV. The interpretation of the Mn2p spectrum is complicated due to the multiple splitting of the Mn2p spectra of Mn^{4+}, Mn^{3+}, and Mn^{2+} ions [325]. Multiple splitting of the core lines only occurs when the valence band 3d electron states are occupied by unpaired electrons, the oxide is therefore in the high spin state. Gupta and Sen [326, 327] calculated the multiplet structure of Mn^{4+}, Mn^{3+}, and Mn^{2+} free ions and demonstrated that the $Mn2p_{3/2}$ spectrum of the simple oxide each oxidation state consists of four or five multiplet emission lines separated from each other by 0.7-1.2 eV. For this reason the Mn2p XP spectra cannot be easily analyzed by a simple fitting produce concerning the contribution of Mn^{2+}, Mn^{3+}, and Mn^{4+} compounds [325].

Because of the fact that the Mn3p XP spectrum (see Fig.7.3) displays a similar shape as the Mn2p spectrum with a main emission at 50.1 eV and a lower binding energy shoulder at 48.8 eV, it can be assumed that there are at least two different kinds of Mn ions in $LiMn_2O_4$. According to the binding energies, they are most likely Mn^{4+} and Mn^{3+}. Under this assumption, the background corrected $Mn2p_{3/2}$ peak has been fitted in Fig.7.2(b) and 7.2(c) using reference data of H.W. Nesbitt et. al. [335, 336]. For the fit in Fig.7.2(b) the ratio of Mn^{3+}/Mn^{4+} is fixed as 1. Some intensity deviations of the fitting curve from the original data are found. They arise due to the fixed intensity contributions of the single line which can be different for various materials. If the single contributions of Mn^{4+} and Mn^{3+} are fixed to the value given from the literature, then it is impossible to fit the experimental intensity as can be seen in the Fig.7.2(b). An adjustment of the fitting data (see Fig.7.2(c)) shows that it is possible to describe the overall spectrum by Mn^{4+} and Mn^{3+} contributions, and therefore it can

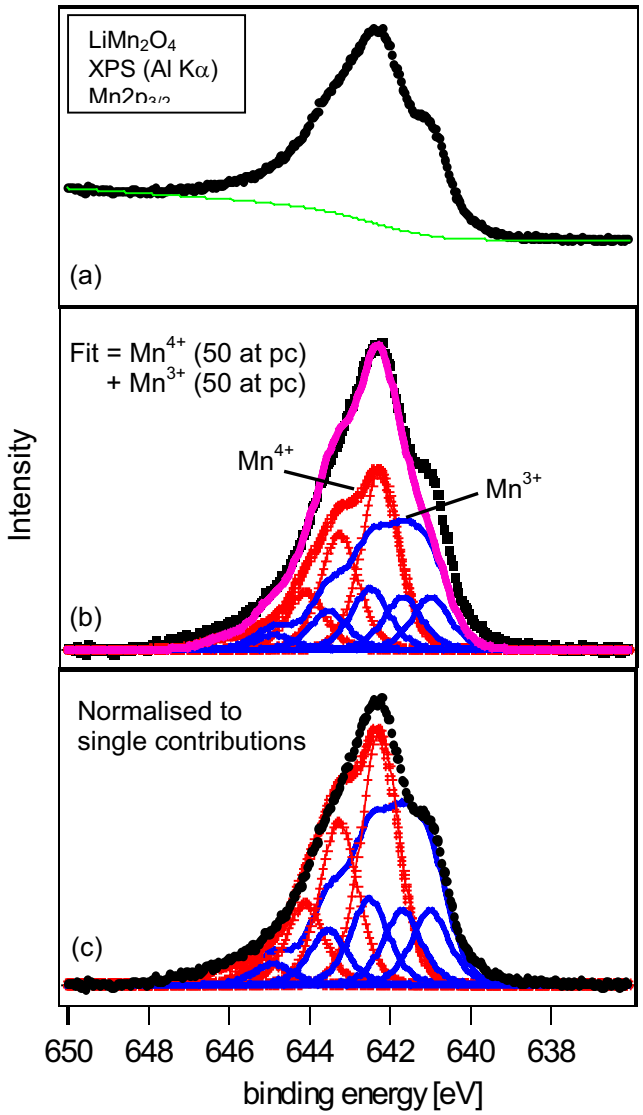

Fig.7.2 XPS core level spectrum of Mn $2p_{3/2}$ with background (a) and fitted spectrum (b, c)

be assumed that there is not further contributions. The additional emission in Fig.7.3 with binding energy of about 54.2 eV corresponds to the Li 1s emission.

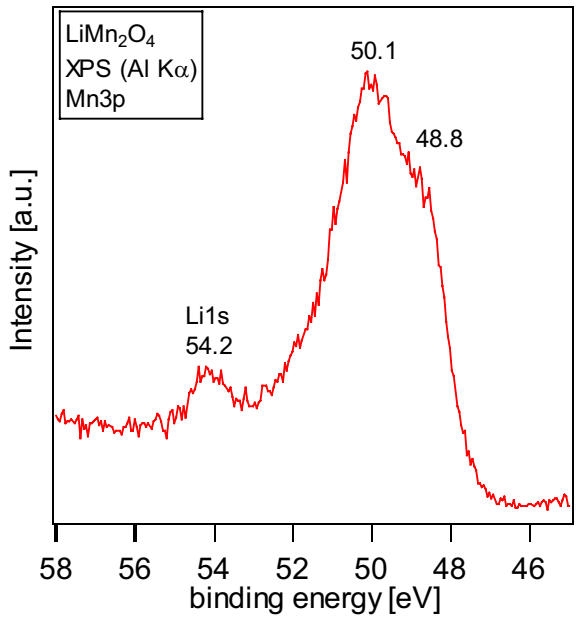

Fig.7.3 XPS core level spectrum of Mn 3p and Li 1s

The 3s core levels of the 3d transition metals are known to exhibit exchange splitting [330]. The binding energies of the split 3s emissions are quite sensitive to the oxidation state of Mn. There is almost a 0.8-1.0 eV of difference between the binding energy of the 3s level of Mn^{2+} and that of Mn^{3+} and also about 0.8-1.0 eV between Mn^{3+} and that of Mn^{4+} [331, 332]. The multiple splitting is smaller for Mn^{3+} than for Mn^{4+}. This results from the different energies of the charge-transfer processes. The expected splitting of the 3s level is about 6.5 for Mn^{2+}, 5.5 for Mn^{3+} and 4.5 for Mn^{4+} [330]. From the spectra in Fig.7.4, the binding energy of the 3s level is determined to be 84.25 eV and the 3s(1)-3s(2) splitting is about 4.95 eV. Thus the splitting energy is about midway between that of Mn^{3+} (5.5eV) and that of Mn^{4+} (4.5eV). This values can be used to construct a calibration to determinate the oxidation state of the Mn ions. Using a linear interpolate of the known splitting energies against the oxidation number, a formal oxidation state of the Mn ions in $LiMn_2O_4$ of +3.55 is found (see Fig.7.5). Furthermore, we have fitted the Mn 3s emission line by two compounds with binding energies of 83.8 eV and 84.6 eV respectively (see Fig.7.4). The splitting energies to the satellite peak are 5.5 eV and 4.5 eV which are consistent with that of Mn^{3+} and Mn^{4+} ions, respectively. The intensity ratio of the two compounds is 0.9, so that the average oxidation state is also 3.55, which is equal to the value which we have calculated from the calibration method. The slightly higher oxidation state than +3.5 is probably due to the formation of lithium oxides on the surface. The intensity ratio of Li1s/Mn3p calculated from Fig.7.3 is 0.57 which is higher

than the expected value 0.5 as given from the formula $LiMn_2O_4$, this indicates that more Li is situated on the surface.

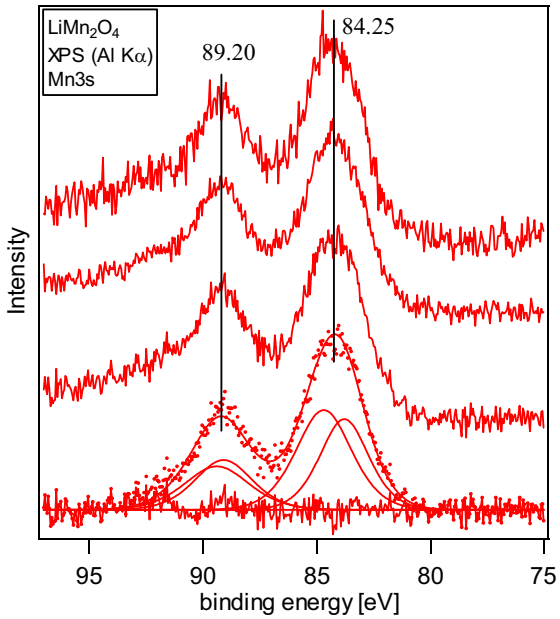

Fig.7.4 Mn 3s core level spectra of three different $LiMn_2O_4$ samples. Fitting data shows the Mn^{3+}- and Mn^{4+}-contributions in an intensity ratio of 0.9

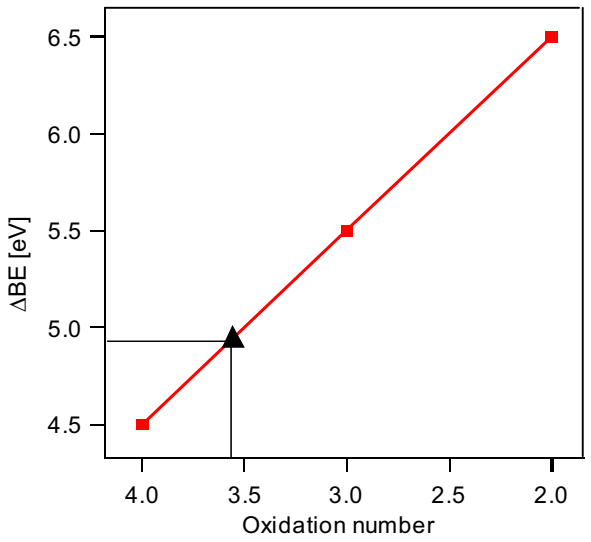

Fig.7.5 Oxidation number versus binding energy multiple splitting (ΔBE) of the Mn 3s lines

7.2 UPS data

In Fig.7.6 the UP spectra of $LiMn_2O_4$ are shown for the different photon energies of He I and He II. The increasing background at higher binding energies in the He I spectrum is due to inelastic losses and secondary electrons appearing in the He II spectrum only to a smaller amount because of the higher photon energy. The intensities of feature A and B seem to be smaller for He I than that for He II excitation. This indicates that features A and B are of Mn 3d character [40] due to the related changes in photoionisation cross section. In octahedral ligand sphere, the degenerate 3d orbitals of Mn^{3+} split into two energy levels, $t_{2g}(\pi)$ and $e_g(\sigma)$. Peak A can be attributed to the e_g and peak B to the t_{2g} level of the Mn 3d state, respectively [333]. The appearance of the e_g state indicates the high spin state of Mn^{3+} ions (see Fig.7.7). Feature C and D show similar intensities in both spectra, which suggest that they are mostly of O 2p character [40]. Feature C can be assigned to O 2p(π) and feature D to O 2p(σ), respectively (see Fig.7.7). Because of the interaction of the Mn 3d states of e_g and t_{2g} symmetry and O 2p state in solids with octahedrally coordinated transition metals, a set of

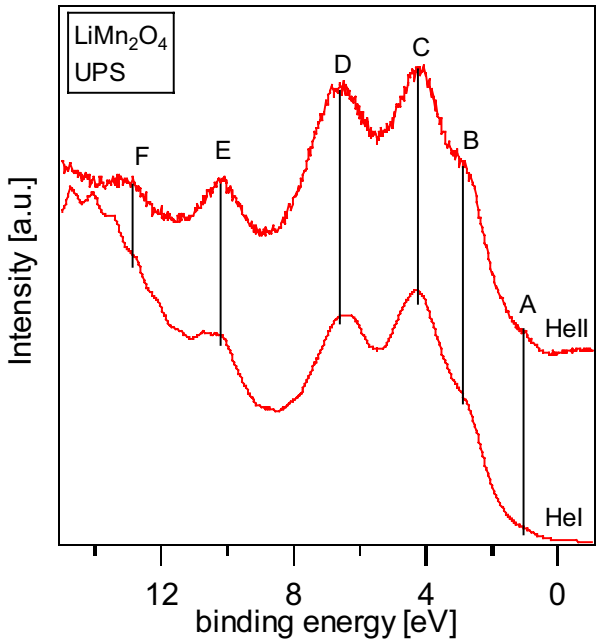

Fig.7.6 UP spectra (He I and He II) of $LiMn_2O_4$

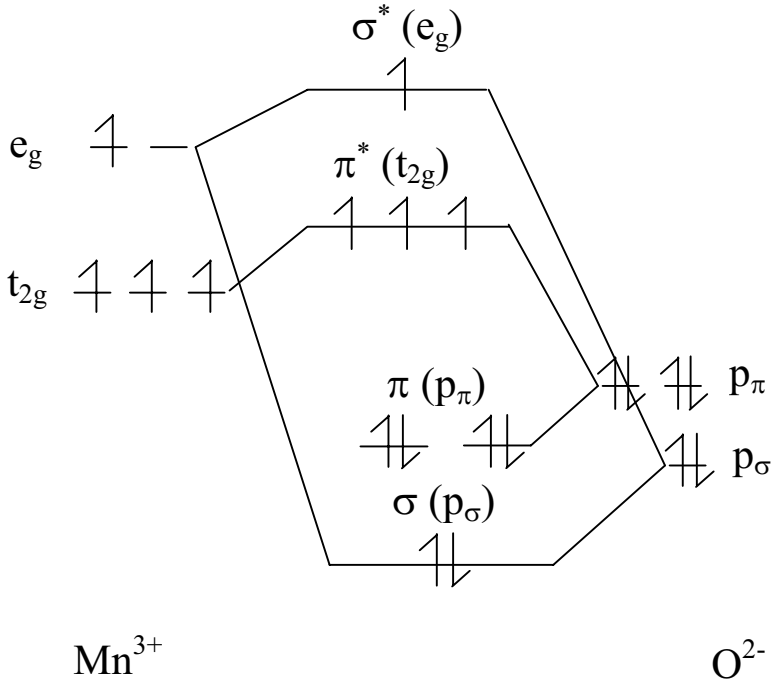

Fig.7.7 Valence band structure of $LiMn_2O_4$

bonding (e_g) and antibonding (e_g^*) bands will be formed. The antibonding bands (e_g^*) are mainly of Mn 3d character and the bonding bands (e_g) are primarily of oxygen 2p-like character. The t_{2g} orbital form mostly nonbonding bands. Therefore, the remaining valence electrons of the transition-metal in octahedral oxides will occupy the t_{2g} band and the e_g^* bands. The O 2p orbitals will form the π (p_π) and σ (p_σ) bands and will be completely filled

(see Fig.7.7). The origin of feature E near 9 eV and F near 13 eV has been debated for years. They were also found in $LiCoO_2$ [334]. Kemp and Cox interpreted these two feature due to the shake-up from the ligand band into empty states on Co. But for $LiMn_2O_4$, the origin of them are still unclear [40, 333, 335]. Because they are also found in Na and Li intercalated V_2O_5, when Na and Li peroxides are found on the surface, they can be also assigned to the O2p levels of the Li oxides. For the better understanding the origin of the electronic structure of $LiMn_2O_4$ also the resonant photoemission spectroscopy has been carried out.

7.3 RPES data

RPES has proven to be an efficient tool to study the electronic structure of solid state materials [143, 144]. Due to the resonance effect it is possible to investigate whether the spectral features given in the valence band spectra are related to Mn 3d or not. In this work, RPES has been used to assign the features A, B, C, D, E and F to their orbital origin. Fig.7.8 shows the RPES spectra of $LiMn_2O_4$ in the photon energy range from 40 to 80 eV covering the range for the 3p-3d transitions in Mn. The expected threshold energy for the Mn3p-3d resonance is about the Mn3p binding energy of 49 eV in $LiMn_2O_4$. In the UPS study we have assigned the feature A and B as the Mn3d e_g and t_{2g} states and feature C and D as the O2p π and σ orbital, respectively. The RPES data show the same results, as feature A and B increase in intensity with the photon energy from 48 to 54 eV due to the resonant enhancement of the Mn3d photoionization cross section. But it seems that the feature B show a stronger intensity enhancement than feature A. Due to the resonance effect the feature D becomes broader and therefore the gap between feature C and D becomes smaller. In contrast the feature C shows no intensity enhancement. Our RPES results confirm mostly the electronic structure which has been suggested from the UPS data. The feature A and B is mostly originated from the Mn3d state due to their intensities enhancement in the photon energy ranging from 48 to 54 eV. The larger enhancement of B is related to the smaller hybridization of the t_{2g} states with O2p states. The intensity of feature D shows more enhancement than feature C (see Fig.7.8(b)) indicating that feature D is stronger hybridized with Mn3d states than feature C (interaction of e_g states). Feature E and F do not show any (or show little) resonant effect, therefore they are probably due to the O2p states of lithium oxides.

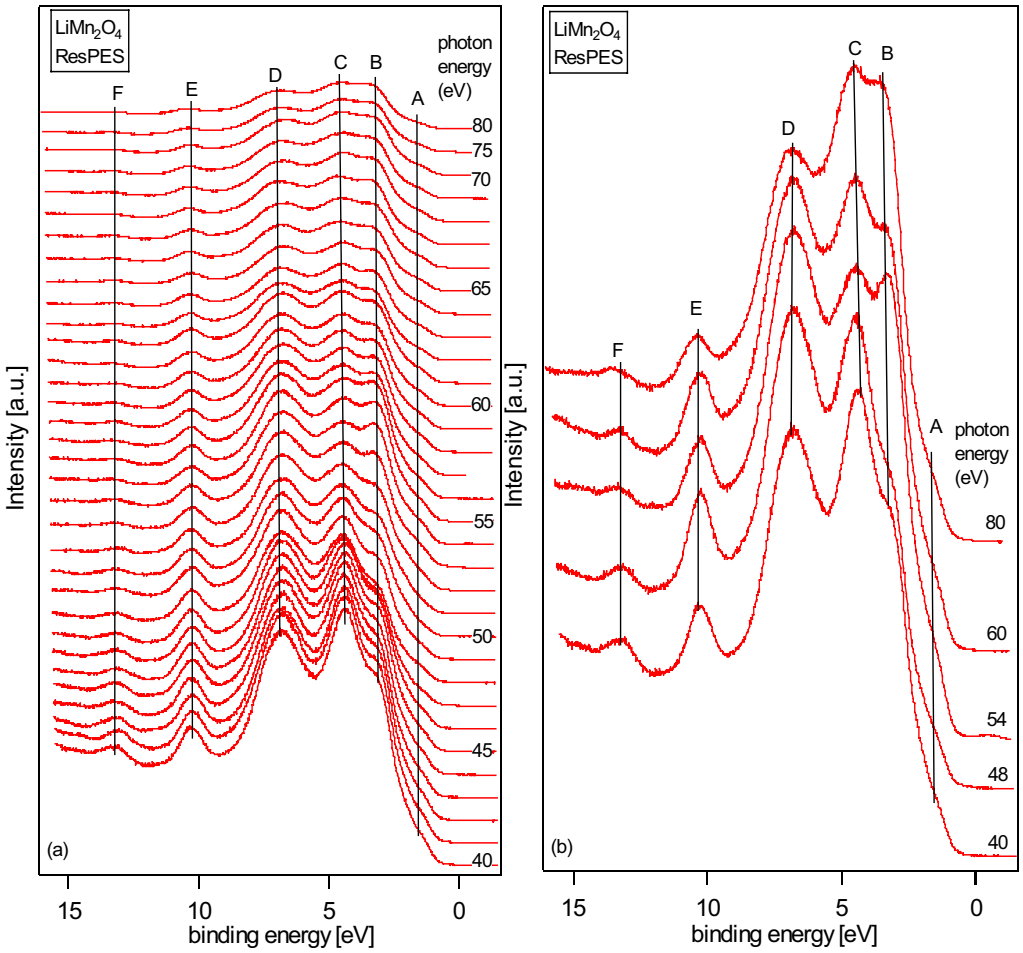

Fig.7.8 The RPES spectra of $LiMn_2O_4$ in the photon energy range from 40 to 80 eV

8 Summary and the suggestions

8.1 Summary of this work

In this work, V_2O_5 thin films are prepared by physical vapor deposition (PVD) at room temperature. XPS and UPS data demonstrate that as prepared V_2O_5 thin films are nearly stoichiometric, only about 4% of V^{4+} defects are found on the surface. AFM data indicates that the PVD grown V_2O_5 thin films on HOPG substrate are homogeneous and uniform. Compared with the substrate the average surface roughness of the V_2O_5 film over the 5×5 μm is found to be only about 1 nm. LEED patterns show that no ordered V_2O_5 thin films are grown with the given conditions in this work. RPES data and band structure calculations show that the valence band of V_2O_5 is formed by high hybridization of O2p and V3d states. The calculation suggests that the valence band consists of 80% O2p and 20% V3d states, respectively. The real charge distributions of O and V ions are determinated to be $V_2^{3+}O_5^{1,2-}$ from the PPES data. Therefore, the electron occupation of V ions in V_2O_5 leads to a "real oxidation state" of about +3 and the simple ionic model of bonding is not valid.

V_2O_5 thin films have been reduced by annealing inside the UHV chamber at temperatures up to 400°C with and without oxygen atmosphere. XPS measurements have shown that the films after heat treatment in vacuum are sub-stoichiometric due to the formation of oxygen vacancy, which have been proven by the decrease of the O1s / $V2p_{3/2}$ ratio. The crystal defect in the remaining thin film leads to the appearance of a new emission line at about 10.3 eV. The V ions are gradually reduced with the increase of temperatures as revealed from their BE shift to lower binding energies and the broadening of the full width at half maximum (FWHM). V^{4+} species are first formed at relatively low temperatures, the V^{4+} is reduced further to V^{3+} species when the temperature increases to 400°C. The V ions will be partially re-oxidized, when sub-stoichiometric V_2O_5 thin films are heated in O_2 with a partial pressure of 10^{-6} mbar. UPS data show that the re-oxidation of V ions occurs only on the topmost surface layers.

Na intercalation into V_2O_5 thin films have been studied in UHV. XPS data show that Na atoms intercalate into the V_2O_5 layers spontaneously after deposition with an amount of 10~20% remaining adsorbed on the surface. The intercalated Na strongly affects the electronic structure of V_2O_5 and causes the Fermi level to shift about of 1.2 eV. The XP spectra shown that V ions are partially reduced from V^{5+} to V^{4+} and even to V^{3+} due to Na intercalation. The adsorbed Na leads to a larger decrease of the work function due to the formation of surface dipole. The band structure calculations suggest that the valence band of

NaV_2O_5 consists of 71% O2p, 21% V3d and 8% Na3s states, respectively. Formally, a fraction of about 0.42 electron is transferred from Na3s to V ions as calculated from the photoelectron spectroscopic data. This is probably the first electron transfer value from the alkali metal to the transition metal obtained from experimental data. The limitation value of reversible intercalation of Na is indicated as $Na_{1.4}V_2O_5$. For higher Na deposition a decomposition reaction takes place with the formation of Na oxides and for even higher deposition time metallic Na is found on the surface. In this regime V ions are further reduced to V^{2+} and V^{1+} states. The work function is increased here because of depolarization effects and the formation of a metallic Na phase on the surface.

The intercalation of Li into V_2O_5 thin films have also been carried out. At low Li concentration most of the Li atoms are found to intercalate into the V_2O_5 layers and cause the reduction of V ions. The electron transfer per intercalated Li into the V3d states is about 0.55 as calculated from the photoelectron spectra. The limitation value of reversible intercalation of Li is $Li_{2.5}V_2O_5$. The shift of the Fermi level is about 0.6 eV. When the content of Li is higher, Li_2O and Li_2O_2 are formed on the surface and the intercalation reaction became irreversible, which was supported by the electrochemical experiments. When the highly intercalated samples were kept in the UHV chamber for few days, lithium deintercalates from the $Li_xV_2O_5$ ($x>2.5$) bulk and reacts with the vanadium oxide forming additional Li_2O_2 and Li_2O layers on the topmost surface.

Finally, the electronic structure and surface composition of powder $LiMn_2O_4$ have been studied. The XPS core level results show that manganese ions exist in two oxidation states: a trivalent state (Mn^{3+}) as well as a tetravalent state (Mn^{4+}). The photoemission intensity ration of Mn^{3+} to Mn^{4+} was about 0.9 as is calculated from the Mn core level emission lines. Thus the average oxidation state is 3.55 which is little higher than +3.5 due to small amounts of lithium oxides formed on the surface. UPS and RPES indicate that the Mn ions are in high spin configuration, and the O2p and Mn3d valence states are strongly hybridized.

This work demonstrates that photoelectron spectroscopy is well suited for studying the intercalation reaction process inside UHV and especially the electronic structure of transition metal oxides. The valence electrons provided by the alkali metal are found to mostly occupy V3d state associated with the host layers. As a consequence the Fermi level of the host shift during the intercalation reaction. In comparison of Li and Na it is found that Li is much easier to intercalate into V_2O_5 thin films than Na due to more favourable physical and chemical properties. Based on the PES data the theoretical voltage of alkali intercalation batteries can

principally be calculated by neglecting the contribution of binding energy. When the limitation values of intercalated alkali are reached, further deposition of alkali leads to a decomposition reaction and alkali oxides are formed on the surface. When the samples with high contents of alkali were kept in the UHV chamber, the decomposition reaction between alkali and host continues due to the instability of the host's crystal structure. This work has provided some new insights into the intercalation reaction based on investigation using surface science techniques in UHV. They are helpful to understand the mechanism and process of the intercalation reaction.

8.2 Suggestions for future work

Further studies are required to resolve the question of whether the in-situ intercalation induces stacking disorder via incomplete structural transitions. In particular, there is a need for studies which probe both crystallographic and electronic structure, which are strongly interrelated. Structural changes occurring upon intercalation may create various kinds of defects, which in turn may have a strong influence on both the alkali-metal adsorption on the surface and the diffusion into the bulk. This is why it is essential that the defect structure and its influence on the in-situ intercalation kinetics are to be investigated. X-ray absorption spectroscopy (XAS) which allows to characterize either the structural or electronic properties of a material is suggested to be uses to investigate the electronic structural change of oxygen and vanadium and the changes of the surrounding environments of oxygen and vanadium during alkali intercalation to further understand the charge transfer processes of intercalated alkali s orbital electrons.

An investigation of the change of the electronic structure of the host by PES during electrochemical intercalation and deintercalation of Li and Na would give further insights on the intercalation processes [336]. It is possible to calculate the electronic and ionic contributions (see detail in Chap.2.3) to the electronic structure and battery voltage. The physical properties of an intercalation material are to a great extent defined by the voltage versus composition relationship. By measuring the voltage as a function of the amount of intercalated ions and electrons, it is possible to obtain information about, e.g., structural phase transition [337], interactions between the intercalated ions and between the ions and the host [338], and also about the difference in energy between available sites for the ions to reside in [339]. These measurement, when combined with detailed analyses of structure and electronic structure will provide detailed experimental fact for a better understanding of the intercalation reaction.

References

1. B.C.H. Steele, Fast Ion Transport in Solids (ed. W. Van Gool), North-Holland, Amsterdam, (1973) 103-109.
2. M.B. Armand, Fast Ion Transport in Solids (ed. W. Van Gool), North-Holland, Amsterdam, (1973) 665-673.
3. D.W. Murphy, F.J. Disalvo, J.N. Carides, and J.V. Waszczak, Mat. Res. Bull **13** (1978) 1395.
4. M. Lazzari, and B. Scrosati, J. Electrochem. Soc. **127** (1980) 773.
5. J.-M. Tarascon, A.S. Gozdz, C. Schmutz, F. Shokoohi, and P.C: Warren, Solid State Ionics **86-88** (1996) 49.
6. L.A. Dominey, Current state of the art on lithium battery electrolytes Industrial Chemistry Library (ed. G. Pistoia), Vol.5 (1994) 137-165.
7. M. Armand, Solid State Ionics **69** (1994) 309.
8. F. Croce, G.B. Appetecchi, L. Persi, and B. Scrosati, Nature **394** (1998) 456.
9. M.M. Thacheray, W.I.F. David, P.G. Bruce, and J.B. Goodenough, Mat. Res. Bull. **18** (1983) 461.
10. T. Shodai, S. Okada, S. Tobidhima, and I. Yamabi, Solid State Ionics **86-88** (1996) 785.
11. J.-M. Tarascon, and M. Armand, Nature **414** (2001) 359.
12. D. Guyomard, New Trends in Electrochemical Technology: Enery Storage Systems for Electronics (eds. T. Osaka, and M. Datta), Gordon & Breach Science Publishers, Vol. 9 (2000) 253-350.
13. J.R. Dahn, U.von Sacken, M.W. Juzkow, and H. Al-Hanady, J. Electrochem. Soc. **138** (1991) 2207.
14. Y. Gao, M.V. Yakovleva, and W.B. Ebner, Electrochem. Solid State Lett. **1** (1998) 117.
15. A.R. Armstrong, and P.G. Bruce, Nature **381** (1996) 499.
16. C.G. Granquist, Handbook of Inorganic Electrochromic Materials, Elsevier Science, Amsterdam, (1995).
17. C. Delmas, S. Brethes, and M. Menetrier, CR Acad. Sci. **310** (1990) 1425.
18. D.B. Le, J. Electrochem. Soc. **143** (1996) 2099.
19. W. Dong, D.R. Rolison, and B. Dunn, Electrochem. Solid State Lett. **3** (2000) 457.
20. J.L. Souquet, and M. Duclot, Solid State Ionics **148** (2002) 375.
21. J.B. Bates, N.J. Dudney, B. Neudecker, A: Ueda, C.D. Evans, Solid State Ionics **135** (2000) 33.

22. C. Julien, Mater. Sci. Eng. B **6** (1990) 9.
23. J.B. Bates, N.J. Dudney, B. Neudecker, A. Uedu, C.D. Evans, Solid State Ionics **135** (2000) 33.
24. Lithium Batteries(ed. J.P. Gabano), Academic Press, (1983).
25. Lithium Battery Technology (ed. H.V. Venkatasetty), Wiley, (1984).
26. Lithium Batteries: New Materials Developments and perspectives (ed. G. Pistoia), Elsevier, (1995).
27. P. Poizot, S. Laruelle, S. Grugeon, L. Dupont, and J-M. Tarascon, Nature **407** (2000) 496.
28. Lithium Batteries: New Materials Developments and Perspectives (ed. G. Pistoia), Elsevier, Amsterdam, (1994).
29. D.G. Wickham, and W.J. Croft, J. Phys. Chem. Solids **7** (1958) 351.
30. H. Gerischer, F. Decker, and B. Bcrosati, J. Electrochem. Soc. **141** (1994) 2297.
31. J.R. Dahn, and W.R. Mckinnon, J. Phys. Chem. **17** (1984) 4231.
32. O. Tillement, and M. Quarton, J. Electrochem. Soc. **140** (1993) 1870.
33. S.T. Coleman, W.R. McKinnon, and J.R. Dahn, Phys. Rev. B **29** (1984) 4147.
34. R. Osorio, and L.M. Falicov, J. Chem. Phys. **77** (1982) 6218.
35. L.S. Selwyn, W.R. McKinnon, J.R. Dahen, and Y.L. Page, Phys. Rev. B **33** (1986) 6405.
36. S. Devautour, J. Vanderschueren, J.C. Giuntini, F. Henn, J.V. Zanchetta, and J. Ginoux, J. Phys. Chem. B **102** (1998) 3749.
37. S. Devautour, J.C. Giuntini, F. Henn, J.M. Douillard, J.V. Zanchetta, and J. Vanderschueren, J. Phys. Chem. B **103** (1999) 3275.
38. J.R. Dahn, J.N. Reimers, A.K. Slergh, and T. Tiedje, Phys. Rev. B **45** (1992) 3773.
39. J. Molenda, T. Bak, and J. Marzec, Phys. Stat. Sol. A **156** (1996) 159.
40. Y. Gao, K. Myrtle, M. Zhang, J.N. Reimers, and J.R. Dahn, Phys. Rev. B **54** (1996) 16670.
41. M.N. Obrovac, Y. Gao, and J.R. Dahn, Phys. Rev. B **57** (1998) 5728.
42. W.R. McKinnon, and L.S. Selwyn, Phys. Rev. B **35** (1987) 7275.
43. C. Wolverton, and A. Zunger, Phys. Rev. Lett. **81** (1998) 606.
44. M.K. Aydinol, A.F. Kohan, G. Ceder, K. Cho, and J. Joannopoulos, Phys. Rev. B **56** (1997) 1354.
45. T. Nagaura, and K. Tozawa, Prog. Batt. Solar Cell. **9** (1990) 209.

46. T. Yamahira, H. Kato, and M. Anzai, SONY Corp. (JP), European Patent EP0391281 (1990).
47. P.G. Bruce, J. Chem. Soc. Chem. Commun. **19** (1997) 1817.
48. S.-T. Myung, S. Komaba, and N. Kumagai, J. Electrochem. Soc. **148** (2001) A482.
49. Y.S. Lee, N. Kumadu, M. Yoshio, J. Power Sources **96** (2001) 376.
50. G. Kumar, H. Schlor, and D. Rahner, Materials Chem. and Phys. **70** (2001) 117.
51. M. Baba, N. Kumagai, H. Kobayashi, O. Nakano, and K. Nishidate, Electrochemical and Solid State Letter **2** (1999) 320.
52. C. Julien, E. Haro-Poniatowski, M.A. Camacho-Lopez, L. Escobar-Alarcón, and J. Jiménez-Jarquin, Materials Science and Engineering B **72** (2000) 36.
53. Transition metal oxides (ed. P.A. Cox), Oxford University Press, (1995).
54. V.E. Henrich, P.A. Cox, The Surface Science of Metal Oxides, Cambridge University Press, New York, (1994).
55. C. Delmas, J.-J. Bracconier, C. Fouassier, and P. Hagenmuller, Rev. Chim. Minter **19** (1982) 343.
56. M.M. Thackeray, M.H. Rossouw, A. de Kock, A.P. de la harpe, R.J. Gummow, K. Pearce, and D.C. Liles, J. Power Sources **43-44** (1993) 289.
57. M.M. Thackeray, Prog. Solid State Chem. **25** (1997) 1.
58. M.M. Thackeray, Prog. In Batt. And Batt. Mat. **14** (1995)1.
59. T. Ohzuku, M. Kitagawa, and T. Hirai, J. Electrochem. Soc. **137** (1990) 769.
60. J.B. Goodenough, M.M. Thackeray, W.I.F. David, and P.G. Bruce, Rev, de Chim. Min. **21** (1984) 435.
61. L. Michailovits, I. Hevesi, L. Phan, Z. Varga, Thin Solid Films **102** (1983) 71.
62. J. Ballot, P. Cordier, P. Gallais, M. Gauthier, F. Babonnean, J. Non-Cryst. Solids **68** (1984) 135.
63. E.E. Chain, Appl. Opt. **30** (1991) 2782.
64. E.J. Jeon, Y.W. Shin, S.C. Nam, W.I. Cho, and Y.S. Yoon, J. Electrochem. Soc. **148** (2001) A318.
65. J.S. Braithwaite, C.R.A. Catlow, J.D. Gale, and J.H. Harding, Chem. Mater. **11** (1999) 1990.
66. D.W. Murphy, P.A. Christian, F.J. Disalvo, J.V. Waszczak, Inorg. Chem. **18** (1979) 2800.
67. I. Loa, A. Grzechnik, U. Schwarz, K. Syassen, M. Hanfland, P. K. Kremer, J. Alloys and Compounds **317-318** (2001) 103.

68. V. Shklover, T. Haibach, F. Ried, R. Nesper, P. Novak, J. Solid State Chem. **123** (1996) 317.
69. J.S. Braithwaite, C.R.A. Catlow, J.D. Gale, J.H. Harding, Chem. Mater. **11** (1999) 1990.
70. A.N. Day, B.P. Sullivan, U.S. Pat., 3655585, (1972).
116
71. K. West, B. Zachau-Christiansen, T. Jacobsen, S. Shaarup, Solid State Ionics **76** (1995) 15.
72. J.J. Galy, Solid State Chem. **100** (1992) 229.
73. H.G. von Schnering, Yu. Grin, M. Somer, P.K. Keremer, O. Jepsen, T. Chatterji, and Weiden, Z. Kristallogr. **213** (1998) 246.
74. H. Nakao, K. Ohwada, N. Takesue, Y. Fujii, M. Isobe, Y. Ueda, J. Phys. and Chem. of Solid **60** (1999) 1101.
75. K. Waltersson, and B. Forslund, Acta Crystallogr. Sect. B: Struct. Crystallogr. Cryst. Chem. **33** (1977) 789.
76. I. Loa, U. Schwarz, M. Haufland, R.K. Kremer, and K. Syassen, Phys. Stat. Sol.(b) **215** (1999) 709.
77. H.A. Jahn, and E. Teller, Proc. R. Soc. London: Ser. A **161** (1937) 220.
78. M.D. Sturge, Solid State Physics (ed. by F. Seitz, D. Turnbull, and H. Ehrenreich), Academic Press, New York, Vol. 20 (1994) 91-211.
79. J.H. Van Vleck, J. Chem. Phys. **7** (1939) 72.
80. I.B. Beruker, Electronic Structure and Properties of Transition Metal Compounds Wiley, New York, (1996).
81. M.P. Kaplan, and B.G. Vekhte, Cooperative Phenomena in Jahn-Teller Crystal, Pienum, New York, (1995).
82. F.A. Cotton, Chemical appocations of group theory (3rd edn), Wiley, New York, (1990).
83. R.G. Burns, Mineralogical applications of crystal field theory, Cambridge University Press, (1970).
84. J.K. Burdett, Molecular Shapes, Wiley, New York, (1980).
85. U. Kleinekathofer, K.T. Tang, J.P. Toennies, and C.L. Yiu, J. Chem. Phys. **111 (8)** (1999) 3377.
86. J.N. Murrell, S.F.A. Kettle, and J.M. Tedder, the Chemical Bond, Wiley, Chichester, (1978).
87. R. WcWeeny, Coulson's Valence (3rd edn.), Oxford University Press, (1979).
88. J.P. Dahl, and C.J. Ballhausen, Adv. Quantum Chem. **4** (1968) 170.
89. C.A. Marianetti, D. Morgan, and G. Ceder, Phys. Rev. B **63** (2001) 224304.

90. F.M.F. de Groot, M. Abbate, J. Van Elp, G.A. Sawatzky, Y.J. Ma, C.T. Chen, F. Sette, J. Phys. : Cond. Matter **5** (1993) 2277.
91. J. van Elp, J.L. Wieland, H. Eskes, P. Kuiper, G.A. Sawatzky, F.M.F. de Groot, and T.S. Turner, Phys. Rev. B **44** (1991) 6090.
92. M. Abbate, F.M.F. de Groot, J.C. Fuggle, A. Fujimori, Y. Tokura, Y. Fujishima, O. Strebel, M. Domke, G. Kaindl, J. van Elp, B.T. Thole, G.A. Sawatzky, M. Sacchi, and N. Tsuda, Phys. Rev. B **44** (1991) 5419.
93. L.A. Montorn, M. Abbate, E.C. Almeida, J.M. Rosolen, Chem. Phys. Letter **309** (1999) 14.
94. E. Zhecheva, and R. Stoyanova, Solid State Ionics **66** (1993) 143.
95. Y. Gao, K. Myrtle, Meijie Zhang, J.N. Reimers, J.K. Dahn, Phys. Rev. B **54** (1996) 16670.
96. M.M. Thackeray, J. Electrochem. Soc. **142** (1995) 2558.
97. G. Ceder, Y.-M. Chiang, D.R. Sadoway, M.K. Aydinol, Y.-I. Jang, B. Huang, Nature **392** (1998) 694.
98. K. Hermann, M. Witko, R. Oruzinic, A. Chakrabarti, B. Tepper, M. Elsner, A. Gorschluter, H. Kuhlenbeck, and H.J. Freund, J. Electron Spectroscopy and Related Phenomena **98-99** (1999) 245.
99. A. Herold, Chemical Physics of Intercalation (ed. A.P. Cegrand and S. Flandrois), Plenum Press, New York, Vol. B (1987) 172.
100. M.E. Arroyoy de Dompablo, C. Marianetti, A. Van der Ven, and G. Ceder, Phys. Rev. B **63** (2001) 144107.
101. R.H. Friend, and A.D. Yoffe, Adv. Phys. **36** (1987) 1.
102. J.V. Acrivos, and J. Salem, Philos. Mag. **30** (1973) 603.
103. Dino Tonti, Ph.D Dissertation, Berlin, August (2000).
104. D.J. Sellmyer, Solid State Physics (ed. H. Ehrenreich, F. Seitz, and D. Turnbull), Academic Press, New York, Vol. 3.3 (1978).
105. C. Umrigar, D.E. Ellis, D. Wang, H. Krakauer, and M. Posternak, Phys. Rev. B **26** (1982) 4935.
106. W.R. Mckinnon, and R.R. Haering, Modern Aspect of Electrochemistry (ed. R.E. White, J.O.M. Bockris, and B.E. Conway), Plenum Press, New York, Vol. 15 (1983).
107. W.R. Mckinnon, Chemical Physics of Intercalation (Ed. A.P. Legrand, and S. Flandrois), Plenum Press, New York, (1987).

108. M.K. Aydinol, A.F. Kohan, G. Ceder, K. Cho, and J. Joannopoulos, Phys. Rev. B **56** (1997) 1354.
109. M.S. Whittingham, Prog. Solid State Chem. **12** (1978) 41.
110. B.G. Silbernagel, and M.S. Whittingham, J. Chem. Phys. **64** (1976) 3670.
111. M. Carewska, S. Scaccia, F. Croce, S. Arumugam, Y. Yang, S. Greenbaum, Solid State Ionics **93** (1997) 227.
112. R.J. Gummow, A. de Kock, and M.M. Thackeray, Solid State Ionics **69** (1994) 59.
113. W.I.F. David, M.M. Thackeray, L.A. de Dicciotto, and J.B. Goodenough, J. Solid State Chem. **67** (1987) 316.
114. Physics and Chemistry of Alkali Metal Adorption, Material Science Monographs (ed. H.P. Bonzel, A.M. Bradshaw, and G. ertl), Elsevier, Amsterdam, Vol. 57 (1989).
115. T. Aruga, and Murata, Progr. Surf. Sci. **31** (1989) 61.
116. H.I. Starnberg, and H.P. Hughes, J. Phys. Chem. **20** (1987) 4429.
117. F.S. Ohuchi, W. Jaegermann, C. Petteenkofer, and B.A. Parkinson, Langmuir **5** (1989) 439.
118. H.H. Weitering, and T. Hibma, J. Phys.: Condens. Matter **3** (1991) 8535.
119. M. Bronold, C. Pettenkofer, and W. Jaegermann, Appl. Phys. A. **52** (1991) 171.
120. H.E. Brauer, H.I. Starnberg, L.J. Holleboon, V.N. Strocov, and H.P. Hugher, Phys. Rev. B **58** (1998) 10031.
121. W. Jaegermann, C. Pettenkofer, A. Schellenberger, C.A. Papageorgopoulos, and M. Kamarators, Chem. Phys. Letters **221** (1994) 441.
122. J.J. Pireaus, R. Sporken, Analysis of Microelectronic Materials and Devices (ed. M. Grasserbauer, H.W. Werner), John Wiley, New York, (1991) p.111.
123. Practical Surface Analysis-Vol.1-Auger and X-ray Photoelectron Spectroscopy (ed. D. Briggs, and M.P. Seah), John Wiley&Sons, Chichester, (1990).
124. Low energy electron and surface chemistry (ed. G. Ertl, and J. Küppers), VCH, Weinheim, (1985).
125. Photoelectron Spectroscopy (Second Edition) (ed. M. Cardona), Springer, (1995).
126. D.P. Woodruff, Modern Techniques of Surface Science (Second Edition) (ed. T.A. Delchar), Cambridge Solid State Science Series, (1994).
127. T.A. Carlson, Photoelectron-Auger Electron Spectroscopy, Plenum, New York, (1975).
128. H. Hertz, Ann. Physik **31** (1887) 983.
129. A. Einstein, Ann. Physik, **17** (1905) 132.

130. C.D. Wagner, W.M. Riggs, L.E. Davis, and J.F. Moulder, Hand Book of X-Ray Photoelectron Spectroscopy, Derkin elemer corporation, Eden Prairie, (1979).
131. D.A. Shirley, Phys. Rev. B **5** (1972) 4709.
132. P.M.A. Sherwood, Practical Surface Analysis (ed. D. Briggs and M.P. Seah), John Wiley & Sons, Chivhester, (1983).
133. Wavemetrics, heep://www.wavemetrics.com/.
134. C.S. Fadley, R.J. Baird, W. Siekhaus, T. Novakov, S.A.L. Bergstron, J. Electro spectrosc. Relat. Phenom. **4** (1974) 93.
135. J.W. Cooper, S.T. Manson, Phys. Rev. **177** (1969) 157.
136. C.D. Wagner, L.E. Davis, M.V. Zeller, J.A. Taylor, R.H. Raymond, C.H. Gale, Surf. Interface Anal. **3** (1981) 211.
137. P. Jiricek, Czech. J. Phys. **44** (1994) 261.
138. B. Lesiak, A. Jablonski, J. Zemek, M. Trchora, J. Stejskal, Langmuir **16** (2000) 1415.
139. A. Jablonski, B. Lesiak, L. Zommer, M.F. Ebel, Y. Fukuda, Y. Suzuki, S. Tougaard, Surf. Interface. Anal. **21** (1994) 724.
140. A. Jablonski, C.J. Powell, J. Vac. Sci. Technol. A **15** (1997) 2095.
141. I. Kojima, and M. Kurahashi, J. Electr. Spectr. Rel. Rhen. **42** (1987) 177.
142. C. Guillot, Y. Ballu, J. Paigne, J. Lecante, K.P. Jain, P. Thiry, R. Pinchaux, Y. Petroff, and L.M. Falicov, Phys. Rev. Lett. **39** 1632 (1977).
143. B.W. Veal, D.J. Lam, W.T. Carnall, and H.R. Hoekstra, Phys. Rev. B **12** (1975) 5651.
144. S.M. Butorin, D.C. Mancini, J.-H. Guo, N. Wassdahl, J. Nordgren, M. Nakazyva, S. Tanaka, T. Uozumi, A. Kotani, Y. Ma, K.E. Myano, B.A. Karlin, and D.K. Shuh, Phys. Rew. Letters **77** (1996) 574.
145. J. Okabayashi, A. Kimura, T. Mizokawa, A. Fujimori, T. Hayashi, M. Tanaka, Physical Review B **59** (1999) R2486.
146. L.C. Davis, and L.A. Feldamp, Physical Review B **23** (1981) 6239.
147. L.C. Davis, Physical Review B **25** (1982) 2912.
148. G. Binnig, C. Quate, and C. Gerber, Phys. Rev. Lett. **56** (1986) 930.
149. A. Talledo, C.G. Granqvist, J. Appl. Phys. **77** (1995) 4655.
150. D.W. Murphy, P.A. Christian, F.J. Disalvo, J.N. Carides, J. Electrochem. Soc. **126** (1979) 497.
151. W. Lambrecht, B. Djafari-Rouhani, M. Lannoo, and J. Vennik, J. Phys. C: Solid State Phys. **13** (1980) 2485.

152. W. Lambrecht, B. Djafari-Rouhani, M. Lannoo, P. Clauws, L. Fiermans, and J. Vennik, J. Phys. C: Solid State Phys. **13** (1980) 2503.
153. G.A. Sawatzky, and D. Post, Phys. Rev. B **20** (1979) 1546.
154. E.A. Meulenkamp, W. van Klinken, and A.R. Schlatmann, Solid State Ionics **126** (1999) 235.
155. C. Sanchez, J. Livage, J.P. Audiere, and A. Madi, J. Non-Cryst. Solids **65** (1984) 285.
156. C.V. Ramana, B.S. Naidu, O.M. Hussain, and R. Pinto, J. Phys. D-Applied Phys. **34(7)** (2001) L35-38.
157. X.L. Yin, A. Fahmi, A. Endou, R. Miura, I. Gunji, R. Yamauchi, M. Kubo, A. Chatterjee, and A. Miyamoto, Applied Surf. Sci. **132** (1998) 539.
158. L. Michailvoits, I. Hevesi, L. Phan, and Zs. Varga, Thin Solid Films **102** (1983) 71.
159. O. Ajaya, A.A. Anani, and A.O. Ababuchi, Thin Solid Films **82** (1981) 151.
160. R.L. Ramke, R.M. Walser, and R.W. Bane, Thin Solid Films **97** (1982) 129.
161. E.E. Chain, J. Vac. Sci. Technol. A **5** (1987) 1836.
162. D. Wruck, S. Ramamurthy, and M. Rubin, Thin Solid Films **182** (1991) 79.
163. A. Talledo, A.M. Anderson, and C.G. Granqvist, J. Mater. Res. **5** (1990)1253.
164. C.R. Aita, J.L. Liou, C.K. Kwok, R.C. Lee, and E. Kolawa, Thin Solid Films **193-194** (1990) 18.
165. Y. Fujita, K. Miyazaki, and T. Tatsuyama, Jpn. J. Appl. Phys. **24** (1985) 1082.
166. S.F. Cogan, N.M. Nguyen, S.T. Perrotti, and R.D. Rauph, Proc. Soc. Photo-Opt. Instrum. Eng. **57-62** (1988) 1016.
167. L. Fiermans, P. Clauws, W. Lambrecht, L. Vandeabroucke, and J. Vennik, Phys. Status Solidi A **59** (1980) 485.
168. Y. Shimizu, K. Nagase, N. Miura, and N. Yamazoe, Jpn. J. Appl. Phys. **29** (1990) L1708.
169. E. Cazzanelli, G. Mariotto, F. Passerini, and F. Decher, Solid State Ionics **70-71** (1994) 412.
170. F. Coustier, S. Padderini, and W.H. Smyrl, J. Electrochem. Soc. **145** (1998) L73.
171. D.W. Murphy, and P.A. Christian, Science **205** (1979) 651.
172. J.-C. Zhang, J.M. McGraw, J. Turner, and D. Ginley, J. Electrochem. Soc. **144** (1997) 1630.
173. K. West, B. Zachau-Christiansen, S.V. Skaarup, and F.W. Poulsen, Solid State Ionics **57** (1992) 41.

174. J.B. Bates, G.R. Gruyalski, N.J. Dudney, C.F. Luck, X.H. Yu, and S.D. Jones, Solid State Technol. **7** (1993) 59.
175. N. Ozer, Thin Solid Films **305** (1997) 80.
176. A. Lourenco, A. Gorenstein, S. Passerini, W.H. Smyrl, M.C.A. Fantini, and M.H. Tabacniks, J. Electrochem. Soc. **145** (1998) 706.
177. J. Cui, D. Da, and W. Jiang, Appl. Surf. Sci. **133** (1998) 225.
178. X.J. Wang, H.D. Li, Y.J. Fei, X. Wang, Y.Y. Xiong, Y.X. Nie, and K.A. Feng, Appl. Surf. Sci. **177** (2001) 8.
179. G.J. Fang, Z.L. Liu, Y. Wang, Y.H. Liu, and K.L. Yao, J. Vac. Sci. Technol. A **19** (2001) 887.
180. H. Watanabe, K.-I. Itoh, O. Matsumoto, Thin Solid Films **386** (2001) 281.
181. R.F. Bunshah, Deposition Technologies for Films and Coatings (ed. R.F. Bunshah) Noyes, New Jersey, (1982) p.5.
182. M. Witko, K. Hermann, and R. Tokarz, Catal. Today **50** (1999) 553.
183. E. Antonides, E.C. Janse, and G.A. Sawatzky, Phys. Rev. B **15** (1977) 4596.
184. M. Sanchez-Agudo, L. Soriano, J.F. Trigo, C. Quiros, G.G. Fuentes, C. Morant, E. Elizalde, and J.M. Sanz, Surf. and Interface Anal. **34** (2002) 244.
185. T. Higuchi, T.Tsukamoto, S. Yamaguchi, Y. Tezuka, and S. Shin, Jpn. J. Appl. Phys. **141** (2002) 2090.
186. H. Sato, A. Tanaka, A. Furuta, S. Senba, H. Okuda, K. Mimura, M. Nakatake, Y. Ueda, M. Taniguchi, and T. Jo, J. Phys. Soc. Jpn. **68** (1999) 2132.
187. V.M. Cherkashenko, E.Z. Kurmaev, A.A. Fotiev, and V.L. Volko, Sov. Phys. Solid State. **17** (1975) 167.
188. R.G. Egdell, M.R. Harrison, M.D. Hill, L. Porte, and G. Wall, J. Phys. C: Solid State Phys. **17** (1984) 2889.
189. Porsonal communication of Prof. P.C. Schmidt, Physical Chem., TU-Darmstadt.
190. E.Z. Kurmaev, V.M. Cherkashenko, Yu.M. Yarmoshenko, St. Bartkowski, A.V. Postnikov, M. Neumann, L.-C. Duda, J.H. Guo, J. Nordgren, V.A. Perelyaev, and W. Reichelt, J Phys-Condens Matt. **10** (1998) 4081.
191. R. Heise, Ph.D thesis, Duisburg, Germany, (1995).
192. R. Heise, R. Courths, and S. Witzel, Solid State Comm. **84** (1992) 599.
193. J.J. Yeh, and I. Lindau, At. Data Nucl. Data Tables. **32** (1985) 28.
194. K. Devriendt, H. Poelman, and L. Fiermans, Surf. Sci. **433-435** (1999) 734.
195. L. Fiermans, and J. Vennik, Surf. Sci. **9** (1968) 187.

196. J. Haber, M. Witko, and R. Tokarz, Applied Catalysis A-Gereral **157** (1997) 3.
197. R.J.D. Tilley, and B.G. Hyde, J. Phys. Chem. Solid **31** (1970) 1613.
198. E. Gillis, Compte Rend. Acad. Sci. Paris **258** (1964) 4765.
199. H.J. Fan, and L.D. Mark, Ultramicroscopy **31** (1989) 357.
200. D.S. Su, M. Wieske, E. Beckmann, A. Blume, G. Mestl, and R. Schlogl, Catal. Lett. **75** (2001) 81.
201. M. Heber, and W. Grunert, J. Phys. Chem. B **104** (2000) 5288.
202. Vanadiumoxide (ed. W. Bruckner), Akademic Verlag, (1983).
203. W. Klemm, and P. Pirschner, Optik **3** (1948) 75.
204. B. Belbeoch, R. Kleinberger, and M. Roulliay, J. Phys. Chem. Sol. **39** (1978) 1007.
205. K.-A. Wilhelmi, J. Waltersson, and L. Kihlborg, Acta Chem. Scand. **25** (1971) 2675.
206. G.A. Sawatzky and D. Post, Phys. Rev. B **20** (1979) 1546.
207. C.V. Ramana, O.M. Hussain, B. Srinivasulu Naidu, and P.J. Reddy, Thin Solid Films **305** (1997) 219.
208. D.W. Bullett, Solid State Phys. **35** (1980) 129.
209. D.W. Bullett, J. Phys. C: Solid State Phys. **13** (1980) L595.
210. J. Connor, M. Considine, H. Hiller, and D. Briggs, J. Electron Spectrosc. Relat. Phenom. **12** (1977) 143.
211. K. Hermann, M. Witko, R. Druzinic, A. Chakrabarti, B. Tepper, M. Elsner, A. Gorschlüter, H. Kuhlenbeck, and H.-J. Freund, J. Electron Spectrosc. Relat. Phenom. **98-99** (1999) 245.
212. M. Heber, and W. Grünert, J. Phys. Chem. B **104** (2000) 5288.
213. M. Heber, and W. Grünert, Topics in Catalysis **15** (2001) 3.
214. K. Kosuge, J. Phys. Chem. Solids **28** (1967)1613.
215. G. Grymonprez, L. Fiermans, and J. Vennik, Acta Crystallogr. A **33** (1977) 383.
216. L. Fiermans, and J. Vennik, Surf. Sci. **9** (1968) 187.
217. K. Devriendt, H. Poelman, and L. Fiermans, Surf. Sci. **433-435** (1999) 734.
218. D.S. Su, and R. Schlogl, Catalysis Letters **83** (2002) 115.
219. G.H. Vurens, M. Salmeron and G.A. Somorjai, Progr. Surf. Sci. **32** (1989) 333.
220. R.A. Groschke, K. Vey, M. Mayer, U. Walter, E. Goering, M. Klemm, and S. Horn, Surf. Sci. **348** (1996) 505.
221. K. Devriendt, H. Poelman, L. Fiermans, G. Creten, and G.F. Froment, Surf. Sci. **352-354** (1996) 750.

222. M.N. Popova, A.B. Sushkov, E.P. Chukalina, E.A. Romanov, M. Isobe, Y. Ueda Phys. of The Solid State **44** (2002) 1450.
223. A. Hubsch, C. Waidacher, K.W. Becker, and W. von der Linden, Physica B **312** (2002) 626.
224. A. Bernert, T. Chatterji, P. Thalmeier, and P. Fulde, J. Euro. Phys. B **21** (2001) 535.
225. P. Liu, J.-G. Zhang, J. A. Turner, C. E. Tracy, D. K. Benson, R. N. Bhattacharya, Solid State Ionics **111** (1998) 145.
226. H.-K. Park, W.H. Smyrl, J. Electrochem. Soc. **142** (1995) 1068.
227. F. Ohuchi, W. Jaegermann, C. Pettenkofer, and B.A. Parkinson, Langmuir **5** (1989) 439.
228. A. Schellenberger, R. Schlaf, C. Pettenkofer, and W. Jaegermann, Phys. Rev. B **45** (1992) 3538.
229. H. Starnberg, H. Bauer, I. Holleboom, and H. Hughes, Phys. Rev. Lett. **70** (1993) 3111.
230. C. Pettenkofer, and W. Jaegermann, Phys. Rev. B **50** (1994) 8816.
231. R. Baddour, J. P. Pereira-Famos, R. Messina, and J. Perichon, J. Electroanal. Chem. **314** (1991) 81.
232. K. West, B. Zachauchristiansen, T. Jacobsen, and S. Skaarup, Electrochim. Acta **38** (1993) 1215.
233. H.K. Park, and W. H. Smyrl. J. Electrochem. Soc. **141** (1994) 25.
234. A.L. Tipton, S. Passerini, B.B. Owens, and W.H. Smyrl, J. Electrochem. Soc. **143** (1996) 3473.
235. E.C. Almeida, M. Abbate, and J.M. Rosolen, Solid State Ionics **140** (2001) 241.
236. A. Chakrabarti, K. Hermann. R. Druzinic, M. Witko, F. Wagner, and M. Petersen, Phys. Rev. B **59** (1999) 10583.
237. Z.S.E. Mandouh, and M.S. Selim, Thin Solid Films **371** (2000) 259.
238. B.K. Chakraverty, M.J. Sienko, and J. Bonnerot, Phys. Rev. B **17** (1978) 3781.
239. M. Lohmann, H. von Nidda, M.V. Eremin, A. Loidl, G. Obermeier, and S. Horn, Phys. Rev. Lett. **85** (2000) 1742.
240. S.G. Bompadre, A.F. Hebard, V.N. Kotov, D. Hall, G. Maris, J. Baas, and T.T.M. Palstra, Phys. Rev. B **61** (2000) 13321.
241. M.H. Whangho, H.J. Koo, and K.S. Lee, Solid State Commun. **114** (2000) 27.
242. T. Ohama, H. Yasuoka, M. Isobe, and Y. Ueda, Phys. Rev. B **59** (1999) 3299.
243. Z.V. Popovic, M.J. Konstantinovic, R. Gajic, V. Popov, Y.S. Raptis, A.N. Vasilev, M. Isobe, and Y. Uda, J. Phys.: Condensed Matter **10** (1998) L513.

244. M. Isobe, Y. Ueda, J. Phys. Soc. Jpn. **65** (1996) 1178.
245. Y. Fujii, H. Nakao, T. Yosihama, M. Nishi, K. Nakajima, K. Kakurai, Y.U. Masahiko Isobe, and H. Sawa, J. Phys. Soc. Jpn. **66** (1997) 326.
246. T. Chatterji, K.D. Liß, G.J. McIntyre, M. Weiden, R. Hauptmann, and C. Geibel, Solid State Commun. **108** (1998) 23.
247. A.F. Carley, S.D. Jackson, M.W. Roberts, J. O'Shea, Surf. Sci. **454-456** (2000) 141.
248. K. Kobayashi, T. Mizokawa, A. Fujimori, M. Isobe, and Y. Ueda, Phys. Rev. Lett. **80** (1998) 3121.
249. K.D. Tsuei, E.W. Plummer, A. Liebsch, K. Kempa, B. Bakshi, Phys. Rev. Lett. **64** (1990) 44.
250. T. Takahashi, and H. Nagasawa, Solid State Commun. **39** (1981) 1125.
251. M. Onoda, and H. Nagasawa, J. Phys. Soc. Jpn. **52** (1983) 2231.
252. J. B. Goodenough, J. Solid State Chem. Phys. **48** (1968) 174.
253. J. Dijkstra, C.F. van Bruggen, and C. de Haas, J. Phys. Condens. Matter **1** (1989) 4297.
254. H. E. Brauer, H. I. Starnberg, L. J. Hollenboom, and H. P. Hughes, Surf. Sci. **333** (1995) 419.
255. M. Pouchard, A. Casalot, J. Galy, and P. Hagenmuller, Bull. Soc. Chim. Fr. **11** (1967) 4343.
256. Y. Kanke, E. Takayama-Muromachi, K. Kato, and Y. Mutsui, J. Solid State Chem. **89** (1990) 130.
257. J.M. Savariault, J.L. Parize, D.B. Tkatchenko, and J. Galy, J. Solid State Chem. **122** (1996) 1.
258. A.D. Wadsley, Acta Crystallogr. **8** (1955) 695.
259. J. Galy, A Casalot, M. Pouchard, and P. Hagenmuller, C.R. Acad. Sci. **262** (1966) 1055.
260. D. Ballivet-Tkatchenko, G. Delahay, J.L. Parize, J.M. Savariault, and J. Galy, Chem. Mater. **5** (1993) 1157.
261. Semiconductor surfaces and interfaces (4^{th} Edition) (ed. W. Mönch), Springer (2001).
262. Q. Wu, D. Ensling, B. Jäckel, D. Kraft, R. Hunger, C. Pettenkofer, A. Thißen, W. Jaegermann, V_2O_{5-x}-Paper, Surf. Sci. (in preparation)
263. A.F. Carley, S.D. Jackson, M.W. Roberts, and J.O'Shea, Surf. Sci. **454** (2000) 141.
264. Gmelins Handbuch der Anorganischen Chemie (ed. A. Kotowski), Springer, Berlin, vol. 21 (1965) pp. 508.
265. S.D. Elliott, and R. Ahlrichs, Phys. Chem. Chem. Phys. **2** (2000) 313.
266. A.D. Wadsley, Acta Cryst. **8** (1955) 695.

267. J.B. Goodenough, J. Solid State Chem. **1** (1970) 349.
268. S. Atzkern, S.V. Borisenko, M. Knupfer, M.S. Golden, J. Fink, A.N. Yaresko, V.N. Antonov, M. Klemm, and S. Horn, Phys. Rev. B **61** (2000) 12792.
269. G.T. Woods, G.P. Zhang, T.A. Callcott, L. Lin, G.S. Chang, B. Sales, D. Mandrus, and J. He, Phys. Rev. B **65** (2002) 165108.
270. W. Lamberrecht, B. Djafari-Rouhani, M. Lannoo, and J. Vennik, J. Phys. C **13** (1980) 2485.
271. D.B. Le, S. Passerini, A.L. Tipton, B.B. Owens, and W.H. Smyrl, J. Electrochem. Soc. **142** (1995) L102.
272. H.K. Park, and W.H. Smyrl, J. Electrochem. Soc. **141** (1994) L25.
273. H.K. Park, W.H. Smyrl, and M.D. Ward, J. Electrochem. Soc. **142** (1995) 1068.
274. A.L. Tipton, S. Passerini, B.B. Owens, and W.H. Smyrl, J. Electrochem. Soc. **143** (1996) 3473.
275. P.E. Stallworth, F.S. Johnson, S.G. Greenbaum, S. Passerini, J. Flowers, W. Smyrl, and J.J. Fontanella, Solid State Ionics **146** (2002) 43.
276. N. Troullier, and J.L. Martins, Phys. Rev. B **43** (1991) 1993.
277. M. Ceperley, and B.J. Alder, Phys. Rev. Lett. **45** (1980) 566.
278. F.P. Koffyberg, and F.A. Benko, Appl. Phys. Lett. **37** (1980) 320.
279. G. Amatucci, C.N. Schmutz, A. Blyr, A. Sigala, A.S. Gozdz, D. Larcher, and J.-M. Tarascon, J. Power Sources **69** (1997) 11.
280. R. Yazami, and P. Touzain, J. Power Sources **9** (1983) 365.
281. J. Friedel, Adv. Phys. **3** (1954) 3.
282. C.D. Wagner, D.A. Zatko, and R.H. Raymond, Anal. Chem. **52** (1980) 1445.
283. J.P. Contour, A. Salesse, M. Froment, M. Garreau, J. Thevenin, and D. Warin, J. Microsc, Spectrosc. Electrom. **4** (1979) 483.
284. M.K. Aydinol, and G. Ceder, J. Electrochem. Soc. **144** (1997) 3835.
285. L. Benco, J.-L. Barras, C.A. Daul, E. Deiss, Inorg. Chem. **38** (1999) 20.
286. R.B. Goldner, F.O. Arntz, G. Berera, T.E. Haas, G. Wei, aK. Wang, and P.C. Yu, Solid State Ionics **53-56** (1992) 617.
287. K.E. Swider-Lyons, C.T. Love, and D.R. Rolison, Solid State Ionics **152** (2002) 99. 126
288. W. Chen, Q. Xu, Y.S. Hu, L.Q. Mai, and Q.Y. Zhu, J. Mater. Chem. **12** (2002)1926.
289. Y. Sakurai, S. Okada, J. Yamaki, and J. Yamaki, J. Power Sources **20** (1987) 173.
290. W.Y. Liang, Microinics-Solid State Integrable Batteries (ed. M. Balkanski), North-Holland, Amsterdam, (1991) pp. 237-251.

291. C. Pettenkofer, W. Jaegermann, A. Kamaratos, and A. Papageorgopoulos, Solid State Commun. **84** (1992) 921.
292. H. E. Brauer, I. Ekvall, H. Olin, H. I. Starnberg, E. Wahlstrom, H. P. Hughes, and V. N. Strocov, Phys. Rev. B **55** (1997) 10022.
293. B. Woratschek, W. Sesselmann, J. Küppers, and G. Ertl , J. Chem. Phys. **86** (1987) 2411.
294. J.M. Cocciantelli, J.P. Doumer, M. Pouchard, M. Broussely, and J. Labat, J. Power Sources **34** (1991) 103.
295. J. Livage, A. Dasturel, and C. Sanchez, Solid State Ionics **1** (1980) 491.
296. A. Tranchant, J.M. Blengino, J. Farcy, and R. Messing, J. Electrochem. Soc. **13** (1992) 243.
297. S. Hub, A. Tranchant, and R. Messina, Electrochim. Acta **33** (1988) 997.
298. D.N. Anderson, and R.D. Willett, Acta Crystallogr. Sect. B **27** (1971) 1476.
299. W. Egelhoff, Surf. Sci. Rep. **6** (1987) 253.
300. G.Y. Guo, and W.Y. Liang, J. Phys. C **20** (1987) 4315.
301. P. Moreau, G. Ouvard, P. Gressier, P. Gannal, and J. Rouxel, J. Phys. Chem. Solids **57** (1996) 1117.
302. S. Aminpirooz, L. Becker, H. Rossner, A. Schellenberger, and E. Holub-Krappe, Surf. Sci. **331-333** (1995) 501.
303. H.I. Starnberg, H.E. Brauer, and H.P. Hugher, Surf. Sci. **377** (1997) 828.
304. D. Tonti, C. Pettenkofer, W. Jaegermann, D.C. Papageorgopoulos, M. Kamaratos, and C.A. Papageorgopoulos, Ionics **4** (1998) 93.
305. M. Abbate, H. Pen, M.T. Czyzyk, F.M.F. de Groot, J.C. Fuggle, Y.J. Ma, C.T. Chen, F. Sette, A. Fujimori, Y. Ueda, and K. Kosuge, J. Electro Spec. Relat. Pheno. **62** (1993) 185.
306. E. Deiss, A. Wokaun, J.-L. Barras, C. Daul, and P. Dufek, J. Electrochem. Soc. **144** (1997) 3877.
307. E.A. Meulenkamp, W. van Klinken, and A.R. Schlatmann, Solid State Ionics **126** (1999) 235.
308. J.E. Ortega, F.J. Himpsel, D. Li, and P.A. Dowben, Solid State Commun. **91** (1994) 807.
309. H.I. Starnberg, H.E. Brauer, P.O. Nilsson, L.J. Holleboom, and H.P. Hughes, Mod. Phys. Lett. B **8** (1994) 1261.

310. J.M. Tarascon, W.R. Mckinnon, F.Coowar, T.N. Bowmer, G. Amatucci, and D. Guyomard, J. Electrochem. Soc. **141** (1994) 1421.
311. Y. Gao, J.R. Dahn, J. Electrochem. Soc. **143** (1996) 100.
312. J.M. Tarascon, and D. Guyomard, J. Electrochem. Soc. **138** (1991) 2864.
313. G. Pistoia, G. Wang, and C. Wang, Solid State Ionics **58** (1992) 285.
314. J. Barker, R. Pynenburg, and R. Koksbang, J. Power Source **52** (1994) 185.
315. Y. Saidi, J. Barker, and R. Koksbang, J. Solid State Chem. **122** (1996) 195.
316. A. Yamada, and M. Tanaka, Mater. Res. Bull. **30** (1995) 715.
317. Y. Jang, B. Huang, F.C. Chou, D.R. Sadoway, and Y.-M. Chiang, J. Appl. Phys. **87** (2000) 7382.
318. C.B. Azzoni, M.C. Mozzati, A. Paleari, V. Massarotti, D. Capsoni, and M. Bini, Z. Naturforsch., A: Phys. Sci. **53** (1998) 693.
319. G.E. Grechnev, R. Ahuja, B. Johansson, and O. Eriksson, Phys. Rev. B **65** (2002) 174408.
320. M. Thackeray, W.I.F. David, P.G. Burce and J.B. Goddenough, Mater. Res. Bull. **18** (1983) 461.
321. D.M. Sherman, Am. Miner. **69** (1984) 788.
322. A. Yamada, and M. Tanaka, Mater. Res. Bull. **30** (1995) 715.
323. J. Sugiyama, T. Atsumi, A. Koiwai, T. Sasaki, T. Hioki, S. Noda, and N. Kamegashira, J. Phys. Condens. Matter. **9** (1997) 1729.
324. L.A. Montoro, M. Abbate, and J.M. Rosolen, J. Electrochem. Soc. **147** (2000) 1651.
325. J.W. Murray, J.G. Dillard, R. Giovanoli, H. Moers, and W. Stumm, Geochimica Cosmochimica Acta **49** (1985) 463.
326. R.P. Grupta and S.K Sen, Phys. Rev. B **10** (1974) 71.
327. R.P. Grupta and S.K. Sen, Phys. Rev. B **10** (1975) 15.
328. H.W. Nesbitt and D. Banerjee, American Mineralogist **83** (1998) 305.
329. H.W. Nesbitt, G.W. Cannng, and G.M. Bancroft, Geochimica et Cosmochimica Acta **62** (1998) 2097.
330. V.A.M.Brabers, F.M.van Setten, and P.S.A.Knapen, J. Solid State Chem. **49** (1983) 93.
331. C.Allen, S.J.Harris, J.A.Jutson, and J.M.Dyke, Appl. Surf. Sci. **37** (1989) 117.
332. M.Oku, K.Hirolawa, and S.Ikeda, J. Electron Spectrosc. Rel. Phen. **7** (1975)465.
333. R.J. Lad, and V.E. henrich, Phys. Rev. B **38** (1988) 10860.
334. J.P. Kemp and P.A. Cox, J. Phys.: Condens. Matter **2** (1990) 9653.
335. Shin-Puu Jeng, R.J. Lad, and V.E. Henrich, Phys. Rev. B **43** (1991) 11971.

336. J.C. Dupin, D. Gonbeau, H. Benqlilou-Moudden, Ph. Vinatier, and A. Levasseur, Thin Solid Films **384** (2001) 23.
337. Q. Zheng, J.R. Dahn, and K. Colbow, Phys. Rev. B **46** (1992) 2554.
338. A.J. Berlinsky, W.G. Unruh, W.R. McKinnon, and R.R. Haering, Solid State Commun. **31** (1979) 135.
339. W.R. McKinnon, Solid State Electrochem. (ed. P.G. Bruce), Cambridge University Press, Cambridge, (1995) Chap.7.

List of abbreviations

Acronyms:

2D	2 Dimensions
3D	3 Dimensions
AFM	Atomic Force Microscopy
BESSY	Berliner ElectromenSpeicherring Gesellschaft für Synchronstrahlung m.b.H.
CVD	Chemical Vapour Deposition
DOS	Density of States
EDC	Energy Distribution Curve
EMF	ElectroMotive Force
FWHM	Full Width at Half Maximum
LEED	Low Energy Electron Diffraction
OCV	Open Circuit Voltage
PES	Photoelectron Spectroscopy
PVD	Physical Vapour Deposition
RPES	Resonant Photoemission Spectroscopy
RT	Room Temperature
SDA	Spherical Deflection Analyzer
STM	Scanning Tunneling Microscopy
SXPS	Synchrotron induced X-ray Photoelectron Spectroscopy
T_D	Deposition Time
$T_{D,Li}$	Lithium deposition Time
$T_{D,Na}$	Sodium Deposition Time
UHV	Ultra High Vacuum
UPS	Ultra-violet Photoelectron Spectroscopy
XAS	X-ray Absorption Sepctroscopy
XPS	X-ray Photoelectron Spectroscopy
XRD	X-ray Diffraction

Experimental quantities

a, **b**, **c**	crystallographic axes

BE	binding energy
ΔE	energy resolution
E_{kin}	electrons kinetic energy
E_F	Fermi level
G	Gibbs' free energy
j	total angular momentum
l	orbital angular momentum quantum number
T	temperatur
V	voltage
x	guest concentration (relative to host)
α	asymmetry parameter
η	electrochemical potential
μ	chemical potential
φ	electrostatic potential
ϕ	Galvani potential
χ	surface potential
Φ	work function
λ_e	electrons free mean path
σ	ionization cross section
ν	photon frequency

Units

Å	Ångstron (1Å = 10^{-10} m)
eV	electronvolt (1eV = 1.6×10^{-19} J)
mbar	millibar (1mbar = 100 Pa)
mol	mole (1mol = $6.02 \cdot 10^{23}$ units of substance)

Constants

F	Faraday constant (9.648×10^4 C·mol^{-1})
h	Plank's constant (6.626×10^{-34} J·s)

Acknowledgements

First of all, I am very grateful to my supervisor Professor Wolfam Jaegermann for this great opportunity to carry out my Ph.D work in his group. It has been an extremely interesting and worthwhile time. I also would like to express my thanks to him for his never-ending enthusiasm and cheerfulness, constant support, encouragement and scientific guidance, especially for the solicitude in my living.

My sincerest thanks go to Dr. Andreas Thißen who has been supervising me and teaching me a good deal about physics. I have found working with you very inspiring. This thesis would not have been realised without your great encouragement and support.

A special thank to Marga Lang for all her help in my general living and the tedious paperwork.

I would like to say my thanks to Prof. K.-P Dinse and Mrs. Ulla Henkes for their help and support.

I also wish to thank Dr. Helmut Ehrenberg, Dr. Joachim Brötz, and Mr. Jean-Christophe Jaud for their help in XRD measurements.

I will keep a bunch of good memories of all the other past and present members of the surface science group: Dr. Thomas Mayer, Dr. Andreas Klein, Dr. Ralf Hunger, Dr. Stefan Gunst, Dr. Martin Beerbom, Dr. Elmar Wisotzki, Dr. A.B.M.O. Islam, Dr. Guangming Liu, Dr. Francisco Javier Fernández Madrigal, Dr. Mikhail Lebedev, Dipl.-Ing. Erich Golusda, Jochen Fritsche, Rainer Fritsche, Daniel Kraft, Frank Säuberlich, David Ensling, Bengt Jäckel, Thomas Schulmeyer, Ulrich Weiler, Yvonne Gassenbauer, Sebastian Taeger, and Martin Bepler. Thank you all for very fruitful scientific collaboration, uninterrupted discussion, and technical assistance whenever I needed it.

I am grateful to many people of the Materials Science Department for the friendly atmosphere there. I have had the pleasure of working with and meeting many people, whom I wish to express my sincere gratitude.

Finally, thank you, Sun Qi and Wu Minfeng for your love and support. I would have never made it without you.

Lebenslauf

Name	WU, Qihui
Sex	Male
Birthday	21 Aug. 1974
Place of Birth	Fujian, China
Family Status	Married, one children

Education:

09/93 – 07/97	Department of Chemistry, Xiamen University, B.Sc.
09/97 – 08/2000	State Key Lab Phys Chem Solid Surfaces, Department of Chemistry, Xiamen University, M.Sc.
08/2000 – Present	Materials Science Department, Darmstadt University of Technology, Ph.D.

Professional Experience:

02/98 – 01/99	Teaching Assistant, Department of Chemistry, Xiamen University.

Hiermit erkläre ich an Eides Statt, dass ich die vorliegende Dissertation selbständig und nur mit den angegebenen Hilfsmitteln ausgeführt habe.

Darmstadt, den 30.04.2003